MORPHOLOGICAL CONTROL OVER COVALENT ORGANIC FRAMEWORKS

A Dissertation

Presented to the Faculty of the Graduate School

of Cornell University

In Partial Fulfillment of the Requirements for the Degree of

Doctor of Philosophy

by

David Nelson Bunck

August 2014

MORPHOLOGICAL CONTROL OVER COVALENT ORGANIC FRAMEWORKS

David Bunck, Ph. D.

Cornell University 2014

Covalent organic frameworks (COFs) are an emerging class of fully crystalline polymers that are characterized by their high surface area and permanent porosity. COFs form as either stacks of sheets covalently bound in two-dimensions (2D) or networks with covalent bonds extending in all three-dimensions (3D). The layered structures of 2D COFs gives rise to intrinsically high charge mobilities and their synthesis as oriented films portends their use in photovoltaics and as supercapacitors. In contrast, few 3D COFs have been crystallized, and despite exhibiting exceptionally high surface areas (>4000 m^2 g^{-1}) and record low densities (0.17 cm^3 g^{-1}), these materials have no well-developed applications. Functionalizing their interior might harness these properties to furnish structurally precise platforms for catalysis, separations, and the storage and release of molecular payloads. Because these polymers are fully crystalline, structural features can be tuned to the atomic level, providing an additional level of control for materials design.

COF synthesis employs highly symmetric building blocks that are inherently devoid of additional reactive groups, impeding the synthesis of functional derivatives. We developed the first strategy to functionalize 3D COFs that avoids making inconvenient modifications to these monomers by employing a comonomer that bears a reduced number of structure-directing moieties while maintaining the geometry of the parent building block. We have defined this co-condensation as a truncated-mixed linker (TML) approach, because the additional monomer acts as a truncated derivative of the parent building block and is incorporated without modifying the framework's topology. Thus these truncated monomers are incorporated as defect sites throughout the network. Furthermore, the process of COF formation is poorly understood and is thought to rely on reversible covalent bond formation for error correction. The following observations indicate unambiguously that the rate of error correction must be slower than the rate of framework growth, a counterintuitive finding with implications for broadening the chemical scope of these polymerizations.

BIOGRAPHICAL SKETCH

David was born in Silver Spring, MD in 1986. In 1996, he moved to Verona, WI, a small farm town that was recently assimilated into Madison suburbs. In high school, he was fortunate to work as a sailing instructor, where his interest and excitement for both materials science and teaching flourished.

After graduating from high school in 2004, David began his undergraduate studies at the University of Wisconsin-Madison. His first research experience began in Jan 2006 in the laboratory of Professor Robert West investigating the reactivity of silylenes and germylenes. In Nov 2006, he took on a second undergraduate research position in the lab of Prof. Mahesh Mahanthappa, working at the time as the first and only researcher in the group. Upon completion of his project in June 2007, he left the West group to work full time on the frontiers of polymer chemistry. After burning through several projects, he began work studying Cobalt Mediated Radical Polymerization , which would eventually comprise his senior honors thesis. During the summer, David also participated in two NSF-sponsored Research Experience for Undergraduates programs. The first, during the summer of 2007, was in the laboratory of Prof. Frank S. Bates at the University of Minnesota, where he investigated toughening mechanisms for block copolymer and silica reinforced epoxies. The second, during the summer of 2008, was in the laboratory of Prof. Todd Emrick, where he worked on functionalizing TiO_2 nanorods with poly(3-hexylthiophene). In spring 2009, he graduated with honors with a Bachelors of Science in Chemistry and Religious Studies.

In the fall of 2009, David started his doctoral work at Cornell University where he was amongst the second cohort of graduate students to join the Dichtel Research Group. His research is summarized in the following pages and will not be elaborated here. In addition to graduate research, he was fortunate to participate in several extracurricular activities. In his first year, he cofounded the Graduate Association for Chemistry (GAC), a group to organize events for graduate students in the department. This organization established the department holiday party and poster session. Later, he also served on the Graduate and Professional Student Assembly (Chemistry Representative and Voting Member) as well as the University Assembly (Executive Vice Chair). Through these experiences, he was able to represent graduate student issues at monthly meetings with President David Skorton, lobby for science funding with NY state representatives in Washington D.C., and organize several campus-wide events to promote graduate student mental health and well-being.

In Fall 2014, he will begin his postdoctoral studies in the laboratory of Prof. James Heath at the California Institute of Technology working on developing high-affinity protein capture agents from oligopeptides.

Dedicated to the residents of the Central Wisconsin Center.

Nothing in here will improve your lives, but I hope my training helps me to.

ACKNOWLEDGEMENTS

I first need to acknowledge my thesis advisor Prof. William R. Dichtel, who was instrumental in both earning my Ph.D. and helping me learn how to approach scientific problems. I am extremely fortunate and grateful to have studied with someone who I can continue to look up to.

My two committee members, Profs. Geoff Coates and Chad Lewis, have also provided excellent feedback throughout my doctoral studies. In addition to insightful opinions on my science, they helped frame my presentation style through our literature lunches.

Throughout my life, I have had a scarcity of mentors, so I need to thank Prof. David Collum for being one during my graduate studies. I could always speak with him about chemistry (both the actual science as well as more philosophical topics), economics, investing, politics, and a myriad of other things. As a bonus, I always enjoyed the cheese sticks. I strive to balance being on top of my chemistry with being myself, like Prof. Collum successfully does.

I have been fortunate to mentor two extremely talented undergraduates during my time in the Dichtel group. I learned as much from them as they have working with me. I first have to thank Spencer Brucks, who helped me reshape my attitude during my time working with him. We met at a tough time of my graduate studies and Spencer was a constant reminder that a positive attitude goes a long way towards improving your environment. He is also an excellent listener, a rare attribute. His contributions were a major part of Chapter Four of this thesis. Jacqueline Carozza, who joined the Dichtel group after Spencer, has been equally inspiring to work with. Her constant curiosity with science and it's broader frameworks will take her to great places. Some of her contributions can be found in Chapter Six of this thesis.

There are, of course, many other Dichtel Group members who played critical roles in my doctoral studies. The first two are Drs. John Colson and Hasan Arslan, who were in my same cohort and helped me become a better scientist while teaching me its interpersonal side. Additional members who I must thank include Dr. Jason Mann, Dr. Eric Spitler, Dr. Arnab Mukjeree, Deepti Gopalakrishnan, Jenny Novotney, Kaylee Underkofler, Marissa Giovino, and Abraham Saldivar. While there will be many future generations of talented scientists in the Dichtel group, the culture and environment during the early years was truly unique. Since then, many talented students and postdocs have made their own contributions both to the group and on my own development. These include Dr. Colin Crick, Dr. Brian Smith, Dr. Fernando Uribe-Romo, Cathy DeBlase, Sam Hein, Ryan Bisbey, Xiangyu Zhang, Anton Chavez, David Fortman, and Chao Sun. They have entered an environment primed for success and it's amazing to see them flourish in it.

TABLE OF CONTENTS

LIST OF FIGURES

CHAPTER ONE

CHAPTER TWO

CHAPTER THREE

CHAPTER FOUR

CHAPTER FIVE

LIST OF TABLES

CHAPTER FOUR

CHAPTER FIVE

Chapter One: Morphological Control Over Framework Materials using Mixed Linker Strategies

Introduction

Framework materials are a class of polymers whose structures impart unique properties distinct from other macromolecular architectures. These materials are defined by their periodicity and permanent porosity, which results in exceptionally large surface areas and makes them privileged for applications in separations, payload storage and release, and catalysis. Framework crystallization employs reversible reactions, which facilitate the correction of defects, loops, and dangling chain ends during the polymerization to furnish ordered macromolecules. These materials can be divided into two classes. Metal-organic frameworks[1] (MOFs) contain organic subunits linked by coordination bonds, which are directed by metal ions or clusters known as secondary building units[2] (SBUs). The diverse set of metal coordination bonds and geometries provides an infinite number of potential network topologies, with thousands of MOFs described thus far. Covalent organic frameworks[3,4] (COFs) are an emerging class of framework materials linked by covalent bonds. These materials are mostly comprised of light elements such as C, B, O, and N. COFs employ linkages that are formed reversibly, including boronate esters,[5] imines,[6] and hydrazones,[7] to yield either layered 2D sheets or 3D nets. The 2D materials exhibit high intrinsic charge mobilities of interest for optoelectronic and energy-storage devices,[8] while 3D COFs exhibit exceptional surface areas (>4000 $m^2\ g^{-1}$) and record low densities (0.17 g cm^{-3}).[4, 9]

The majority of MOFs and COFs are high-symmetry structures synthesized from the minimum number of monomers (usually 1-2) dictated by their linkage chemistry. However, employing multiple monomers provides an opportunity to access frameworks with new properties. Frameworks might be functionalized to improve their gas adsorption behavior, enable

covalent attachment of molecular payloads, or to include active catalysts. In this Chapter, we highlight three strategies for functionalizing framework materials by cocrystallizing mixtures of organic building blocks. These strategies are illustrated in Figure 1.1 for a cubic framework.

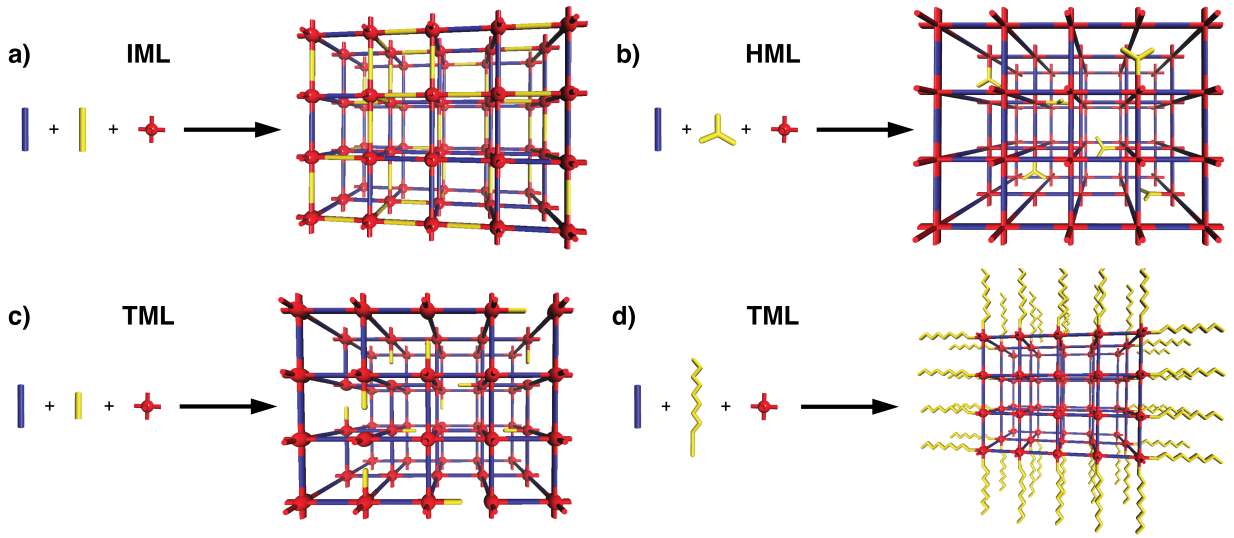

Figure 1.1 Illustrations of the (a) isostructural mixed linker (IML), (b) heterostructural mixed linker (HML), and (c, d) two outcomes of truncated mixed linker (TML) approaches to framework functionalization.

The first and most straightforward method is an isostructural mixed linker (IML) approach, which involves mixing two or more monomers with identical linking geometry.[10] The IML approach is often employed to incorporate reactive functionality along the walls of a framework. Alternatively, monomers bear different linkage geometries in a heterostructural mixed linker (HML) strategy. At some monomer feed ratios, the resulting framework distributes the minority component throughout a defective lattice of the majority component. However, certain ratios provide lower symmetry topologies that are less prone to forming interpenetrated structures. The last strategy employs a second monomer with a reduced number of functional groups, denoted as a truncated mixed linker (TML) approach. Here, the second monomer acts as a capping agent that, depending on the kinetics of framework crystallization, either directs crystallite morphology and surface chemistry or enables functionalization of the framework interior.

Isostructural Mixed Linker Approaches

Perhaps the most simple and versatile way to incorporate multiple monomers into framework materials is to crystallize them using two or more organic building blocks with identical size and linkage chemistry, denoted as an isostructural mixed linker (IML) approach.[10, 11] For example, combining two (or more) terephthalic acid derivatives yields the mixed-composition MOF-5 cubic framework (Figure 1.2). Mixing multiple isostructural monomers provides a simple means to change framework properties, such as surface area, pore volume, reactivity, sorbant selectivity, and loading capacity, by varying the identity and ratio of these building blocks. The

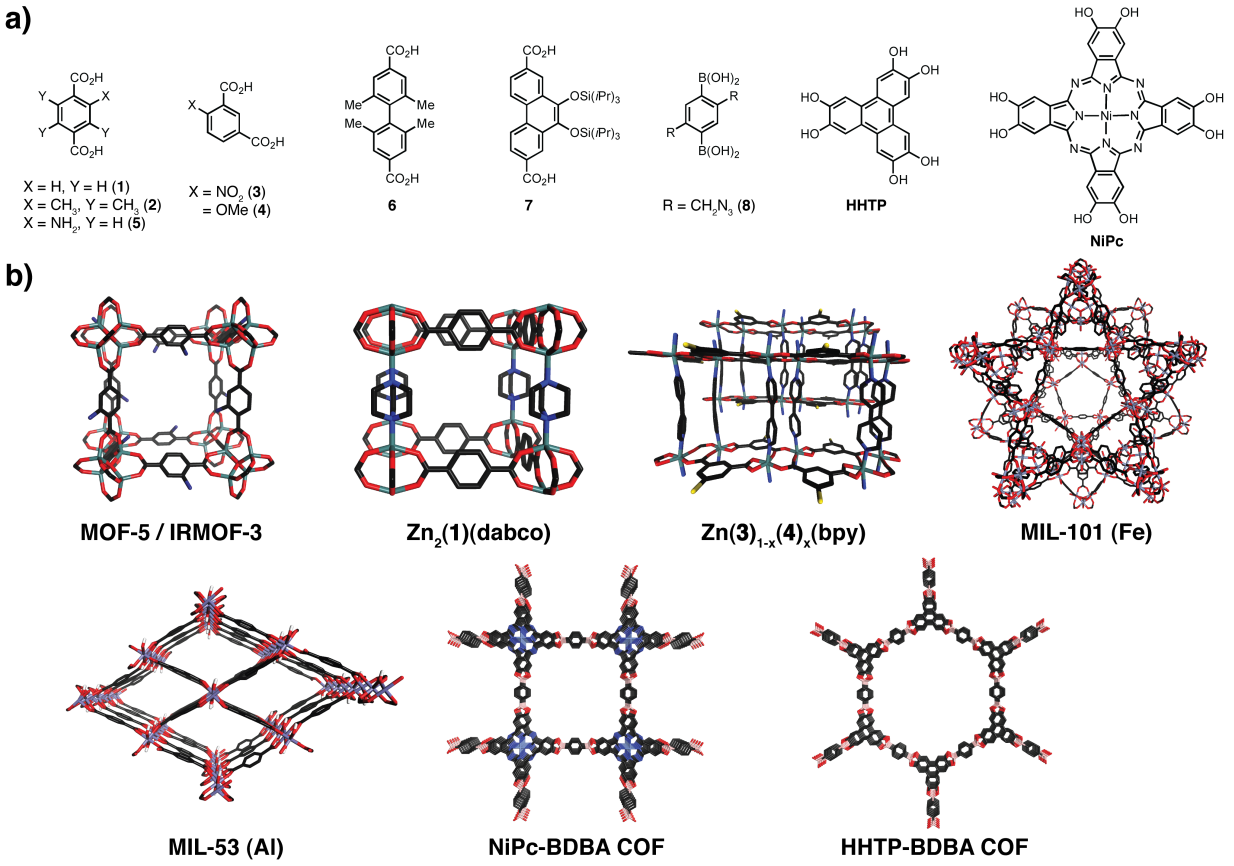

Figure 1.2 (a) Monomers employed in the IML strategy with (b) depictions of their corresponding frameworks.

IML strategy sometimes provides frameworks with emergent properties distinct from the corresponding single component MOFs, as has been demonstrated in several examples highlighted below.

To the best of our knowledge, Kim and coworkers were the first to employ the IML strategy when they incorporated a mixture of terephthalic acid (**1**) and tetramethylterephthalic acid (**2**) into the [Zn_2(**1**)$_2$dabco] framework (Figure 1.2b).[12] The two monomers were incorporated into the framework in a 1:1 ratio, matching their feed ratio, as determined by ^{1}H NMR of the digested MOF. Refinement of the site occupancy factors for **1** and **2** derived from single-crystal X-ray diffraction revealed equal contributions from each monomer throughout the framework, suggesting that they are distributed randomly throughout the MOF. Materials with increased fractions of **2** exhibited linear decreases in surface area over three data points (0, 50, and 100 mol% **2**). These data suggest that many framework properties of IML MOFs will scale linearly between those of MOFs derived from the individual linkers in the absence of cooperative effects.

Kitagawa and coworkers subsequently tuned pore flexibility across a series of MOFs containing varying ratios of 5-nitroisophthalic acid (**3**) and 5-methoxyisophthalic acid (**4**) within a [Zn(**3**)$_{1-x}$(**4**)$_x$(bpy)] network (Figure 1.2b).[13] At ambient pressure, the pure [Zn(**4**)(bpy)] MOF adopts an open-pore structure and the [Zn(**3**)(bpy)] MOF is nonporous. However, [Zn(**3**)(bpy)] undergoes a nonporous to porous transition at a specific gate-opening pressure (P_{go}). Frameworks containing mixtures of **3** and **4** showed a tunable P_{go} for CO_2 adsorption, and a network containing 13% **4** (x = 0.13) showed promise for separating CO_2 from CH_4. In contrast, the permanently porous [Zn(**4**)(bpy)] MOF adsorbed CO_2 and CH_4 nonselectively.

Several studies have employed mixtures of terephthalic acids to load specific functionality into the pores of various frameworks, including MOF-5 (based on Zn),[14] MIL-53 (Al),[15, 16] and MIL-101 (Fe)[17] (Figure 1.2b). Baiker and coworkers characterized the thermal stability of amine-functionalized MOF-5 derivatives and used these amines both as nucleophilic catalysts[18] and as ligands for Pd-catalyzed cross-coupling reactions.[19] The authors also characterized the phase purity of mixed component frameworks using convenient thermogravimetric analysis (TGA) measurements.[15] Cohen and coworkers incorporated amine- and bromoterephthalic acids into MOF-5 to demonstrate sequential and orthogonal reactions of these two groups, providing a means to prepare elaborate MOFs with multiple pendant functionalities.[20] More recently, the same group obtained IML frameworks through postsynthetic ligand exchange, in which a second functionalized monomer was substituted into the intact framework.[21] Lin and coworkers recently used the IML approach to load biologically relevant payloads into MIL-101,[17] including a fluorescent dye and a cisplatin prodrug. HT-29 human colon adenocarcinoma cells show uptake of silica-coated, fluorescently labeled MIL-101-NH_2 nanoparticles, suggesting that such functionalized MOFs might be useful materials for bioimaging and drug-delivery applications.

Matzger and coworkers highlight another useful aspect of the IML approach using the MOF-5/IRMOF-3 system, in which a building block that crystallizes reliably is used to template the formation of a MOF whose monomers otherwise crystallize poorly.[22] The authors identified conditions in which **5** and $Zn(NO_3)_2$ yield crystalline, high surface area IRMOF-3, but using **1** produces phase-impure, low surface area MOF-5. Cocrystallizing the two building blocks provided high surface area materials over a wide range of monomer ratios, even as low as 10% **5** (Figure 1.3a). Interestingly, this MOF also showed a higher surface area than even the pure

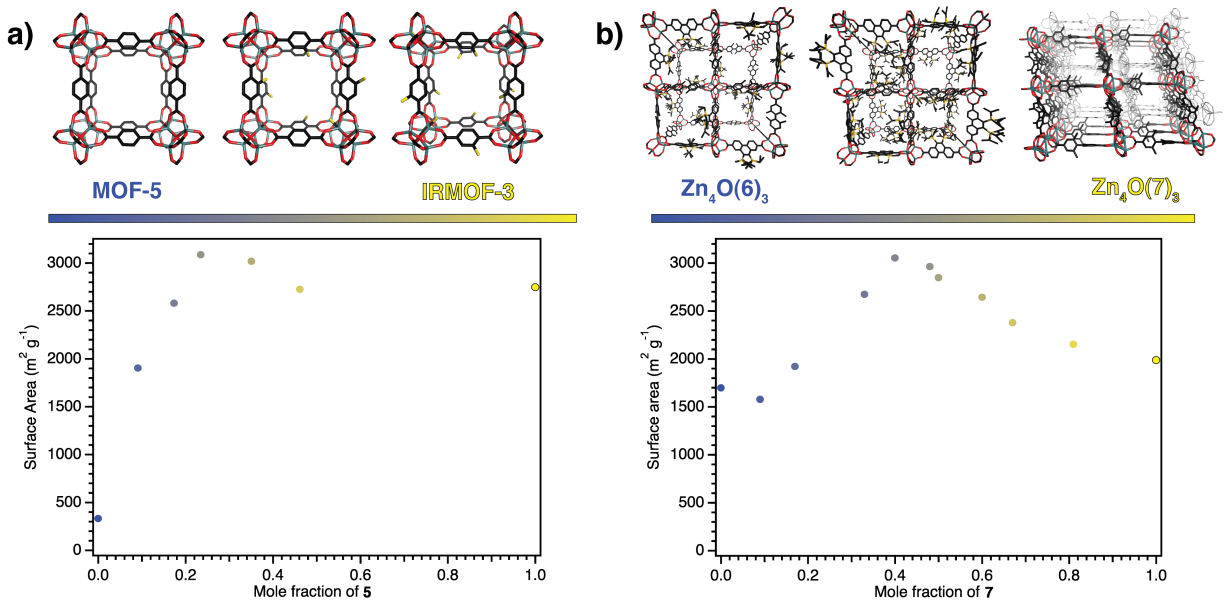

Figure 1.3 (a) Cocondensation of **1** and **5** yield IML frameworks with higher surface area than either single-component framework. (b) Incorporating **7** into MOFs composed of **6** prevents framework interpenetration and also provides increased surface area.

IRMOF-3. While MOF-5 can be crystallized effectively under other conditions, this approach, if general, could streamline the empirical and often labor-intensive process of identifying growth conditions for new or poorly behaved building blocks.

The same report also describes an approach to suppress MOF interpenetration, in which one or more additional networks form within the pore volume of the first.[22] This phenomenon arises from free volume effects, often occurring in highly symmetric networks containing long linkers. Interpenetrated MOFs typically exhibit decreased pore volume and surface area and increased density. For example, a framework formed exclusively from dicarboxylate **6** yields a doubly interpenetrated structure with a Brunauer-Emmett-Teller surface area (S_{BET}-N_2) of 1700 m^2 g^{-1}. This surface area increases as phenanthrene dicarboxylate **7** is incorporated into the material, up to 3000 m^2 g^{-1}, at 40% **7** (Figure 1.3b). The powder X-ray diffraction patterns of the mixed composition MOFs indicated the preferential formation of noninterpenetrated cubic

phases, although interpenetrated networks were also observed in many cases. The results from this study highlight the utility of the IML approach for crystal engineering.

Yaghi and coworkers demonstrated the versatility of the IML strategy by preparing eighteen mixed-composition MOF-5 derivatives using nine substituted terephthalic acid building blocks.[23] Nine of these MOFs were comprised of binary mixtures, while the other nine were ternary or higher order. Remarkably, two different ternary mixtures showed increased H_2 storage capacity and adsorption selectivity for CO_2 over CO. In separate work, Yaghi and coworkers used an IML approach to prepare MOFs linked by binary mixtures of imidazolates, often referred to as zeolitic imidazolate frameworks (ZIFs).[24, 25] ZIFs containing two different imidazole linkers exhibited higher CO_2/CO selectivities compared to single component ZIFs or the ternary MOF-5 derivatives.[26] These MOFs of increasingly complex composition will inspire significant future challenges of rationally predicting the properties of binary, ternary, and higher order frameworks, given that the number of possible materials increases exponentially with the number of building blocks. It will also be important to measure the reactivity ratios of each monomer, as Yaghi and coworkers showed that the composition of several of their binary MOFs did not reflect the monomer feed ratios. Disparate rates of nucleation and incorporation could produce individual crystals with varying local compositions or the formation of single-monomer domains.

Jiang and coworkers used an IML approach to functionalize the pores of 2D COFs.[27] Benzyl azide moieties were incorporated into the pores of the known HHTP-BDBA (COF-5) and NiPc-BDBA COF (Figure 1.2b) lattices by modifying the diboronic acid building block **8**. The amount of azide incorporated into each material was varied by changing the [**8**]:[BDBA] feed ratio. After COF formation, the azide groups were transformed into 1,4-triazoles using the Cu-

catalyzed azide-alkyne cycloaddition (CuAAC) reaction, a transformation previously used to functionalize alkyne-containing MOFs. The efficiency of the CuAAC reaction was characterized through the disappearance of the azide stretch using FTIR spectroscopy when large excesses of the alkynes (>80 equivalents per azide) were employed. A reduced S_{BET}-N_2 was observed as a consequence of filling the pores with new functionality. These results indicate that postsynthetic functionalization of COFs can be performed in a similar fashion to MOFs,[28] offering a means to engineer the pores of this emerging class of materials.

As is evident from the above examples, the IML approach is an intuitive and well-established method to modify framework properties and incorporate additional functionality into the pores. Its key advantage is that the framework topology is retained[29] as the structures and relative ratios of the monomers are varied. Nevertheless, the structures of IML-derived materials are less defined than their corresponding single-component networks and offer additional challenges in their characterization. Many existing reports assume that the building blocks are randomly mixed throughout the materials, but differences in reactivity or compatibility between monomers, as observed in some of the above studies, might lead to heterogeneous distributions, such as radial gradients, core-shell architectures, or even segregation into single-component domains. Each of these phenomena is an intriguing possibility and should be considered when evaluating new systems. Characterizing the precise locations of each monomer is challenging in most cases and might benefit from advances in spectroscopy. On the bulk scale, TGA can infer and quantify the presence of phase impurities, but diagnostic bimodal differential mass loss curves have also been observed for imidazolate-linked MOFs (ZIFs) with monodisperse pore-size distributions.[25] Single crystal X-ray diffraction is a powerful tool for atomic-scale characterization, but is unable to resolve the nonperiodic arrangements of multiple monomers

throughout the framework. In one notable example, the two isostructural linkers used to make a series of imidazolate-linked MOFs occupied crystallographically distinct sites, allowing for their exact locations to be identified.[30] Yaghi and coworkers also demonstrated homogeneous distribution over 100 μm length scale by dividing large single crystals of two-component MOF-5 derivatives and analyzing their composition.[23] Developing a molecular-level understanding, along with an improved ability to predict the properties of binary, ternary, and even higher order IML frameworks, will provide a rational means to explore the vast chemical space available through the IML strategy. Mixing isostructural linkers has proven to be a simple and effective way to enhance framework properties and enabled the synthesis of COFs with tunable functionality. The stage is now set for using mixed-composition networks, combined with modular pore-functionalization strategies, to obtain otherwise inaccessible high-performance porous materials.

Heterostructural Mixed Linker Approaches

Though less intuitive than the IML strategy, mixing building blocks with different coordination geometries, denoted as a heterostructural mixed linker (HML) approach, provides opportunities to functionalize existing frameworks and to access lower symmetry topologies with large pore sizes. First demonstrated in MOF synthesis in 2003,[31] HML topologies show a strong dependence on the monomer feed ratio and linker length, resulting in reduced predictability over network topology that complicates rational design. Contemporary studies continue to explore the design criteria for HML MOFs while optimizing their promising framework properties.

Matzger and coworkers performed the first rigorous study of a MOF derived from the HML strategy, in which **1** and a trifunctional carboxylic acid (**9**) were cocrystallized in the presence of $Zn(NO_3)_2$.[32] On their own, **1** produces MOF-5, and **9** produces MOF-177 (Figure

1.4). Cocrystalization of the two linkers produces a new MOF (UMCM-1) containing 3.1 nm mesoporous hexagonal channels surrounded by 1.4 nm microporous cages. Mesoporous crystalline networks are less common than their microporous counterparts, because they are susceptible to pore collapse or interpenetration. Avoiding these phenomena is crucial for achieving high H_2 storage capacities.[33] The HML approach, along with other strategies to desymmetrize MOF building blocks,[34] show great promise in this area. UMCM-1 is non-interpenetrated and retains its high surface area (4160 m^2 g^{-1}) even after heating at 300 ºC for 3 h. Its formation is notably dependent on the building block feed ratio, crystallizing exclusively at ratios between 3:2 and 1:1 of **1**:**9**. Outside of this range, excess **1** produced either MOF-5 loaded with **9** occupying defect sites or physical mixtures of the two MOFs. Similarly, excess **9** produced either MOF-177 containing small amounts of **1** or mixtures of MOF-177 and UMCM-1 (Figure 1.4).

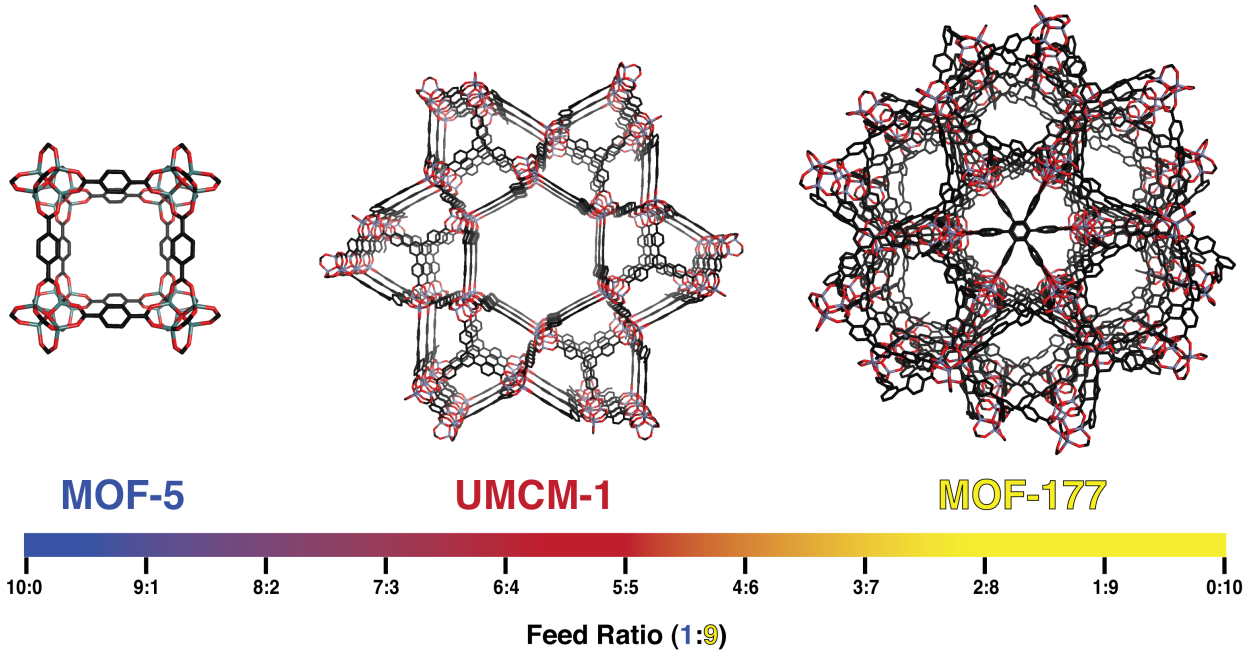

Figure 1.4 Phase diagram for UMCM-1 synthesis.

Interestingly, the phase window for forming UMCM-1 does not correspond to its 1:1.33 ratio of **1**:**9** found in the framework. The authors rationalized this finding by calculating the probability of the possible coordination modes of the two linkers to the Zn_4O secondary building unit (SBU). This study suggested that the maximum probability of forming the SBU coordination geometry found in UMCM-1 matched the feed ratios that yielded it in phase pure form. This model offers a first step towards rational design of HML frameworks and highlights the open question of which factors influence their growth. Once conditions likely to produce phase-pure materials were identified, other linear dicarboxylates were used in place of 1 to provide other HML MOF topologies (Figure 1.5).[35] It is thought that the relative sizes of the two linkers influence which of these networks are formed. These topological differences have important consequences for guest uptake and release, as illustrated by the vastly different diffusion behaviors observed in a single-molecule study of diffusion within the pores of UMCM-1, -2, and -4.[36]

UMCM-2 is synthesized from mixtures of **9** and benzodithiophene (**10**) and adopts a similar structure to UMCM-1, with microporous cages surrounding a central micropore, but the central micropore is blocked by the trifunctional linker and is surrounded by two distinct microporous cages.[37] UMCM-2 exhibits an exceptionally high BET surface area (5200 $m^2\ g^{-1}$). Interestingly, improvement in H_2 storage capacity (6.9 wt% at 77 K and 46 bar) is not commensurate with its exceptional surface area. Subsequent studies on UMCM-1 revealed the H_2 storage capacity to be 6.23 wt% at 77 K and 20 bar, which was predicted to be as high as 9.5 wt% at elevated pressure (100 bar).[38]

The increased pore size in UMCM-1 has also been exploited for postsynthetic modification. Cohen and coworkers synthesized an amine functionalized UMCM-1 derivative

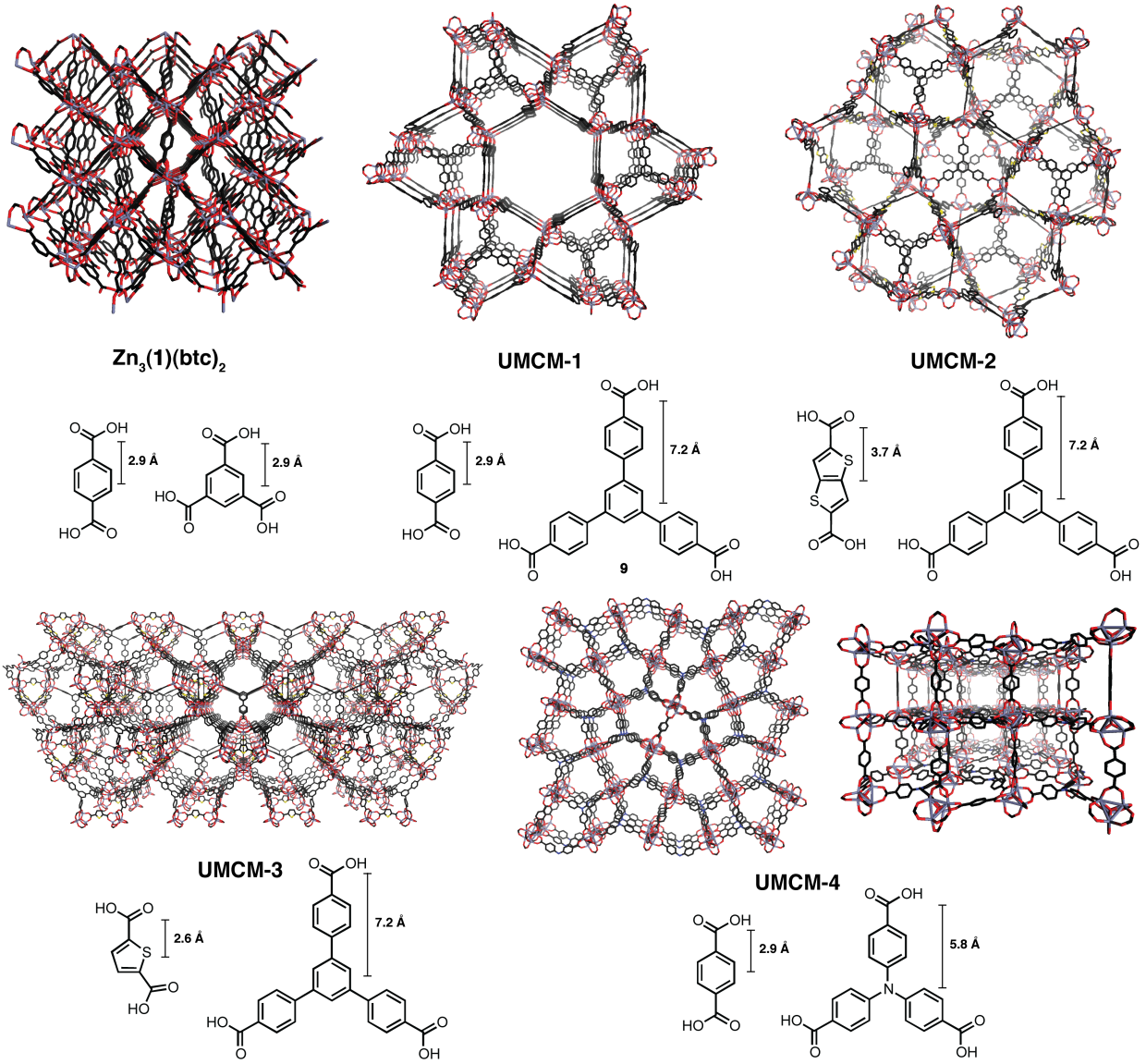

Figure 1.5 Small variations of relative linker lengths of mixtures of di- and trifunctional linkers dramatically affect the topologies of HML MOFs.

(UMCM-1-NH_2) by replacing **1** with **2**.[39, 40] Acylation of the amines in the pores of UMCM-1-NH_2 with increasingly bulky carboxylic acid anhydrides indicated that its larger pores accommodated longer alkyl chains relative to amines located within cubic MOFs.[39] Cohen and coworkers subsequently demonstrated that terminal olefins introduced into UMCM-1-NH_2 undergo Diels-Alder cycloadditions with an s-tetrazine.[40] UMCM-1-NH_2 was also condensed

with 2-formylpyridine, providing a chelate for Pd^{2+} ions, although its catalytic properties were not investigated.[41] Kaskel and coworkers condensed a terephthalic acid derivative bearing a S-oxazolidinone to yield optically active UMCM-1.[42] When employed as an HPLC stationary phase, this MOF separated enantiomers of 1-phenylethanol with a moderate but unoptimized selectivity factor (α) of 1.6 and resolution (R_S) of 0.65. The wide variety of potential functional groups that might be incorporated into its large pores make UMCM-1 derivatives promising from the standpoint of framework integrity and internal accessibility. Elsewhere on the UMCM-1 phase diagram, Matzger and coworkers noted the presence of phase pure MOF-5 containing **9** within the crystal.[43] **9** is presumed to occupy defect sites within the lattice, leaving free carboxylic acids within the pores. Exposing this framework to $Pd(OAc)_2$ yields Pd^{2+}-functionalized materials capable of catalyzing C-H activation. Interestingly, the regioselectivity for the arylation of naphthalene changed from 1-phenylnaphthalene to 2-phenylnaphthalene when using the MOF catalyst as compared to dissolved $Pd(OAc)_2$.

As shown from the examples above, the HML strategy provides access to unavailable topologies and larger pore sizes not easily achieved in single component frameworks. These desirable properties come at the expense of the predictability of the network topology. Small changes in both the di- and trifunctional linker sizes induce significant topological differences, directly impacting framework properties. Existing frameworks were rationalized empirically and great opportunity lies in the ability to predict topologies and phase windows in HML systems.

Truncated Mixed Linker Approaches

A third strategy to obtain multicomponent frameworks employs a truncated mixed-linker (TML) approach, in which a polyfunctional monomer is cocondensed with a monomer bearing fewer reactive groups. The relative rates of bond formation and exchange dictate the role of the

truncated monomer in the crystallization. If growth is faster than exchange, the truncated monomer is incorporated throughout the network, which grows around these defect sites. If exchange is rapid relative to framework growth, the truncated monomer will preferentially reside at the faces of the growing crystal, providing a means to control its size, shape, and surface functionality.

Operating in the slow exchange regime, we recently utilized the TML strategy to functionalize the interior of a boroxine-linked 3D COF (COF-102) derived from the dehydration of tetrakis(boronic acid) **11**.[44] A second monomer, bearing either a n-dodecyl (-$C_{12}H_{25}$) or allyl group in place of one phenylboronic acid moiety, was included in the crystallization (Figure 1.6).

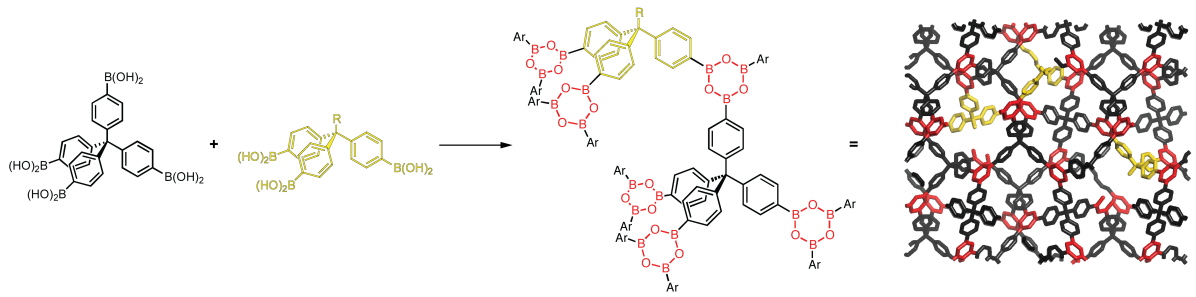

Figure 1.6 Truncated monomers included in COF-102 crystallization yield functionalized frameworks.

The rate of incorporation of the dodecyl-truncated comonomer into the framework scaled with the feed ratio and the resulting frameworks were essentially indistinguishable from pristine COF-102 by scanning electron microscopy (SEM) and powder X-ray diffraction (PXRD). The S_{BET}-N_2 and pore volume of the functionalized materials were inversely proportional to dodecyl loading, consistent with the alkyl chains occupying the interior pore volume. The presence of the truncated monomer within the framework was supported by a TEM study in which crystallites of allyl-functionalized COF-102 were stained with OsO_4 and microtomed, revealing the presence of

Os within their interior. Loadings of up to 33% truncated monomer were observed, offering an opportunity for facile loading of these high surface area materials with large amounts of payload

The Kitagawa group used the TML strategy under faster exchange conditions to grow microporous nanorods of the Cu_2(**12**)(dabco) framework, which has carboxylate-Cu coordination oriented in the [100] direction and N-Cu coordination in the [001] orientation (Figure 1.7).[45] Including acetic acid during the crystallization results in competitive coordination with **12**, thus slowing growth in the [100] direction. Growth in the [001] direction remains uninhibited, yielding anisotropic nanorods. A study of the crystallization process using TEM revealed nanoparticle formation at short growth times, which aggregate into cubic structures that grew selectively in the [001] direction.

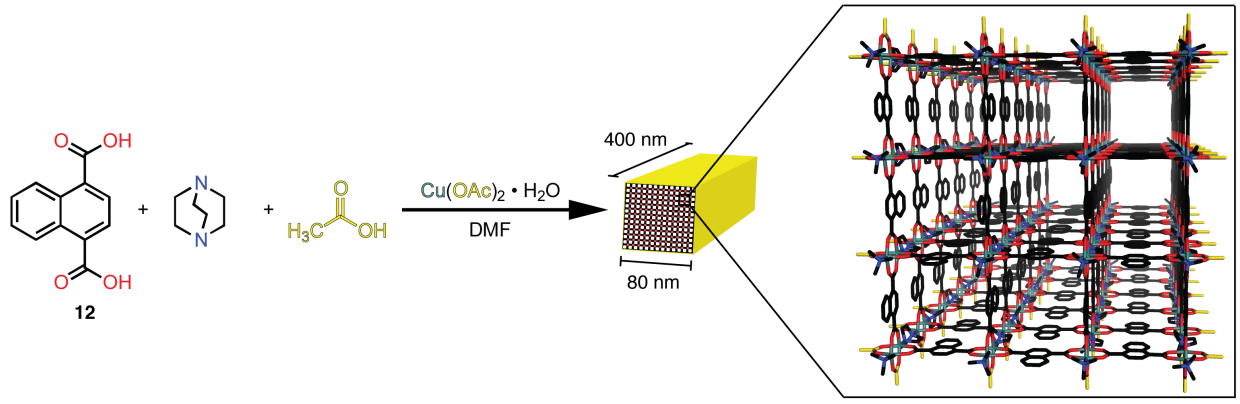

Figure 1.7 Acetic acid mediates the growth of the [100] face of Cu_2(**12**)(dabco), favoring nanorod growth in the [001] direction.

The Kitagawa group subsequently demonstrated similar morphological control in MOFs linked exclusively by metal-carboxylate coordination.[46] Increasing concentrations of lauric acid included in a prenucleation step with $Cu(NO_3)_2$, followed by subsequent framework growth with benzenetri(carboxylic acid) (btc), provided the $Cu_3(btc)_2$ framework with varying crystallite morphologies. These morphologies changed from octahedral to cuboctahedral to cubic as the

lauric acid concentration was increased. Monte-Carlo simulations of a coarse grain model of this framework suggested that the observed morphologies were consistent with the lauric acid preferentially inhibiting growth at the [100] face. Prenucleation and subsequent framework growth also yielded oriented cuboctahedral and cubic crystallites on bare Au substrates, representing a straightforward protocol for orienting MOFs through crystal engineering strategies.

Yaghi and coworkers applied a similar TML approach to the cubic MOF-5 structure, whose symmetry precludes selective directional growth.[47] In this case, MOF-5 crystallizes in the presence of varying amounts of a dodecyloxybenzoic acid and yields macroporous crystallites that retain the cubic framework structure, a morphology reminiscent of Swiss cheese. Interestingly, digested solutions of these materials did not contain the dodecyloxybenzoic acid, suggesting that it was washed out of the macroporous structures during isolation or activation. This change in crystallite morphology was associated with a reduced Langmuir surface area as measured by N_2 adsorption, yet these samples showed increased capacity for CO_2.

The TML approach operates across a broad continuum of exchange and error correction rates, providing outcomes ranging from internal functionalization to anisotropic crystallization. These results also highlight the unanswered question of what reaction and exchange rates are required for framework formation. COF-102 growth occurred too rapidly for truncated monomers to be removed through boroxine exchange reactions, demonstrating that rapid exchange is not necessary for framework crystallization. Faster exchange enabled engineering of the size and shape of MOF crystallites, allowing specific morphologies to be targeted. Currently, reaction exchange rates are uncontrolled and often rationalized empirically after framework synthesis. An improved understanding of the kinetics of exchange as it relates to framework

growth will provide fundamental insight into reliably applying the TML strategy. This strategy also parallels the field of molecular capsules, in which all linkers are truncated. In 1990, Fujita first employed an intuitive design approach whereby a metal vertex and organic linker predictably formed a square-shaped macrocycle following fundamental geometric principles.[48] This directional bonding approach, which predates all but the earliest three-dimensional coordination networks,[49] has since been applied to a wide range of 2D and 3D structures.[50] Knowledge gained in this field over the past two decades serves as a basis for understanding the related chemistry involved in TML framework synthesis. Further investigation into the kinetics of crystallization using the TML strategy will elucidate the role of the truncating agent, enabling reliable crystal engineering or framework functionalization as dictated by the specific application.

Outlook

The three mixed linker strategies highlighted in this Chapter enable the synthesis of functionalized topologies and underline their potential use in separations, payload storage and release, and catalysis. The focus of the framework materials field is now broadening beyond established applications, such that designing functional platforms whose properties can be tuned modularly is increasingly important. Moving from empirical to rational design remains an outstanding challenge among each of the mixed linker strategies. Predicting emerging properties (via IML), framework topologies (via HML), and crystallization kinetics (via TML) represent important frontiers for which improved understanding will enhance framework utility. These strategies will also provide a means to optimize many framework properties, including gas sorption, loading/release kinetics, and improvements in catalytic performance.

References

(1) J. R. Long, O. M. Yaghi, *Chem. Soc. Rev.* **2009**, *38*, 1213.

(2) D. J. Tranchemontagne, J. L. Mendoza-Cortés, M. O'Keeffe, O. M. Yaghi, *Chem. Soc. Rev.* **2009**, *38*, 1257.

(3) a) X. Feng, X. Ding, D. Jiang, *Chem. Soc. Rev.* **2012**, *41*, 6010; b) A. P. Côté, A. I. Benin, N. W. Ockwig, M. O'Keeffe, A. J. Matzger, O. M. Yaghi, *Science* **2005**, *310*, 1166.

(4) H. M. El-Kaderi, J. R. Hunt, J. L. Mendoza-Cortés, A. P. Côté, R. E. Taylor, M. O'Keeffe, O. M. Yaghi, *Science* **2007**, *316*, 268.

(5) a) E. L. Spitler, W. R. Dichtel, *Nature Chem.* **2010**, *2*, 672; b) E. L. Spitler, M. R. Giovino, S. L. White, W. R. Dichtel, *Chem. Sci.* **2011**, *2*, 1588; c) E. L. Spitler, B. T. Koo, J. L. Novotney, J. W. Colson, F. J. Uribe-Romo, G. D. Gutierrez, P. Clancy, W. R. Dichtel, *J. Am. Chem. Soc.* **2011**, *133*, 19416; d) R. W. Tilford, W. R. Gemmill, H.-C. zur Loye, J. J. Lavigne, *Chem. Mater.* **2006**, *18*, 5296; e) E. L. Spitler, J. W. Colson, F. J. Uribe-Romo, A. R. Woll, M. R. Giovino, A. Saldivar, W. R. Dichtel, *Angew. Chem. Int. Ed.* **2012**, *51*, 2623.

(6) a) S.-Y. Ding, J. Gao, Q. Wang, Y. Zhang, W.-G. Song, C.-Y. Su, W. Wang, *J. Am. Chem. Soc.* **2011**, *133*, 19816; b) F. J. Uribe-Romo, J. R. Hunt, H. Furukawa, C. Klöck, M. O'Keeffe, O. M. Yaghi, *J. Am. Chem. Soc.* **2009**, *131*, 4570.

(7) F. J. Uribe-Romo, C. J. Doonan, H. Furukawa, K. Oisaki, O. M. Yaghi, *J. Am. Chem. Soc.* **2011**, *133*, 11478.

(8) a) J. W. Colson, A. R. Woll, A. Mukherjee, M. P. Levendorf, E. L. Spitler, V. B. Shields, M. G. Spencer, J. Park, W. R. Dichtel, *Science* **2011**, *332*, 228; b) S. Wan, J. Guo, J. Kim, H. Ihee, D. Jiang, *Angew. Chem. Int. Ed.* **2008**, *47*, 8826; c) S. Wan, J. Guo, J. Kim, H. Ihee, D. Jiang, *Angew. Chem. Int. Ed.* **2009**, *48*, 5439.

(9) H. Furukawa, O. M. Yaghi, *J. Am. Chem. Soc.* **2009**, *131*, 8875.

(10) A. D. Burrows, *CrystEngComm* **2011**, *13*, 3623.

(11) A. D. Burrows, C. G. Frost, M. F. Mahon, C. Richardson, *Angew. Chem. Int. Ed.* **2008**, *47*, 8482.

(12) H. Chun, D. N. Dybtsev, H. Kim, K. Kim, *Chem. Eur. J.* **2005**, *11*, 3521.

(13) T. Fukushima, S. Horike, Y. Inubushi, K. Nakagawa, Y. Kubota, M. Takata, S. Kitagawa, *Angew. Chem. Int. Ed.* **2010**, *49*, 4820.

(14) A. D. Burrows, L. C. Fisher, C. Richardson, S. P. Rigby, *Chem. Commun.* **2011**, *47*, 3380.

(15) S. Marx, W. Kleist, J. Huang, M. Maciejewski, A. Baiker, *Dalton Transactions* **2010**, *39*, 3795.

(16) a) Y. Huang, S. Gao, T. Liu, J. Lü, X. Lin, H. Li, R. Cao, *ChemPlusChem* **2012**, *77*, 106; b) T. Lescouet, E. Kockrick, G. Bergeret, M. Pera-Titus, S. Aguado, D. Farrusseng, *J. Mater. Chem.* **2012**, *22*, 10287.

(17) K. M. L. Taylor-Pashow, J. D. Rocca, Z. Xie, S. Tran, W. Lin, *J. Am. Chem. Soc.* **2009**, *131*, 14261.

(18) W. Kleist, F. Jutz, M. Maciejewski, A. Baiker, *Eur. J. Inorg. Chem.* **2009**, *2009*, 3552.

(19) W. Kleist, M. Maciejewski, A. Baiker, *Thermochim. Acta* **2010**, *499*, 71.

(20) M. Kim, J. F. Cahill, K. A. Prather, S. M. Cohen, *Chem. Commun.* **2011**, *47*, 7629.

(21) a) M. Kim, J. F. Cahill, Y. Su, K. A. Prather, S. M. Cohen, *Chem. Sci.* **2012**, *3*, 126; b) M. Kim, J. F. Cahill, H. Fei, K. A. Prather, S. M. Cohen, *J. Am. Chem. Soc.* **2012**, *134*, 18082.

(22) T.-H. Park, K. Koh, A. G. Wong-Foy, A. J. Matzger, *Cryst. Growth Des*. **2011**, *11*, 2059.

(23) H. Deng, C. J. Doonan, H. Furukawa, R. B. Ferreira, J. Towne, C. B. Knobler, B. Wang, O. M. Yaghi, *Science* **2010**, *327*, 846.

(24) a) J. Kahr, J. P. S. Mowat, A. M. Z. Slawin, R. E. Morris, D. Fairen-Jimenez, P. A. Wright, *Chem. Commun.* **2012**, *48*, 6690; b) S. Bernt, M. Feyand, A. Modrow, J. Wack, J. Senker, N. Stock, *Eur. J. Inorg. Chem.* **2011**, *2011*, 5378.

(25) J. A. Thompson, C. R. Blad, N. A. Brunelli, M. E. Lydon, R. P. Lively, C. W. Jones, S. Nair, *Chem. Mater.* **2012**, *24*, 1930.

(26) R. Banerjee, A. Phan, B. Wang, C. Knobler, H. Furukawa, M. O'Keeffe, O. M. Yaghi, *Science* **2008**, *319*, 939.

(27) A. Nagai, Z. Guo, X. Feng, S. Jin, X. Chen, X. Ding, D. Jiang, *Nat. Commun.* **2011**, *2*, 536.

(28) a) S. M. Cohen, *Chem. Rev.* **2011**, *112*, 970; K. K. Tanabe, S. M. Cohen, *Chem. Soc. Rev.* **2011**, *40*, 498; b) T. Gadzikwa, O. K. Farha, C. D. Malliakas, M. G. Kanatzidis, J. T. Hupp, S. T. Nguyen, *J. Am. Chem. Soc.* **2009**, *131*, 13613.

(29) For a recent IML example using two monomers of different lengths to obtain new topologies, see K. Koh, J. D. Van Oosterhout, S. Roy, A. G. Wong-Foy, A. J. Matzger, *Chem. Sci.* **2012**, *3*, 2429.

(30) R. Banerjee, H. Furukawa, D. Britt, C. Knobler, M. O'Keeffe, O. M. Yaghi, *J. Am. Chem. Soc.* **2009**, *131*, 3875.

(31) W. Chen, J.-Y. Wang, C. Chen, Q. Yue, H.-M. Yuan, J.-S. Chen, S.-N. Wang, *Inorg. Chem.* **2003**, *42*, 944.

(32) K. Koh, A. G. Wong-Foy, A. J. Matzger, *Angew. Chem. Int. Ed.* **2008**, *47*, 677.

(33) H. Frost, R. Q. Snurr, J. Phys. Chem. C 2007, 111, 18794; L. J. Murray, M. Dincă, J. R. Long, *Chem. Soc. Rev.* **2009**, *38*, 1294.

(34) a) F. Nouar, J. F. Eubank, T. Bousquet, L. Wojtas, M. J. Zaworotko, M. Eddaoudi, *J. Am. Chem. Soc.* **2008**, *130*, 1833; b) O. K. Farha, C. E. Wilmer, I. Eryazici, B. G. Hauser, P. A.

Parilla, K. O'Neill, A. A. Sarjeant, S. T. Nguyen, R. Q. Snurr, J. T. Hupp, *J. Am. Chem. Soc.* **2012**, *134*, 9860.

(35) K. Koh, A. G. Wong-Foy, A. J. Matzger, *J. Am. Chem. Soc.* **2010**, *132*, 15005.

(36) Y. Liao, S. K. Yang, K. Koh, A. J. Matzger, J. S. Biteen, *Nano Lett.* **2012**, *12*, 3080.

(37) K. Koh, A. G. Wong-Foy, A. J. Matzger, *J. Am. Chem. Soc.* **2009**, *131*, 4184.

(38) a) B. Mu, P. M. Schoenecker, K. S. Walton, *J. Phys. Chem. C* **2010**, *114*, 6464; b) Z. Xiang, J. Lan, D. Cao, X. Shao, W. Wang, D. P. Broom, *J. Phys. Chem. C* **2009**, *113*, 15106.

(39) Z. Wang, K. K. Tanabe, S. M. Cohen, *Inorg. Chem.* **2009**, *48*, 296.

(40) C. Chen, C. A. Allen, S. M. Cohen, *Inorg. Chem.* **2011**, *50*, 10534.

(41) C. J. Doonan, W. Morris, H. Furukawa, O. M. Yaghi, *J. Am. Chem. Soc.* **2009**, *131*, 9492.

(42) M. Padmanaban, P. Muller, C. Lieder, K. Gedrich, R. Grunker, V. Bon, I. Senkovska, S. Baumgartner, S. Opelt, S. Paasch, E. Brunner, F. Glorius, E. Klemm, S. Kaskel, *Chem. Commun.* **2011**, *47*, 12089.

(43) T.-H. Park, A. J. Hickman, K. Koh, S. Martin, A. G. Wong-Foy, M. S. Sanford, A. J. Matzger, *J. Am. Chem. Soc.* **2011**, *133*, 20138.

(44) D. N. Bunck, W. R. Dichtel, *Angew. Chem. Int. Ed.* **2012**, *51*, 1885.

(45) T. Tsuruoka, S. Furukawa, Y. Takashima, K. Yoshida, S. Isoda, S. Kitagawa, *Angew. Chem. Int. Ed.* **2009**, *48*, 4739.

(46) A. Umemura, S. Diring, S. Furukawa, H. Uehara, T. Tsuruoka, S. Kitagawa, *J. Am. Chem. Soc.* **2011**, *133*, 15506.

(47) K. M. Choi, H. J. Jeon, J. K. Kang, O. M. Yaghi, *J. Am. Chem. Soc.* **2011**, *133*, 11920.

(48) M. Fujita, J. Yazaki, K. Ogura, *J. Am. Chem. Soc.* **1990**, *112*, 5645.

(49) B. F. Hoskins, R. Robson, *J. Am. Chem. Soc.* **1989**, *111*, 5962.

(50) a) R. Chakrabarty, P. S. Mukherjee, P. J. Stang, *Chem. Rev.* **2011**, *111*, 6810; b) D. J. Tranchemontagne, Z. Ni, M. O'Keeffe, O. M. Yaghi, *Angew. Chem. Int. Ed.* **2008**, *47*, 5136.

Chapter Two: Internal Functionalization of 3D Covalent Organic Frameworks

Covalent organic frameworks (COFs) represent an emerging class of porous crystalline materials comprised of light elements,[1] typically C, N, O, and/or B, that crystallize into two-dimensional (2D) layered structures or three-dimensional (3D) networks.[2, 3] The nearly eclipsed structures[4, 5] of most 2D COFs give rise to high intrinsic charge mobilities[6] and their recent synthesis as oriented thin films[7] portends their use in optoelectronic and energy storage devices. In contrast, few 3D COFs have been crystallized, and despite exhibiting exceptionally high surface areas (>4000 m^2 g^{-1}) and record low densities (0.17 g cm^{-3}),[8] these networks have no well developed applications. Functionalizing the interior of 3D COFs might harness these desirable properties to provide structurally precise platforms for catalysis,[9] separations,[10] or the storage and release of molecular payloads.[11] However, no functionalized 3D COFs have been reported, while 2D COF functionalization has been limited to alkyl chains.[12] Postsynthetic functionalization of related metal-organic frameworks (MOFs) relies on incorporating reactive groups,[13] such as alkynes[14] or amines,[15] on the organic linkers, but these moieties are not readily incorporated onto symmetric, polyvalent 3D COF building blocks.

Here we report a general approach to functionalize 3D COFs using a new monomer truncation strategy. A tetrahedral building block, which self-condenses to form the 3D **ctn** network known as COF-102 (Figure 2.1a),[2] was modified to replace one of its four arylboronic acid moieties with an arbitrary functional group. The resulting trigonal tris(boronic acid) is co-condensed with the parent tetrahedral monomer to provide functionalized COF-102 (Figure 2.1b). The degree of functionalization is determined by the feed ratio of the two monomers and tolerates relatively high loadings of the truncated monomer (>30%), while maintaining the crystallinity, permanent porosity, and high surface area of the unfunctionalized material. This

method also requires no modification of the solvothermal growth conditions used to crystallize COF-102. The truncated monomer is incorporated throughout the lattice, rather than on the crystallite surface, which might be unexpected given the reversible bond-forming conditions employed in COF synthesis.[16] However, growth conditions that produce crystalline materials are optimized empirically, and COF nucleation and growth processes are poorly understood. Our results indicate that boroxine hydrolysis is too slow to liberate truncated monomers from the COF-102 interior, thus distributing their pendant functionality throughout the material.[17]

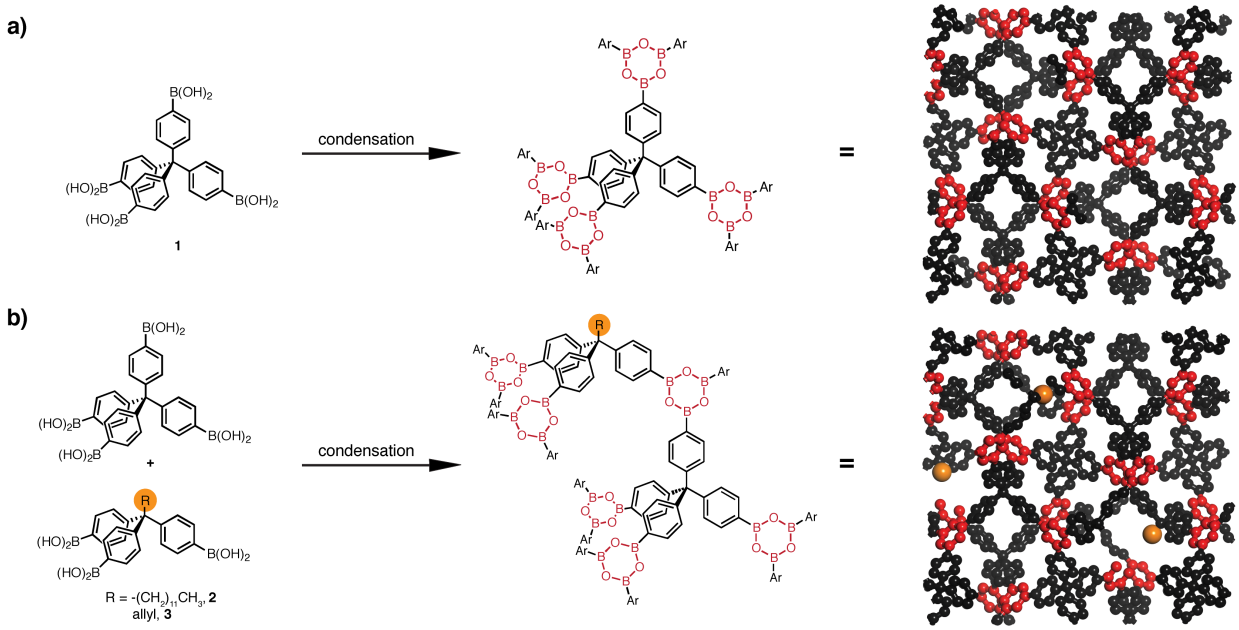

Figure 2.1 (a) The self-condensation of tetrafunctional boronic acid **1** yields the boroxine-linked **ctn** network known as COF-102. (b) Co-crystallization of **1** with truncated monomer **2** or **3** produces internally functionalized 3D COF

Dodecyl-functionalized COF-102 (COF-102-C_{12}) was obtained by condensing mixtures of **1** and **2** under solvothermal conditions (mesitylene/1,4-dioxane 1:1 *v/v*, 90 °C, 24 h). Samples of COF-102-C_{12} were isolated by filtration as microcrystalline powders and were activated under vacuum at 90 °C for 13 h. Fourier transform infrared (FTIR) spectroscopy of activated COF-102 and COF-102-C_{12} were indicative of boroxine-linked materials, as judged by the intense B–O

stretch at 1343 cm^{-1} and attenuated O–H stretch relative to their boronic acid precursors (Figure 2.2a). These spectra are consistent with those previously reported. The spectrum of a COF-102-C_{12} sample containing a 27% loading of the dodecyl-functionalized monomer **2** showed sp^3-hybridized C–H stretches at 2900 cm^{-1} not observed in the unfunctionalized COF-102 samples. COF-102-C_{12} samples also typically showed more intense residual O–H stretches, which we attribute to dangling boronic acid moieties opposite the dodecyl chains in the lattice. Overall, these spectra indicate that the co-condensation strategy produces a dodecyl functionalized, boroxine-linked material similar to COF-102.

The percent incorporation of **2** into the COF-102-C_{12} lattice (T_{C12}) was evaluated by ^{1}H NMR spectroscopy after digesting the material in CD_3CN / D_2O (3:1 *v/v*). The ratio of **1**:**2** was determined by comparing the integration of the resonance at 0.84 ppm, corresponding to the –CH_3 protons of the dodecyl chain, to that at 7.25 ppm, corresponding to an aromatic resonance found in both monomers (Figure 2.2b). The T_{C12} values calculated using this approach were very close to the feed ratios of the monomers used in the COF-102-C_{12} synthesis, up to feed ratios of 33%. Higher feed ratios (50%) still produced crystalline COF-102-C_{12}, albeit with T_{C12} levels that did not exceed 37%. This loading level might represent an upper limit for incorporating truncated monomers into the COF-102 lattice, in which the truncated building block comprises more than one-third of the network. In preliminary experiments, we isolated **2** as an amorphous boroxine-linked network instead of as a monomeric tris(boronic acid). When co-condensed with **1**, the boroxine form of **2** provided low T_{C12} values, further suggesting that boroxine hydrolysis is slow relative to the rate of COF-102 growth. **2** was obtained as a tris(boronic acid) following lyophilization from wet 1,4-dioxane, and these samples consistently gave T_{C12} values similar to the monomer feed ratio.

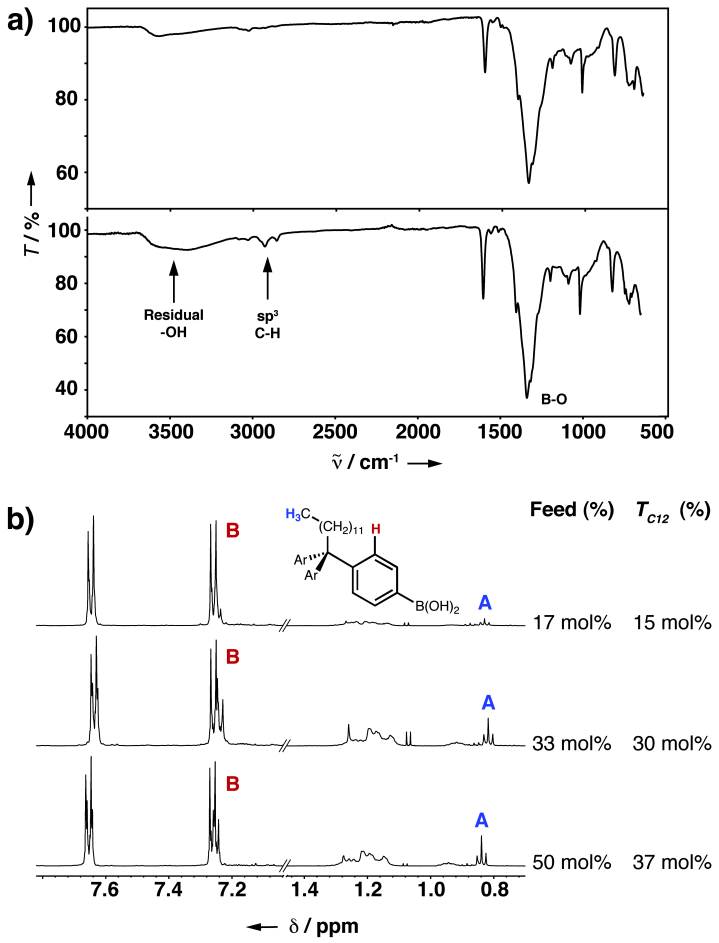

Figure 2.2 (a) FTIR spectra of unfunctionalized COF-102 (top) and COF-102-C_{12} (T_{C12} = 27%, bottom). (b) Quantitative partial ^{1}H NMR spectra (CD_3CN / D_2O, 500 MHz, 293 K) of digested COF-102-C_{12} samples used to determine the percent loading of **2** (T_{C12}).

COF-102-C_{12} is formed as a microcrystalline powder with an identical powder X-ray diffraction (PXRD) pattern to unfunctionalized COF-102, indicating that the functionalized material adopts the same **ctn** network structure (Figure 2.3). For example, the PXRD pattern of a COF-102-C_{12} sample with relatively high loading of **2** (T_{C12} = 24%) exhibits peaks (Cu Kα) at 2θ = 7.9, 9.2, 12.1, 13.0, 14.5, 15.2, and 16.0° corresponding to the (211), (220), (321), (400), (420), (332), and (422) reflections. This powder diffraction pattern is nearly identical to that obtained for activated, unfunctionalized COF-102 and matches that previously reported. PXRD

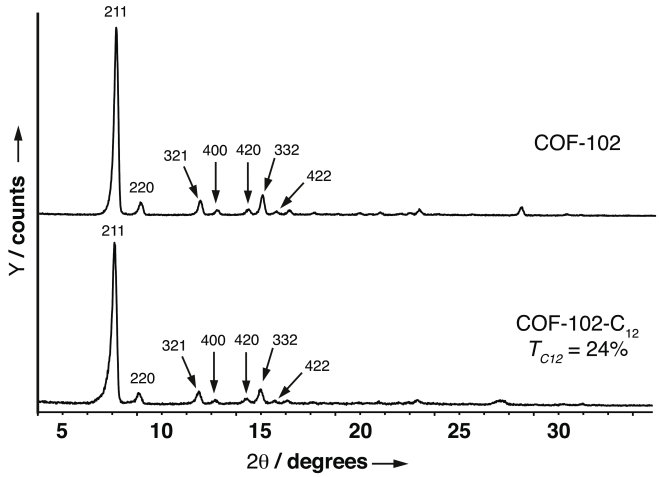

Figure 2.3 PXRD patterns of activated (a) COF-102 and (b) COF-102-C_{12} (T_{C12} = 24%).

patterns of COF-102 and COF-102-C_{12} obtained prior to activation show consistent differences in the intensities of their Bragg peaks relative to the patterns shown in Figure 2.3 (See Appendix 2-1, p. 35). COF-102-C_{12} samples with $T_{C12} \leq 24\%$ each displayed similar PXRD patterns after activation. Materials with T_{C12} above this value (34% and 37%) showed similar diffraction patterns prior to activation, indicating formation of the crystalline network. However, activating these samples gave rise to amorphous materials, suggesting the decreased stability of these networks at the highest loading levels.[5] Scanning electron micrographs of unfunctionalized COF-102 and COF-102-C_{12} (T_{C12} = 37%, Figure 2.4) show indistinguishable spherulites. These micrographs suggest that the truncated monomer **2** is distributed throughout the COF-102-C_{12} lattice, because differences in spherulite size would be expected if **2** was confined exclusively to the exterior surface at this loading level.

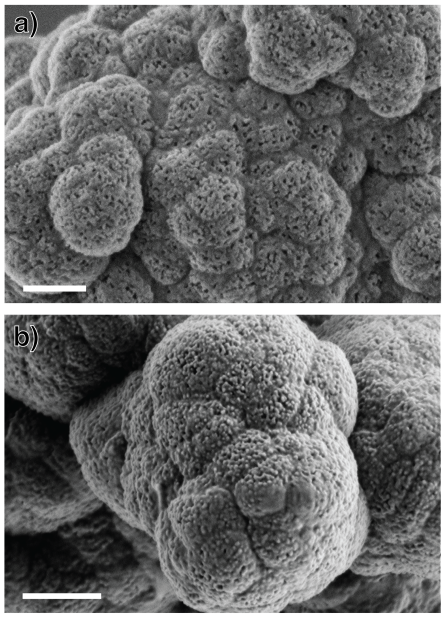

Figure 2.4 Scanning electron micrographs of (a) unfunctionalized COF-102 and (b) COF-102-C_{12} (T_{C12} = 37%). Scale bars are 300 nm.

Gas adsorption isotherms (N_2 and Ar) indicate that COF-102-C_{12} exhibits permanent porosity and high surface areas that approach those of COF-102. Activated samples of COF-102-C_{12} with 5% ≤ T_{C12} ≤ 24% show Type I N_2-adsorption isotherms with a single adsorption into the pores at low relative pressure (P/P_o < 0.10, see Appendix). Desorption is fully reversible with no observed hysteresis. The Brunauer-Emmett-Teller (BET) surface area model was applied to the 0.01 < P/P_o < 0.27 region to provide the surface areas (S_{BET}) plotted in Figure 2.5a as a function of T_{C12}. These data indicate that COF-102-C_{12} samples retain high surface areas (>2000 m^2 g^{-1}) that are inversely proportional to T_{C12}. By expressing this decrease as a percentage, the reduction in S_{BET} (S_{red}) scales linearly with T_{C12} with a slope of 1.01. Nonlocal density functional theory (NLDFT) analysis of the Ar adsorption isotherms provided identical pore size distributions for unfunctionalized COF-102 and all COF-102-C_{12} samples and indicated a pore width of 12 Å (see Appendix 2-1, p. 35). The total pore volume ($V_{P,NLDFT}$) also decreases (Figure 2.5b) as a function

of loading level. The percent volume reduction (V_{red}) scales linearly with T_{C12} with a slope of 1.08. The trends of reduced S_{BET} and $V_{P,NLDFT}$ with increased T_{C12} suggest that the dodecyl chains occupy the interior pore volume of the COF.

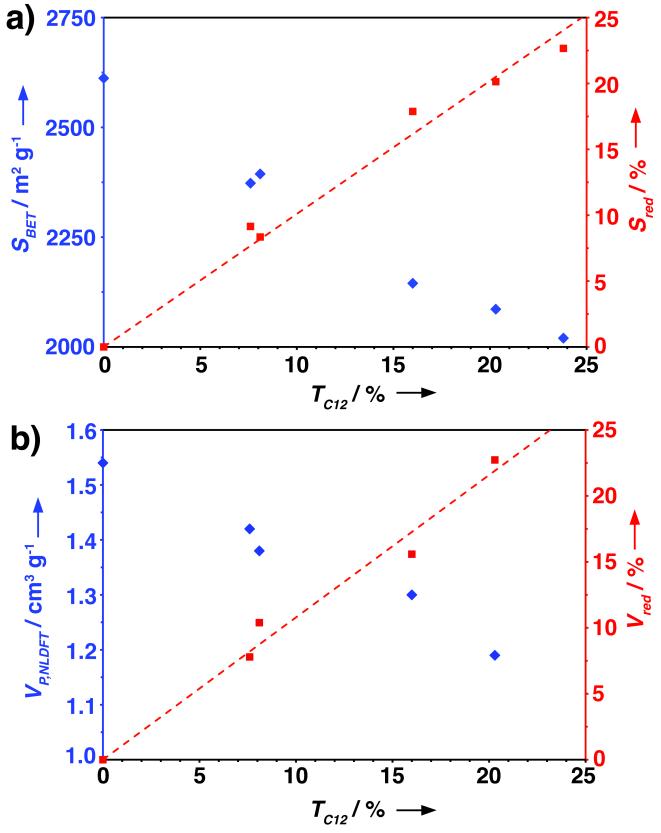

Figure 2.5 a) BET surface area (S_{BET}, N_2 adsorption, 77 K, blue points) and its percent reduction (S_{red}, red points) plotted as a function of the loading of **2** (T_{C12}). b) Cumulative pore volume ($V_{p,NLDFT}$, Ar adsorption, 87 K, blue points) and percent pore volume reduction (V_{red}, red points) plotted as a function of T_{C12}. For the gas adsorption isotherms corresponding to these data, see the Appendix to this Chapter.

By employing the allyl-functionalized monomer **3**, COF-102-allyl was synthesized with a loading level (T_{allyl}) of 23%. FTIR and PXRD indicated that COF-102-allyl is a boroxine-linked **ctn** network similar to COF-102-C_{12}. Its pendant olefin is amenable to staining using OsO_4, which provides increased contrast in transmission electron micrographs. Samples of COF-102

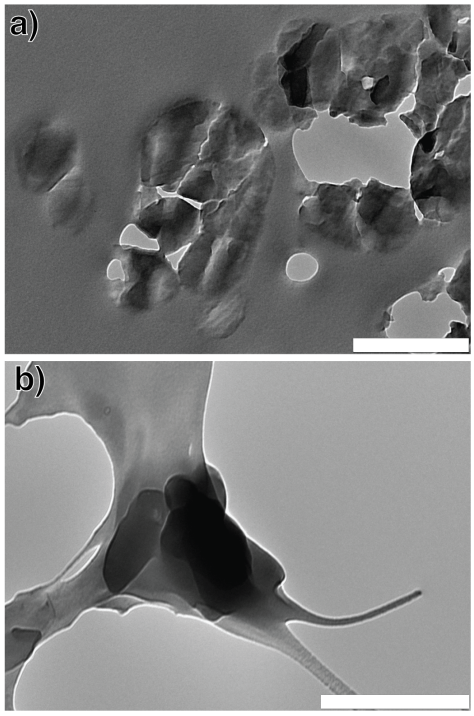

Figure 2.6 Transmission electron micrographs of microtomed samples (60 nm thickness) of (a) unfunctionalized COF-102 and (b) COF-102-allyl (T_{allyl} = 22%) suspended in epoxy after the OsO_4 staining procedure. Scale bars are 500 nm.

and COF-102-allyl were exposed to OsO_4 vapor for 15 minutes. During this time both frameworks darkened in color, suggesting uptake into both materials. The samples were next placed under high vacuum to remove adsorbed OsO_4. While under vacuum, the unfunctionalized COF-102 lightened in color, while the COF-102-allyl sample remained dark, suggesting selective functionalization of its alkene moieties. Each COF was suspended in an epoxy resin, which was cured and microtomed to 60 nm thickness. The crystallites of Os-stained COF-102-allyl and COF-102 are similar in size and shape, but the allyl-functionalized crystallites are uniformly darker (Figure 2.6). The presence of Os was confirmed by energy dispersive X-ray microanalysis (EDX), and the COF-102-allyl samples consistently showed more intense Os signals than COF-102 samples. These observations suggest that the allyl moieties are distributed throughout the crystallite and are accessible to OsO_4 vapor.

Finally, we evaluated the accessibility of the pores of COF-102 and COF-102-C_{12} to dissolved organic guests using pyridinium iodide **10** as a probe (Figure 2.7). Compound **10** exhibits a solvatochromic charge transfer (CT) absorbance whose λ_{max} in various solvents forms the basis of the solvent polarity index known as the Z-scale.[18] Equal masses of COF-102 and COF-102-C_{12} (T_{C12} = 20%) were suspended in solutions of **10** dissolved in dry CH_3CN (6.5 mL, 0.035 M). After 26 h, excess solution was removed and the COF samples were dried under high vacuum. Diffuse-reflectance UV-visible spectra of the two samples show the CT band of **10** as a broad shoulder of the COF aromatic absorbances (Figure 2.7). These absorbance bands are

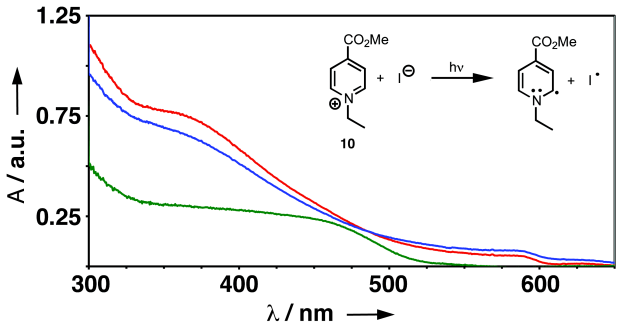

Figure 2.7 Diffuse reflectance UV-visible spectra of equal masses of unfunctionalized COF-102 (red trace) and COF-102-C_{12} (T_{C12} = 20%, blue trace) loaded with solvatochromic dye **10**. A spectrum of a physical mixture of unfunctionalized COF-102 and **10** (green trace).

distinct from a sample of COF-102 physically mixed with **10**. These data indicate that **10** is loaded into the pores of both COF-102 and COF-102-C_{12} from solution and that both materials feature distinct interior microenvironments. The COF-102 and COF-102-C_{12} samples take up comparable amounts of **10**, with slightly lower loading observed for the functionalized material. This difference is consistent with their gas adsorption data, which also showed lower specific surface area as a function of T_{C12}. Finally, the similar appearance of the CT band of **10** in the functionalized and unfunctionalized COFs suggests that their interiors are similar, perhaps

because the probe molecules preferentially reside in the unfunctionalized pore volume of COF-102-C_{12} rather than in pores already containing the dodecyl chains.

Here we have demonstrated a modular and versatile strategy to functionalize the interior of 3D COFs by co-condensing tetrahedral and truncated, trigonal monomers. The functionalized materials tolerate high loading levels of the truncated building blocks while retaining the crystallinity and high surface area of the parent 3D COFs. We are currently expanding the generality of this approach to other COF linking chemistries and developing these materials for applications in catalysis and payload release. It should also be noted that many of the tools commonly used to characterize COFs are surprisingly insensitive to the presence of high loadings of the functionalized monomers (which can be considered as defects). While the crystallinity of COFs derives from reversible bond formation, our results show that these exchange processes are not rapid enough to preclude incorporation of a truncated monomer into the lattice interior. Although the relative rates of bond formation and exchange processes during COF synthesis are not generally understood, control of these parameters, in concert with our truncated monomer strategy, might furnish functionalized 3D COFs with designed crystallite morphology.

References

(1) a) A. P. Côté, A. I. Benin, N. W. Ockwig, M. O'Keeffe, A. J. Matzger, O. M. Yaghi, *Science* **2005**, *310*, 1166; b) R. W. Tilford, W. R. Gemmill, H.-C. zur Loye, J. J. Lavigne, *Chem. Mater.* **2006**, *18*, 5296; c) S. Wan, J. Guo, J. Kim, H. Ihee, D. Jiang, *Angew. Chem. Int. Ed.* **2008**, *47*, 8826; S. Wan, J. Guo, J. Kim, H. Ihee, D. Jiang, *Angew. Chem.* **2008**, *120*, 8958; d) E. L. Spitler, W. R. Dichtel, *Nature Chem.* **2010**, *2*, 672.

(2) H. M. El-Kaderi, J. R. Hunt, J. L. Mendoza-Cortés, A. P. Côté, R. E. Taylor, M. O'Keeffe, O. M. Yaghi, *Science* **2007**, *316*, 268.

(3) F. J. Uribe-Romo, J. R. Hunt, H. Furukawa, C. Klöck, M. O'Keeffe, O. M. Yaghi, *J. Am. Chem. Soc.* **2009**, *131*, 4570.

(4) a) E. L. Spitler, B. T. Koo, J. L. Novotney, J. W. Colson, F. J. Uribe-Romo, G. D. Gutierrez, P. Clancy, W. R. Dichtel, *J. Am. Chem. Soc.* **2011**, *133*, 19416; b) B. Lukose, A. Kuc, T. Heine, *Chem. Eur. J.* **2011**, *17*, 2388.

(5) W. Zhou, H. Wu, T. Yildirim, *Chem. Phys. Lett.* **2010**, *499*, 103.

(6) a) S. Wan, J. Guo, J. Kim, H. Ihee, D. Jiang, *Angew. Chem. Int. Ed.* **2009**, *48*, 5439; S. Wan, J. Guo, J. Kim, H. Ihee, D. Jiang, *Angew. Chem.* **2009**, *121*, 5547; b) X. Ding, L. Chen, Y. Honsho, X. Feng, O. Saengsawang, J. Guo, A. Saeki, S. Seki, S. Irle, S. Nagase, V. Parasuk, D. Jiang, *J. Am. Chem. Soc.* **2011**, *133*, 14510.

(7) a) E. L. Spitler, J. W. Colson, F. J. Uribe-Romo, A. R. Woll, M. R. Giovino, A. Saldivar, W. R. Dichtel, *Angew. Chem. Int. Ed.*, accepted; b) J. W. Colson, A. R. Woll, A. Mukherjee, M. P. Levendorf, E. L. Spitler, V. B. Shields, M. G. Spencer, J. Park, W. R. Dichtel, *Science* **2011**, *332*, 228.

(8) J. R. Holst, A. I. Cooper, *Adv. Mater.* **2010**, *22*, 5212.

(9) S.-Y. Ding, J. Gao, Q. Wang, Y. Zhang, W.-G. Song, C.-Y. Su, W. Wang, *J. Am. Chem. Soc.* **2011**, *133*, 19816.

(10) S. Han, Y. Wei, C. Valente, I. Lagzi, J. J. Gassensmith, A. Coskun, J. F. Stoddart, B. A. Grzybowski, *J. Am. Chem. Soc.* **2010**, *132*, 16358.

(11) P. Horcajada, T. Chalati, C. Serre, B. Gillet, C. Sebrie, T. Baati, J. F. Eubank, D. Heurtaux, P. Clayette, C. Kreuz, J.-S. Chang, Y. K. Hwang, V. Marsaud, P.-N. Bories, L. Cynober, S. Gil, G. Ferey, P. Couvreur, R. Gref, *Nature Mater.* **2010**, *9*, 172.

(12) a) R. W. Tilford, S. J. Mugavero, P. J. Pellechia, J. J. Lavigne, *Adv. Mater.* **2008**, *20*, 2741; b) L. M. Lanni, R. W. Tilford, M. Bharathy, J. J. Lavigne, *J. Am. Chem. Soc.* **2011**, *133*, 13975.

(13) K. K. Tanabe, C. A. Allen, S. M. Cohen, *Angew. Chem. Int. Ed.* **2010**, *49*, 9730; K. K. Tanabe, C. A. Allen, S. M. Cohen, *Angew. Chem.* **2010**, *122*, 9924.

(14) T. Gadzikwa, O. K. Farha, C. D. Malliakas, M. G. Kanatzidis, J. T. Hupp, S. T. Nguyen, *J. Am. Chem. Soc.* **2009**, *131*, 13613.

(15) a) K. K. Tanabe, S. M. Cohen, *Chem. Soc. Rev.* **2011**, *40*, 498; b) K. K. Tanabe, S. M. Cohen, *Angew. Chem. Int. Ed.* **2009**, *48*, 7424; K. K. Tanabe, S. M. Cohen, *Angew. Chem.* **2009**, *121*, 7560.

(16) For an intriguing example of a defect-incorporation strategy used to functionalize metal-organic frameworks, see: T.-H. Park, A. J. Hickman, K. Koh, S. Martin, A. G. Wong-Foy, M. S. Sanford, A. J. Matzger, *J. Am. Chem. Soc.* **2011**, *133*, 20138.

(17) E. L. Spitler, M. R. Giovino, S. L. White, W. R. Dichtel, *Chem. Sci.* **2011**, *2*, 1588.

(18) E. M. Kosower, *J. Am. Chem. Soc.* **1958**, *80*, 3253.

Appendix 2-1: Supplementary Information

I. Materials and Instrumentation

Materials. All reagents were obtained from Sigma-Aldrich (Milwaukee, WI). Toluene, tetrahydrofuran, triethylamine, and CH_3CN were obtained from a custom designed solvent purification system employing activated alumina under argon. Air and water sensitive reactions were performed on a Schlenk line under a N_2 atmosphere. (Methanetetrayltetra-4,1-phenylene)tetrakisboronic acid (**1**) was made according to a previously reported procedure.[1]

Instrumentation. Infrared spectra of solid samples were recorded using a Thermo Nicolet iS10 FT-IR spectrometer with a diamond ATR attachment and are uncorrected.

NMR spectra were recorded on a Varian INOVA 400 MHz spectrometer using a $^{1}H/X$ Z-PFG probe or a Varian INOVA 500 MHz spectrometer using a standard $^{1}H\{^{13}C, ^{15}N\}$ Z-PFG probe with a 20 Hz sample spin rate. ^{1}H NMR spectra for quantitative determination of capping agent were acquired at 500 MHz with a 3 s acquisition time and a 1 s relaxation delay. The integral accuracy was confirmed on a pure sample of compound **2**.

Gas chromatography/electron impact mass spectrometry was performed on an Agilent 6890N Network GC System with a JEOL JMS-GCmate II Mass Spectrometer (magnetic sector) using a gradient oven temperature from 120 °C to 270 °C over 30 min.

Scanning electron microscopy was done on a LEO 1550 FESEM (Keck SEM) operating at 1.00 kV and a working distance of 1.2 mm. Samples were prepared by adsorption onto a silicon wafer, which was then attached to a flat aluminum platform sample holder and exposed to high vacuum for 3 h. The sample was then placed directly into the instrument. No metal coating was applied.

Transmission electron microscopy was performed on a FEI Technai T12 Spirit operating at 120 kV. Samples were prepared by first embedding them in Ultra Bed Low Viscosity Epoxy (Electron Microscopy Sciences, #14310) followed by curing at 60 °C overnight. The samples were microtomed to 60 nm thickness using a DuPont Sorvall MT 5000 ultramicrotome equipped with a diamond knife, floated onto H_2O, and transferred to 300 mesh Au grids. Staining was conducted by exposing the sample to OsO_4 vapors in an enclosed Petri dish for 15 minutes, followed by removal of any physisorbed species under high vacuum. Energy dispersive X-ray microanalysis was performed directly on the samples in the TEM. The presence of osmium was confirmed by the observation of the Lα emission at 8.91 KeV using a detection time of 197.12 s. Emissions from the brass sample holder (Cu) obfuscated the Os Kα and Mα emissions.

UV/Vis spectra were recorded on a Cary 5000 UV-Vis-NIR spectrophotometer using a Praying Mantis diffuse reflectance accessory with a Teflon powder reference. Samples were settled in the holder through tapping on the bench top and flattened with a spatula.

Surface area measurements were conducted on a Micromeritics ASAP 2020 Accelerated Surface Area and Porosimetry Analyzer using *ca.* 35 mg samples degassed at 23 °C for 6 h and then 100 °C for 3 h and backfilled with N_2. Nitrogen isotherms were generated by incremental exposure to ultra high purity nitrogen up to *ca.* 1 atm in a liquid nitrogen (77 K) bath and surface parameters were determined using BET adsorption models included in the instrument software (Micromeritics ASAP 2020 V4.00). Ar isotherms were generated by incremental exposure to ultra high purity argon up to *ca.* 1 atm in a liquid argon (87 K) bath. BET surface area and calculation of pore width using nonlocal density functional theory were determined though models included in the instrument software.[2]

Powder X-ray diffraction (PXRD) patterns were obtained on a Rigaku Smartlab X-Ray diffractometer in reflectance parallel beam/parallel slit alignment geometry. The measurement employed Cu Kα line focused radiation at 1760 W (40 kV, 44 mA) power and a Ge crystal detector fitted with a 1.0 mm incident slit. Samples were mounted on zero-background quartz sample holders and flattened with a glass microscope slide. No sample grinding or sieving was done prior to analysis. Samples were observed using a 0.0200° 2θ step scan from 2.0 – 34.0° with a scan speed of 5° min^{-1}. No peaks could be resolved from the baseline for $2\theta > 35°$ and this region was not considered for further analysis. Crystallite size was determined by applying the Scherrer equation to the powder patterns based on an alumina standard.

II. Experimental Protocols.

Figure A2.1 Synthesis of dodecyl-truncated COF-102 monomer.

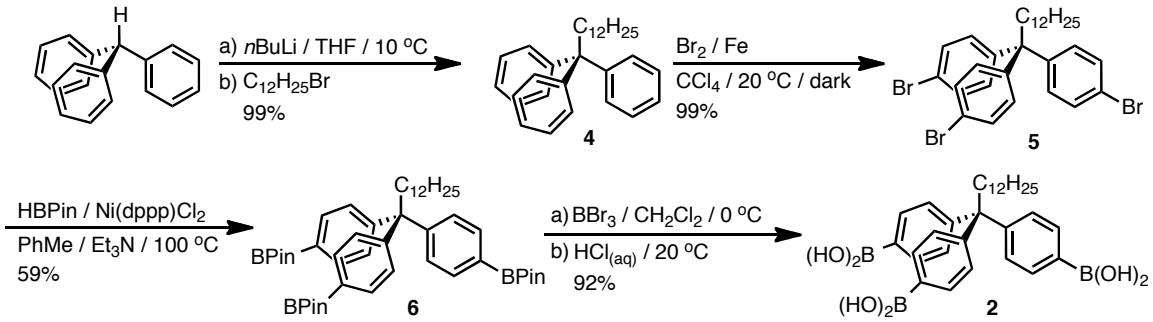

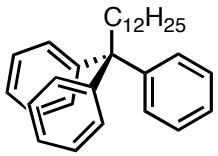

1,1,1-triphenyltridecane (4). Triphenylmethane (5.00 g, 20.4 mmol) and THF (102 mL) were added to a dry, 250 mL 2-neck round-bottom flask equipped with a stir bar and vacuum adapter under a N_2 atmosphere. The reaction mixture was cooled to 10 °C and *n*-BuLi (18.0 mL, 2.5 M in hexanes) was added dropwise over 30 min, producing a deep red solution. After stirring at 10 °C for 1 h, dodecyl bromide (5.46 g, 21.9 mmol) was added dropwise, after which the red color disappeared. After 20 min, the reaction was quenched with aqueous HCl (1 M, 30 mL). The crude mixture was extracted with EtOAc (3 x 50 mL). The combined organic fractions were dried with anhydrous $MgSO_4$, filtered, and the solvent was evaporated to provide **4** (8.16 g, 97%) as a white solid. **4** was used in subsequent reactions without purification. **4**: ^{1}H NMR (500 MHz, $CDCl_3$, 298 K): δ 7.27 (m, Ph-**H**, 12H), 7.16 (m, Ph-**H**, 3H), 2.57 (m, Ph_3C-C**H**$_2$-CH_2-, 2H), 1.26 (m, -(C**H**$_2$)$_9$-, 18H), 1.08 (m, -CH_2-C**H**$_2$-CH_3, 2H), 0.89 (t, -C**H**$_3$, 3H, J = 6.9 Hz). ^{13}C NMR (125 MHz, $CDCl_3$, 298 K): δ 147.8, 129.3, 127.8, 125.8, 56.8, 40.7, 32.1, 30.6, 29.9, 29.8 (3 peaks), 29.6,

29.5, 25.9, 22.9, 14.3. FTIR (solid, ATR): 2913, 2847, 1489, 1443, 699 cm^{-1}. EI-MS: m/z [M^+] 412.3130 calc'd, 412.3119 found.

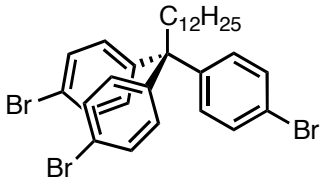

1,1,1-tris(4-bromophenyl)tridecane (5). Carbon tetrachloride (84 mL) was added to a 300 mL roundbottom flask containing **4** (7.00 g, 17.0 mmol), iron powder (0.853 g, 55.8 mmol), and a magnetic stir bar. The flask was closed with a septum and covered with aluminum foil. A needle was placed through the septum to vent any HBr formed. Bromine (3.1 mL, 59.7 mmol) was added dropwise via syringe and the reaction mixture was allowed to stir for 1.5 h. Upon completion of the reaction by TLC, the volatiles were removed *in vacuo*. The crude solids were dissolved in hexanes and run through a plug of silica yielding **5**, 10.9 g (99%). [Note: The bromination in this step is not entirely regioselective and two regioisomers were carried forward] **5**: ^{1}H NMR (500 MHz, $CDCl_3$, 298 K): δ 7.39 (AA'BB', **Φ-H**, 6H), 7.09 (AA'BB', **Φ-H**, 6H), 2.46 (m, Φ_3C-C**H**$_2$-CH_2-, 2H), 1.26 (m, -(C**H**$_2$)$_9$-, 18H), 1.01 (dq, J = 7.9, 7.8 Hz, -CH_2-C**H**$_2$-CH_3, 2H), 0.89 (t, -CH_3, J = 6.9 Hz). ^{13}C NMR (125 MHz, $CDCl_3$, 298 K) δ 145.8, 131.3, 130.9, 120.4, 56.0, 40.3, 32.1, 30.4, 29.9, 29.8 (2 peaks), 29.7, 29.6, 29.5, 25.7, 22.8, 14.3. FTIR: (solid, ATR): 2921, 2851, 1487, 1465, 1078, 1007, 807, 758 cm^{-1}. EI-MS: m/z [M^+] 646.04454 calc'd, 646.03134 found.

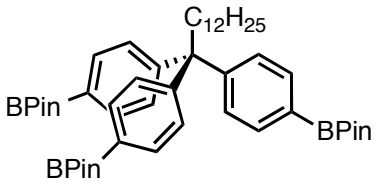

1,1,1-tris(4-pinacolatoborophenyl)tridecane (6). **5** (13.2 g, 20 mmol) and Ni(dppp)Cl_2 (0.882 g, 1.628 mmol) were added to a dry 250 mL round bottom flask equipped with a magnetic stir bar, condenser, and three-way vacuum inlet adapter and the system was subjected to three pump-

purge cycles with N_2. Toluene (65 mL) and triethylamine (25.4 mL, 183 mmol) were added by syringe and the resulting solution was subjected to three freeze-pump-thaw cycles. Pinacol borane (13.3 mL, 91.6 mmol) was added by syringe and the reaction mixture was heated to reflux for 17 h. The reaction was then cooled to 23 °C and HCl (20 mL, 1 M) was added slowly to avoid rapid H_2 evolution from residual pinacol borane. The isolated aqueous phase was extracted with $CHCl_3$ (3x, 15 mL). The combined organic phases were then washed with brine, dried with $MgSO_4$, filtered, and the solvents were removed via rotary evaporation. The crude product was recrystallized from CH_3CN to yield 9.48 g (59%) of light yellow crystals. [Note: side products resulting from impurities in **5** did not prevent isolation of pure **6**] **6**: ^{1}H NMR (400 MHz, CDCl3, 298 K): δ 7.69 (AA'BB', **Φ-H**, 6H), 7.27 (AA'BB', **Φ-H**, 6H), 2.53 (m, Φ_3C-C**H**$_2$-CH$_2$-, 2H), 1.32 (s, BPin, 36H), 1.24 (m, -(C**H**$_2$)$_9$-, 18H), 1.00 (m, -CH$_2$-C**H**$_2$-CH$_3$, 2H), 0.88 (t, J = 6.9 Hz, -CH$_2$-CH$_2$-C**H**$_3$, 3H). ^{13}C NMR (125 MHz, $CDCl_3$, 298 K): δ 150.5, 134.4, 128.8, 83.2, 57.5, 40.1, 32.1, 30.5, 29.8, 29.6, 29.5, 25.7, 25.0, 24.8, 14.3. Note: ^{13}C-B coupling makes ^{13}C-BPin unobservable. FTIR (solid, ATR): 2977, 2925, 2853, 1606, 1357, 1143, 1091, 859, 661 cm^{-1}. EI-MS: m/z [M$^+$] 790.56805 calc'd, 790.56864 found.

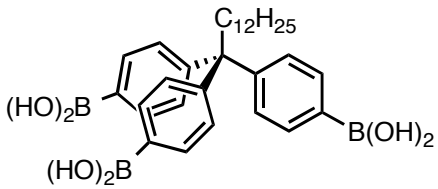

1,1,1-tris(4-phenylboronic acid)tridecane (2). 6 (2.3 g, 2.91 mmol) was dissolved in CH_2Cl_2 (6 mL) in a dry 50 mL round-bottom flask equipped with a stir bar under N_2. BBr_3 solution (1M in CH_2Cl_2, 20 mL) was added slowly at 0 °C. After 20 min, the reaction mixture was quenched with HCl (20 mL, 1 M) at 0 °C. The aqueous layer was then extracted with EtOAc (3x, 20 mL). The organic fractions were combined and the solvent was subsequently removed by rotary evaporation. The wet solid was freeze-dried from dioxane to provide **2** (1.46 g, 92%) as a

slightly yellow solid. **2**: ^{1}H NMR (400 MHz, $CDCl_3$, 298 K): δ (AA'BB', **Φ-H**, 6H), (AA'BB', **Φ-H**, 6H), (m, Φ_3C-C**H**$_2$-CH_2-, 2H), (m, -(C**H**$_2$)$_9$-, 18H), 1.01 (dq, J = 7.9, 7.8 Hz, -CH_2-C**H**$_2$-CH_3, 2H), 0.89 (t, -CH_3, J = 6.9 Hz). ^{13}C NMR (125 MHz, DMSO-d_6, 298 K): δ 149.1, 133.7, 128.0, 83.6, 56.6, 31.4, 29.1, 29.0 (5), 28.7, 24.7, 22.2, 14.1. Note: ^{13}C-B coupling makes ^{13}C-$B(OH)_2$ unobservable. FTIR (solid, ATR): 3364, 2923, 2852, 1603, 1331, 1193, 1118, 1017, 822, 701 cm^{-1}. EI-MS: m/z [M-($B(OH)_2$)-4H]$^+$ 495.28780 calc'd, 495.28916 found.

Figure A2.2. Synthesis of allyl-truncated COF-102 monomer.

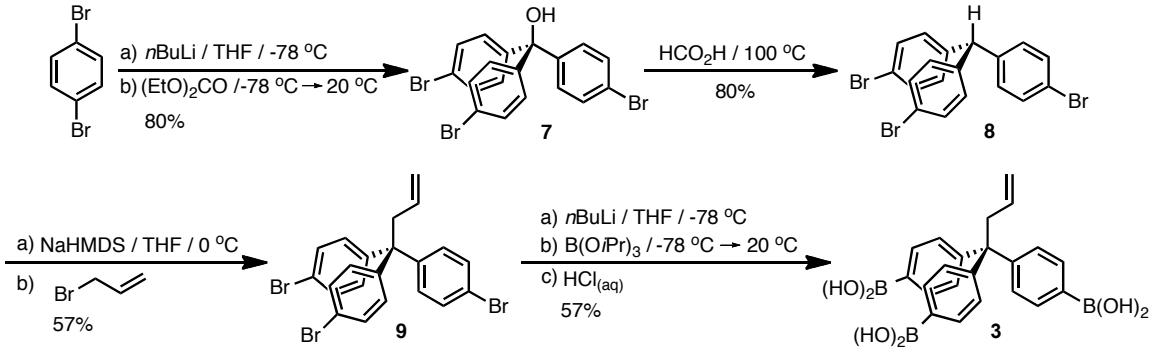

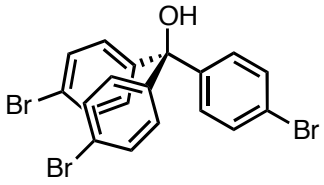

Tris(4-bromophenyl)methanol (7). *p*-dibromobenzene (8.7 g, 37.2 mmol) and THF (135 mL) were added to a flame-dried 3-neck 300 mL round-bottom flask equipped with a stirbar, three-way vacuum inlet adapter, glass stopper, and septum. The solution was cooled to -78 °C and *n*-BuLi (2.5 M in hexanes, 13.5 mL, 33.8 mmol) was added dropwise. Separately, diethyl carbonate (1.02 mL, 8.5 mmol) was dissolved in THF (3 mL) in a flame-dried 300 mL round-bottom flask equipped with a stirbar, septum, and nitrogen inlet needle and cooled to -78 °C. After 3 h, the solution containing the lithiated species was transferred to the diethyl carbonate solution through a cannula and the solution was subsequently allowed to warm to 23 °C. After 6 h, the reaction

mixture was quenched with saturated aqueous NH_4Cl (50 mL). The crude product was extracted with EtOAc (3 x 5 mL). The organic fractions were collected, washed with brine, and dried over anhydrous $MgSO_4$. The crude solid was dry loaded onto SiO_2 and chromatographed (SiO_2) using a gradient of hexanes to 25% EtOAc:hexanes (*v/v*) to yield 3.38 g (80%) of **7** as a white solid. **7**: ^{1}H NMR (500 MHz, $CDCl_3$, 298 K): δ 7.45 (AA'BB', Ar-**H**, 6H), 7.12 (AA'BB', Ar-**H**, 6H), 2.70 (Ar_3C-O**H**, 1H). ^{13}C NMR (125 MHz, $CDCl_3$, 298 K) δ 145.01, 131.5, 129.6, 122.1 [Note: Ar_3**C**-OH was not observed]. EI-MS: m/z [M^+] 493.8516 calc'd, 493.8506 found.

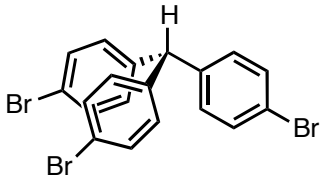

Tris(4-bromophenyl)methane (8). 7 (1.25 g, 2.52 mmol) was added to a 50 mL round-bottom flask. Formic acid (95% in H_2O, 25 mL) was added slowly. A condenser was then attached to the flask and the bright yellow suspension was heated to 100 °C for 19 h to give a dull yellow suspension. The remaining acid was neutralized with saturated aqueous Na_2CO_3 (100 mL), which caused a white solid to precipitate. The aqueous suspension was washed with Et_2O (3x40 mL) and the combined organic phases were washed with brine, dried with $MgSO_4$ and evaporated. The resulting crude solid was run through a plug of SiO_2 in pentane, enabling the isolation of **8** (0.897 g, 74% yield) as a white crystalline solid. **8**: ^{1}H NMR (500 MHz, $CDCl_3$, 298 K): δ 7.42 (AA'BB', Ar-**H**, 6H), 6.93 (AA'BB', Ar-**H**, 6H), 5.40 (s, Φ_3C-**H**, 1H). ^{13}C NMR (125 MHz, $CDCl_3$, 298 K) δ 141.9, 131.8, 131.1, 120.9, 55.2. FTIR (solid, ATR): 1483 cm^{-1} EI-MS: m/z [M^+] 477.8567 calc'd, 477.8564 found.

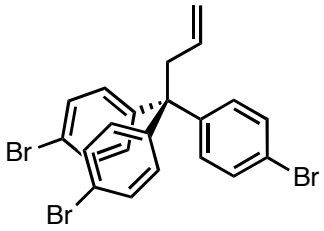

1,1,1-tris(4-bromophenyl)but-3-ene (9). 8 (375 mg, 0.78 mmol) and sodium hexamethyldisilazane (429 mg, 2.33 mmol) were added to a

flame dried 10 mL round-bottom flask equipped with a three-way vacuum inlet adapter. The flask was subjected to 3 pump/purge cycles with N_2, placed in an ice bath (0 °C), and THF (8 mL) was added, resulting in a deep red solution. The reaction was allowed to stir at 0 °C for 5.5 h, after which allyl bromide (0.6 mL, 7.0 mmol) was added, immediately changing the solution color to yellow. After 24 h of stirring, the reaction mixture was quenched with aqueous HCl (1M, 10 mL). The aqueous layer was extracted with Et_2O (3x, 15 mL). The combined organic fractions were then washed with brine, dried with $MgSO_4$, filtered, and evaporated to produce a yellow oil. The yellow crude product was passed through a plug of SiO_2 / pentane and isolated by evaporation. The resulting colorless oil was dissolved in CH_3CN and chromatographed (C_{18}-capped SiO_2, CH_3CN) to yield 215 mg (53%) of **9** as a viscous oil that slowly solidified. **9**: ^{1}H NMR (500 MHz, $CDCl_3$, 298 K): δ 7.39 (AA'BB', Ar-**H**, 6H), 7.04 (AA'BB', Ar-**H**, 6H), 5.55 (ddt, J = 17.2, 10.3, 6.7 Hz, -CH_2-C**H**=CH_2, 1H), 5.03 (ddd, J = 17.2, 1.7, 1.5 Hz, -CH_2-CH=C**H**$_2$, 1H), 4.98 (ddd, J = 10.3 1.7, 1.5 Hz, -CH_2-CH=C**H**$_2$, 1H), 3.31 (dt, J = 6.7, 1.5 Hz, -C**H$_2$**-CH=CH_2, 2H). ^{13}C NMR (125 MHz, $CDCl_3$, 298 K) δ 145.4, 134.6, 131.3, 131.0, 120.7, 118.7, 55.7, 45.3. FTIR (solid, ATR): 1483, 1404, 1071, 1008, 807, 780, 731 cm^{-1}. EI-MS: m/z [M-allyl$^+$] 476.8489 calc'd, 476.8534 found.

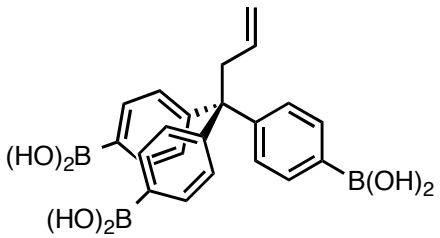

1,1,1-tris(4-phenylboronic acid)but-3-ene (3). To a flame-dried 25 mL round-bottom flask equipped with a stirbar and three-way vacuum inlet adapter was added **9** (0.141 g, 0.271 mmol). The flask was subjected to three pump/purge cycles with N_2. Next, THF (17 mL) was added to the flask, which was then cooled to -78 °C with a dry-ice/acetone bath. *n*-BuLi (1.6 M in hexanes, 1.02 mL, 1.62 mmol) was added dropwise and the

reaction mixture was allowed to stir. After confirmation of complete Li/Br exchange by thin-layer chromatography (pentane), $B(O\textit{i}Pr)_3$ (0.56 mL, 2.44 mmol) was added dropwise and the dry-ice/acetone bath was removed. After stirring for 1 h, a white precipitate had formed and the reaction was quenched with aqueous HCl (1M, 15 mL). The organic solvent from this mixture was removed by rotary evaporation and the remaining aqueous solution was basified to pH = 14 using aqueous KOH (1M). The hazy solution was filtered through Celite, and the filtrate was acidified to pH = 1.5 with aqueous HCl (1M), causing a white precipitate to form, which was isolated by centrifugation to yield **3** (0.064 g, 57%) as a white powder. **3**: ^{1}H NMR (500 MHz, DMSO, 298 K): δ 7.98 (-B(O**H**)$_2$, 6H), 7.66 (AA'BB', Ar-**H**, 6H), 7.14 (AA'BB', Ar-**H**, 6H), 5.55 (ddt, J = 17.5, 10.3, 6.6 Hz, -CH_2-C**H**=CH_2, 1H), 5.00 (ddd, J = 17.5, 1.8, 1.5 Hz, -CH_2-CH=C**H**$_2$, 1H), 4.88 (ddd, J = 10.3 1.8, 1.5 Hz, -CH_2-CH=C**H**$_2$, 1H), 3.4 (dt, J = 6.6, 1.5 Hz, -C**H$_2$**-CH=CH_2, 2H). ^{13}C NMR (125 MHz, $CDCl_3$, 298 K) δ 148.6, 135.6, 133.6, 128.1, 117.5, 109.5, 56.2. Note: ^{13}C-B coupling makes ^{13}C-$B(OH)_2$ unobservable. FTIR (solid, ATR): 3282, 1604, 1333, 1106, 1015, 909, 821, 711 cm^{-1}. EI-MS: m/z [M-$(B(OH_2))_2$+2H]$^+$ 328.16347 calc'd, 328.162235 found.

General Functionalized COF-102 Synthesis

Tetrakis(boronic acid) **1** (100 mg, 0.202 mmol) and truncating agent **2** or **3** (0.1 eq – 1 eq) were sonicated in 2 mL mesitylene/dioxane (1:1 *v/v*) in a 20 mL vial until a fine suspension was obtained. The suspension was then transferred by pipet to a pre-scored 5 mL ampoule, flash frozen in $N_{2\,(l)}$, and flame sealed. The ampoule was put in an oven at 90 °C for 27.5 h, after which the ampoule was cooled to rt, opened, and the solid was isolated by filtration. The solid was dried under vacuum for 12 h. For activated materials, after drying at 23 °C, the sample was

heated to 90 °C under vacuum for 13 h. Heating during activation was necessary to remove residual mesitylene adsorbed in the pores.

COF-102-allyl was activated by placing the COF into a flame dried Schlenk tube with a septum. 5 mL dry THF was added and after 30 min, the solvent was then removed by syringe. This process was repeated three times and the COF was subsequently dried under vacuum.

Internal Loading with Solvatochromic Pyridinium Iodide

A 25 mL Schlenk tube equipped with a stir bar and glass stopper was flame dried under vacuum and backfilled with N_2. Subsequently either unfunctionalized or dodecyl functionalized (20%) COF-102 (19 mg) and 1-ethyl-4-(methoxycarbonyl)pyridinium iodide **11** (67 mg) were added under positive N_2 pressure and subjected to 3 vacuum-N_2 purge cycles. The glass stopper was then replaced with a rubber septum under positive N_2 pressure. Anhydrous CH_3CN (6.5 mL) was added by syringe and the suspension was stirred rapidly for 1 min. The stirring rate was then reduced to 120 rpm for 16 h, at which time, the stirring was turned off and the suspended solids were allowed to settle for 1 h. The supernatant was then removed by syringe with a 22-gauge needle and the solids were dried under high vacuum, providing a pale orange solid. These dry powders were used directly for UV-Vis characterization.

III. ^{1}H and ^{13}C NMR Spectra

Figure A2.3 ^{1}H NMR spectrum of 1,1,1-triphenyltridecane (**4**) ($CDCl_3$, 500 MHz).

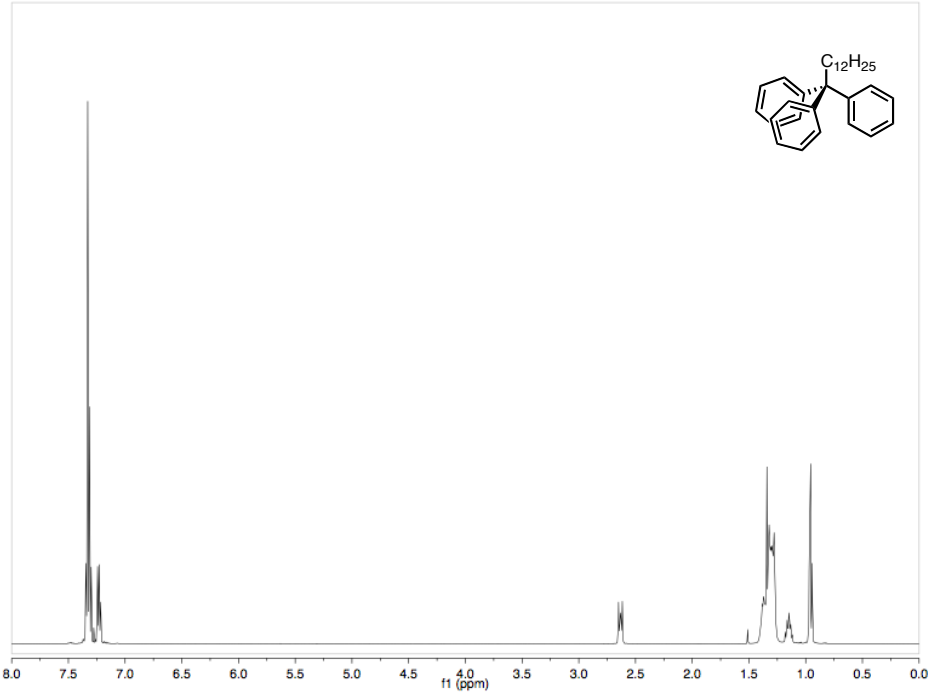

Figure A2.4 ^{13}C NMR spectrum of 1,1,1-triphenyltridecane (**4**) ($CDCl_3$, 125 MHz).

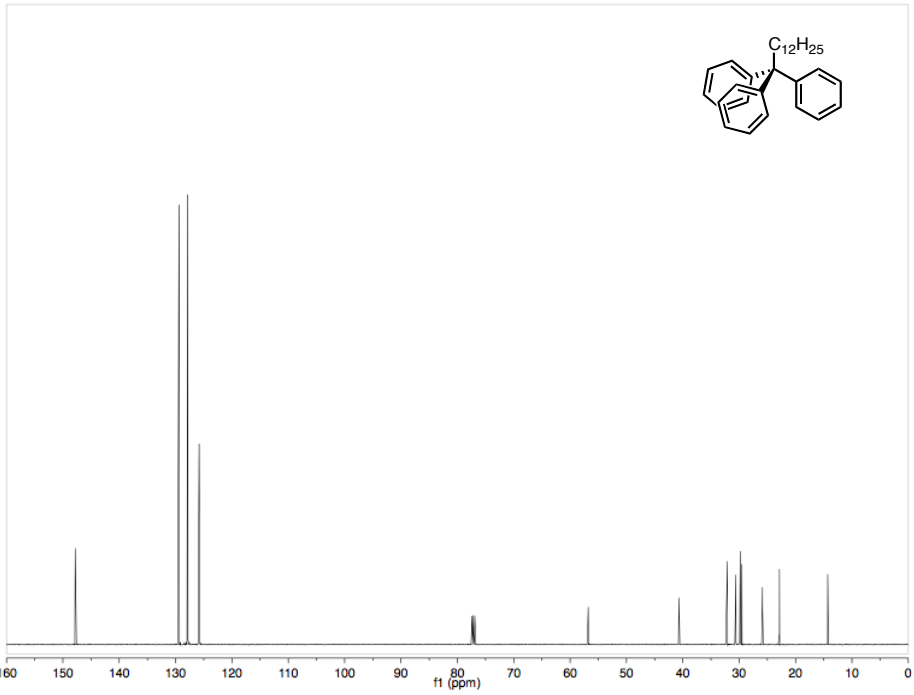

Figure A2.5 ^{1}H NMR spectrum of 1,1,1-tris(4-bromophenyl)tridecane (**5**) ($CDCl_3$, 500 MHz). Impurities are denoted by a *.

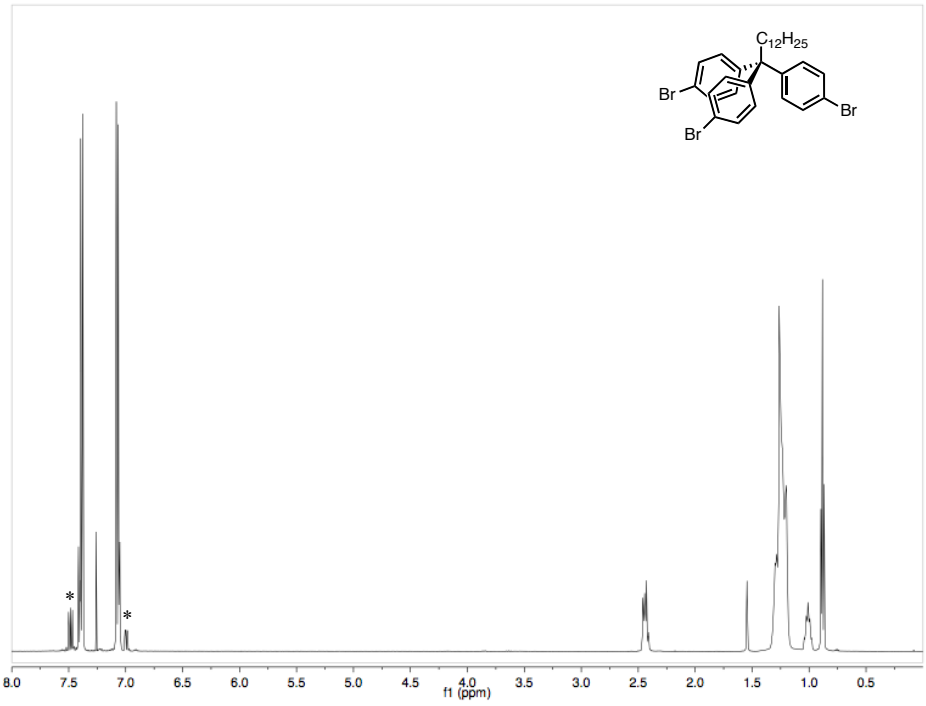

Figure A2.6 ^{13}C NMR spectrum of 1,1,1-tris(4-bromophenyl)tridecane (**5**) ($CDCl_3$, 125 MHz). Impurities are denoted by a *.

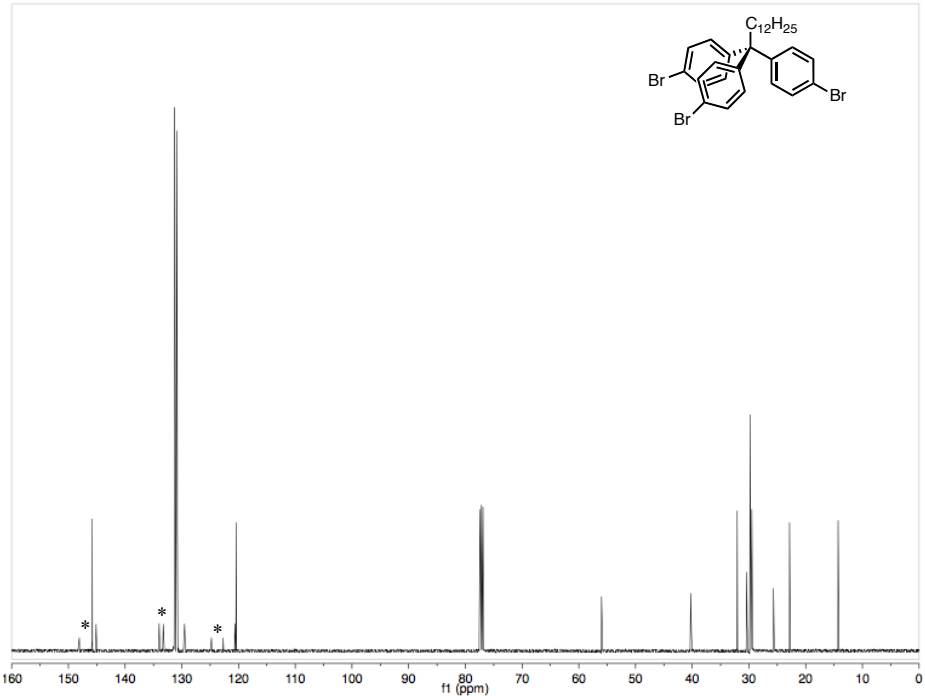

Figure A2.7 ^{1}H NMR spectrum of 1,1,1-tris(4-pinacolatoborophenyl)tridecane (**6**) ($CDCl_3$, 500 MHz).

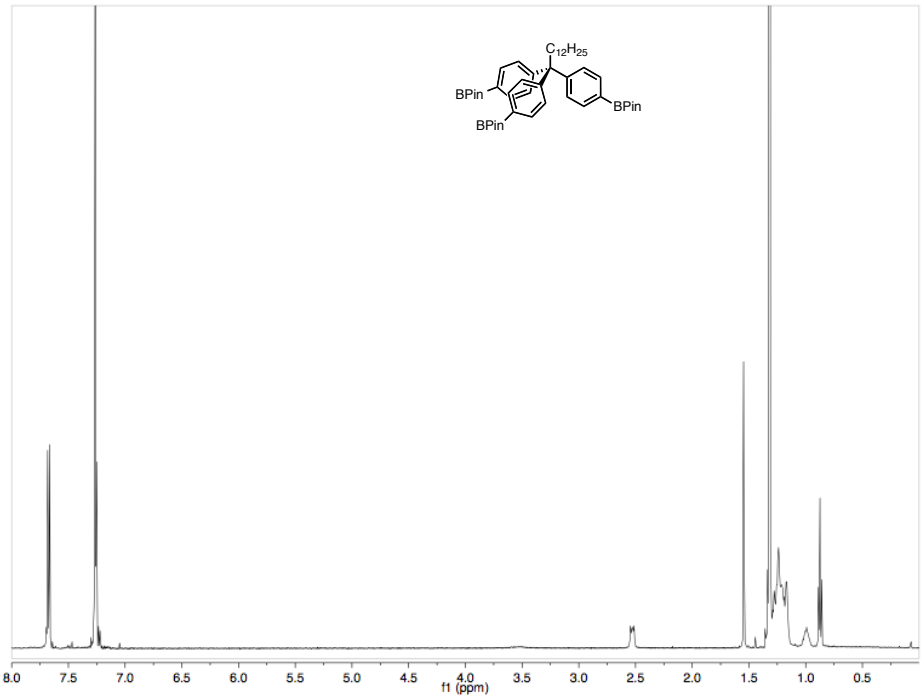

Figure A2.8 ^{13}C NMR spectrum of 1,1,1-tris(4-pinacolatoborophenyl)tridecane (**6**) ($CDCl_3$, 125 MHz). ^{13}C-B is not observed due to the large coupling constant between the nuclei.

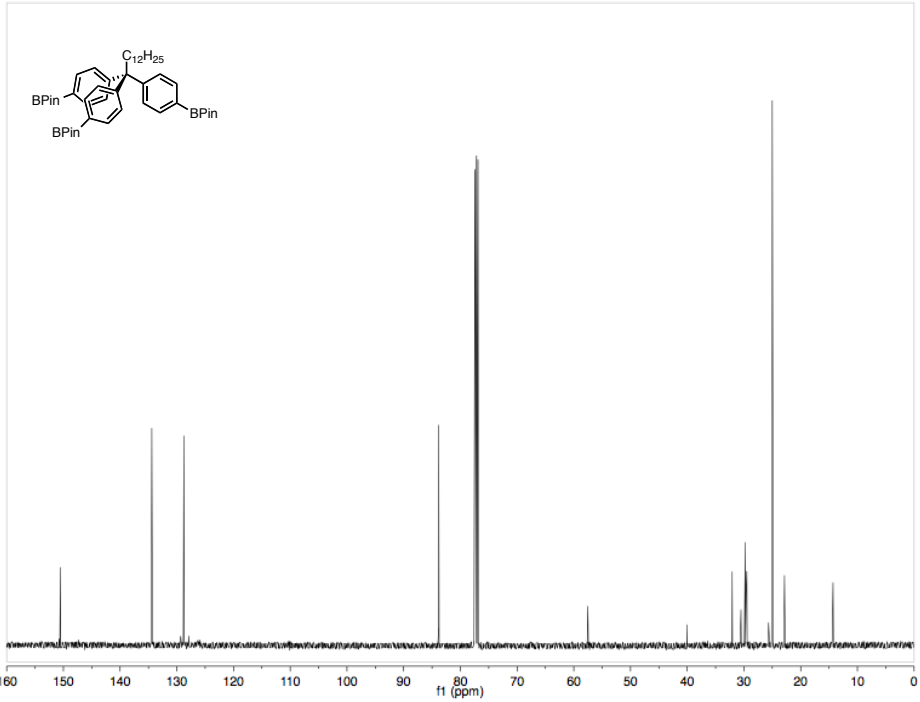

Figure A2.9 ^{1}H NMR spectrum of 1,1,1-tris(4-phenylboronic acid)tridecane (**2**) ($CDCl_3$, 400 MHz).

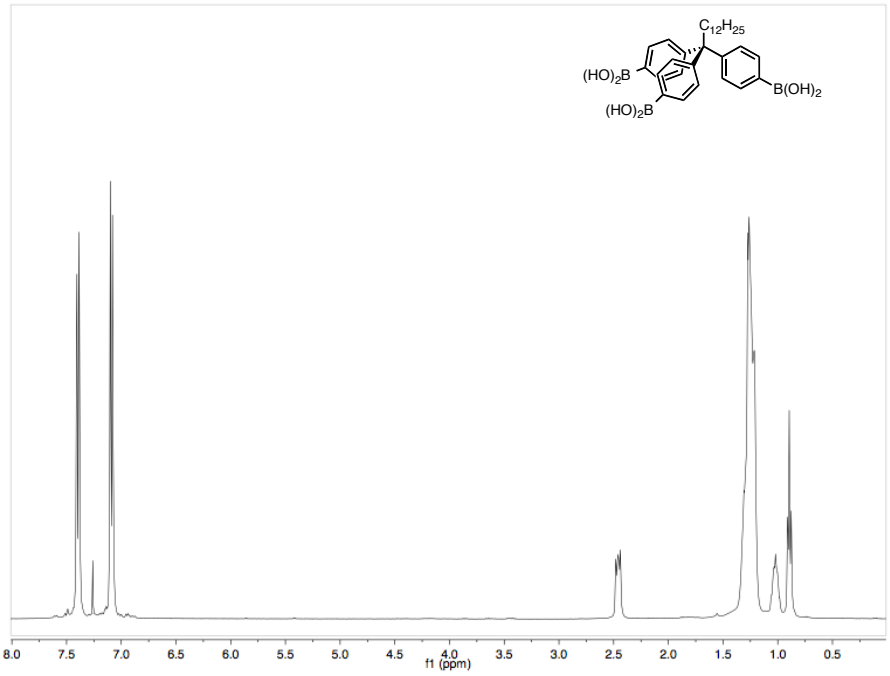

Figure A2.10 ^{13}C NMR spectrum of 1,1,1-tris(4-phenylboronic acid)tridecane (**2**) (DMSO-d_6, 125 MHz). ^{13}C-B is not observed due to the large coupling constant between the nuclei.

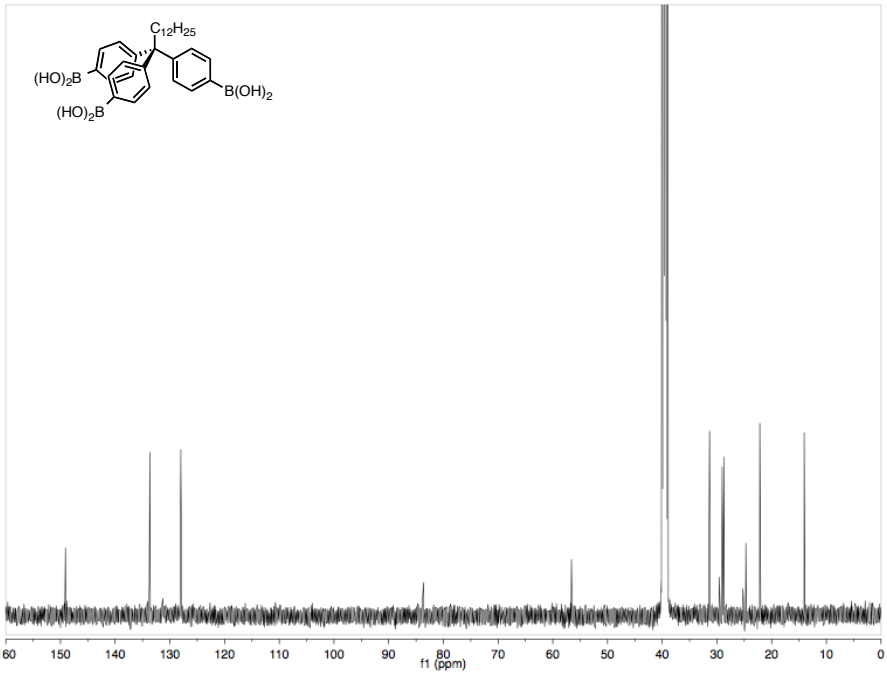

Figure A2.11 ^{1}H NMR spectrum of tris(4-bromophenyl)methanol (**7**) ($CDCl_3$, 500 MHz).

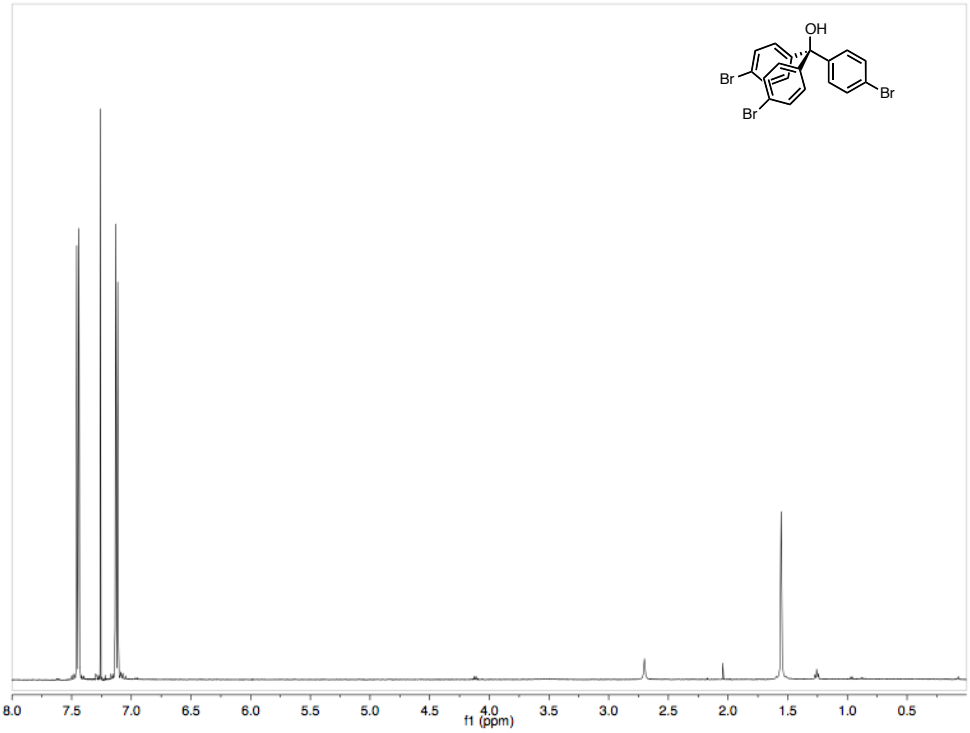

Figure A2.12 ^{13}C NMR spectrum of tris(4-bromophenyl)methanol (**7**) ($CDCl_3$, 125 MHz).

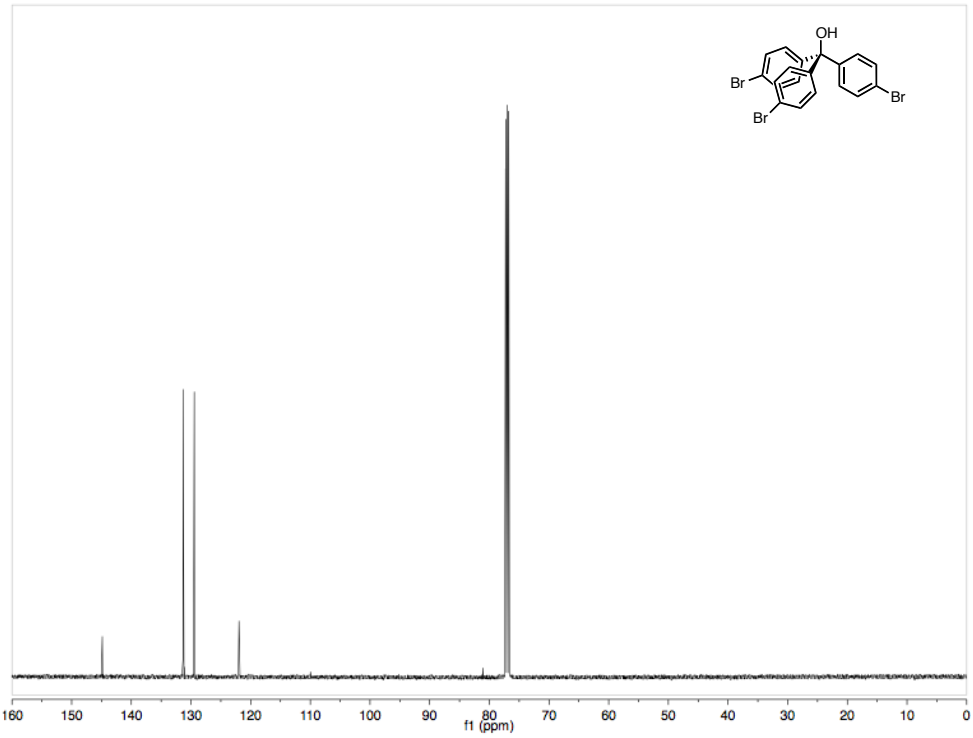

Figure A2.13 ^{1}H NMR spectrum of tris(4-bromophenyl)methane (**8**) ($CDCl_3$, 500 MHz).

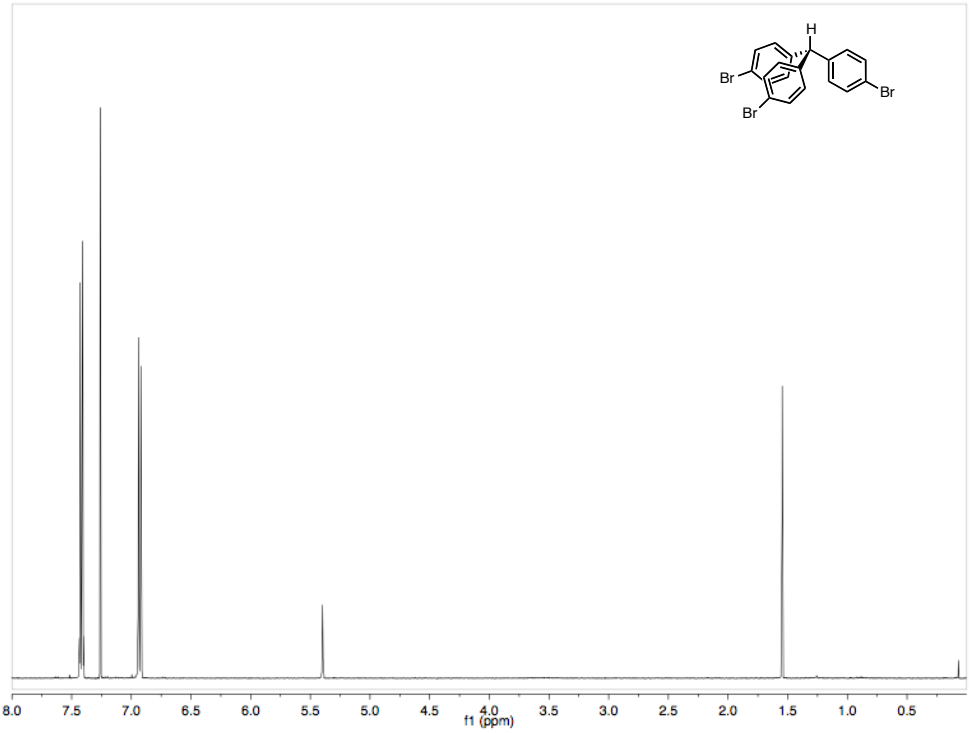

Figure A2.14 ^{13}C NMR spectrum of tris(4-bromophenyl)methane (**8**) ($CDCl_3$, 125 MHz).

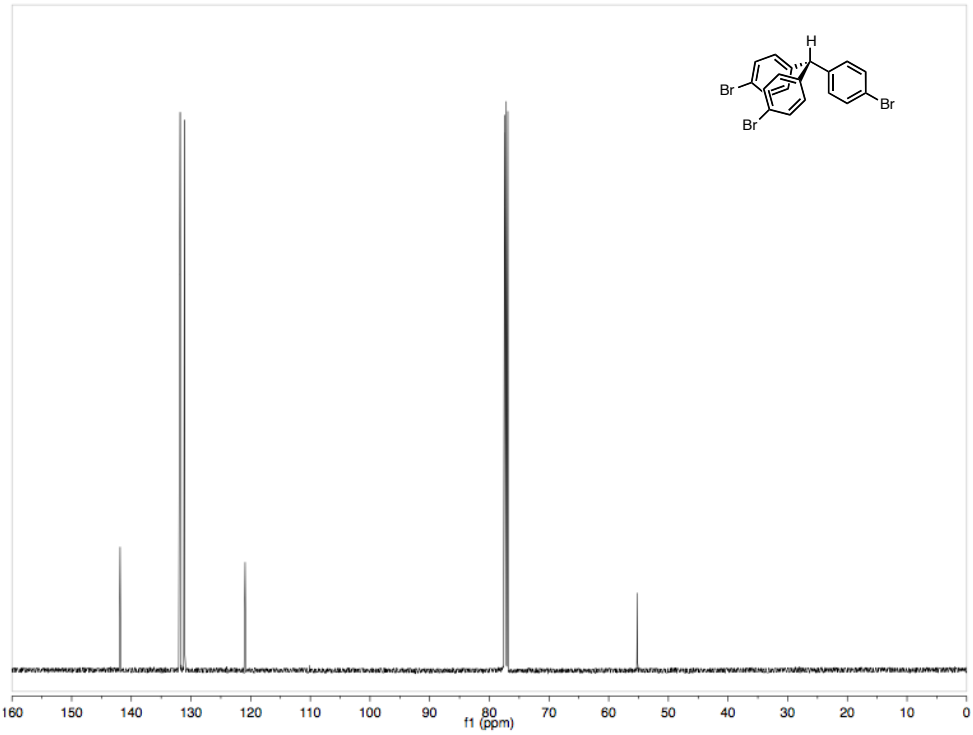

Figure A2.15 ^{1}H NMR spectrum of 1,1,1-tris(4-bromophenyl)but-3-ene (**9**) ($CDCl_3$, 500 MHz).

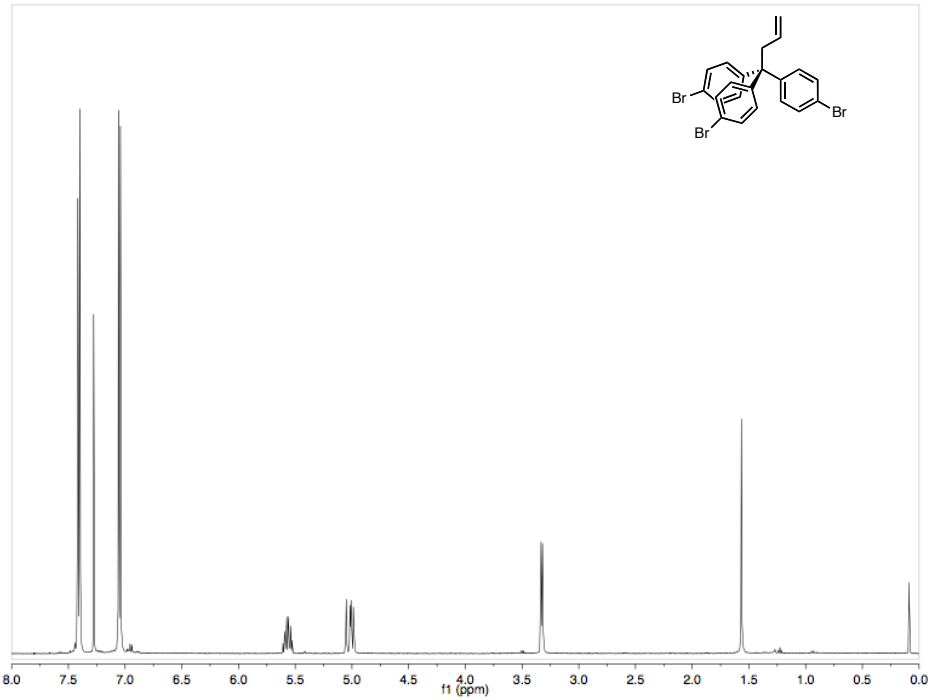

Figure A2.16 ^{13}C NMR spectrum of 1,1,1-tris(4-bromophenyl)but-3-ene (**9**) ($CDCl_3$, 125 MHz).

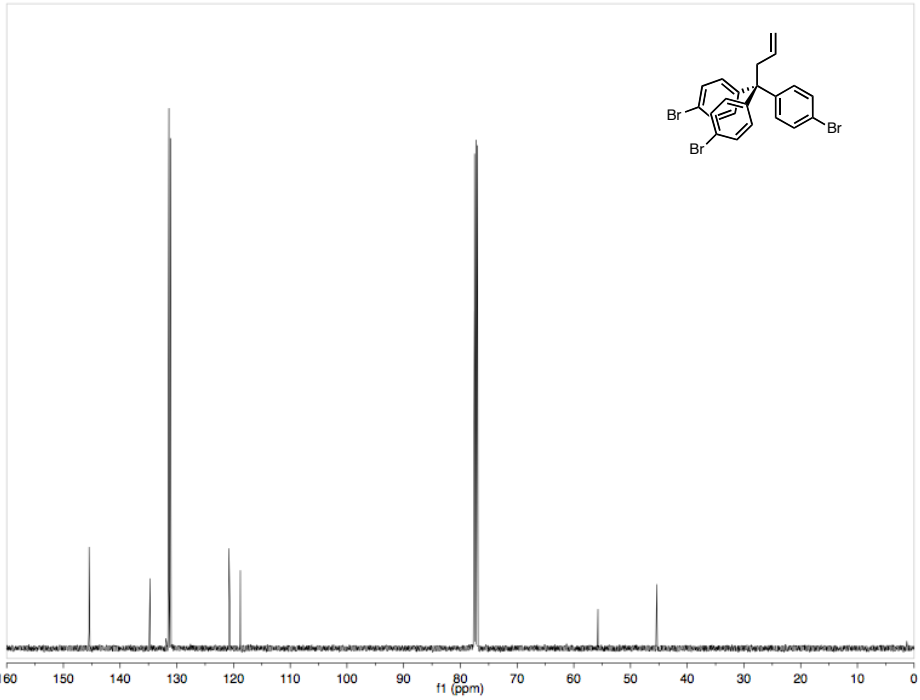

Figure A2.17 ^{1}H NMR spectrum of 1,1,1-tris(4-phenylboronic acid)but-3-ene (**3**) ($CDCl_3$, 500 MHz).

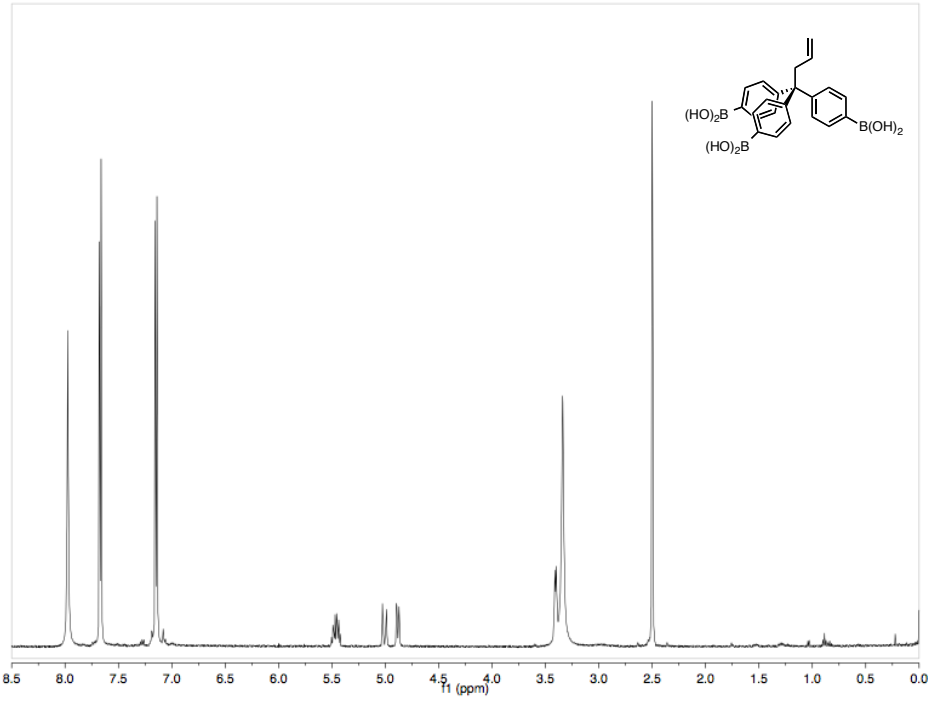

Figure A2.18 ^{13}C NMR spectrum of 1,1,1-tris(4-phenylboronic acid)but-3-ene (**3**) ($CDCl_3$, 125 MHz). ^{13}C-B is not observed due to the large coupling constant between the nuclei.

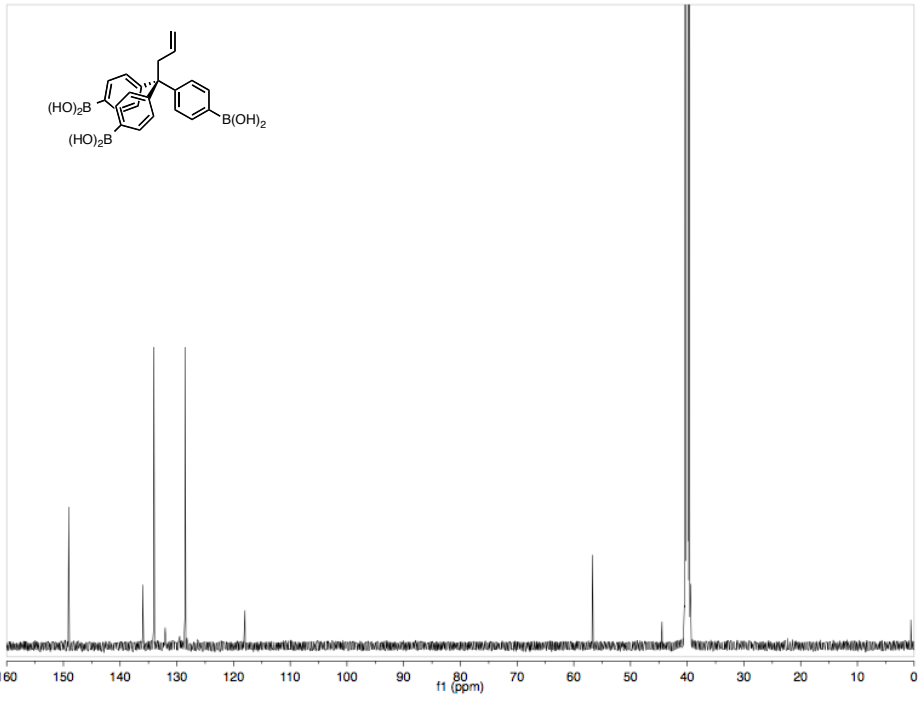

IV. Additional Characterization of COF Powders

Figure A2.19. FTIR spectrum of dodecyl functionalized (7.6%) COF-102.

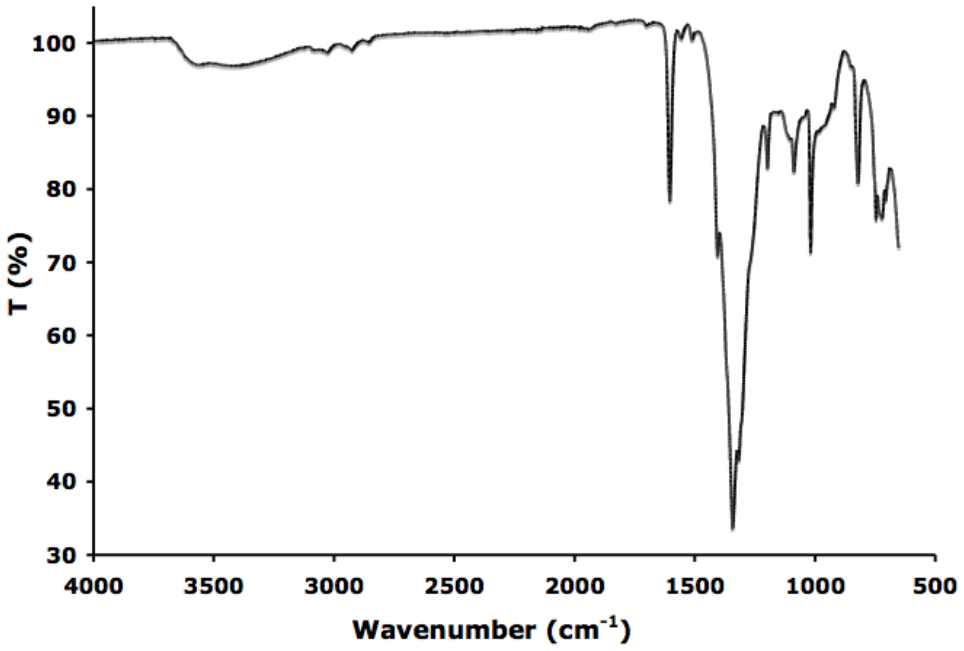

Figure A2.20 PXRD pattern of dodecyl functionalized (7.6%) COF-102, as synthesized.

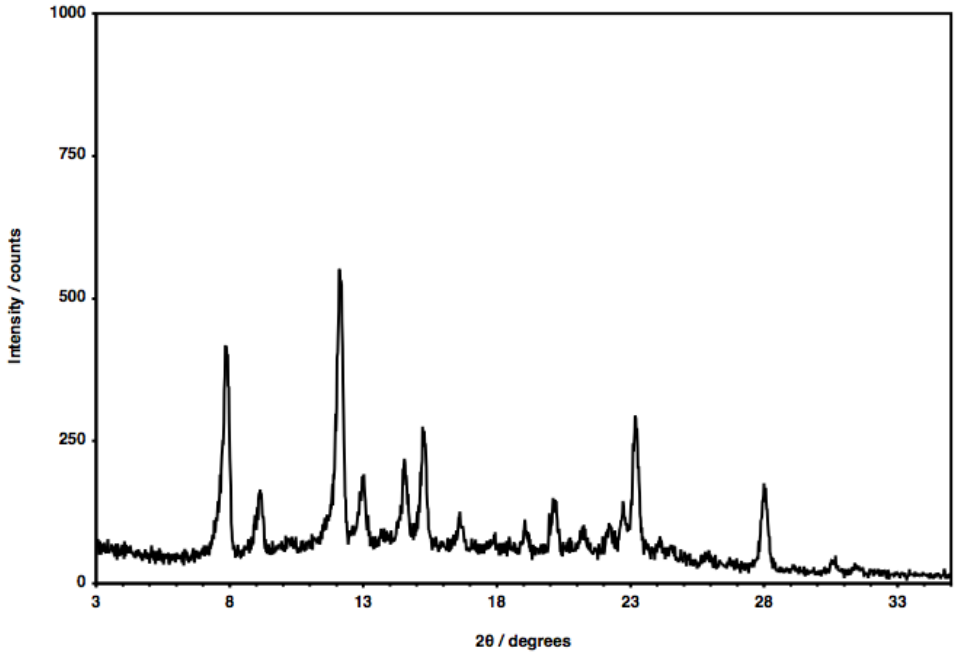

Figure A2.21 PXRD pattern of dodecyl functionalized (7.6%) COF-102, activated.

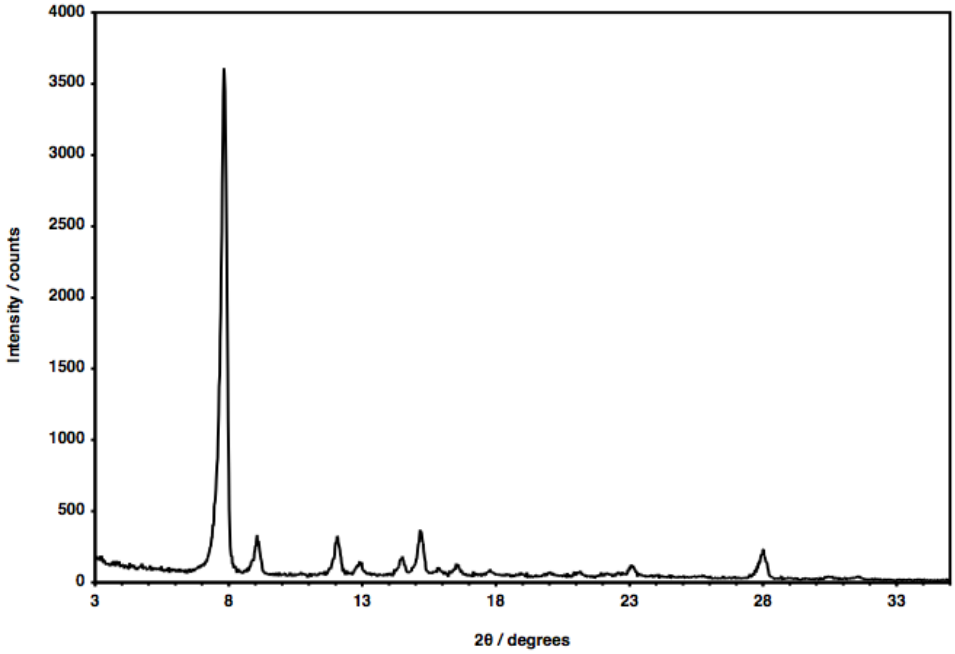

Figure A2.22 ^{1}H NMR spectrum (500 MHz) of dodecyl functionalized (7.6%) COF-102 digested in CD_3CN / D_2O (3:1 *v/v*).

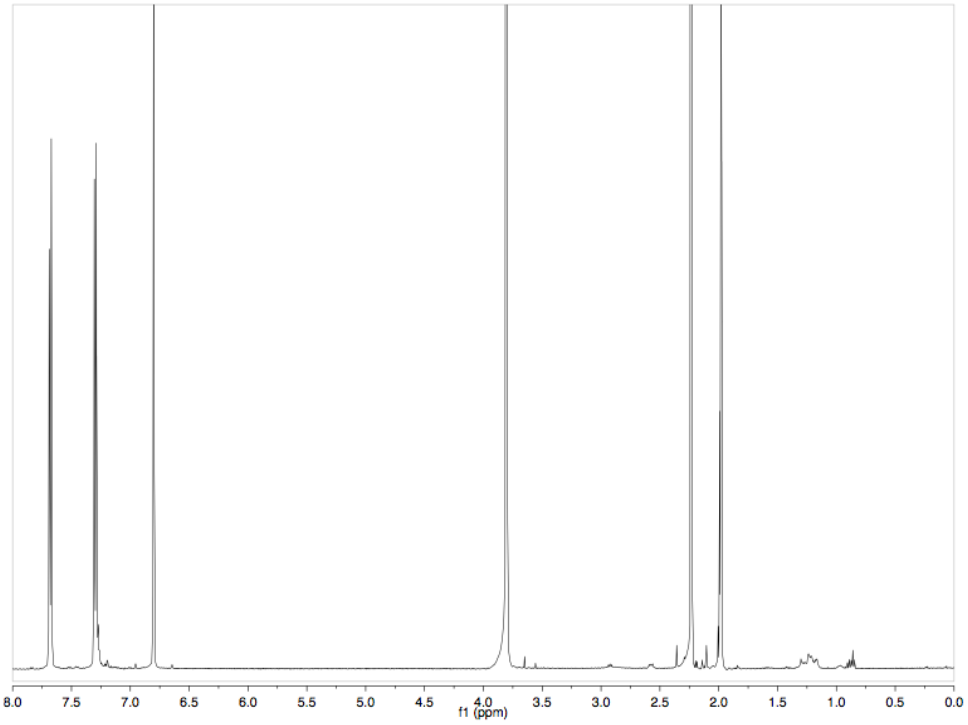

Figure A2.23 N_2 adsorption isotherm (blue: adsorption, red: desorption) of dodecyl functionalized (7.6%) COF-102.

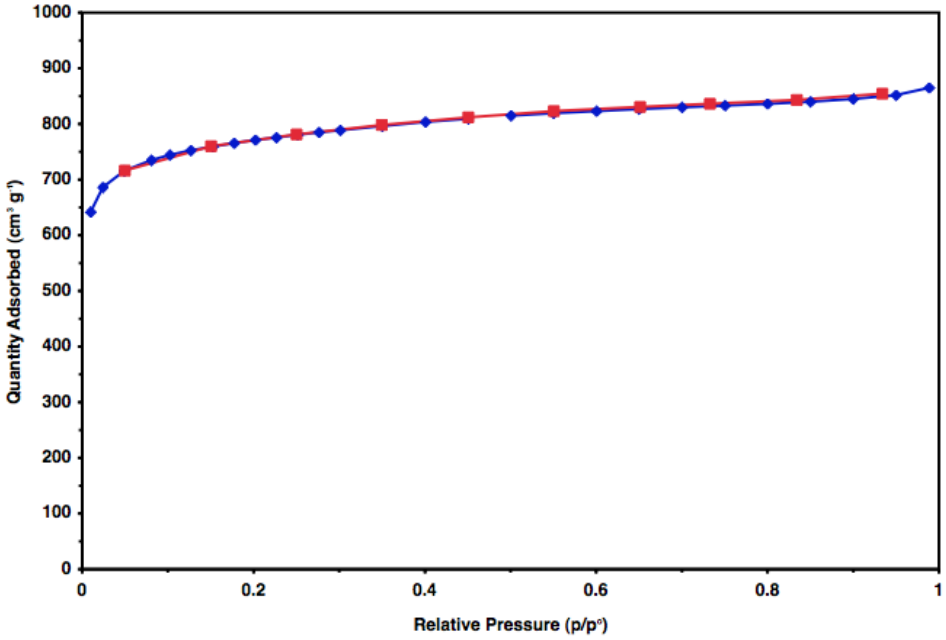

Figure A2.24 Ar adsorption isotherm (blue: adsorption, red: desorption) of dodecyl functionalized (7.6%) COF-102.

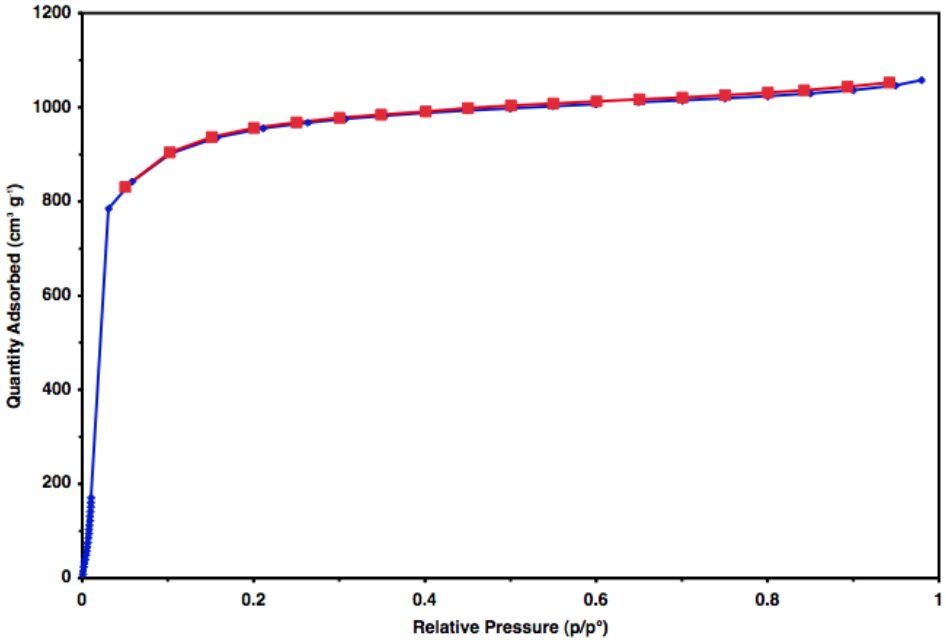

Figure A2.25 Cumulative pore volume versus pore width for dodecyl functionalized (7.6%) COF-102.

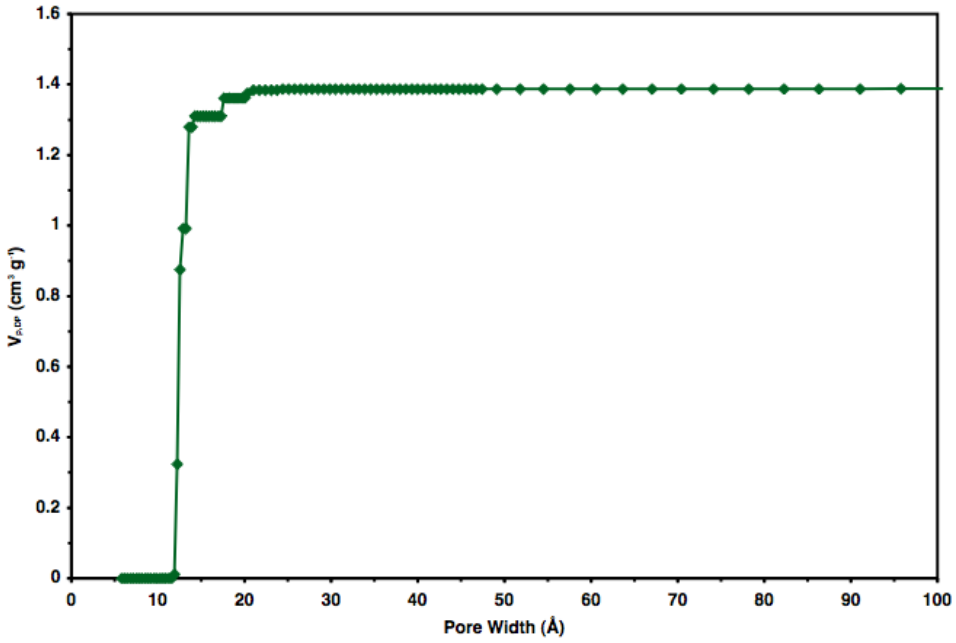

Figure A2.26 FTIR spectrum of dodecyl functionalized (8.1%) COF-102.

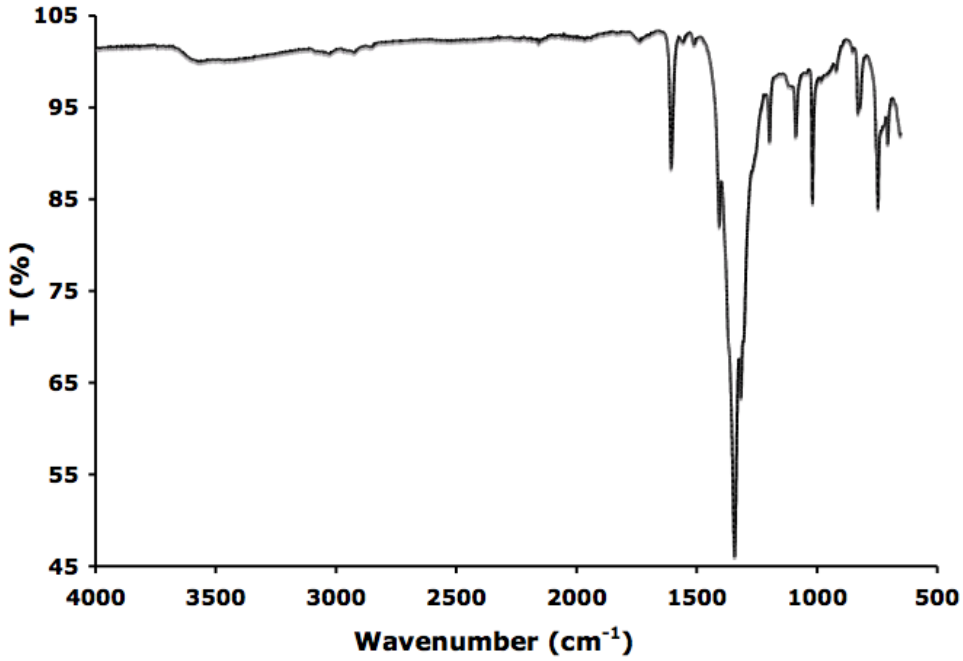

Figure A2.27 PXRD pattern of dodecyl functionalized (8.1%) COF-102, as synthesized.

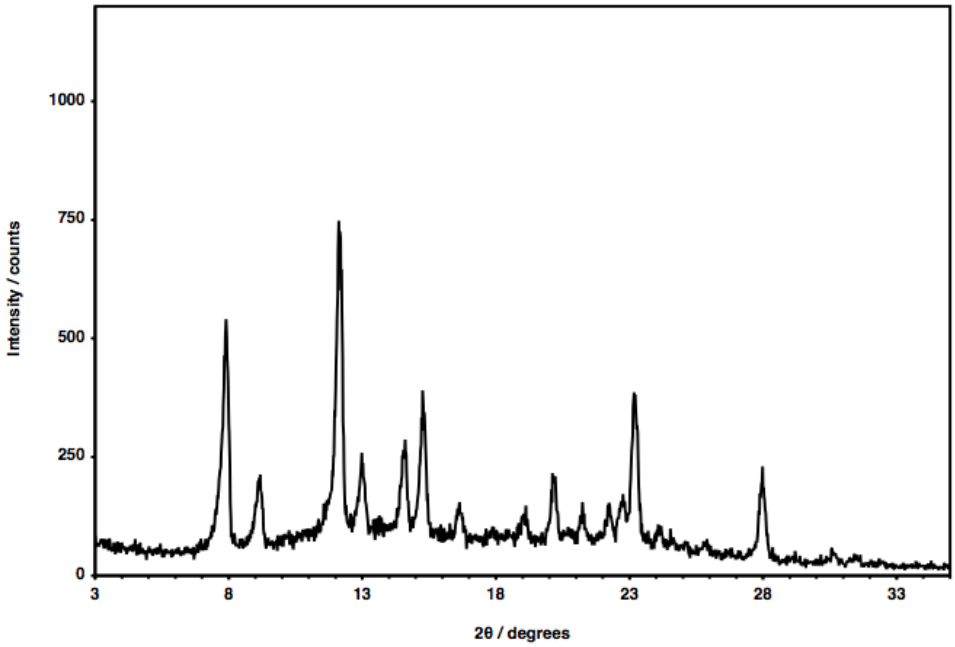

Figure A2.28 PXRD pattern of dodecyl functionalized (8.1%) COF-102, activated.

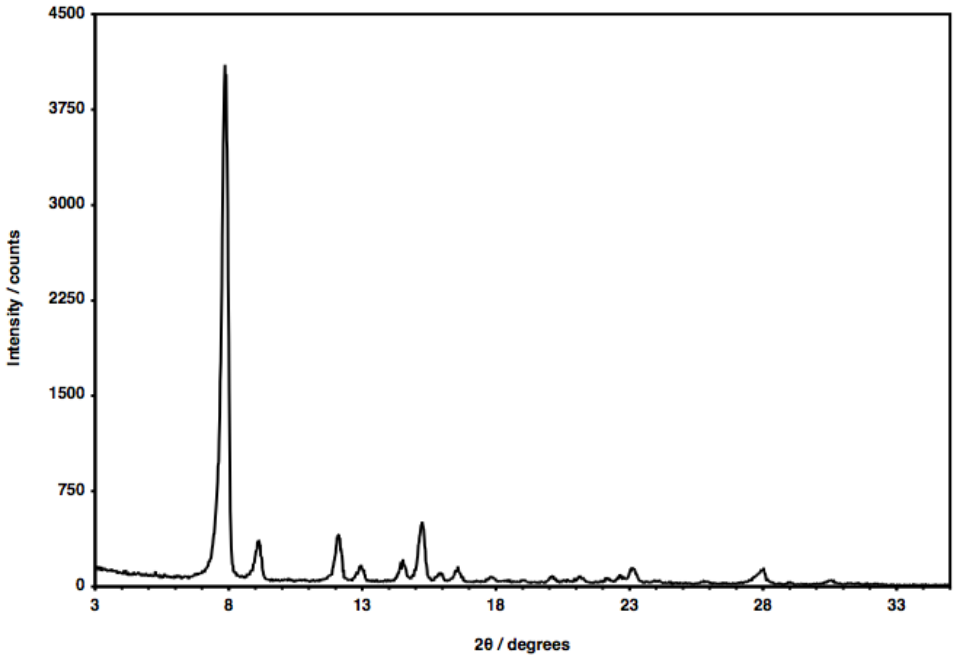

Figure A2.29 ^{1}H NMR spectrum (500 MHz) of dodecyl functionalized (8.1%) COF-102 digested in CD_3CN / D_2O (3:1 *v/v*).

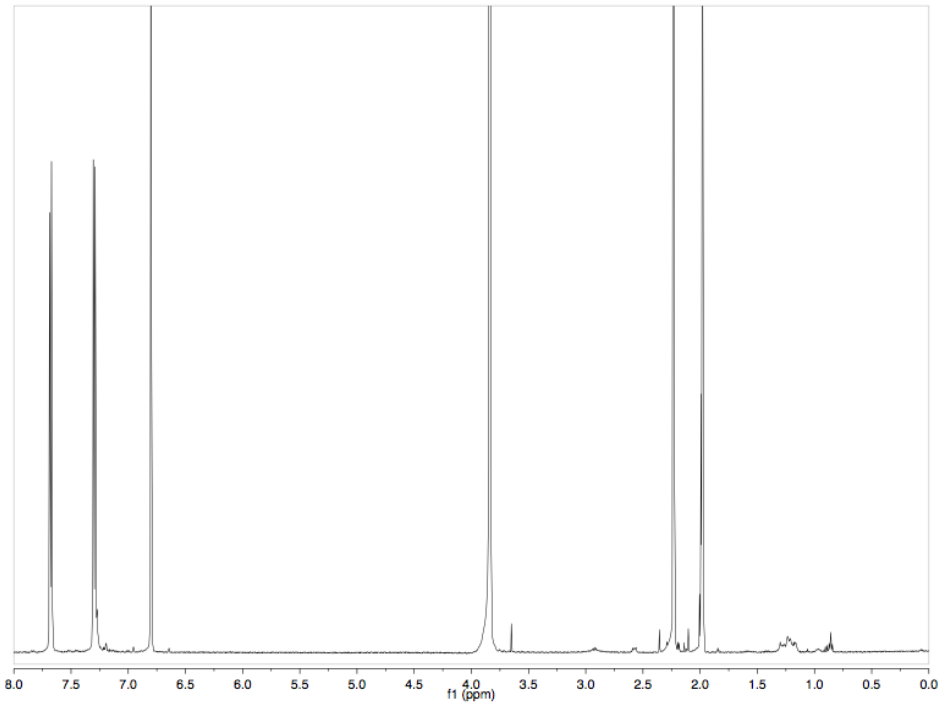

Figure A2.30 N_2 adsorption isotherm (blue: adsorption, red: desorption) of dodecyl functionalized (8.1%) COF-102.

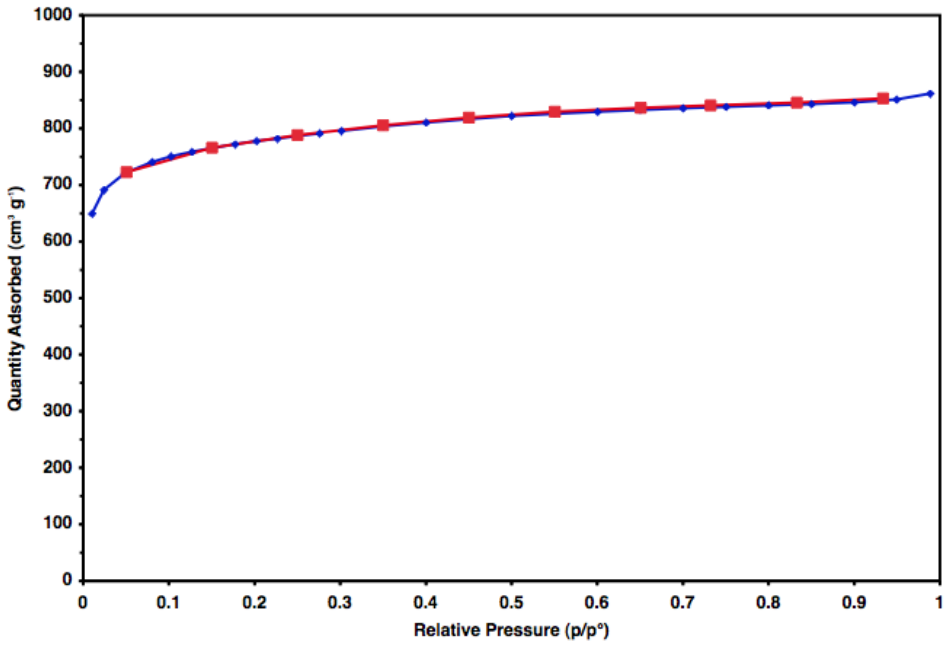

Figure A2.31 Ar adsorption isotherm (blue: adsorption, red: desorption) of dodecyl functionalized (8.1%) COF-102.

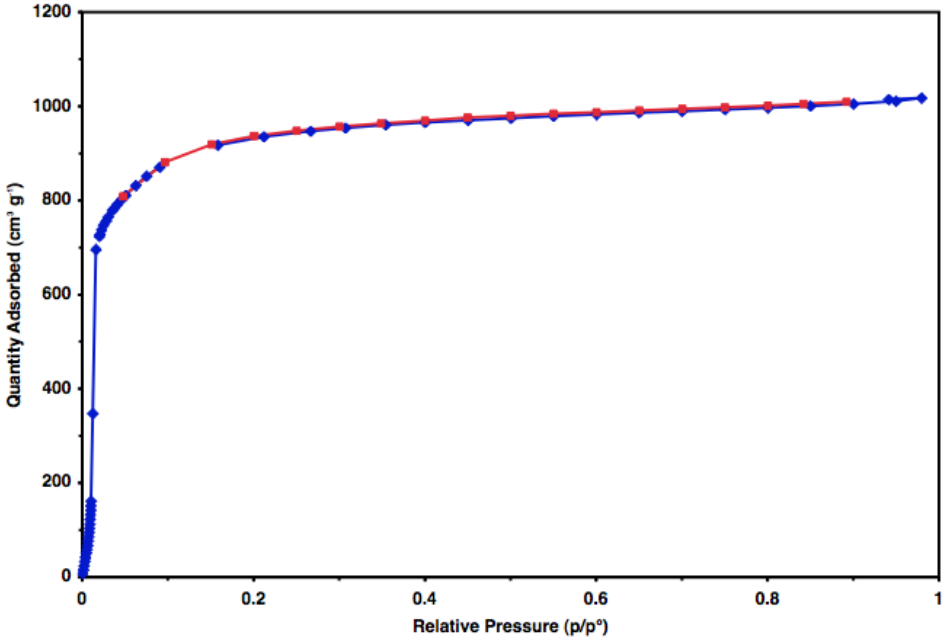

Figure A2.32 Cumulative pore volume versus pore width for dodecyl functionalized (8.1%) COF-102.

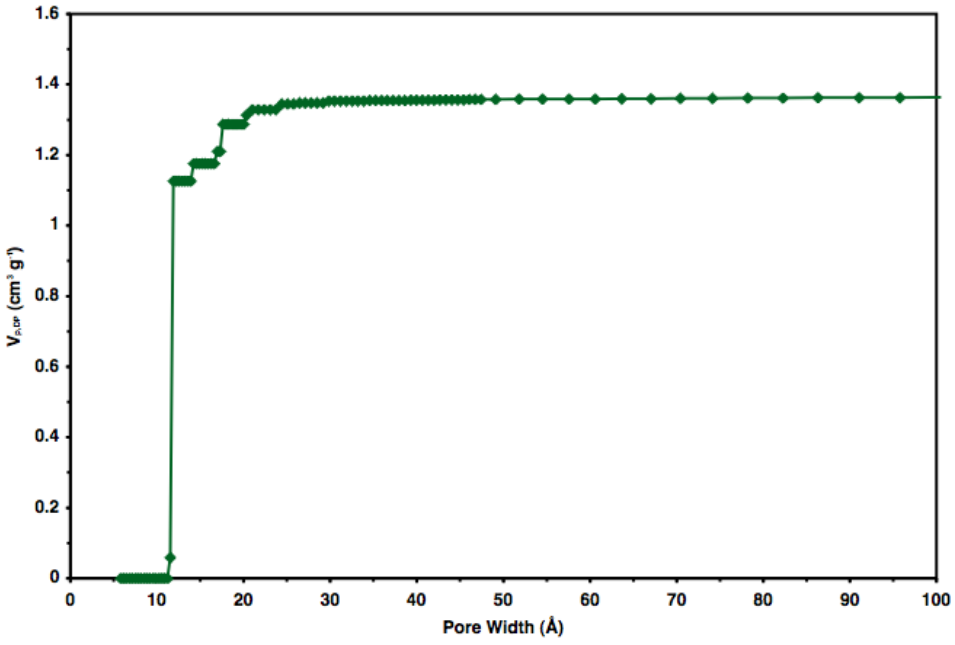

Figure A2.33 FTIR spectrum of dodecyl functionalized (16%) COF-102.

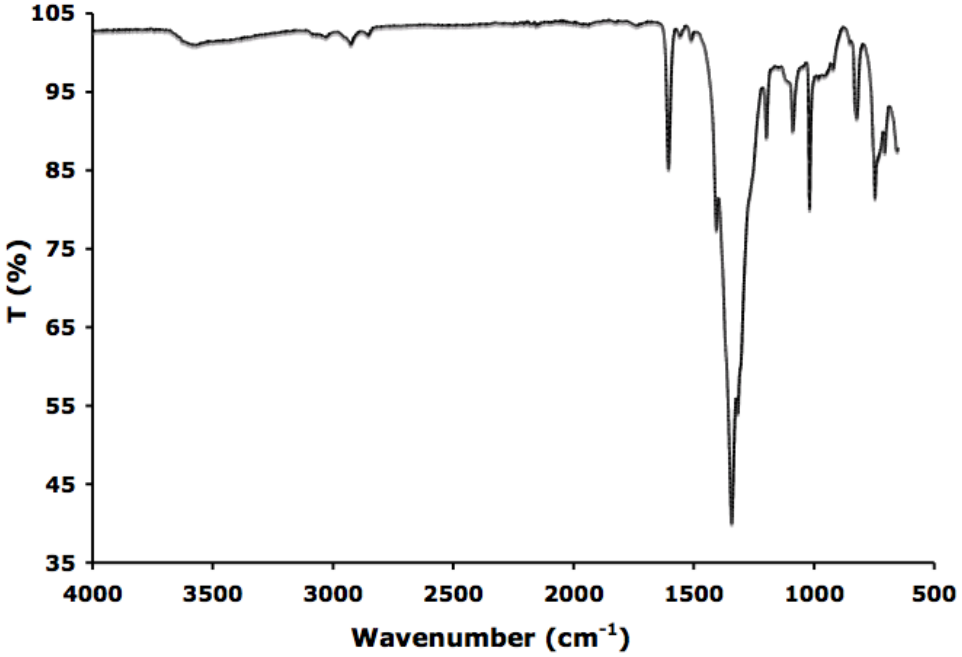

Figure A2.34 PXRD pattern of dodecyl functionalized (16%) COF-102, as synthesized.

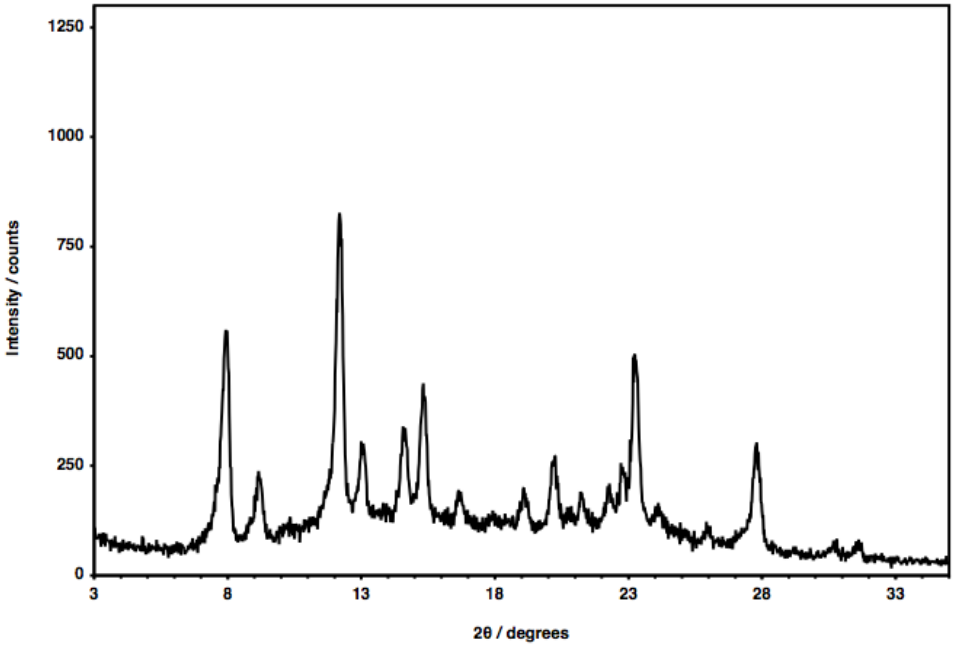

Figure A2.35 PXRD pattern of dodecyl functionalized (16%) COF-102, activated.

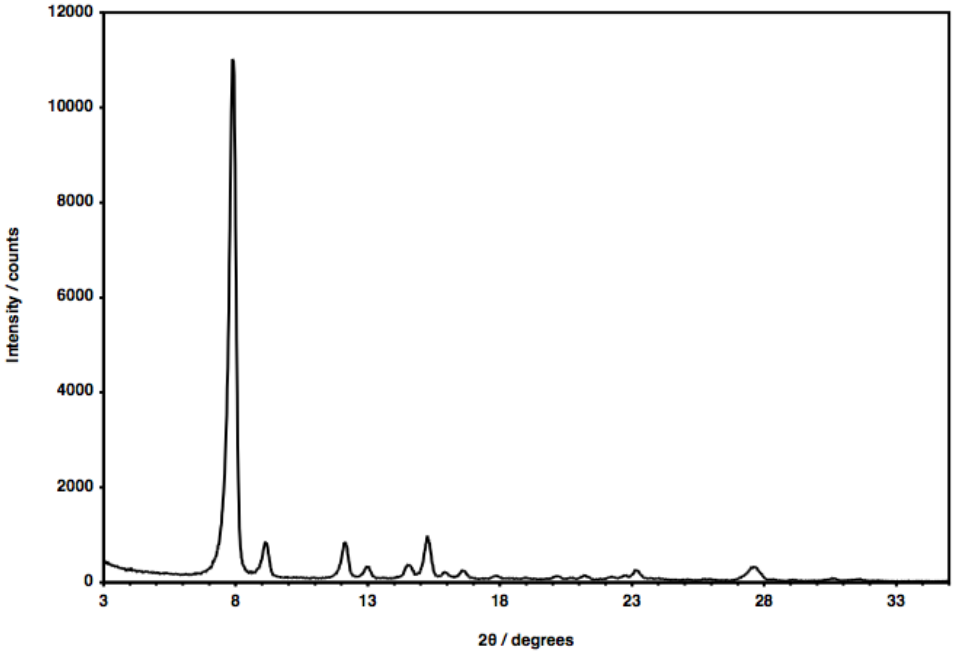

Figure A2.36 ^{1}H NMR spectrum (500 MHz) of dodecyl functionalized (16%) COF-102 digested in CD_3CN / D_2O (3:1 *v/v*).

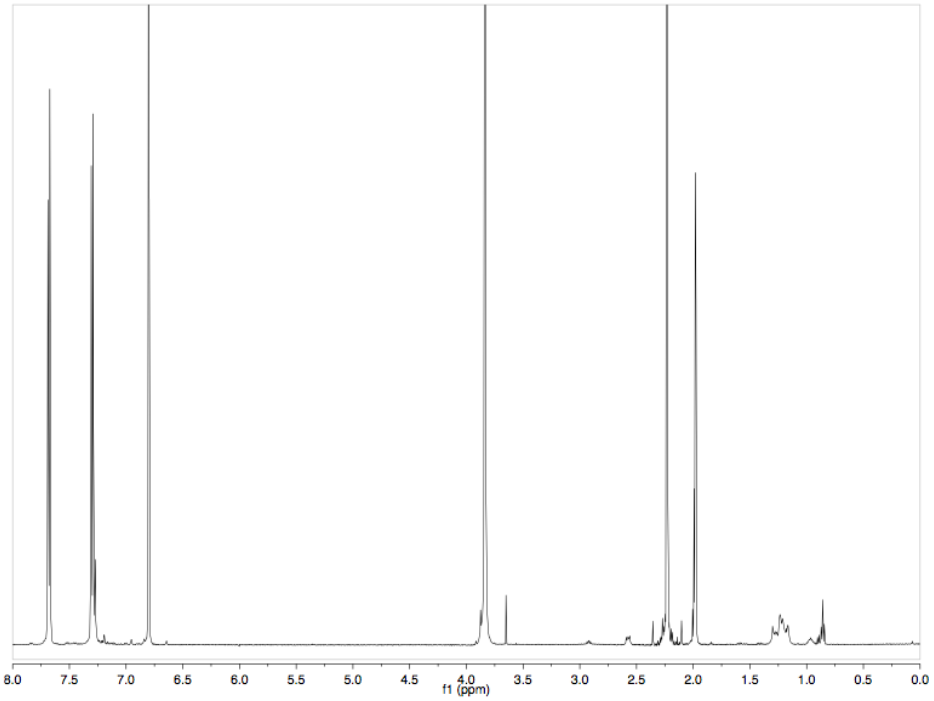

Figure A2.37 N_2 adsorption isotherm (blue: adsorption, red: desorption) of dodecyl functionalized (16%) COF-102.

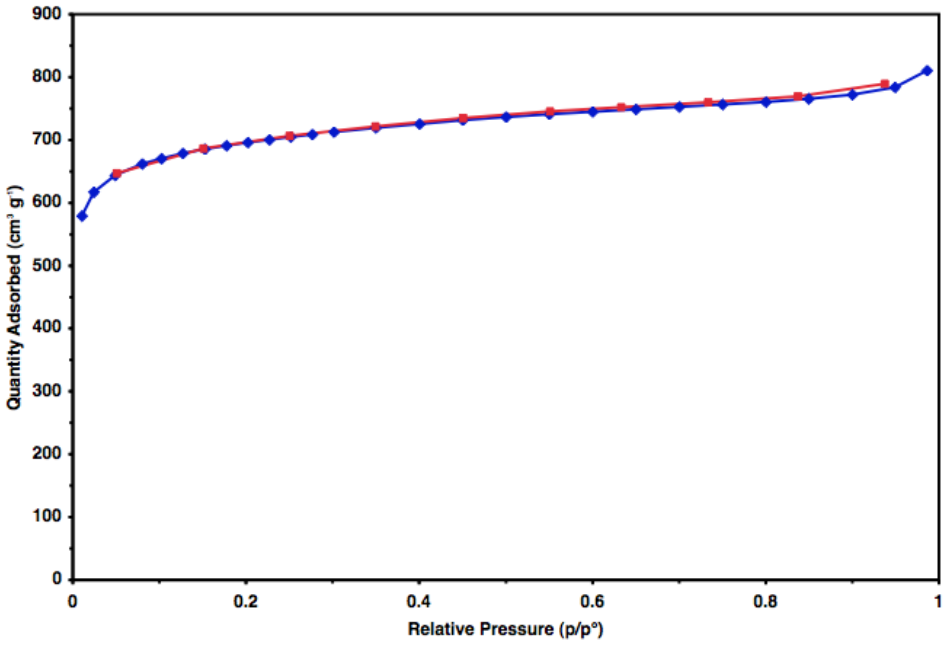

Figure A2.38 Ar adsorption isotherm (blue: adsorption, red: desorption) of dodecyl functionalized (16%) COF-102.

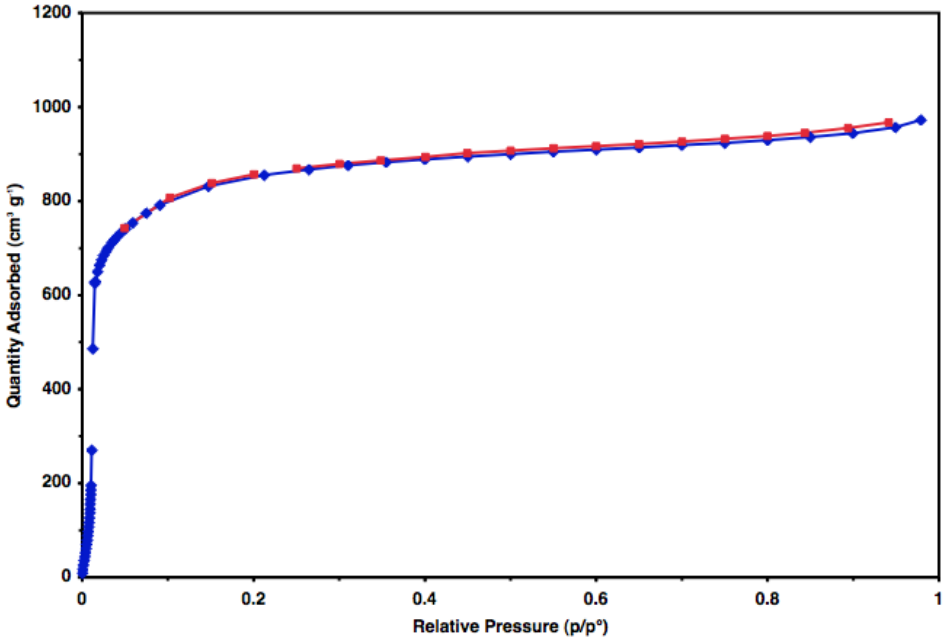

Figure A2.39 Cumulative pore volume versus pore width for dodecyl functionalized (16%) COF-102.

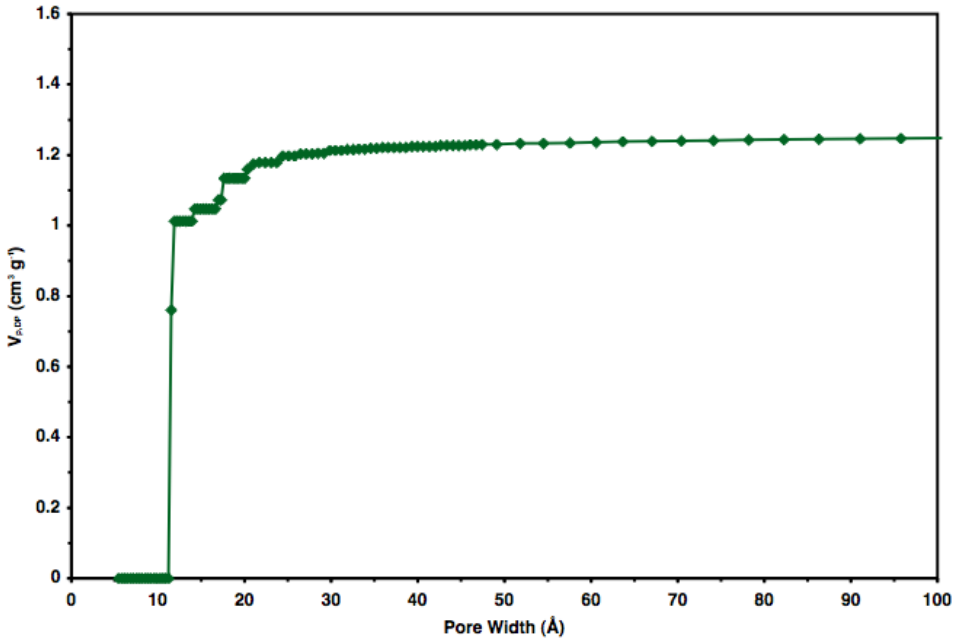

Figure A2.40 FTIR spectrum of dodecyl functionalized (20%) COF-102.

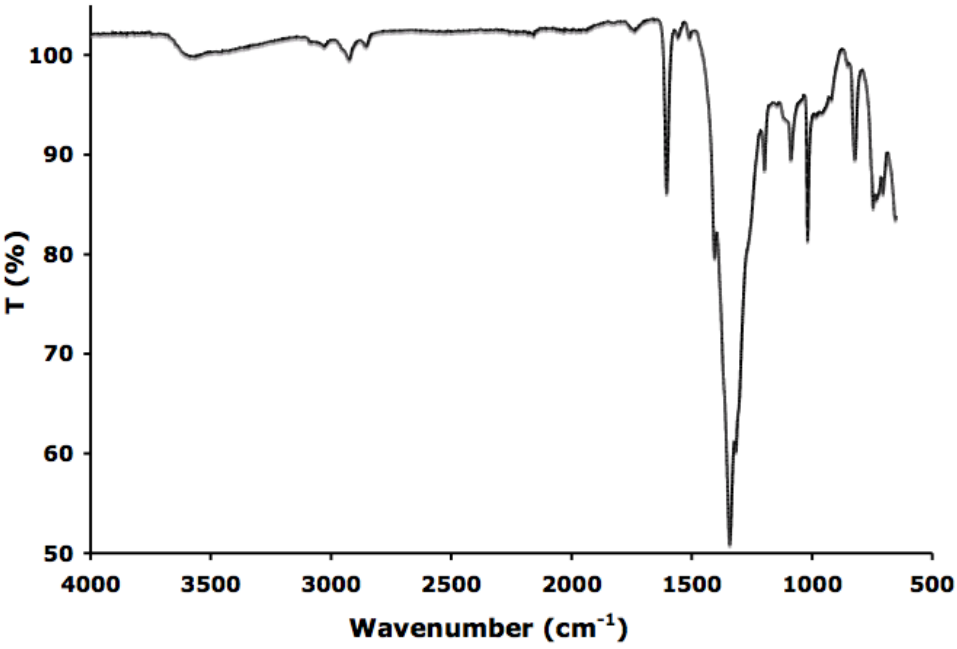

Figure A2.41 PXRD pattern of dodecyl functionalized (20%) COF-102, as synthesized.

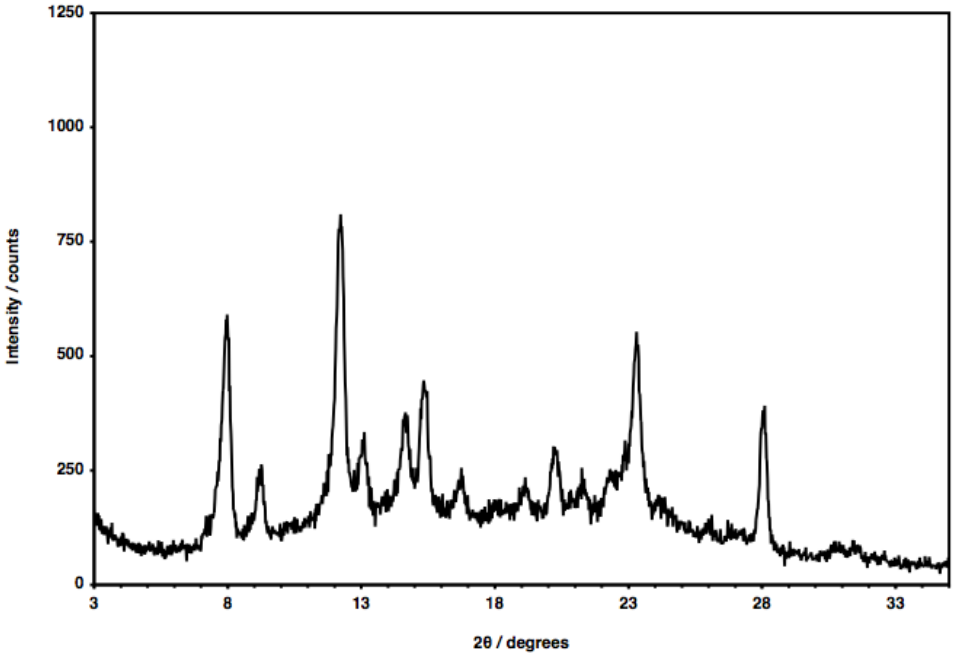

Figure A2.42 PXRD pattern of dodecyl functionalized (20%) COF-102, activated.

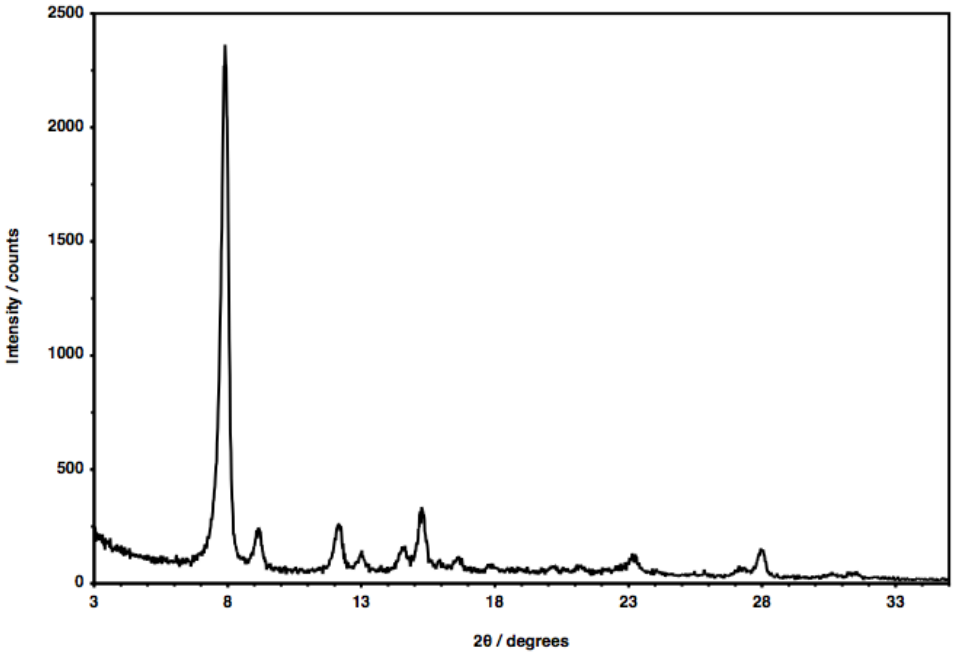

Figure A2.43 ^{1}H NMR spectrum (500 MHz) of dodecyl functionalized (20%) COF-102 digested in CD_3CN / D_2O (3:1 *v/v*).

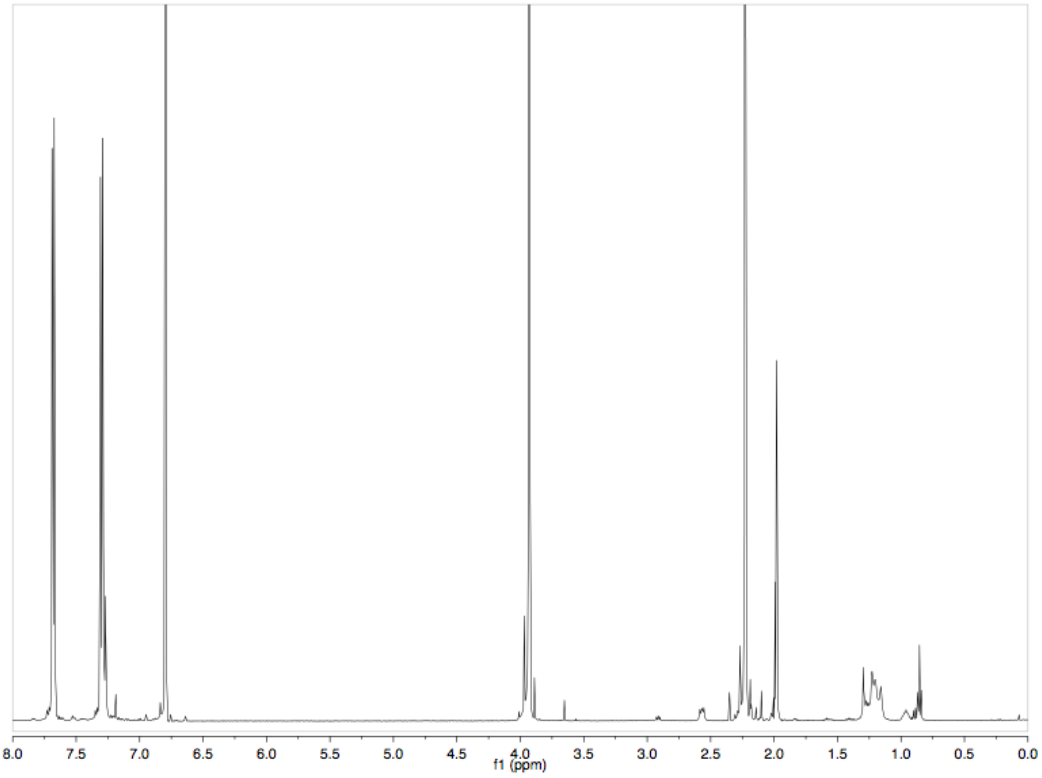

Figure A2.44 N_2 adsorption isotherm (blue: adsorption, red: desorption) of dodecyl functionalized (20%) COF-102.

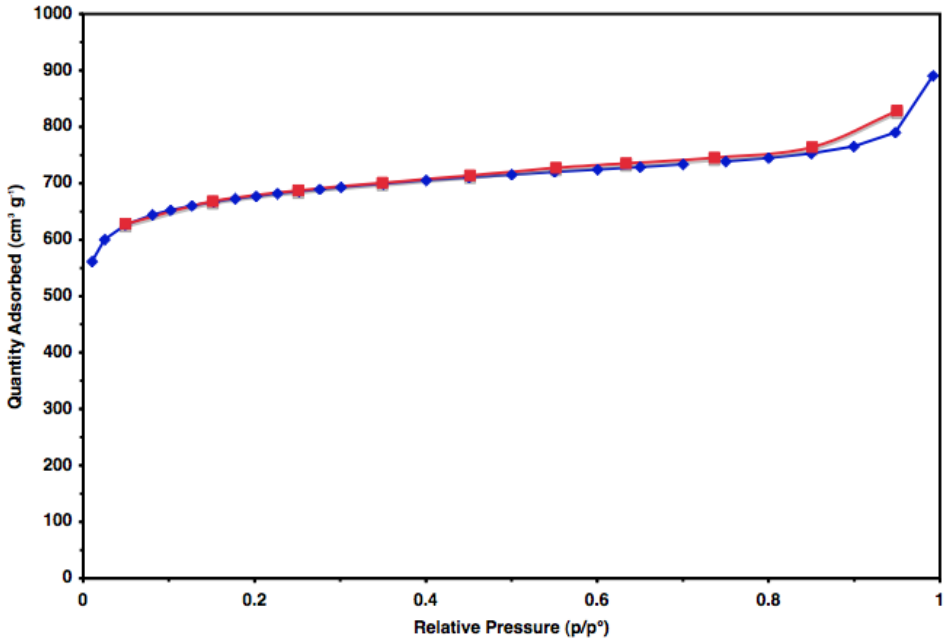

Figure A2.45 Ar adsorption isotherm (blue: adsorption, red: desorption) of dodecyl functionalized (20%) COF-102.

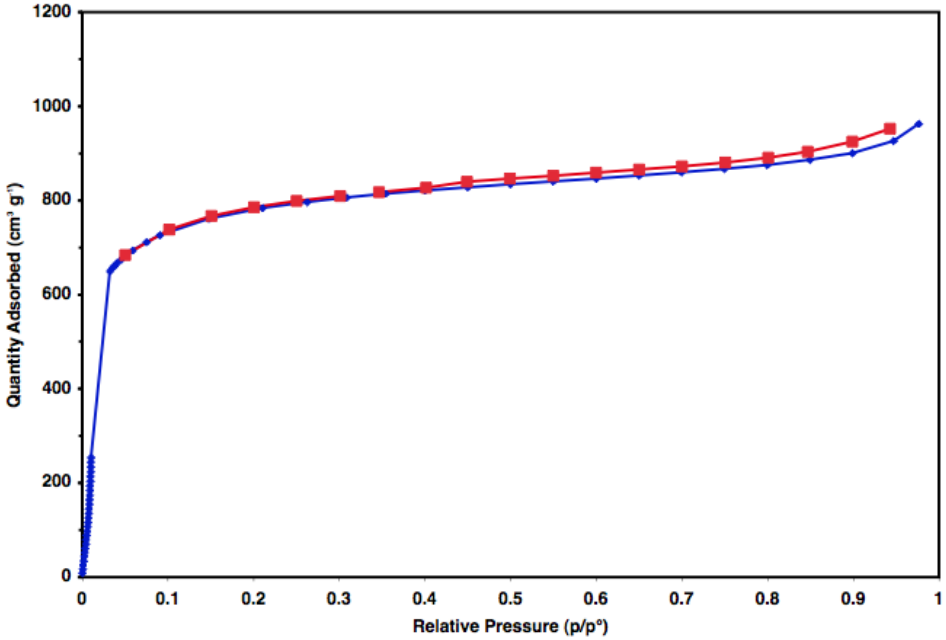

Figure A2.46 Cumulative pore volume versus pore width for dodecyl functionalized (20%) COF-102.

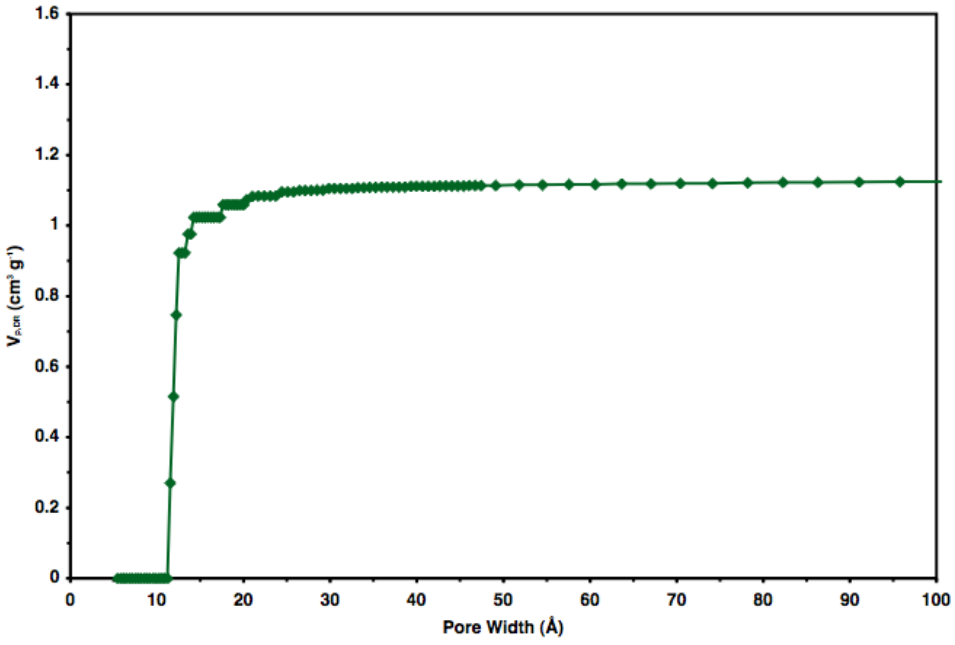

Figure A2.47 FTIR spectrum of dodecyl functionalized (24%) COF-102.

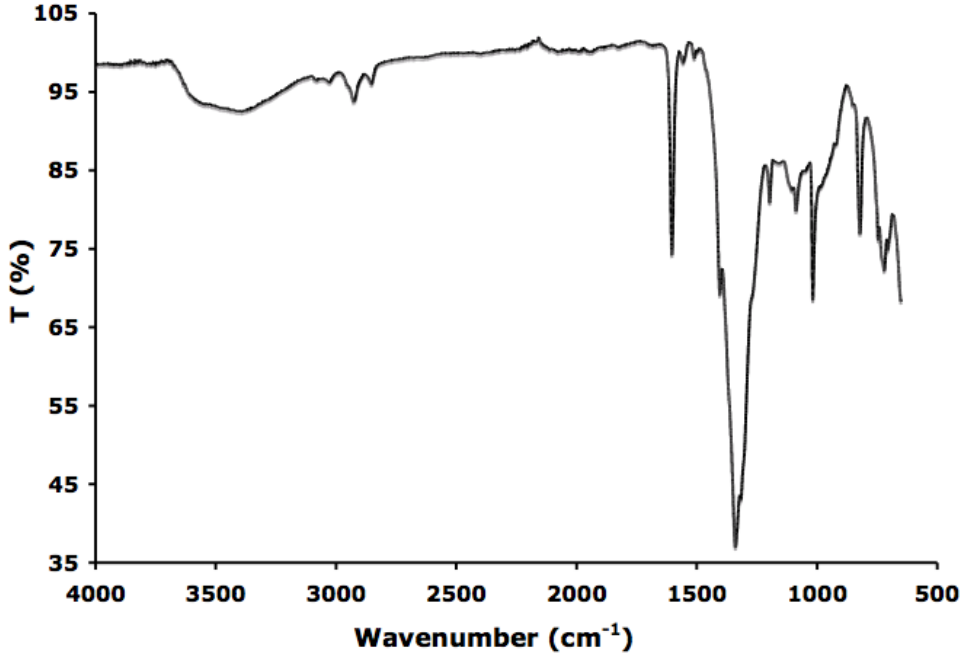

Figure A2.48 ^{1}H NMR spectrum (500 MHz) of dodecyl functionalized (24%) COF-102 digested in CD_3CN / D_2O (3:1 *v/v*).

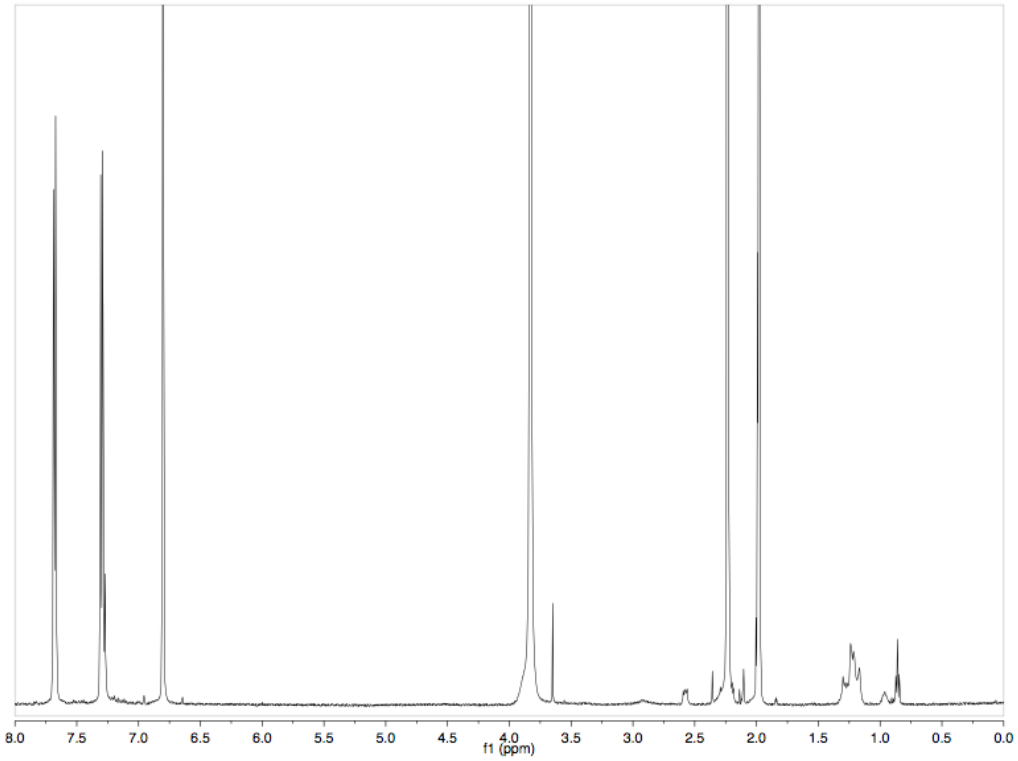

Figure A2.49 N_2 adsorption isotherm (blue: adsorption, red: desorption) of dodecyl functionalized (24%) COF-102.

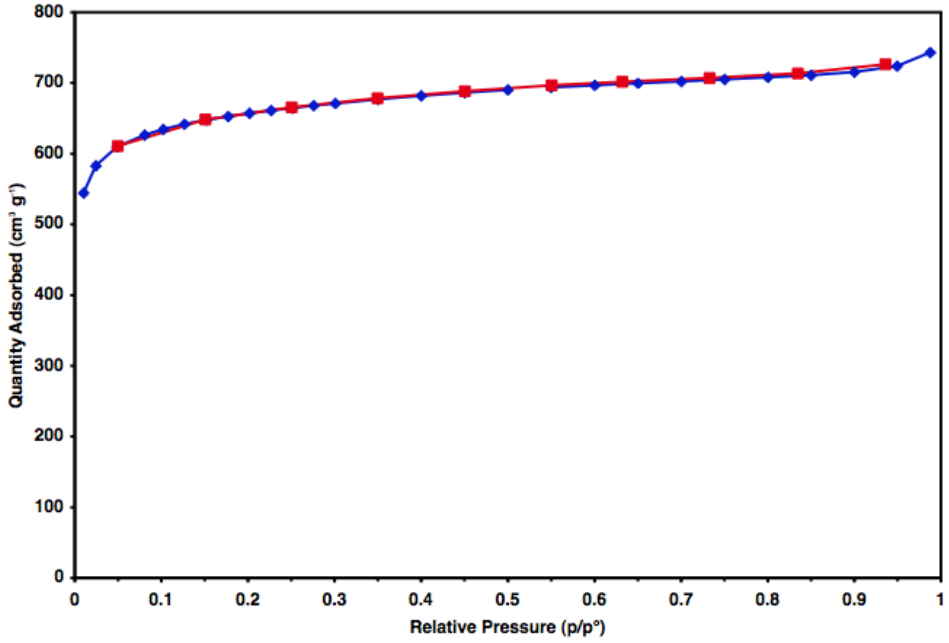

Figure A2.50 FTIR spectrum of dodecyl functionalized (30%) COF-102.

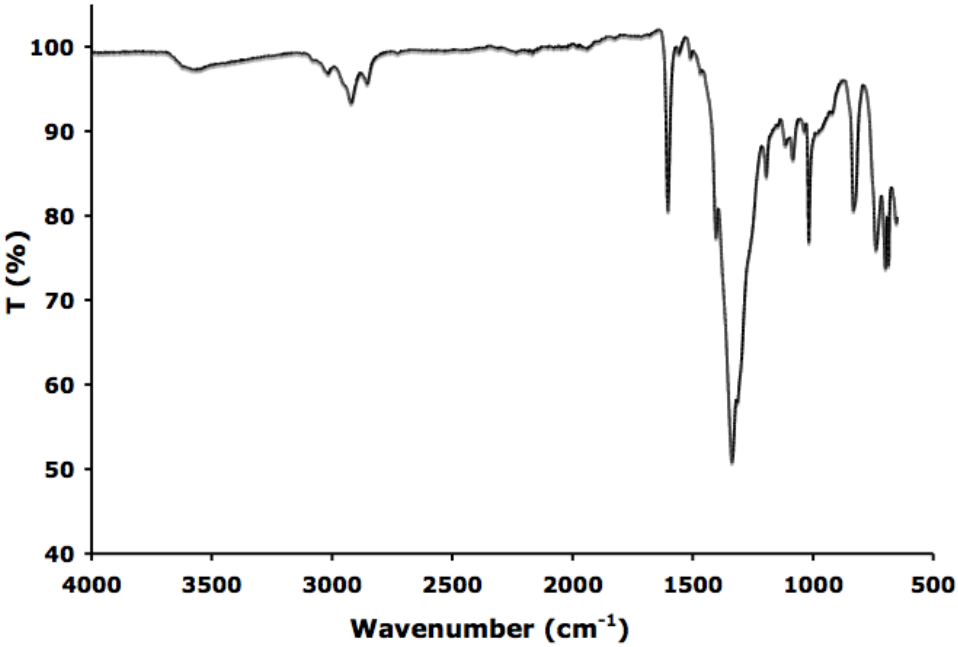

Figure A2.51 PXRD pattern of dodecyl functionalized (30%) COF-102, as synthesized.

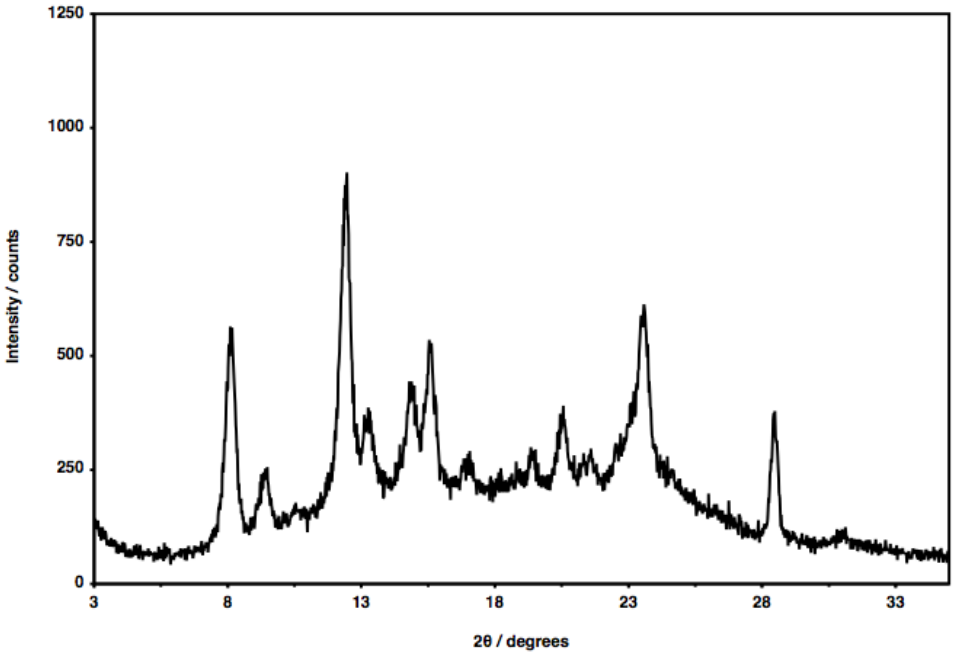

Figure A2.52 PXRD pattern of dodecyl functionalized (30%) COF-102, activated.

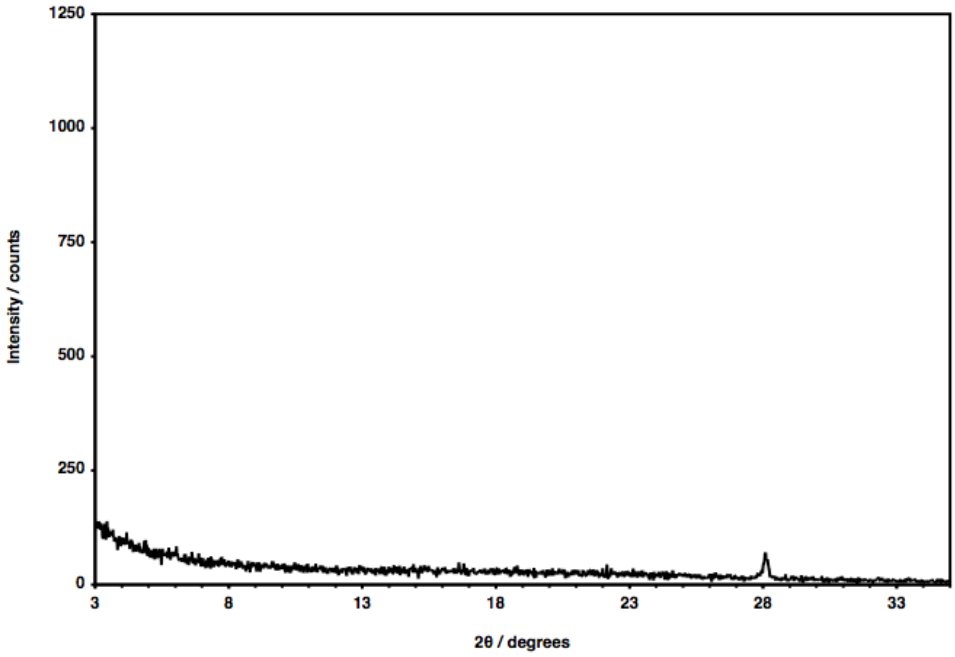

Figure A2.53 FTIR spectrum of dodecyl functionalized (37%) COF-102.

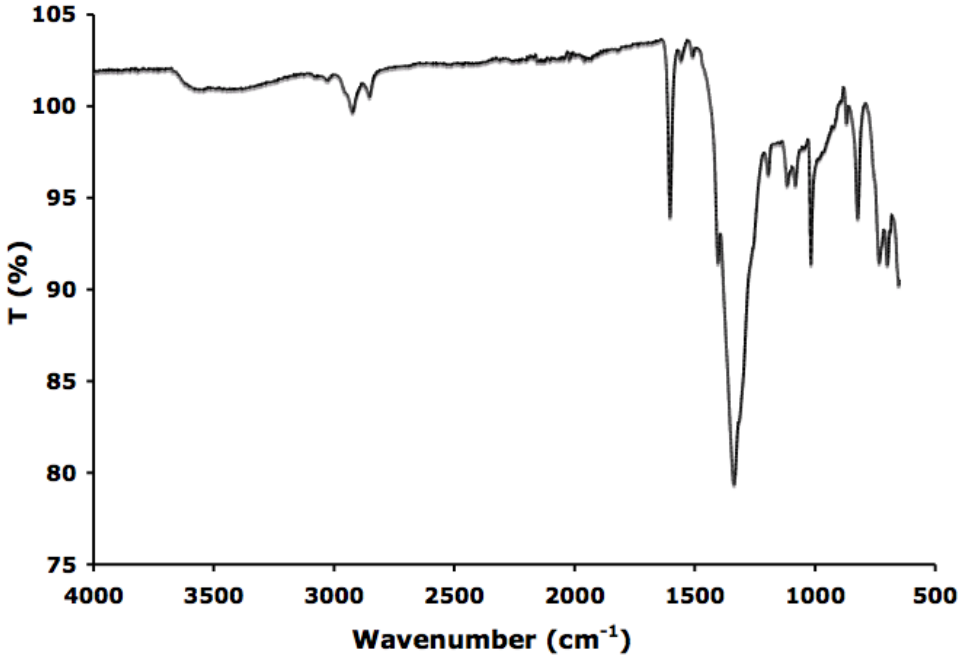

Figure A2.54 PXRD pattern of dodecyl functionalized (37%) COF-102, as synthesized.

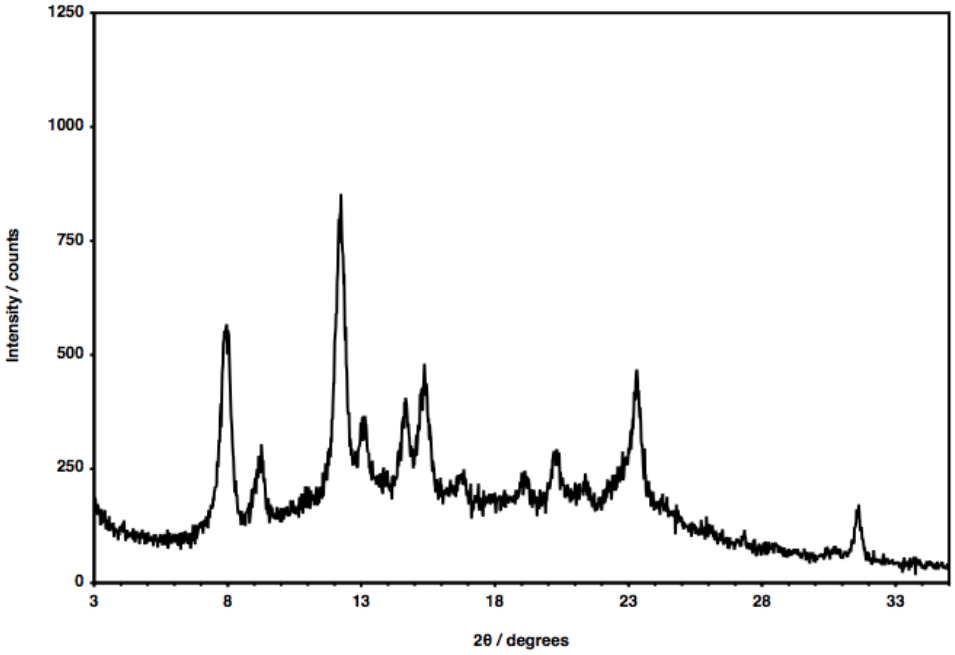

Figure A2.55 PXRD pattern of dodecyl functionalized (37%) COF-102, activated.

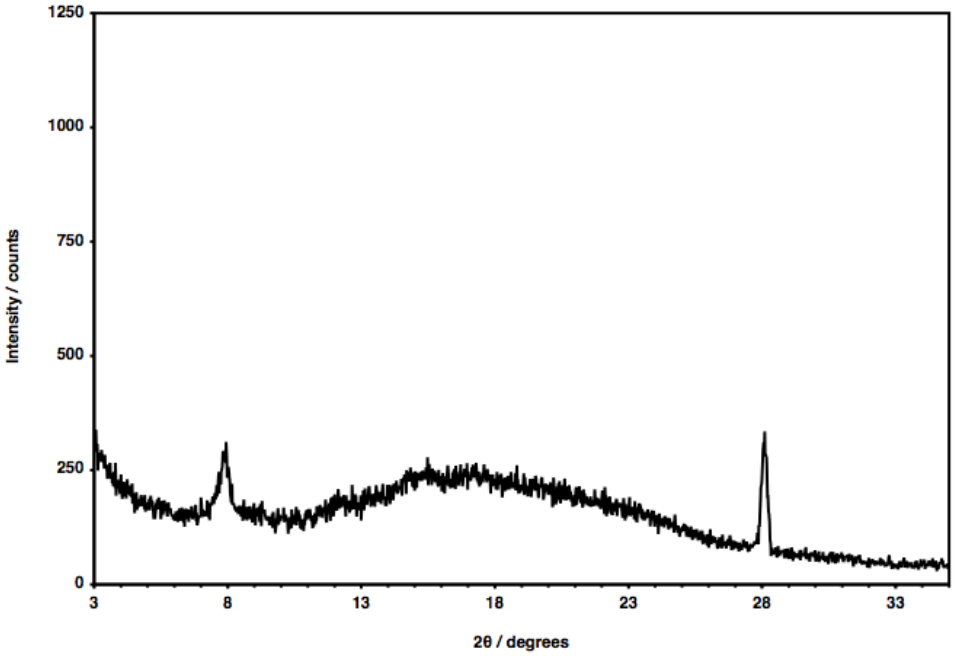

Figure A2.56 PXRD pattern of COF-102, as synthesized.

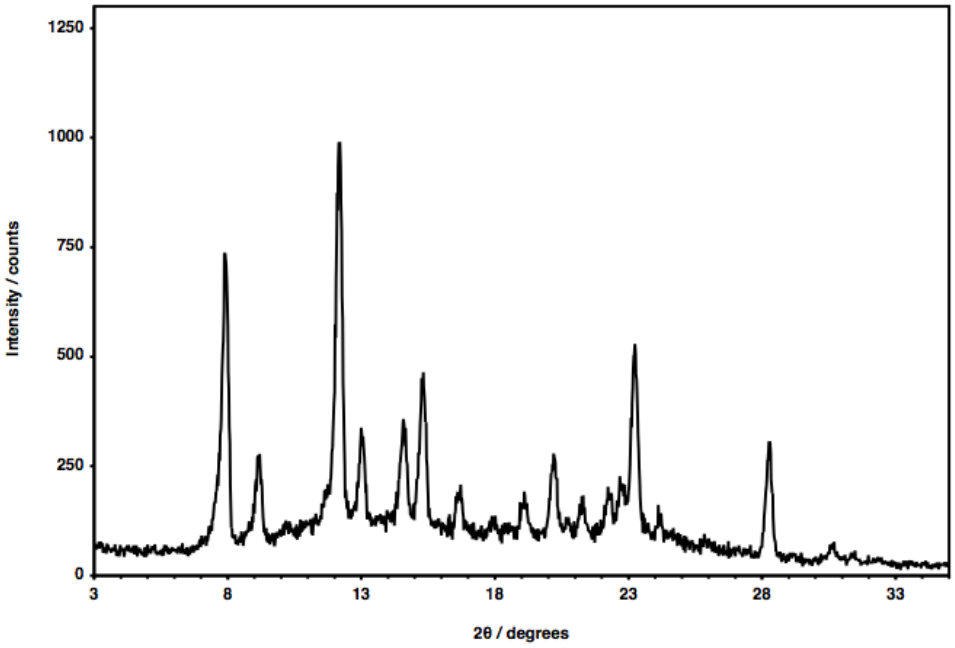

Figure A2.57 N_2 adsorption isotherm (blue: adsorption, red: desorption) of unfunctionalized COF-102.

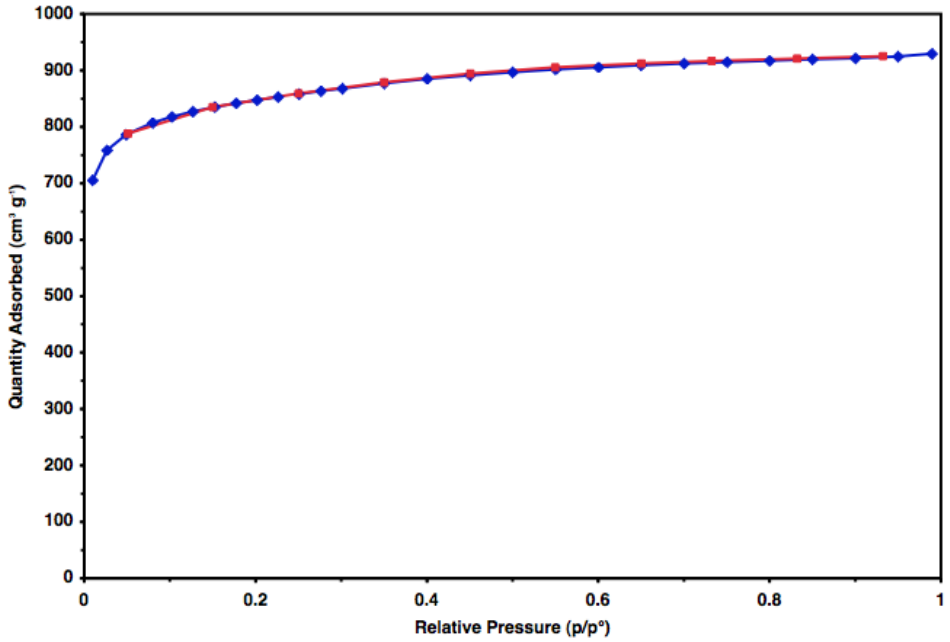

Figure A2.58 Ar adsorption isotherm (blue: adsorption, red: desorption) of pristine COF-102.

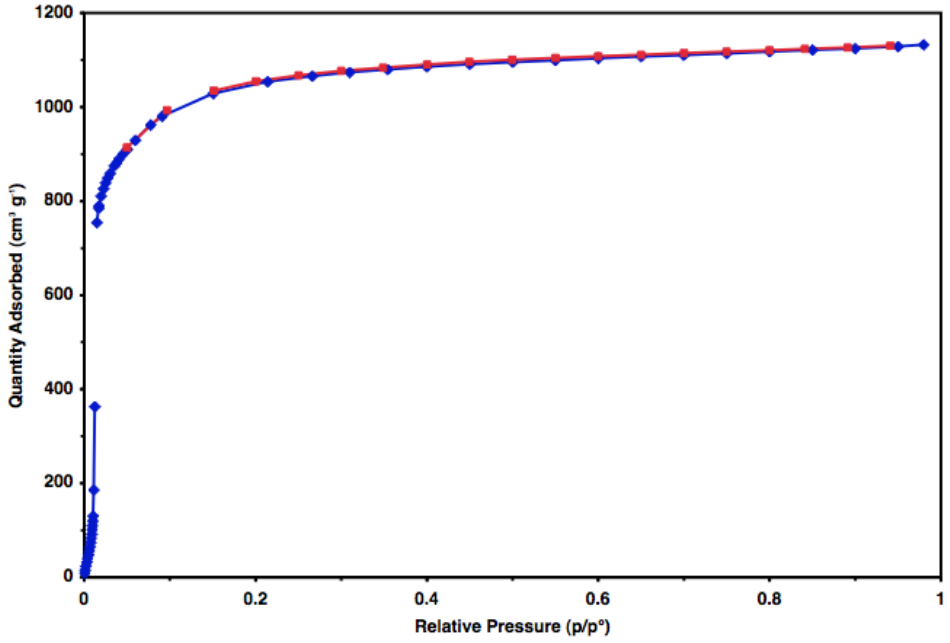

Figure A2.59 Cumulative pore volume versus pore width for pristine COF-102.

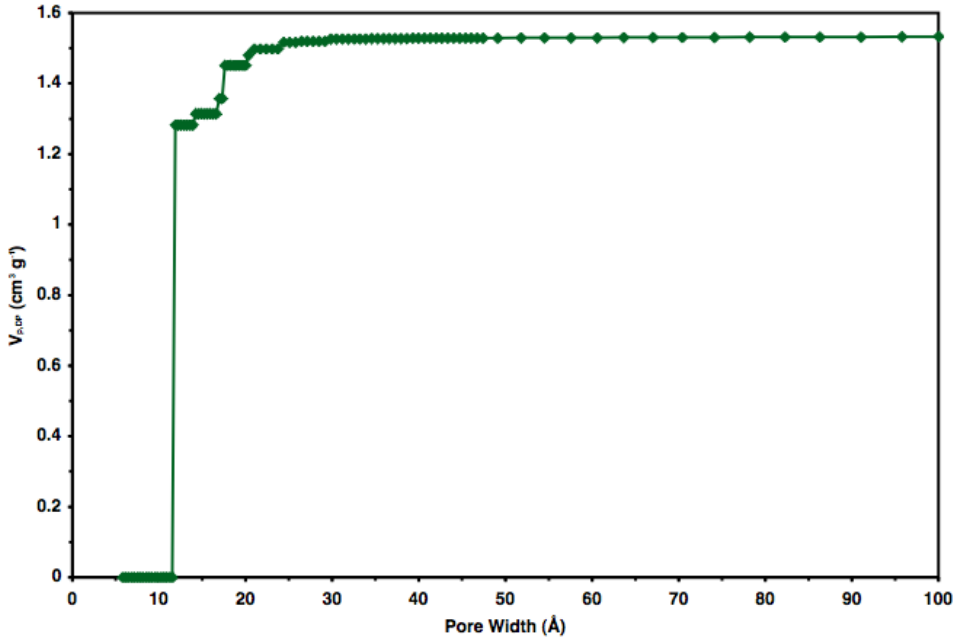

Figure A2.60 FTIR spectrum of allyl functionalized (23%) COF-102.

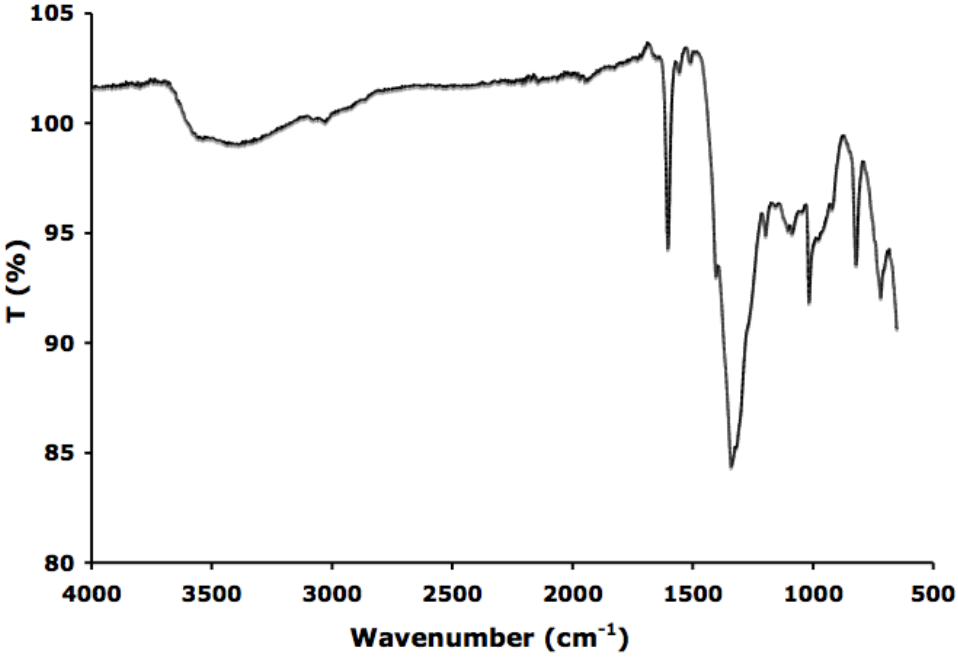

Figure A2.61 PXRD pattern of allyl functionalized (23%) COF-102, as synthesized.

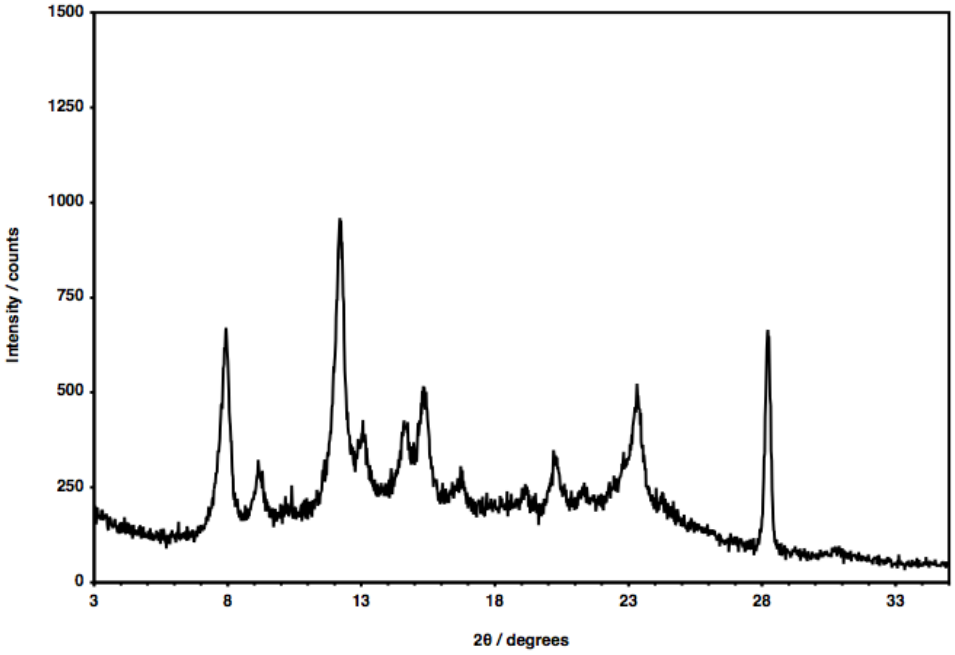

Figure A2.62 PXRD pattern of allyl functionalized (23%) COF-102, activated.

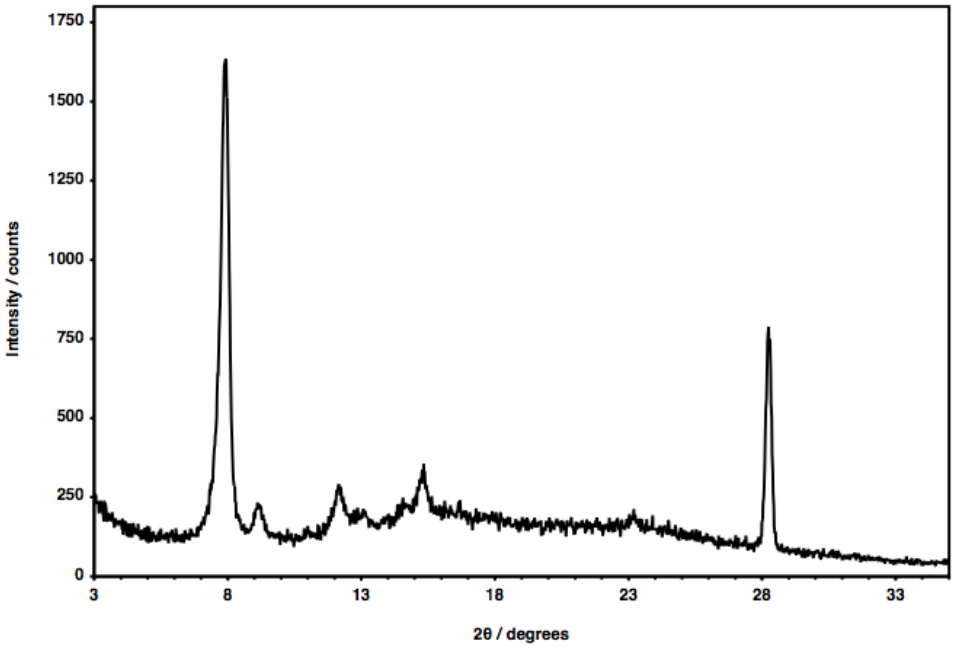

Figure A2.63 ^{1}H NMR spectrum (500 MHz) of allyl functionalized (23%) COF-102 digested in CD_3CN / D_2O (3:1 *v/v*).

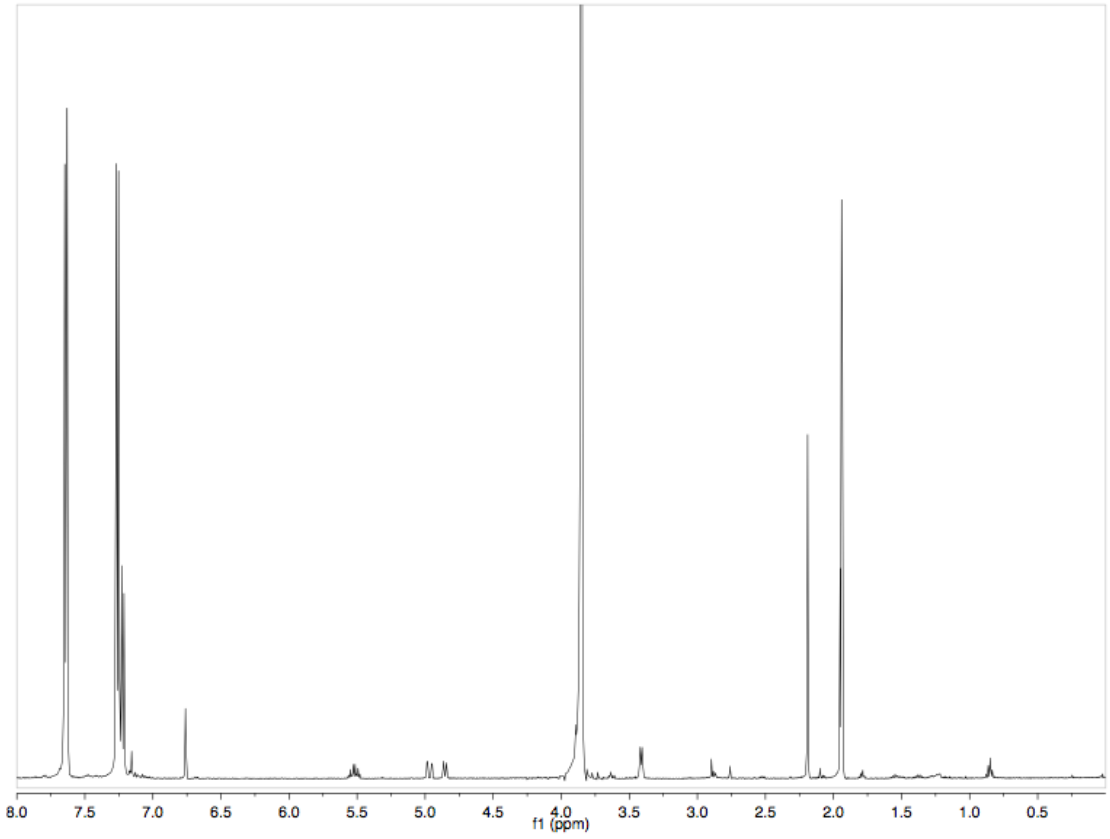

References

[1] J.-H. Fournier, T. Maris, J. D. Wuest, W. Guo, E. Galoppini, *J. Am. Chem. Soc.* **2002**, *125*, 1002.

[2] K. Schumacher, P. I. Ravikovitch, A. Du Chesne, A. V. Neimark, K. K. Unger, *Langmuir* **2000**, *16*, 4648.

Chapter Three: Postsynthetic Modification of 3D Covalent Organic Frameworks

Functionalizing the pores of framework materials, such as metal-organic frameworks (MOFs)[1] or covalent organic frameworks (COFs),[2, 3] offers a versatile method to tune their properties or incorporate catalysts,[4] molecular payloads, and other active groups. Versatile and efficient strategies to functionalize MOFs have been reported,[5, 6] including those capable of two orthogonal derivitzation steps.[7] Methods for functionalizing COFs, a class of crystalline two-dimensional (2D)[8-17] and three-dimensional (3D)[18-20] porous polymers linked by covalent bonds, are less well developed. Jiang and coworkers pioneered the functionalization of 2D COFs by incorporating azides onto their pore walls. The azides subsequently reacted with excess alkynes from solution under copper-catalyzed 1,3-dipolar cycloaddition conditions.[21] It remains valuable to identify efficient reactions that are sufficiently mild to preserve framework integrity and to develop novel approaches to incorporate reactive functionality within framework materials.

We recently introduced a truncated mixed linker (TML) approach to incorporate arbitrary functional groups within the interior of 3D COFs. The TML approach involves cocrystallizing a 3D COF monomer with a "truncated" monomer bearing a reduced number of structure-directing groups and identical relative geometry (Figure 3.1).[19, 22]

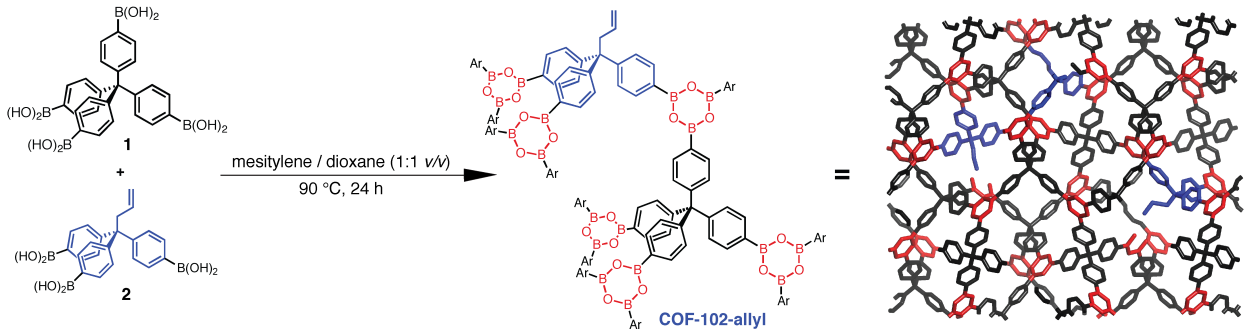

Figure 3.1 Cocrystallization of **1** with **2** yields COF-102 derivatized with allyl groups.

This strategy obviates the need to derivitize 3D COF monomers with additional reactive moieties, which is synthetically inconvenient due to their high symmetry and compact structure. We previously demonstrated the fidelity of the TML approach by incorporating *n*-dodecyl chains into the boroxine linked 3D COF-102. The functionalized COFs retained their crystallinity, high surface area, and particle morphology. Here we employ a modular truncation/functionalization strategy, based on the efficient thiol-ene reaction,[23] to derivitize allyl groups within COF-102 (Figure 3.2). This approach will be broadly applicable to arbitrarily modify both COF-102 and other truncated framework materials.

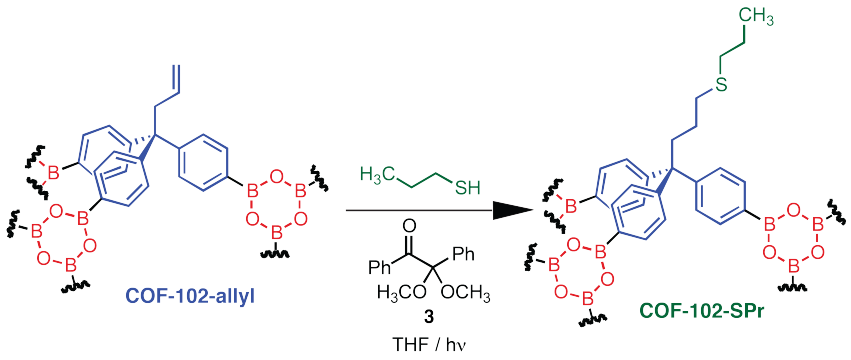

Figure 3.2 Subjecting COF-102-allyl to thiol-ene conditions yields COF-102-SPr.

We employed the TML approach to prepare an allyl-derivative of COF-102. This COF adopts a **ctn** net derived from the self-condensation of tetrahedral tetrakis(boronic acid) monomer **1** and was noted for its high Brunauer-Emmett-Teller (BET) surface area (3620 m^2 g^{-1}) and low density (0.43 g cm^{-1}).[20, 24] We prepared the allyl-functionalized derivative, COF-102-allyl, by co-condensing **1** with the allyl-functionalized tris(boronic acid) **2** under solvothermal conditions identical to those used to prepare the parent network. COF-102-allyl is a microcrystalline powder that retains the **ctn** topology and high surface area of pristine COF-102. Scanning electron micrographs of its crystallite morphology (Figure A3.3) are indicative of internal functionalization, which match the size and shape of the unfunctionalized framework

(Figure A3.2). Allyl group loadings within the COF reflect the feed ratio of monomers **1** and **2** up to at least 30% of the truncated monomer. This feature enables facile variation of the density of internal functionality within the network.

COF-102-allyl samples with 22% allyl loading were subjected to typical thiol-ene reaction conditions. Propanethiol was added to a THF solution containing dissolved photoinitiator **3** and the insoluble COF-102-allyl. The solution was irradiated for 18 h at room temperature using a long-wave UV lamp (maximum emission intensity at 385 nm). After irradiation, the THF solution was decanted and the COF was washed twice with fresh solvent to remove the soluble degradation products of **3** and unreacted propanethiol. The resulting thiol-modified material, COF-102-SPr, was subsequently dried under vacuum and isolated as a white, odorless powder.

The efficiency of the thiol-ene reaction within the COF pores was evaluated by hydrolyzing the isolated COF-102-SPr material to its soluble monomers and analyzing its composition by ^{1}H NMR spectroscopy. The ^{1}H NMR spectrum of hydrolyzed COF-102-allyl (Figure 3.3a) contains resonances at 4.91, 5.52, and 3.41 ppm that correspond to the vinylic protons, A and B, and allylic protons C, respectively. The integrations of these peaks relative to resonances in the aromatic region of the spectrum (not shown) are used to determine the allyl loading level. ^{1}H NMR analysis of hydrolyzed COF-102-SPr (Figure 3.3b) indicates complete disappearance of these three resonances associated with unmodified allyl groups. The signal corresponding to the A protons shifts upfield to 2.45 ppm and appears as a triplet, in contrast to the two doublets observed when these nuclei comprise the nonequivalent geminal position of the terminal alkene. Resonances B and C undergo similar upfield shifts also consistent with thioether formation. Finally, resonances corresponding to the newly installed thiopropyl chains are

observed at 2.38, 1.42, and 0.84 ppm (green highlight, Figure 3.3b), which do not correspond to those of free propanethiol. Overall, these observations confirm the high efficiency of the thiol-ene reaction within the pores of COF-102-allyl.

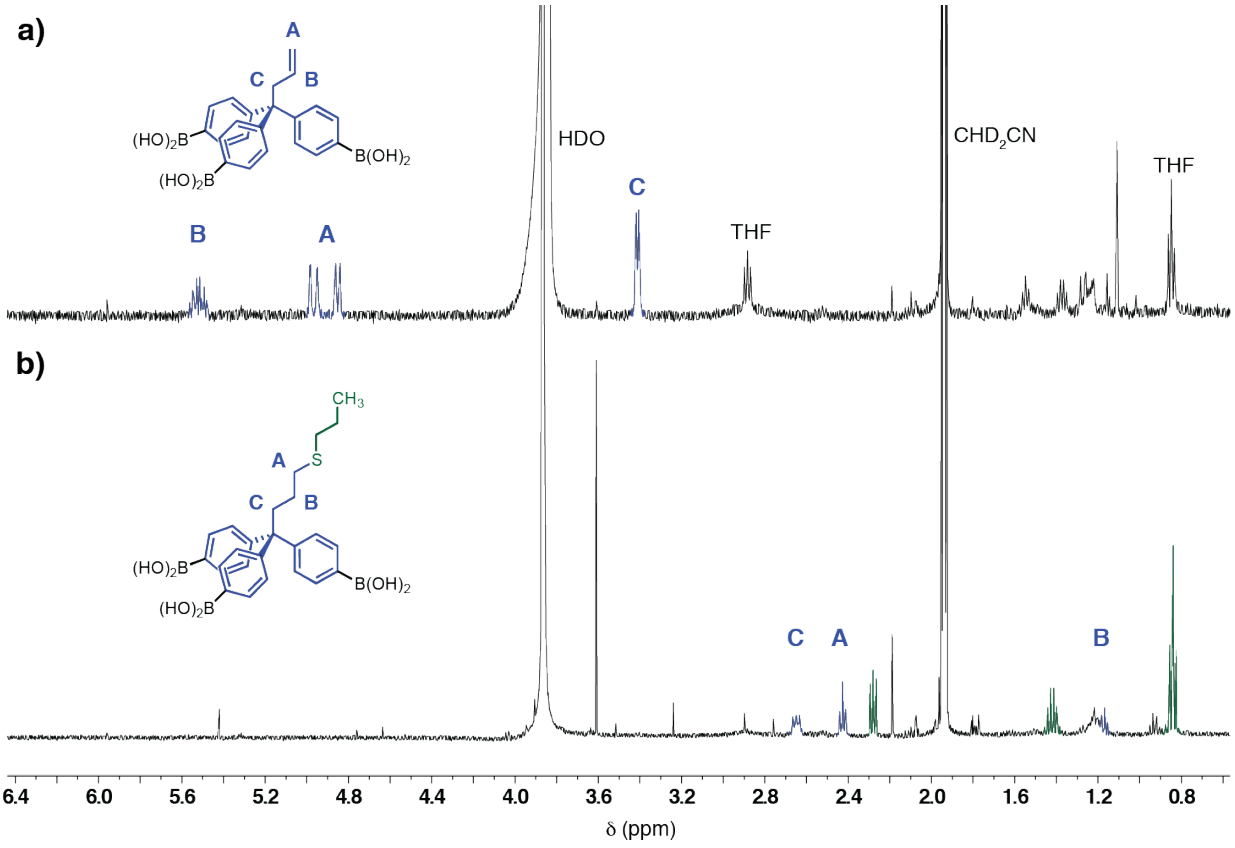

Figure 3.3 (a) COF-102-allyl and (b) COF-102-SPr hydrolyzed in CD_3CN/D_2O (3:1 *v/v*).

Powder X-ray diffraction (PXRD) confirmed the long-range order and identical network topologies of COF-102-allyl and COF-102-SPr. COF-102-allyl exhibits peaks (CuK_α) at 2θ = 7.9, 9.2, 12.1, 13.0, 14.5, 15.2, and 16.0° corresponding to the (211), (220), (321), (400), (420), (332), and (422) reflections, which are characteristic of the COF-102 **ctn** network structure (Figure 3.4, blue).[19, 20] Isolated COF-102-SPr shows reflections at identical angles, signifying the retention of framework topology (Figure 3.4, green). The slight peak broadening observed in the diffraction pattern of COF-102-SPr is indicative of a decrease in crystallite size. This decrease

might result either from the coupling reaction procedure itself or from slight background hydrolysis during workup. This hypothesis is also consistent with the slight increase in the O-H stretch seen by FT-IR spectroscopy after the thiol-ene reaction (Figure A3.1). These observations demonstrate the retention of the **ctn** topology in COF-102-SPr and further suggest that the thiol-ene reaction occurs within the framework interior.

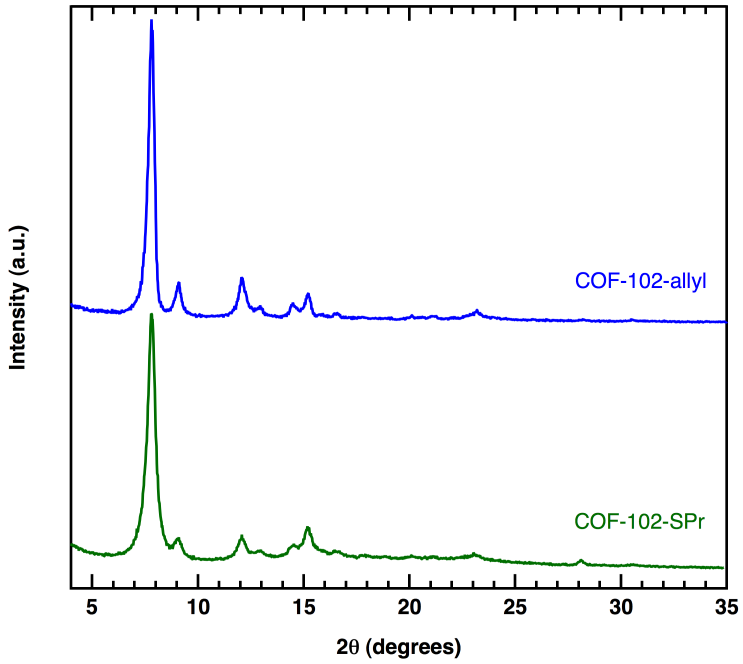

Figure 3.4 PXRD patterns of COF-102-allyl (blue) and COF-102-SPr (green) reveal retention of crystallinity after the thiol-ene reaction.

Nitrogen adsorption isotherms of COF-102-allyl and COF-102-SPr indicate that both the truncated and functionalized COFs are high surface area, microporous materials. The gas adsorption isotherm of COF-102-allyl shows Type I behavior, with some hysteresis at higher P/P_0, and a BET surface area of 1445 $m^2\ g^{-1}$ (Figure 3.5, blue) Microporosity is retained after the thiol-ene reaction, with a BET surface area of 1424 $m^2\ g^{-1}$ (Figure 3.5, green). Adding longer aliphatic chains is expected to decrease the surface area within the porous framework as a result of adding mass without a significant area to adsorb guests. The BET surface areas measured for

both COF-102-allyl and COF-102-SPr are lower than that reported for COF-102 and might be increased by optimizing their growth and activation procedures. For example, COF-102-allyl samples that we subjected to thiol-ene conditions after high vacuum activation within the surface area analyzer showed incomplete reaction of their allyl groups (80% as compared to nearly 100% prior to this procedure). This observation is also consistent with partial pore collapse. In spite of these observations, the nitrogen adsorption isotherm of COF-102-SPr indicates that its microporosity and high surface area are retained after the thiol-ene reaction.

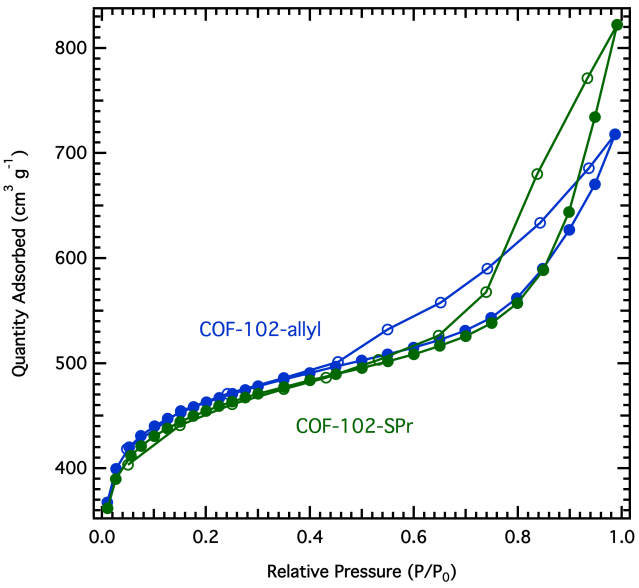

Figure 3.5 N_2 adsorption isotherms of COF-102-allyl (blue) and COF-102-SPr (green). Closed circles: adsorption, open circles: desorption.

The truncation/modification strategy is an efficient method to synthesize functionalized COF-102 derivatives. By subjecting COF-102-allyl to the thiol-ene reaction, we achieved full functionalization of the incorporated allyl groups. The crystallinity and microporosity of the resulting COF-102-SPr remained intact, highlighting the compatibility of the mild conditions with the boroxine-linked framework. Future work will involve generalizing this system to other 3D COFs as well as other MOFs, for which the first truncated example was recently reported.[25]

References

(1) J. R. Long, O. M. Yaghi, *Chem. Soc. Rev.*, **2009**, *38*, 1213.

(2) X. Feng, X. Ding, D. Jiang, *Chem. Soc. Rev.*, **2012**, *41*, 6010.

(3) A. P. Côté, A. I. Benin, N. W. Ockwig, M. O'Keeffe, A. J. Matzger, O. M. Yaghi, *Science*, **2005**, *310*, 1166.

(4) S.-Y. Ding, J. Gao, Q. Wang, Y. Zhang, W.-G. Song, C.-Y. Su, W. Wang, *J. Am. Chem. Soc.*, **2011**, *133*, 19816.

(5) S. M. Cohen, *Chem. Rev.*, **2011**, *112*, 970.

(6) K. K. Tanabe, S. M. Cohen, *Chem. Soc. Rev.*, **2011**, *40*, 498.

(7) C. Chen, C. A. Allen and S. M. Cohen, *Inorg. Chem.*, **2011**, *50*, 10534.

(8) E. L. Spitler, J. W. Colson, F. J. Uribe-Romo, A. R. Woll, M. R. Giovino, A. Saldivar, W. R. Dichtel, *Angew. Chem. Int. Ed.*, **2012**, *51*, 2623.

(9) S. Wan, J. Guo, J. Kim, H. Ihee, D. Jiang, *Angew. Chem. Int. Ed.*, **2008**, *47*, 8826.

(10) S. Wan, J. Guo, J. Kim, H. Ihee, D. Jiang, *Angew. Chem. Int. Ed.*, **2009**, *48*, 5439.

(11) R. W. Tilford, W. R. Gemmill, H.-C. zur Loye, J. J. Lavigne, *Chem. Mater.*, **2006**, *18*, 5296.

(12) E. L. Spitler, B. T. Koo, J. L. Novotney, J. W. Colson, F. J. Uribe-Romo, G. D. Gutierrez, P. Clancy, W. R. Dichtel, *J. Am. Chem. Soc.*, **2011**, *133*, 19416.

(13) J. W. Colson, A. R. Woll, A. Mukherjee, M. P. Levendorf, E. L. Spitler, V. B. Shields, M. G. Spencer, J. Park, W. R. Dichtel, *Science*, **2011**, *332*, 228.

(14) R. W. Tilford, S. J. Mugavero, P. J. Pellechia, J. J. Lavigne, *Adv. Mater.*, **2008**, *20*, 2741.

(15) K. T. Jackson, T. E. Reich, H. M. El-Kaderi, *Chem. Commun.*, **2012**, *48*, 8823.

(16) Z. Kahveci, T. Islamoglu, G. A. Shar, R. Ding, H. M. El-Kaderi, *CrystEngComm*, **2013**, *15*, 1524.

(17) S. Kandambeth, A. Mallick, B. Lukose, M. V. Mane, T. Heine, R. Banerjee, *J. Am. Chem. Soc.*, **2012**, *134*, 19524.

(18) F. J. Uribe-Romo, J. R. Hunt, H. Furukawa, C. Klöck, M. O'Keeffe, O. M. Yaghi, *J. Am. Chem. Soc.*, **2009**, *131*, 4570.

(19) D. N. Bunck, W. R. Dichtel, *Angew. Chem. Int. Ed.*, **2012**, *51*, 1885.

(20) H. M. El-Kaderi, J. R. Hunt, J. L. Mendoza-Cortés, A. P. Côté, R. E. Taylor, M. O'Keeffe, O. M. Yaghi, *Science*, **2007**, *316*, 268.

(21) A. Nagai, Z. Guo, X. Feng, S. Jin, X. Chen, X. Ding, D. Jiang, *Nat. Commun.*, **2011**, *2*, 536.

(22) D. N. Bunck, W. R. Dichtel, *Chem. Eur. J.*, **2013**, *19*, 818.

(23) C. E. Hoyle, C. N. Bowman, *Angew. Chem. Int. Ed.*, **2010**, *49*, 1540.

(24) H. Furukawa, O. M. Yaghi, *J. Am. Chem. Soc.*, **2009**, *131*, 8875.

(25) J. Park, Z. U. Wang, L.-B. Sun, Y.-P. Chen, H.-C. Zhou, *J. Am. Chem. Soc.*, **2012**, *134*, 20110.

Appendix 3-1: Supplementary Information

I. Materials and Instrumentation

Materials. All reagents were obtained from Sigma-Aldrich (Milwaukee, WI). Toluene, tetrahydrofuran, was obtained from a custom designed solvent purification system employing activated alumina under argon. Air and water sensitive reactions were performed on a Schlenk line under a N_2 atmosphere. (Methanetetrayltetra-4,1-phenylene)tetrakisboronic acid (**1**) was made according to a previously reported procedure.[1] Allyl functionalized tris(boronic acid) (**2**) was synthesized as previously reported.[2]

Instrumentation. Infrared spectra of solid samples were recorded using a Thermo Nicolet iS10 FTIR spectrometer with a diamond ATR attachment and are uncorrected.

NMR spectra were recorded on a Varian INOVA 500 MHz spectrometer using a standard $^{1}H\{^{13}C, ^{15}N\}$ Z-PFG probe with a 20 Hz sample spin rate. ^{1}H NMR spectra for quantitative determination of capping agent were acquired at 500 MHz with a 4 s acquisition time and a 20 s relaxation delay. The integral accuracy was confirmed on a pure sample of compound **2**.

Scanning electron microscopy was done on a LEO 1550 FESEM (Keck SEM) operating at 1.00 kV and a working distance of 3 mm. Samples were prepared by adsorption onto a silicon wafer, which was then attached to a flat aluminum platform sample holder. The sample was then placed directly into the instrument. No metal coating was applied.

Surface area measurements were conducted on a Micromeritics ASAP 2020 Accelerated Surface Area and Porosimetry Analyzer using *ca.* 35 mg samples degassed at 23 °C for 6 h and then 90 °C for 6 h and backfilled with N_2. Nitrogen isotherms were generated by incremental exposure to ultra high purity nitrogen up to *ca.* 1 atm in a liquid nitrogen (77 K) bath and surface

parameters were determined using BET adsorption models included in the instrument software (Micromeritics ASAP 2020 V4.00). BET surface area was determined though models included in the instrument software.

Powder X-ray diffraction (PXRD) patterns were obtained on a Rigaku Smartlab X-Ray diffractometer in reflectance parallel beam/parallel slit alignment geometry. The measurement employed Cu Kα line focused radiation at 1760 W (40 kV, 44 mA) power and a Ge crystal detector fitted with a 1.0 mm incident slit. Samples were mounted on zero-background quartz sample holders and flattened with a glass microscope slide. No sample grinding or sieving was done prior to analysis. Samples were observed using a 0.0200° 2θ step scan from 2.0 – 34.0° with a scan speed of 5° min^{-1}. No peaks could be resolved from the baseline for $2\theta > 35°$ and this region was not considered for further analysis. Crystallite size was determined by applying the Scherrer equation to the powder patterns based on an alumina standard.

A Spectroline ENF-260C hand-held UV lamp from Spectronics Corporation (Westbury, New York) was used to generate light at 365 nm.

II. Experimental Protocols

Synthesis of COF-102-allyl. Tetrakis(boronic acid) **1** (50.0 mg, 0.101 mmol) and allyl-functionalized truncating agent **2** (0.1 eq – 0.5 eq) were sonicated in 1 mL mesitylene / dioxane (1:1 *v/v*) in a 20 mL vial until a fine suspension was obtained. The suspension was then transferred by pipet to a pre-scored 5 mL ampoule, flash frozen in $N_{2\,(l)}$, and flame sealed. The ampoule was put in an oven at 90 °C for 27.5 h, after which the ampoule was cooled to rt, opened, and the solid was isolated by filtration. The solid was washed with 5 mL dry THF was

added and after 30 min, the solvent was then removed by syringe. This process was repeated three times and the COF was subsequently dried under vacuum.

Synthesis of COF-102-SPr. COF-102-allyl (30 mg, 22 mol% allyl) and 2,2-dimethoxy-2-phenyl acetophenone (1 mg, 0.1 eq/allyl group) were added to a dry Schlenk tube under N_2 atmosphere. Dry, degassed THF (0.372 mL) followed by propane thiol (6 mg, 1.1 eq) were subsequently added. The reaction was allowed to stir at 23 °C for 18 h under irradiation at 385 nm (Figure 2), at which point the resulting suspension was allowed to settle and the THF was removed. Washing twice with THF yielded COF free of the remaining photodegradation products. COF-102-SPr was subsequently dried under vacuum and isolated as a white, odorless powder.

III. Additional Characterization

Figure A3.1 FTIR spectrum of COF-102-allyl (blue) and COF-102-SPr (green).

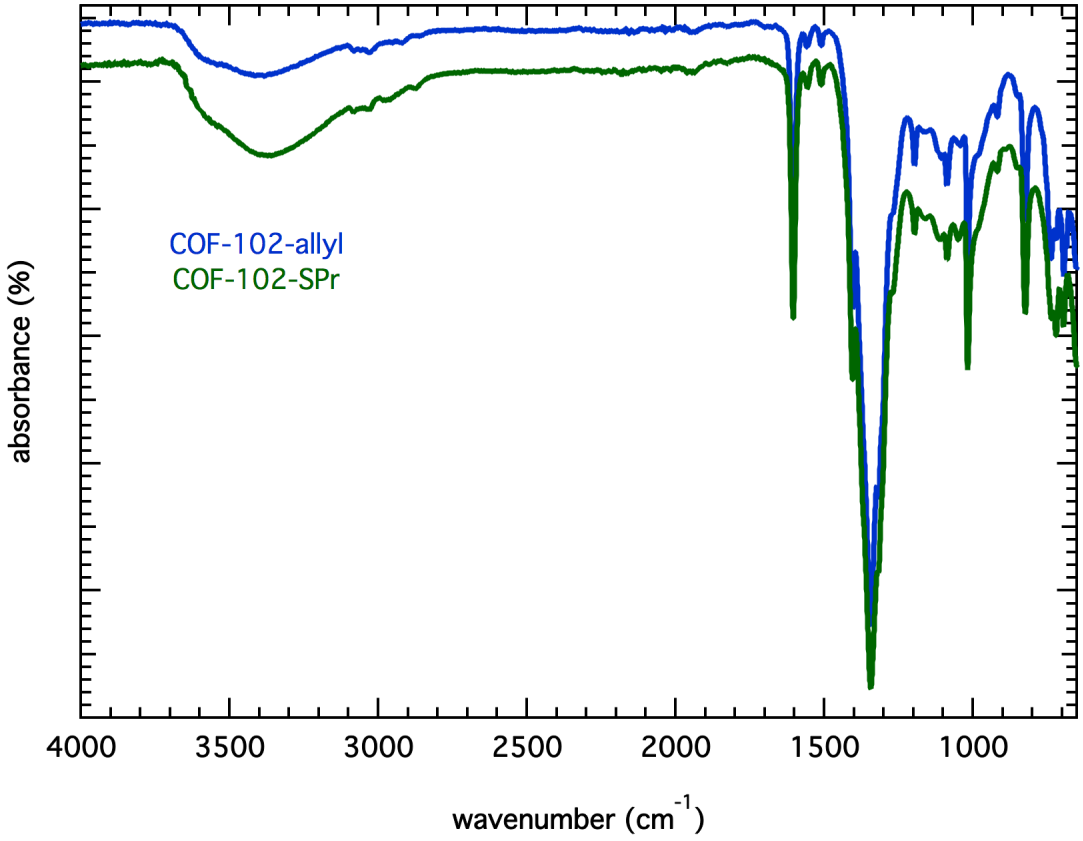

Figure A3.2 Scanning electron micrographs of COF-102-allyl.

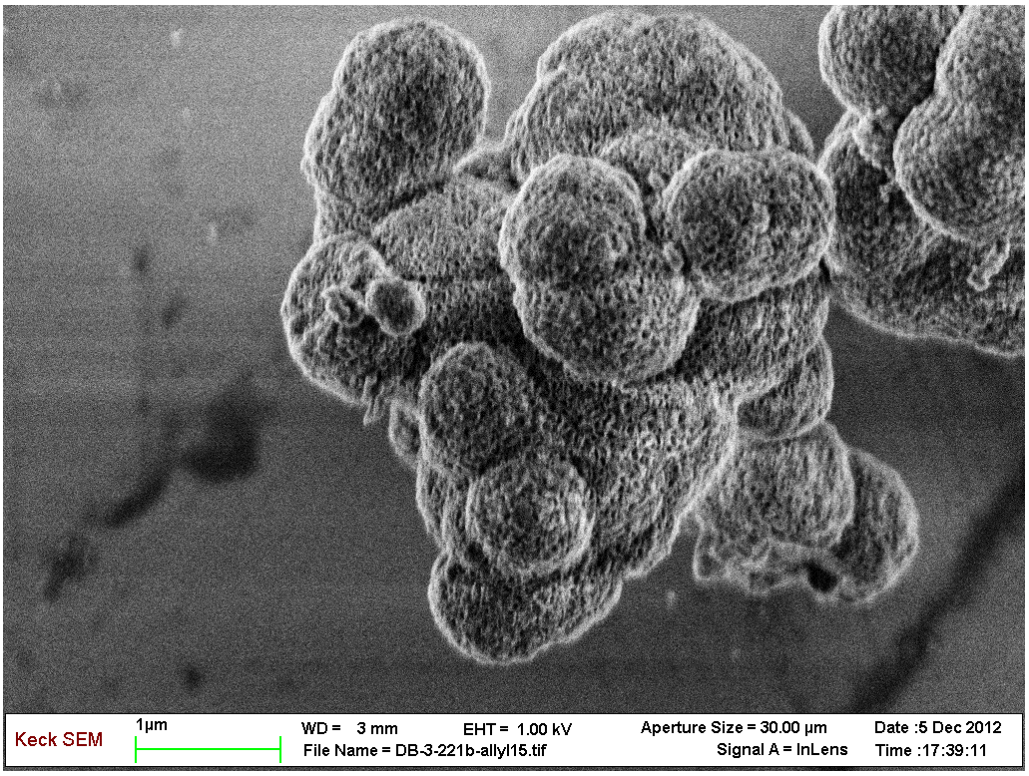

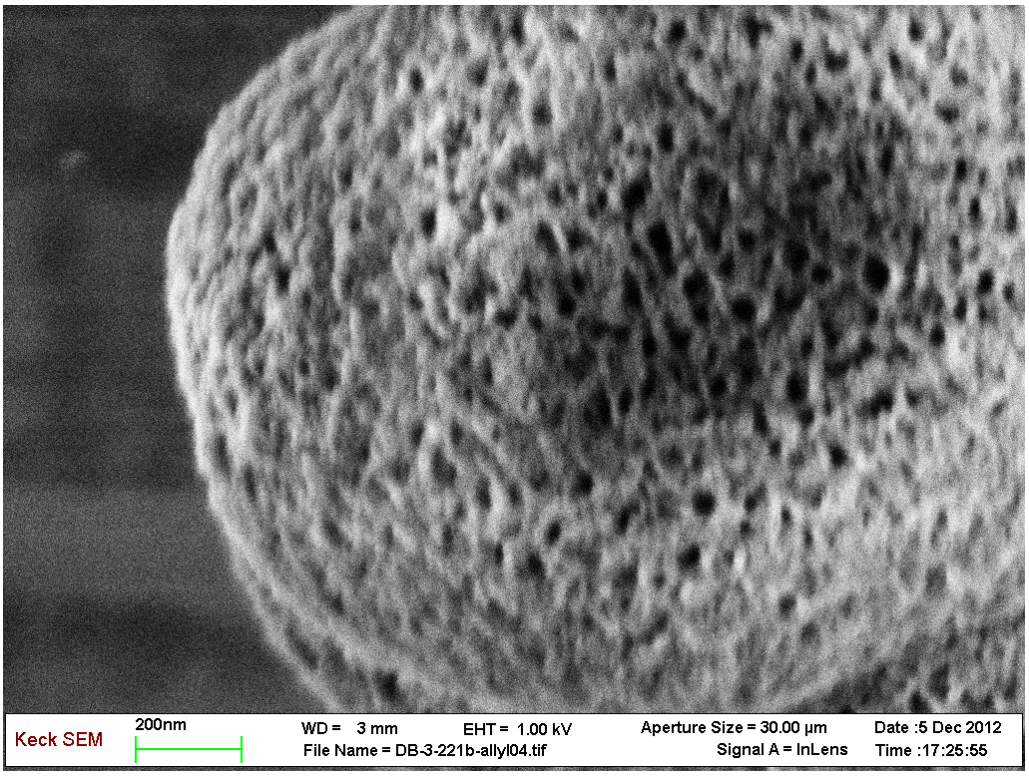

Figure A3.3 Scanning electron micrographs of COF-102-SPr.

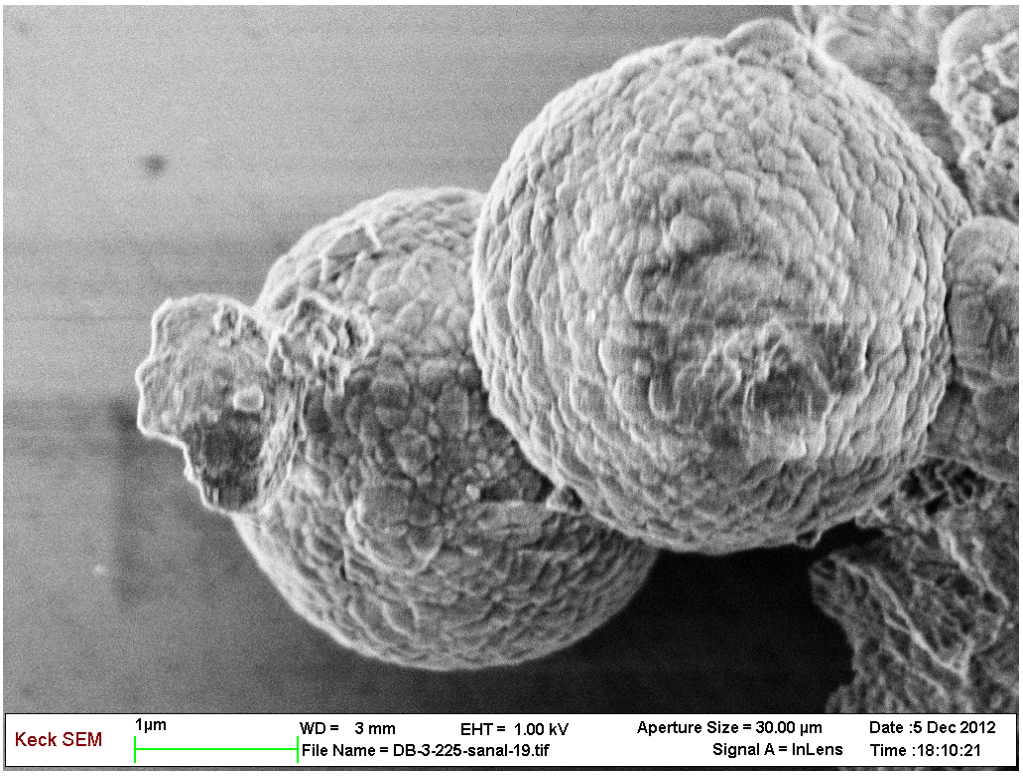

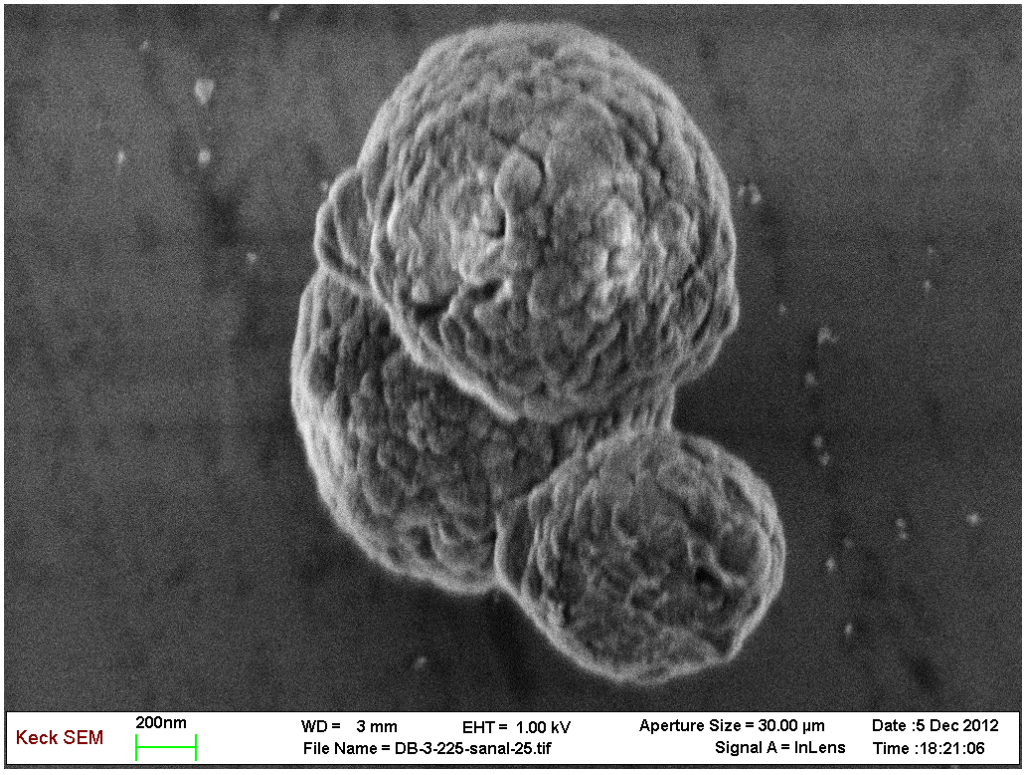

References

(1) Fournier, J.-H.; Maris, T.; Wuest, J. D.; Guo, W.; Galoppini, E. *J. Am. Chem. Soc.* **2003**, *125*, 1002–1006.

(2) Bunck, D. N.; Dichtel, W. R. *Angew. Chem. Int. Ed.* **2012**, *51*, 1885–1889.

Chapter Four: Functionalization of 3D Covalent Organic Frameworks using Monofunctional Boronic Acids

Covalent organic frameworks (COFs) are an emerging class of crystalline, high surface-area polymers with layered two-dimensional (2D)[1,2] or three-dimensional (3D)[3-5] periodic bonding. COFs incorporate covalent linkages that may be formed reversibly, such as boroxines,[1, 3, 6, 7] boronate esters,[8-13] imines,[14-16] hydrazones,[17] and others,[18-20] thus providing a means to correct miss-formed bonds in the networks[7] during their simultaneous polymerization and crystallization. A diverse range of 2D COFs have been described, and their stacked π-electron systems and vertically aligned pores show promise for applications in photovoltaic devices,[21-27] catalysis,[28] and gas storage.[29] Furthermore, the pores of 2D COFs have been modified using an Isostructural Mixed Linker (IML) approach,[30, 31] in which multiple monomers with identical linking geometries are incorporated into a single framework.[32, 33] In contrast, 3D COFs are comparatively rare, and reports of crystalline 3D networks, even using existing linkage chemistries, have lagged behind their 2D counterparts.[34] This difficulty underscores the need to develop efficient methods to functionalize 3D COFs, so as to maximize the utility of the existing networks.

We recently reported the functionalization[35] and subsequent postsynthetic modification[36] of a boroxine-linked 3D COF, known as COF-102, using a truncated mixed-linker (TML) approach. Tetrahedral tetrakis(boronic acid) **1** was co-crystallized with similar truncated monomers, in which an arbitrary functional group replaces one of the aryl boronic acids. Under typical solvothermal growth conditions, the reversibility of boroxine formation might give rise to externally functionalized networks,[37,38] but we instead found that network growth was faster than boroxine hydrolysis such that the truncated monomer was incorporated throughout the network interior. Truncated monomers have since also proven effective for functionalizing the pores of

metal-organic frameworks.[35] Given this broadening scope, the internal functionalization of COFs with truncated monomers raises both fundamental and practical questions about monomer design, the inherent upper limits of truncated monomer incorporation within a crystalline polymer network, and the interplay between the rates of framework growth and error correction that yield crystalline products.

Here we address these questions by employing monofunctional, rather than trifunctional, comonomers to truncate COF-102. Because phenylboronic acid derivatives are incorporated into the network through only a single boroxine linkage, we hypothesized that they might instead be excluded to the face of the growing framework, providing a means to control crystallite morphology or enable external functionalization. However, we found that these monomers are also incorporated throughout the COF-102 network, even in the presence of large excesses of the

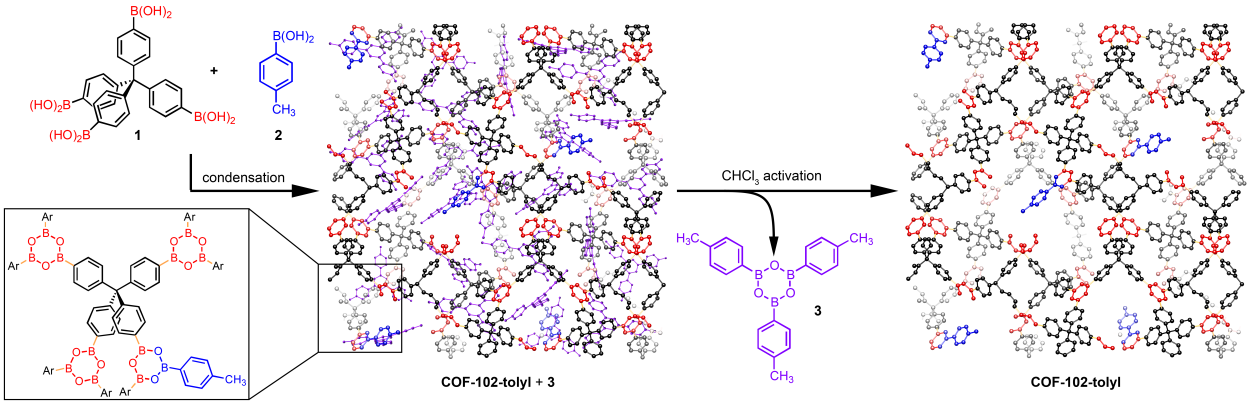

Figure 4.1 Co-crystallization of **1** and **2** yields the COF-102 network truncated with tolyl groups. When excess **2** is employed, the initially isolated COF-102-tolyl is intercalated with tritolylboroxine **3**, which is removed upon activation with $CHCl_3$.

monofunctional monomer. The resulting functionalized COFs retain their crystallinity and high surface area with an incorporation limit of *ca.* 36 mol% of the truncated monomer, which is identical to that observed with the trifunctional monomers used previously.[35] We postulate that this level of truncation represents a fundamental limit for the **ctn** COF-102 net, in which one

third of the aryl boronate functions do not contribute to the network structure. We also demonstrate that truncation occurs for several aryl boronic acids, such that it represents a simple and readily available 3D COF functionalization strategy.

We initially truncated COF-102 using monofunctional capping agents by co-crystallizing **1** with *p*-tolylboronic acid **2** under the same solvothermal conditions used to prepare the parent framework (Figure 4.1). FTIR spectroscopy of the resulting microcrystalline powders are consistent with boroxine-linked materials (Figure A4.1), and their network topology matches that of unfunctionalized COF-102 (Figure 4.2, a-b). Powder X-ray diffraction (PXRD) patterns of these samples with varying loadings of **2** exhibit peaks (CuK_α) at 2θ = 7.9, 9.2, 12.1, 13.0, 14.5, 15.2, and 16.0° corresponding to the (211), (220), (321), (400), (420), (332), and (422) reflections, respectively. This pattern is indicative of the **ctn** topology that is characteristic of COF-102. Feed ratios between 0–36 equiv of **2** were employed, which provided crystalline COF-102-tolyl samples in all cases. We found this result surprising given that the majority of available aryl boronic acid moieties in the reaction mixture are monofunctional at feed ratios of **2** > 4 equiv. At ≥ 7 equiv of **2**, additional peaks appear in the PXRD patterns that correspond to tritolyl boroxine **3** co-crystalized with the COF-102 network (Figure 4.2c), as assigned by comparison to the PXRD pattern of a pure sample of **3** (Figure A4.3). These peaks disappear from the PXRD patterns upon activation of the COF-102 sample by soaking or sonicating the isolated powder in anhydrous $CHCl_3$, after which the characteristic COF-102 PXRD pattern is observed (Figures 4.2d and A4.2). This activation procedure does not induce changes to the particle morphology, as characterized by scanning electron microscopy (SEM), which indicated spherulites similar to the parent

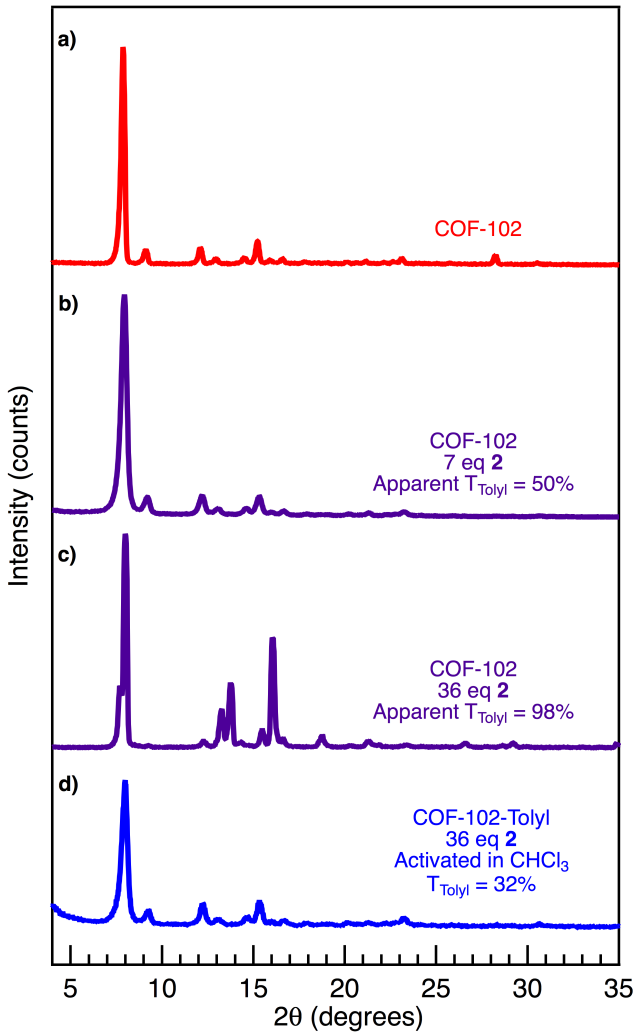

Figure 4.2 PXRD patterns show the crystalline COF-102 network (a) is conserved with incorporation of **2** (b). Frameworks with excess **3** (c) were activated with $CHCl_3$ to yield the parent framework with covalently bound **2** incorporated (d).

COF-102 framework (Figures A4.20-24). We also identified the soluble products removed upon activation of COF-102-tolyl using ^{1}H NMR spectroscopy by performing the activation with $CDCl_3$ containing methyl *tert*-butyl ether (MTBE) as an internal standard. Activation of COF-102-tolyl samples prepared from < 6 equiv of **2** liberated no molecular components from the framework other than the mesitylene growth solvent (Figure A4.10). At higher feed ratios of **2**, ^{1}H NMR spectra of the activation solvent indicated increasing amounts of **3** as the only soluble

species. These combined observations indicate that COF-102-tolyl crystallizes even in the presence of large excesses of **2**. Boroxine **3** co-crystallizes with the framework when large excesses of **2** are employed and is removed by activating the functionalized COF-102-tolyl samples with $CHCl_3$.

The incorporation of **2** into COF-102-tolyl was quantified using ^{1}H NMR spectroscopy after hydrolyzing the activated boroxine-linked powders in CD_3CN / D_2O (3:1 *v/v*). The molar ratio of **1** to **2** was calculated by comparing the integration of the resonance at 2.30 ppm (Figure 4.3b, H_C), corresponding to the methyl protons of the tolyl functionality, with that at 7.65 ppm, corresponding to aromatic protons found in both monomers (Figure 4.3b, $H_{A,A'}$). Incorporation

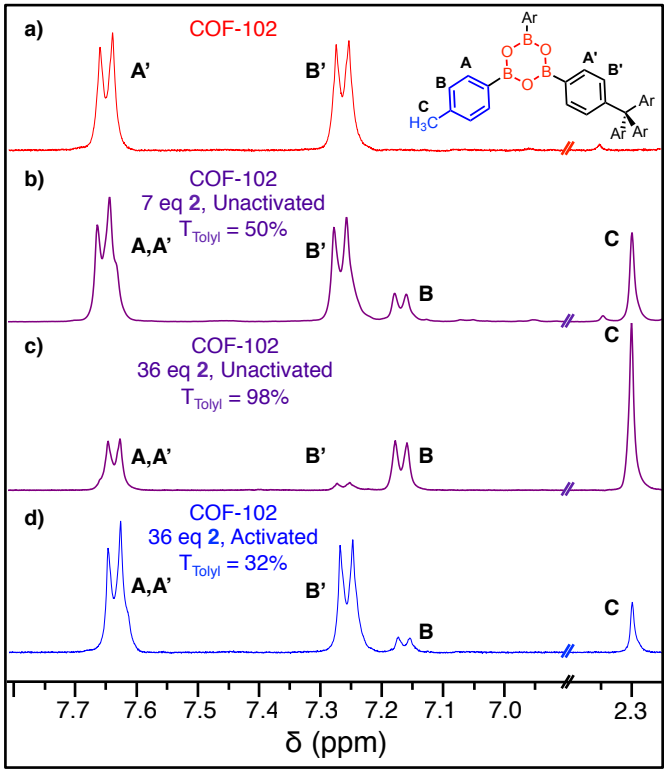

Figure 4.3 Quantitative ^{1}H NMR spectra of COF-102 (a) and COF-102-tolyl (b-d) digested in CD_3CN / D_2O (3:1 *v/v*) gives percent loading of tolylboronic acid (T_{Tolyl}).

values (T_{Tolyl}) are expressed as the mol percentage of **2** found in the framework after hydrolysis. When this analysis was applied to unactivated COF-102-tolyl samples derived from high feed

ratios of **2**, unreasonably high apparent T_{Tolyl} values were determined, consistent with contamination of the COF with excess boroxine **3**. For example, hydrolysis of the unactivated COF-102-tolyl derived from 36 equiv of **2** showed an apparent T_{Tolyl} of 98% (Figure 3c). After

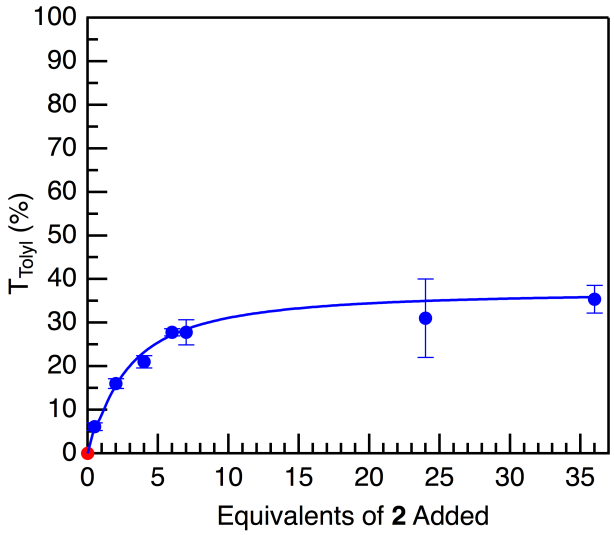

Figure 4.4 Loading of tolylboronic acid (T_{Tolyl}) after $CHCl_3$ activation as a function of tolylboronic acid added to framework growth. Each point represent an average of 3 experiments, with error bars showing one standard deviation. The line is added to guide the eye.

removing the excess **3** using the $CHCl_3$ activation procedure, the spectrum of the hydrolyzed COF shows a T_{Tolyl} of 32% (Figure 4.3d), which is similar to the maximum T_{Tolyl} values obtained when excess **2** was employed. We also noted a decreased yield of the activated COF-102-tolyl from *ca*. 60% at low feed ratios of **2** to *ca.* 33% when higher feed ratios were employed, which we attribute to larger amounts of **1** being sequestered as soluble species at high loadings of **2**. SEM analysis of the filtrate of COF reaction mixtures also indicated significant differences based on the feed ratio of **2**. Filtrate derived from the preparation of COF-102 without added **2** contained monodisperse, sphere-shaped particles about 1 μm in diameter (Figure A4.25), whereas the COF-102-tolyl filtrate prepared from 36 equiv of **2** reveals two distinct phases

dominated by extended ribbon-like morphologies that presumably correspond to **3** (Figure A4.26).

The T_{Tolyl} for activated COF-102-tolyl approaches its maximum value as the feed ratio of monomer **2** is increased beyond 6 equiv (Figure 4.4). **2** is increasingly incorporated into the framework at feed ratios below 6 equiv, which provide T_{Tolyl} values ranging from 6 ± 1% when 0.5 equiv of **2** were used, to 28 ± 1% at a feed ratio of 6 equiv. Over this range, only trace amounts of **3** are isolated alongside the COF-102-tolyl powder, as indicated by the nearly identical T_{Tolyl} observed before and after $CHCl_3$ activation (Table 4.1; Figures A4.11-16). Between 7 and 36 equiv of **2**, the T_{Tolyl} of activated COF-102-tolyl samples saturates around 36%. The excess **2** also forms increasing amounts of **3**, as indicated by the large differences

Feed Ratio of **2** (equiv)	Apparent T_{Tolyl} unactivated (%)	T_{Tolyl} activated (%)	S_{BET} Unactivated (m^2g^{-1})	S_{BET} Activated (m^2g^{-1})
0.5	6 ± 1	6 ± 1	--	--
2	16 ± 2	16 ± 1	--	--
4	22 ± 5	21 ± 2	--	--
6	30 ± 2	28 ± 1	2000	2400
7	52 ± 3	28 ± 3	2350	2600
24	91 ± 6	31 ± 9	60	750
36	99 ± 0.2	35 ± 3	17	1500

Table 4.1 Loading and BET surface areas obtained for COF-102-tolyl samples before after activation. Loadings are reported as averages of triplicate experiments ± one standard deviation.

between the T_{Tolyl} measured for unactivated and activated COFs. These observations are also consistent with the peaks corresponding to **3** in the PXRD patterns of unactivated COF-102-tolyl samples derived from feed ratios of **2** in excess of 6 equiv (see above). The formation of significant amounts of COF-102-tolyl in the presence of a large excess of monofunctional reactive groups provides insight into the maximum allowable defects within the COF-102 lattice

as well as the framework crystallization process. The T_{Tolyl} saturation value around 36% is virtually identical to the maximum loading of trifunctional boronic acids observed previously,[35] and most likely represents an upper limit for incorporating truncated monomers into the COF-102 network. We postulate that framework formation involves an irreversible process, such as crystallite aggregation, after which boroxine exchange does not occur. In the absence of this kinetic sink, little or no COF-102-tolyl should form under conditions that statistically favor boroxine formation with the monofunctional monomer when it is present in such large excess.

The COF-102-tolyl framework exhibits permanent porosity and high surface area that is characteristic of both unfunctionalized and functionalized COF-102, as evidenced by N_2 adsorption isotherms. At lower feed ratios, activated COF-102-tolyl samples showed Type I isotherms with a single adsorption process and Brunauer-Emmett-Teller (BET) surface areas ranging from 2400-2600 m^2g^{-1} (Table 4.1). These values are comparable to our measurements of the parent COF-102 framework synthesized under similar conditions. Relatively small differences in surface area between unactivated and activated samples were observed, consistent with our observations that minimal amounts of **3** co-crystallize with the COF at these feed ratios. In contrast, unactivated COF-102-tolyl samples prepared from higher feed ratios of **2** show dramatically reduced BET surface areas (as low as 17 m^2 g^{-1} for 36 equiv of **2**) prior to activation. High surface-area materials are obtained upon activation, consistent with the removal of **3** from the pores (Figure 4.5). These findings indicate that the COF-102-tolyl samples are porous, high surface area materials over the entire attainable range of tolyl group loadings. Interestingly, we previously observed pore collapse of COF-102 samples functionalized with trifunctional truncated monomers at incorporation values above 30%, which may indicate

improved mechanical stability of COF-102 samples truncated with monofunctional arylboronic acids.

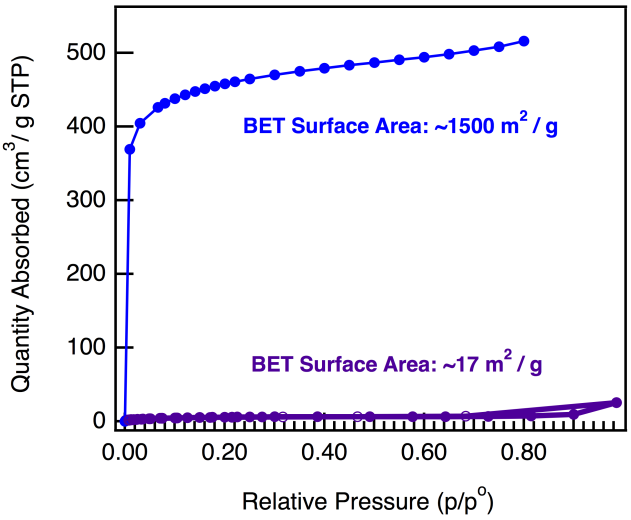

Figure 4.5 $N_{2\,(g)}$ adsorption isotherms at 77 K of COF-102-tolyl before (purple, T_{Tolyl} = 98%) and after (blue, T_{Tolyl} = 36%) $CHCl_3$ activation (closed circles = adsorption; open circles = desorption).

We also investigated the generality of this approach using other boronic acids, including 4-nonylphenylboronic acid (**4**), 4-vinylphenylboronic acid (**5**), and 4-formylphenylboronic acid (**6**). Each of these monomers were incorporated into COF-102 by including them in the framework crystallization to provide COF-102-nonyl, COF-102-vinyl, and COF-102-formyl, respectively. PXRD patterns of powders obtained from each of these experiments show the expected COF-102 topology (Figure 4.6). FTIR and ^{1}H NMR analysis of the frameworks confirmed that these monomers are covalently bound within the network with intact *n*-nonyl, vinyl, or formyl substituents. Monomer **4** is incorporated into COF-102-nonyl as a function of its feed ratio, as was observed for COF-102-tolyl. T_{nonyl} also saturates at *ca.* 36% at feed ratios of **4** >6 equiv (Table A4.1; Figures A4.17-19), which further suggests that this level of truncation is the maximum allowed within the COF-102 network. In contrast to COF-102-tolyl, which

tolerated the $CHCl_3$ activation procedure across the full range of feed ratios of **2**, we observed a loss of crystallinity in COF-102-nonyl samples upon activation (Figure A4.4). We attribute this to the sonication used during the activation procedure, although it is unclear why COF-102-nonyl is less mechanically stable than COF-102-tolyl. Computational studies have suggested that the parent COF-102 framework suffers from poor mechanical stability,[39-41] such that minor perturbations in network structure cause it to be more prone to pore collapse upon activation.

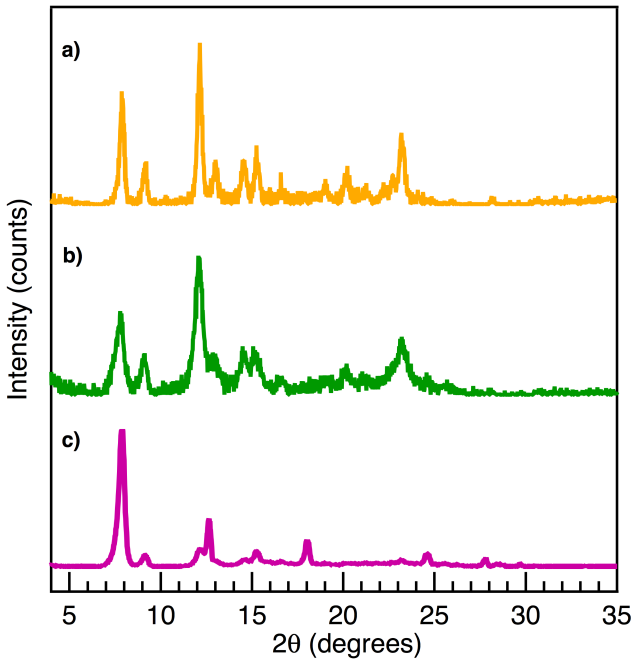

Figure 4.6 PXRD indicates that the crystalline COF-102 net is conserved after incorporation of other monofunctional boronic acids (6 equiv).

Activated samples of COF-102-vinyl and COF-102-formyl retained their crystallinity, but provided apparent incorporation values greater than 36%, suggesting that the activation procedure was not fully effective in removing excess soluble boroxines. Despite the difficulties in activating these highly functionalized COF-102 samples, which are of interest for studying the fundamental limits of COF-102 truncation, these monomers may be incorporated into COF-102

at lower feed ratios, offering a facile route to incorporate diverse functionality into the COF-102 net using readily accessible monomers.

This study of COF-102 crystallization in the presence of large amounts of monofunctional boronic acid explores the limits of truncation and functionalization of 3D COFs. It is remarkable that COF-102 crystallizes in the presence of excess tolyl boronic acid (up to 36 equiv relative to the tetrafunctional COF-102 monomer). Under these conditions, the resulting COF-102-tolyl contains *ca.* 36 mol% *p*-tolylboronic acid while maintaining its long-range order, permanent porosity, and high surface area. This tolyl group loading is observed across a wide range of feed ratios and represents an upper limit of truncated defects tolerated by the COF-102 network. The observation of COF-102 formation in the presence of excess boronic acid indicates that framework crystallization is irreversible under these conditions. This conclusion is an essential early step towards understanding the mechanism of COF growth, of which almost nothing is known, and has important implications for improving COF crystallinity. The truncation of COF-102 with readily available aryl boronic acid monomers also represents a facile and general functionalization strategy. Although improved activation procedures for COF-102 networks will be needed to take full advantage of the most highly functionalized materials described here, these design rules are likely to be applicable to both other COF networks and other classes of framework materials.

References

(1) A. P. Côté, A. I. Benin, N. W. Ockwig, M. O'Keeffe, A. J. Matzger, O. M. Yaghi, *Science* **2005**, *310*, 1166.

(2) J. W. Colson, W. R. Dichtel, *Nat. Chem.* **2013**, *5*, 453.

(3) H. M. El-Kaderi, J. R. Hunt, J. L. Mendoza-Cortés, A. P. Côté, R. E. Taylor, M. O'Keeffe, O. M. Yaghi, *Science* **2007**, *316*, 268.

(4) X. Feng, X. Ding, D. Jiang, *Chem. Soc. Rev.* **2012**, *41*, 6010.

(5) S. -Y. Ding, W. Wang, *Chem. Soc. Rev.* **2013**, *42*, 548.

(6) S. B. Kalidindi, C. Wiktor, A. Ramakrishnan, J. Weβing, A. Schneemann, G. Van Tendeloo, R. A. Fischer, *Chem. Commun.* **2013**, *49*, 463.

(7) C. -Z. Guan, D. Wang, L. -J. Wan, *Chem. Commun.* **2012**, *48*, 2943.

(8) E. L. Spitler, B. T. Koo, J. L. Novotney, J. W. Colson, F. J. Uribe-Romo, G. D. Gutierrez, P. Clancy, W. R. Dichtel, *J. Am. Chem. Soc.* **2011**, *133*, 19416.

(9) R. W. Tilford, W. R. Gemmill, H. -C. zur Loye, J. J. Lavigne, *Chem. Mater.* **2006**, *18*, 5296.

(10) E. L. Spitler, W. R. Dichtel, *Nature Chem.* **2010**, *2*, 672.

(11) Z. Kahveci, T. Islamoglu, G. A. Shar, R. Ding, H. M. El-Kaderi, *CrystEngComm* **2013**, *15*, 1524.

(12) R. W. Tilford, S. J. Mugavero, P. J. Pellechia, J. J. Lavigne, *Adv. Mater.* **2008**, *20*, 2741.

(13) E. L. Spitler, M. R. Giovino, S. L. White, W. R. Dichtel, *Chem. Sci.* **2011**, *2*, 1588.

(14) F. J. Uribe-Romo, J. R. Hunt, H. Furukawa, C. Klöck, M. O'Keeffe, O. M. Yaghi, *J. Am. Chem. Soc.* **2009**, *131*, 4570.

(15) M. G. Rabbani, A. K. Sekizkardes, Z. Kahveci, T. E. Reich, R. Ding, H. M. El-Kaderi, *Chem. Eur. J.* **2013**, *19*, 3324.

(16) X. Chen, M. Addicoat, S. Irle, A. Nagai, D. Jiang, *J. Am. Chem. Soc.* **2013**, *135*, 546.

(17) F. J. Uribe-Romo, C. J. Doonan, H. Furukawa, K.Oisaki, O. M. Yaghi, *J. Am. Chem. Soc.* **2011**, *133*, 11478.

(18) S. Kandambeth, A. Mallick, B. Lukose, M. V. Mane, T. Heine, R. Banerjee, *J. Am. Chem. Soc.* **2012**, *134*, 19524.

(19) P. Kuhn, M. Antonietti, A. Thomas, *Angew. Chem. Int. Ed.* **2008**, *47*, 3450.

(20) K. T. Jackson, T. E. Reich, H. M. El-Kaderi, *Chem. Commun.* **2012**, *48*, 8823.

(21) S. Wan, F. Gándara, A. Asano, H. Furukawa, A. Saeki, S. K. Dey, L. Liao, M. W. Ambrogio, Y. Y. Botros, X. Duan, S. Seki, J. F. Stoddart, O. M. Yaghi, *Chem. Mater.* **2011**, *23*, 4094.

(22) S. Wan, J. Guo, J. Kim, H. Ihee, D. Jiang, *Angew. Chem. Int. Ed.* **2008**, *47*, 8826.

(23) S. Wan, J. Guo, J. Kim, H. Ihee, D. Jiang, *Angew. Chem. Int. Ed.* **2009**, *48*, 5439.

(24) M. Dogru, M. Handloser, F. Auras, T. Kunz, D. Medina, A. Hartschuh, P. Knochel, T. Bein, *Angew. Chem. Int. Ed.* **2013**, *52*, 2920.

(25) S. Jin, X. Ding, X. Feng, M. Supur, K. Furukawa, S. Takahashi, M. Addicoat, M. E. El-Khouly, T. Nakamura, S. Irle, S. Fukuzumi, A. Nagai, D. Jiang, *Angew. Chem. Int. Ed.* **2013**, *52*, 2017.

(26) J. W. Colson, A. R. Woll, A. Mukherjee, M. P. Levendorf, E. L. Spitler, V. B. Shields, M. G. Spencer, J. Park, W. R. Dichtel, *Science* **2011**, *332*, 228.

(27) X. Ding, L. Chen, Y. Honsho, X. Feng, O. Saengsawang, J. Guo, A. Saeki, S. Seki, S. Irle, S. Nagase, V. Parasuk, D. Jiang, *J. Am. Chem. Soc.* **2011**, *133*, 14510.

(28) S.-Y. Ding, J. Gao, Q. Wang, Y. Zhang, W. -G. Song, C. -Y. Su, W. Wang, *J. Am. Chem. Soc.* **2011**, *133*, 19816.

(29) H. Furukawa, O. M. Yaghi, *J. Am. Chem. Soc.* **2009**, *131*, 8875.

(30) A. Nagai, Z. Guo, X. Feng, S. Jin, X. Chen, X. Ding, D. Jiang, *Nat. Commun.* **2011**, *2*, 536.

(31) D. N. Bunck, W. R. Dichtel, *Chem. Eur. J.* **2013**, *19*, 818.

(32) K. K. Tanabe, S. M. Cohen, *Chem. Soc. Rev.* **2011**, *40*, 498.

(33) E. L. Spitler, J. W. Colson, F. J. Uribe-Romo, A. R.Woll, M. R. Giovino, A. Saldivar, W. R. Dichtel, *Angew. Chem. Int. Ed.* **2012**, *51*, 2623.

(34) Y. Zhu, H. Long, W. Zhang, *Chem. Mater.* **2013**, *25*, 1630.

(35) D. N. Bunck, W. R. Dichtel, *Angew. Chem. Int. Ed.* **2012**, *51*, 1885.

(36) D. N. Bunck, W. R. Dichtel, W. R. *Chem. Commun.* **2013**, *49*, 2457.

(37) T. Tsuruoka, S. Furukawa, Y. Takashima, K. Yoshida, S. Isoda, S. Kitagawa, *Angew. Chem. Int. Ed.* **2009**, *48*, 4739.

(38) A. Umemura, S. Diring, S. Furukawa, H. Uehara, T. Tsuruoka, S. Kitagawa, *J. Am. Chem. Soc.* **2011**, *133*, 15506.

(39) B. Lukose, A. Kuc, T. Heine, *J. Mol. Model.* **2013**, *19*, 2143.

(40) R. Schmid, M. Tafipolsky, *J. Am. Chem. Soc.* **2008**, *130*, 12600.

(41) W. Zhou, H. Wu, T. Yildirim, *Chem. Phys. Lett.* **2010**, *499*, 103.

Appendix 4-1: Supplementary Information

I. Materials and Instrumentation

Materials. All reagents were obtained from Sigma-Aldrich (Milwaukee, WI). $CDCl_3$ was dried over activated 3 Å molecular sieves and stored under N_2 atmosphere. (Methanetetrayltetra-4,1-phenylene)tetrakisboronic acid (**1**) was prepared according to a previously reported procedure[1].

Instrumentation. Infrared spectra of solid samples were recorded using a Thermo Nicolet iS10 FTIR spectrometer with a diamond ATR attachment and are uncorrected.

NMR spectra were recorded on a Varian INOVA 400 MHz spectrometer using a standard $^{1}H\{^{13}C, ^{15}N\}$ Z-PFG probe with a 20 Hz sample spin rate. ^{1}H NMR spectra for quantitative determination of capping agent were acquired at 400 MHz with a 3 s acquisition time and a 10 s relaxation delay.

Scanning electron microscopy was done on a LEO 1550 FESEM (Keck SEM) operating at 2.00 kV and a working distance of 3-4 mm with an aperture size of 30 μm. Samples were prepared by adsorption onto a silicon wafer, which was then attached to a flat aluminum platform sample holder. The sample was then placed directly into the instrument. No metal coating was applied.

Surface area measurements were conducted on a Micromeritics ASAP 2020 Accelerated Surface Area and Porosimetry Analyzer using *ca.* 25 mg samples degassed at 90 °C for 24 h and backfilled with N_2. N_2 isotherms were generated by incremental exposure to ultra high purity nitrogen up to *ca.* 1 atm in a liquid nitrogen (77 K) bath and surface parameters were determined using BET adsorption models included in the instrument software (Micromeritics ASAP 2020 V4.00).

Powder X-ray diffraction (PXRD) patterns were obtained on a Rigaku SmartLab X-Ray diffractometer in reflectance parallel beam/parallel slit alignment geometry. The measurement employed Cu K_α line focused radiation at 1760 W (40 kV, 44 mA) power and a Ge crystal detector fitted with a 1.0 mm incident slit. Samples were mounted on zero-background quartz sample holders and flattened with a glass microscope slide. No sample grinding or sieving was done prior to analysis. Samples were observed using a 0.0200° $\theta/2\theta$ step scan from 1.0 – 35.0° with a scan speed of 5° min^{-1}. No peaks could be resolved from the baseline for $2\theta > 35°$ and this region was not considered for further analysis. Crystallite size was determined by applying the Scherrer equation to the powder patterns based on an alumina standard using MDI JADE.

Sonication was performed on a Branson 3510 ultrasonic cleaner with a power output of 100W and a frequency of 42 kHz.

II. Experimental Protocols

Synthesis of COF-102-Tolyl. Tetrakis(boronic acid) **1** (50.0 mg, 0.101 mmol) and *p*-tolylboronic acid **2** (0.5 equiv – 36 equiv) were sonicated in mesitylene / dioxane (1:1 *v/v*, 1 mL) in a 1-dram vial until a fine suspension was obtained. The suspension was then transferred by pipet to a pre-scored 5 mL ampoule, flash frozen in liquid nitrogen, and flame sealed under vacuum. The ampoule was put in an oven at 90 °C for 48 h, after which the ampoule was cooled to 23 °C, opened, and the solid was isolated by filtration. The COF was subsequently dried under vacuum, and isolated as an off-white powder.

Activation of COF-102-Tolyl. Approximately 75 mg of the COF powder was sonicated in 2 mL chloroform in a 1-dram vial until a fine suspension was obtained. The suspension was then filtered and the isolated powder was subsequently dried under vacuum, yielding activated COF.

III. Additional Characterization

Figure A4.1 Stacked FTIR spectra of COF-102 (red) and COF-102-tolyl with indicated loadings of tolylboronic acid before (purple) and after (blue) $CHCl_3$ activation.

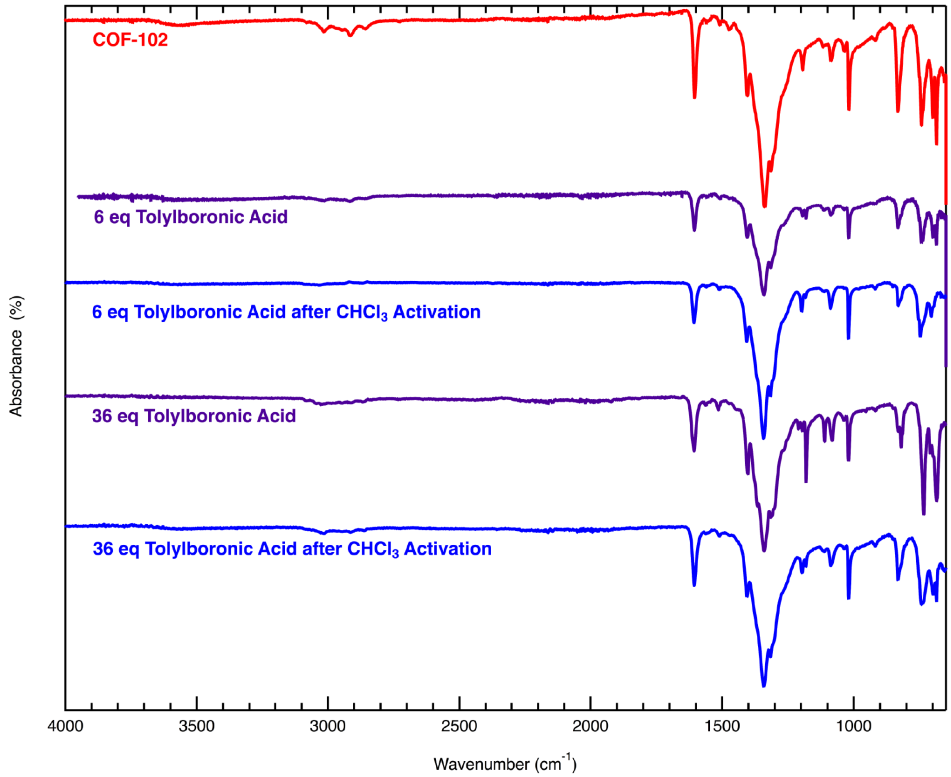

Figure A4.2 PXRD patterns of COF-102-tolyl with varying feed ratios of tolylboronic acid.

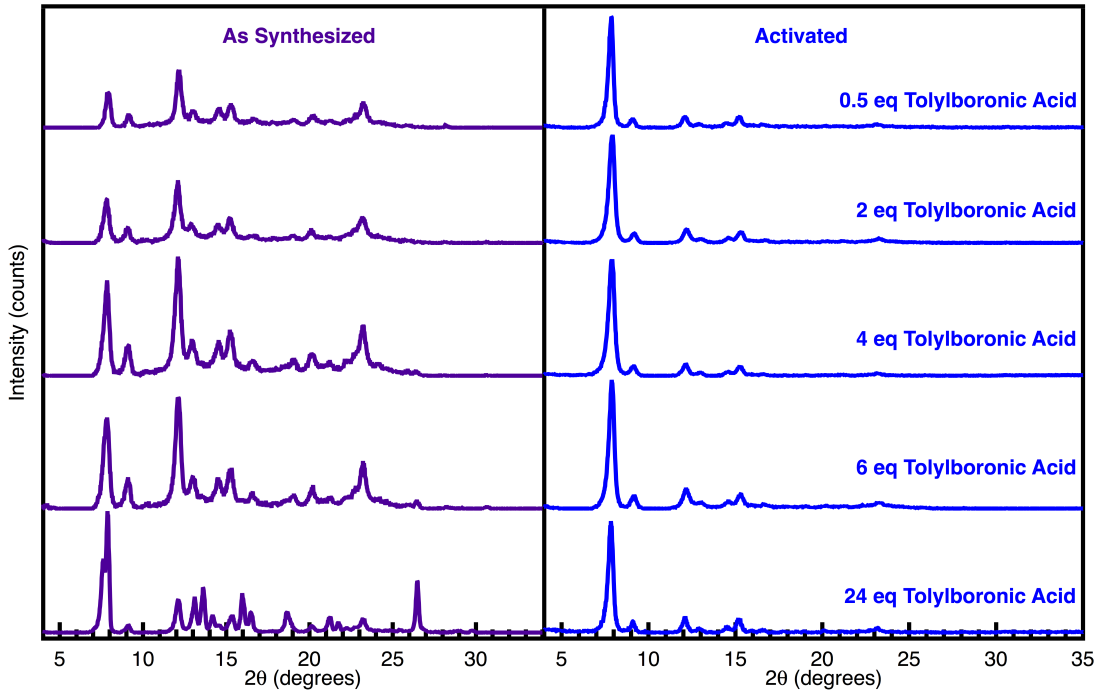

Figure A4.3 PXRD pattern of tritolyl boroxine **3**.

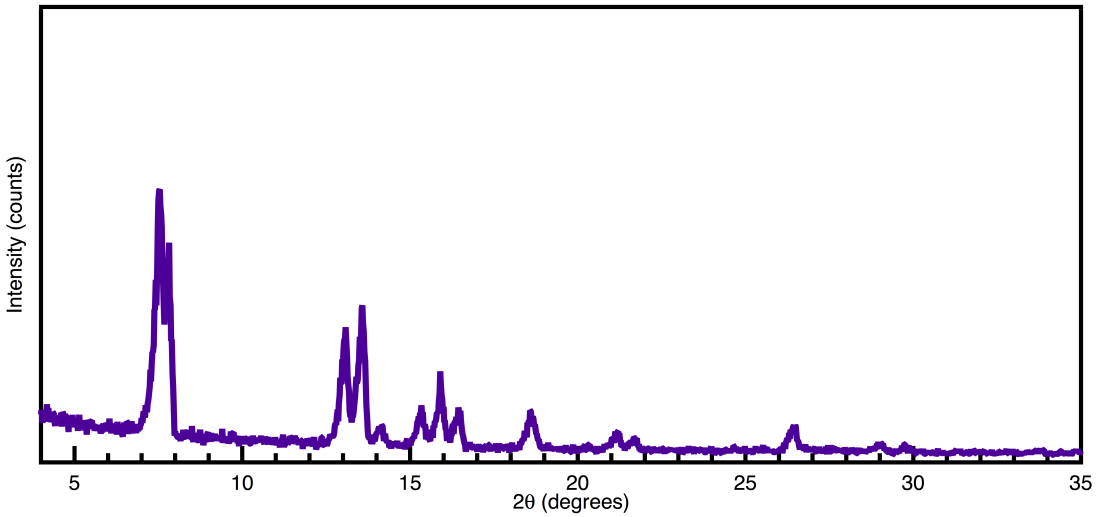

Figure A4.4 PXRD patterns of COF-102-nonyl before (gold) and after (blue) $CHCl_3$ activation.

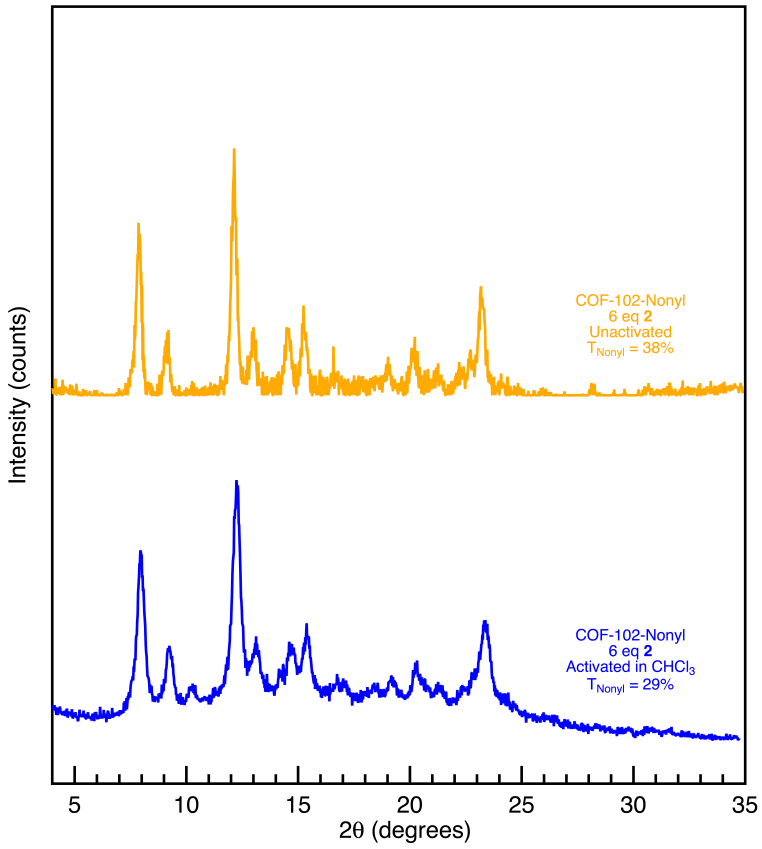

Figure A4.5 N_2 adsorption isotherm (77 K) of COF-102-tolyl (6 eq **2**, activated).

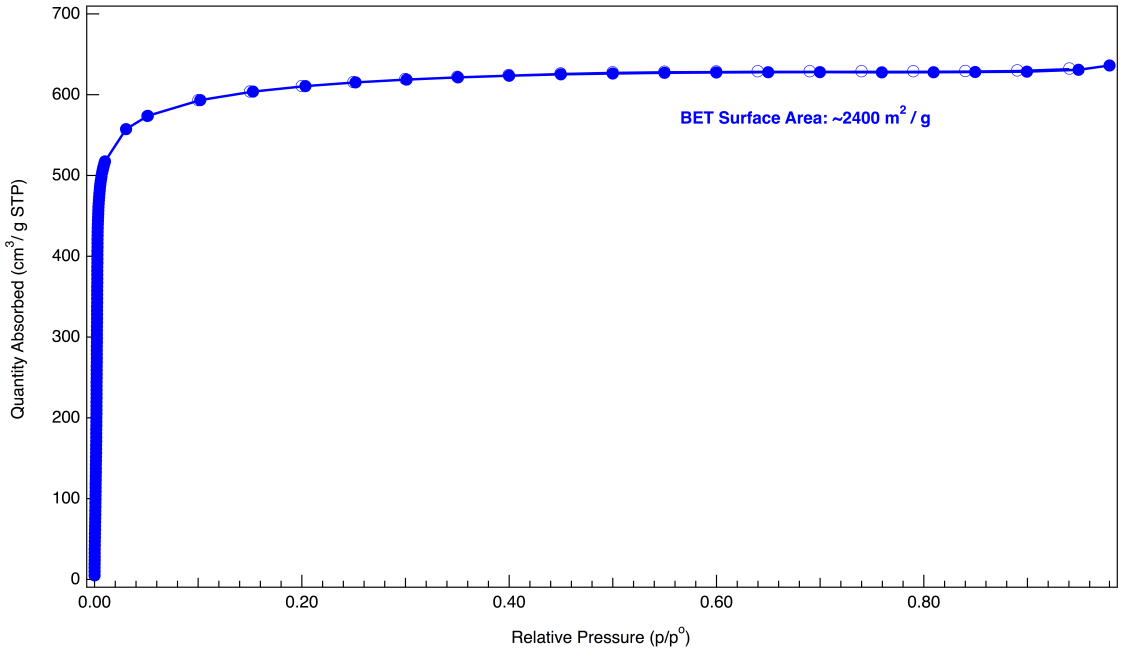

Figure A4.6 N_2 adsorption isotherm (77 K) of COF-102-tolyl (7 eq **2**, unactivated).

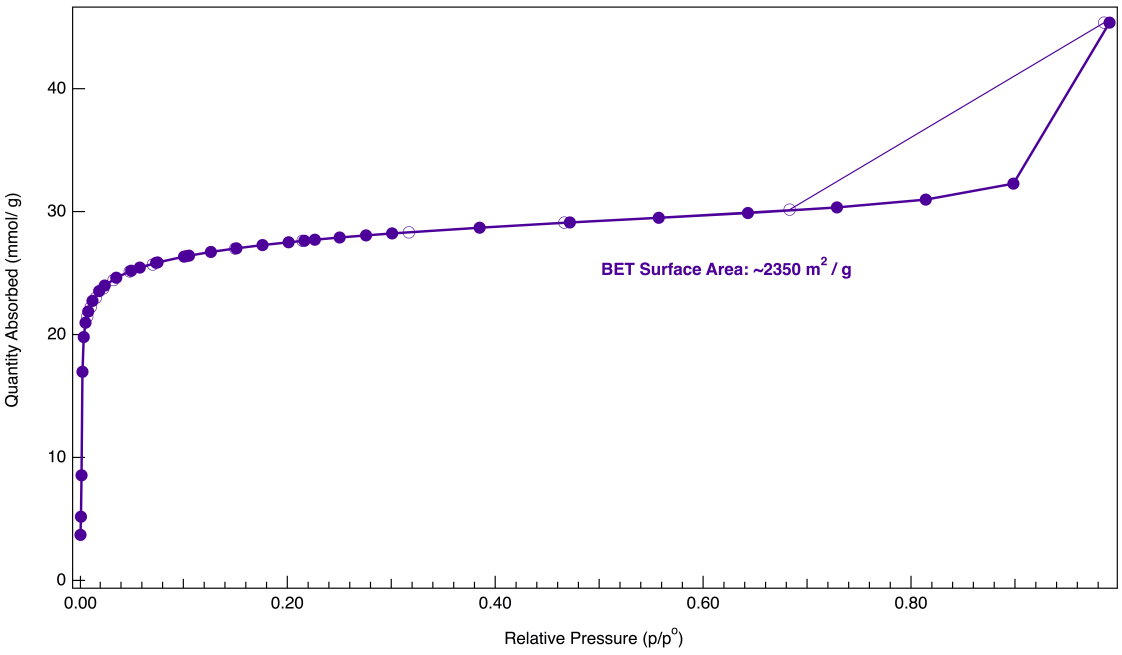

Figure A4.7 N_2 adsorption isotherm (77 K) of COF-102-tolyl (7 eq **2**, activated).

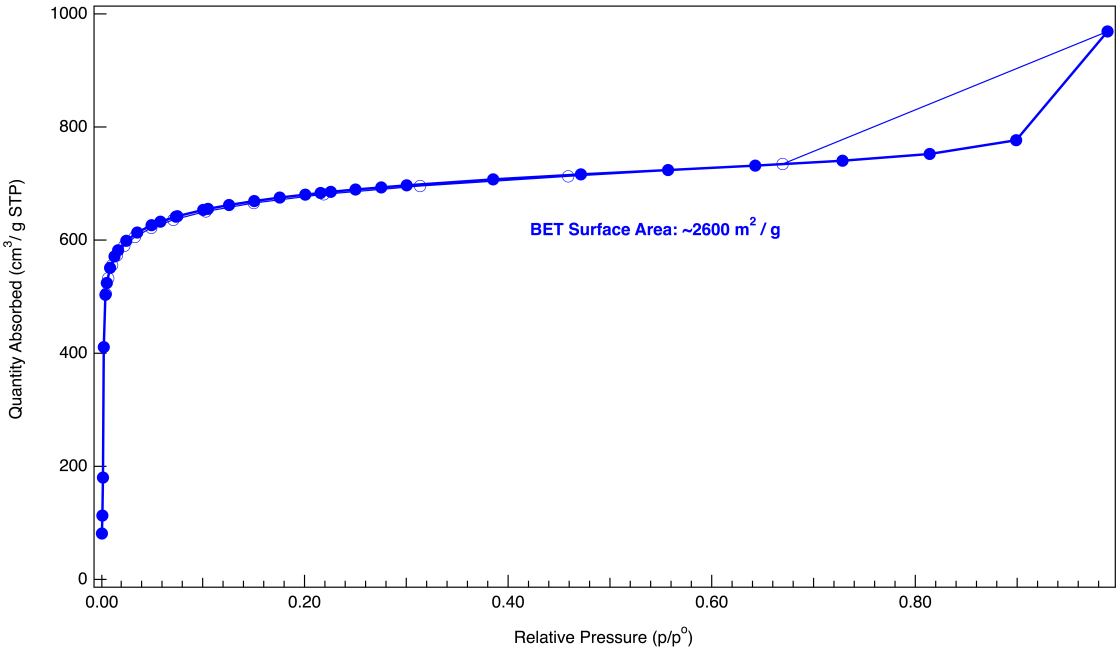

Figure A4.8 N_2 adsorption isotherm (77 K) of COF-102-tolyl (24 eq **2**, unactivated).

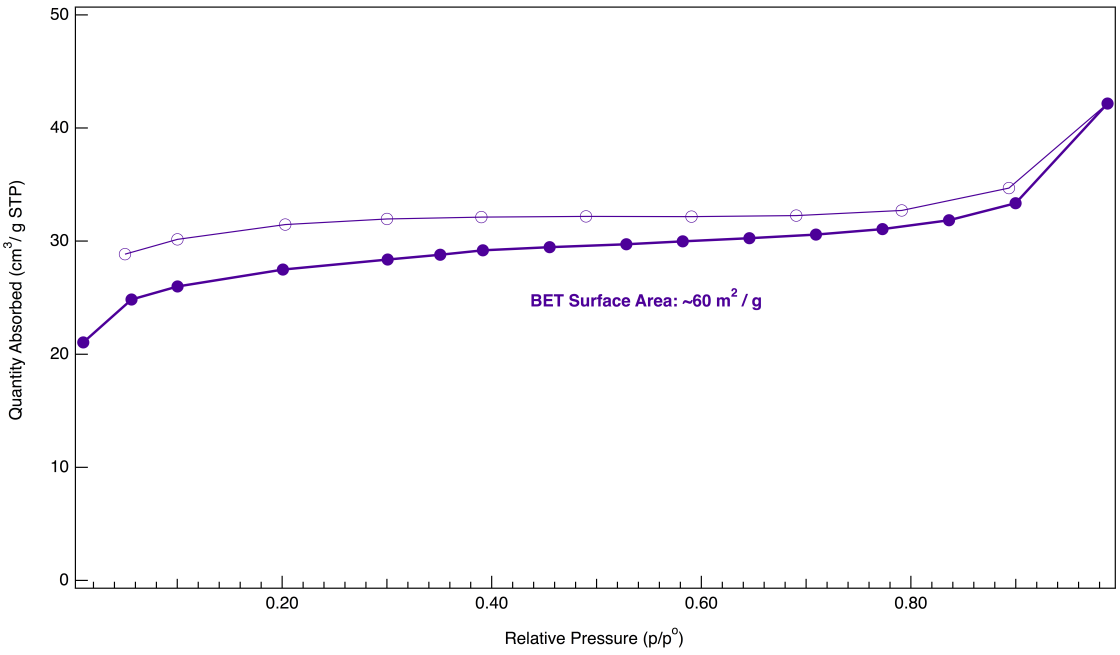

Figure A4.9 N_2 adsorption isotherm (77 K) of COF-102-tolyl (24 eq **2**, activated).

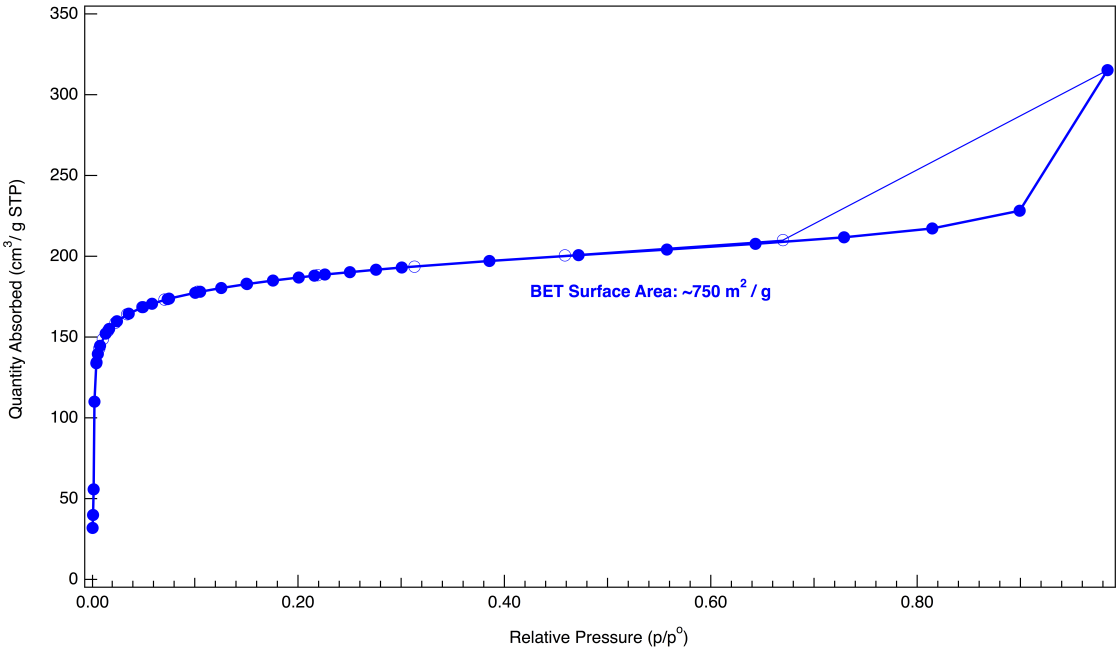

Figure A4.10 ^{1}H NMR spectra (400 MHz, 298 K, $CDCl_3$ with methyl *t*-butyl ether (MTBE) internal standard) of soluble species derived from the activation of COF-102 (red), COF-102-tolyl (6 eq **2**, blue), and COF-102-tolyl (36 eq **2**, purple). The spectra of COF-102 and COF-102-tolyl (6 eq) only show resonances corresponding to residual $CHCl_3$, the mesitylene growth solvent, and the MTBE internal standard. The spectrum of COF-102-tolyl (36 eq) shows additional resonances corresponding to **3**.

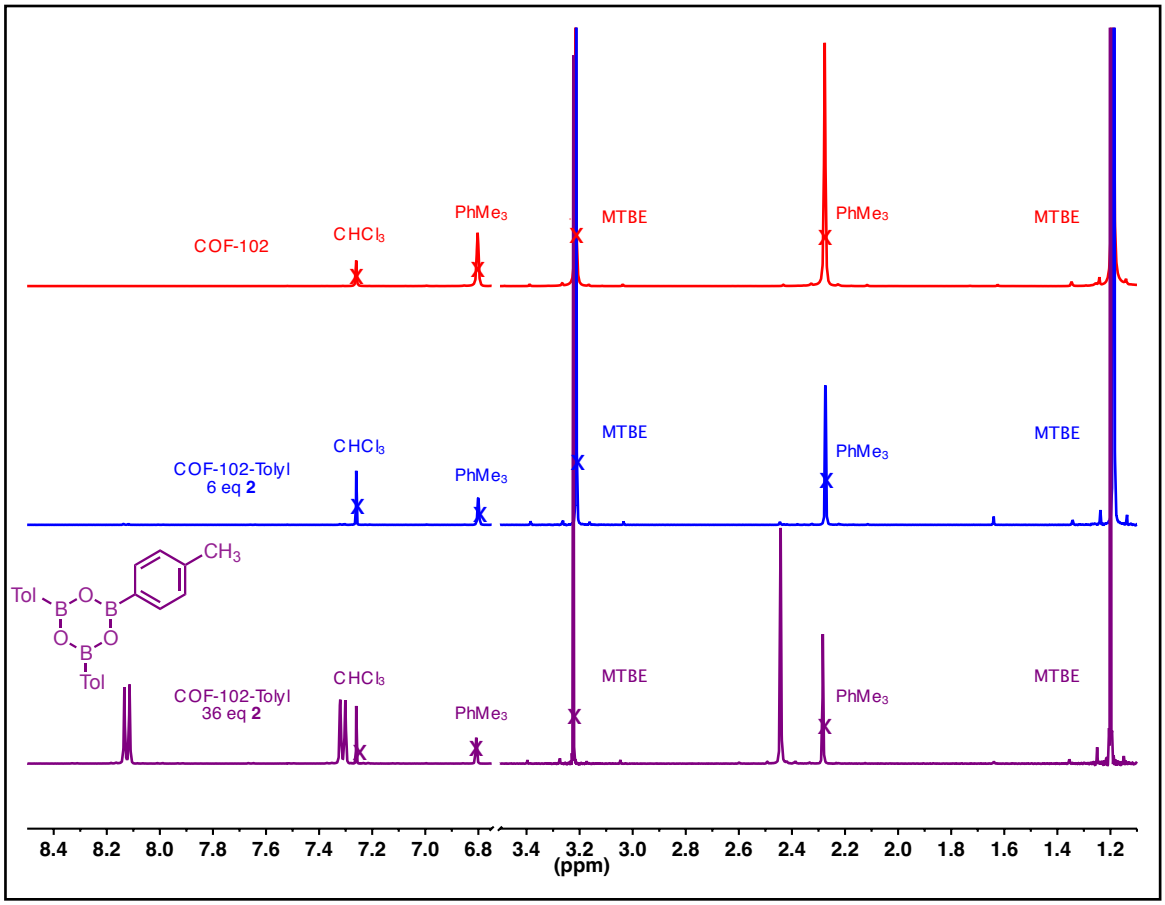

Figure A4.11 ^{1}H NMR spectra (400 MHz, 298 K, CD_3CN/D_2O (3:1 *v*/*v*)) of COF-102-tolyl (T_{Tolyl} = 7%) before (purple) and after (blue) $CHCl_3$ activation.

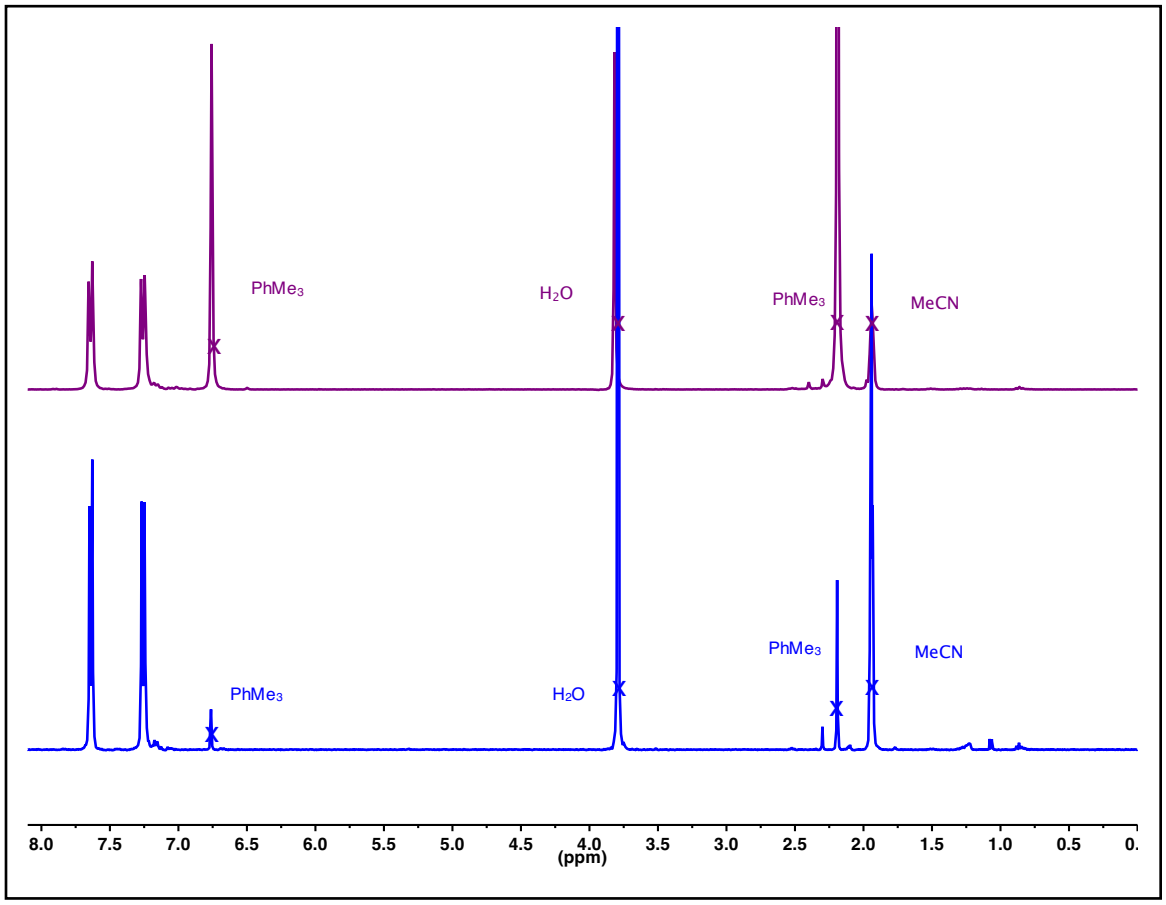

Figure A4.12 ^{1}H NMR spectra (400 MHz, 298 K, CD_3CN/D_2O (3:1 *v*/*v*)) of COF-102-tolyl (T_{Tolyl} = 15%) before (purple) and after (blue) $CHCl_3$ activation.

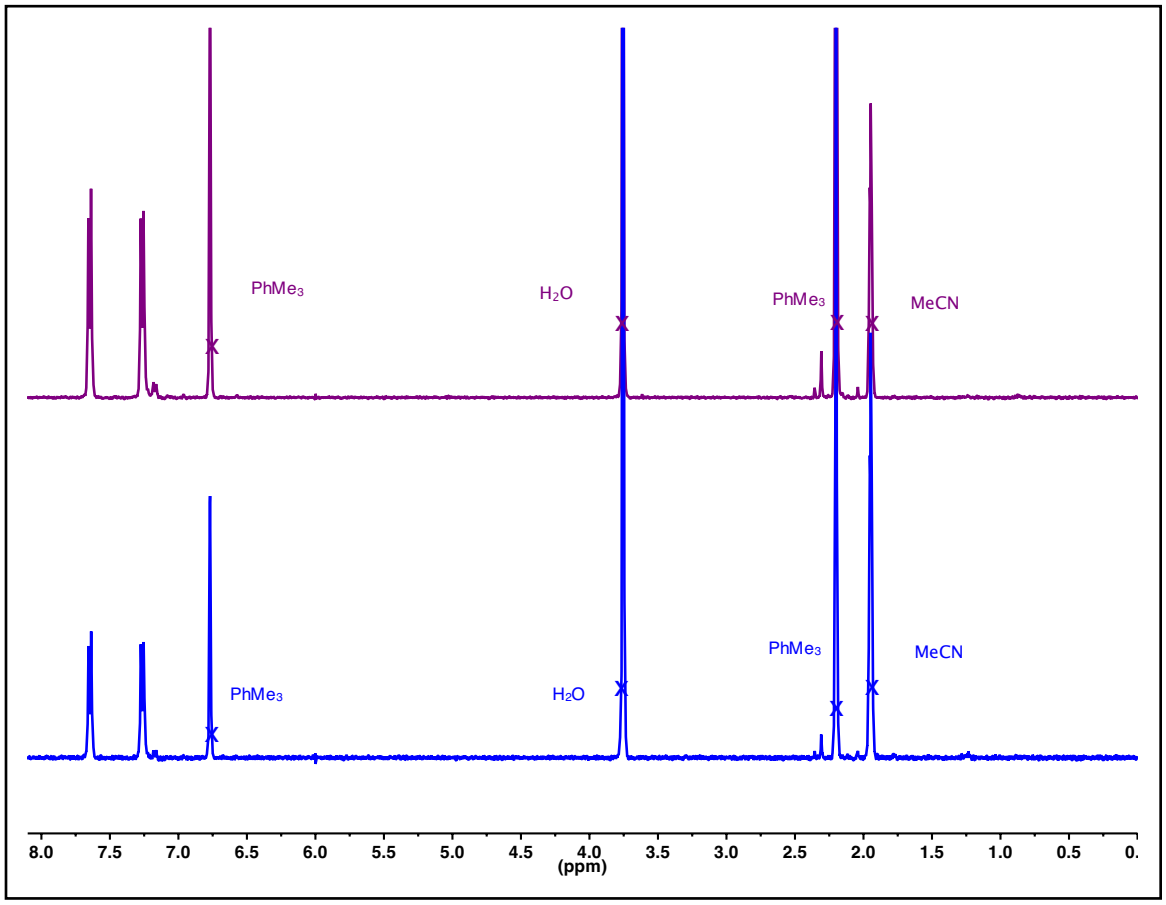

Figure A4.13 ^{1}H NMR spectra (400 MHz, 298 K, CD_3CN/D_2O (3:1 *v*/*v*)) of COF-102-tolyl (T_{Tolyl} = 20%) before (purple) and after (blue) $CHCl_3$ activation.

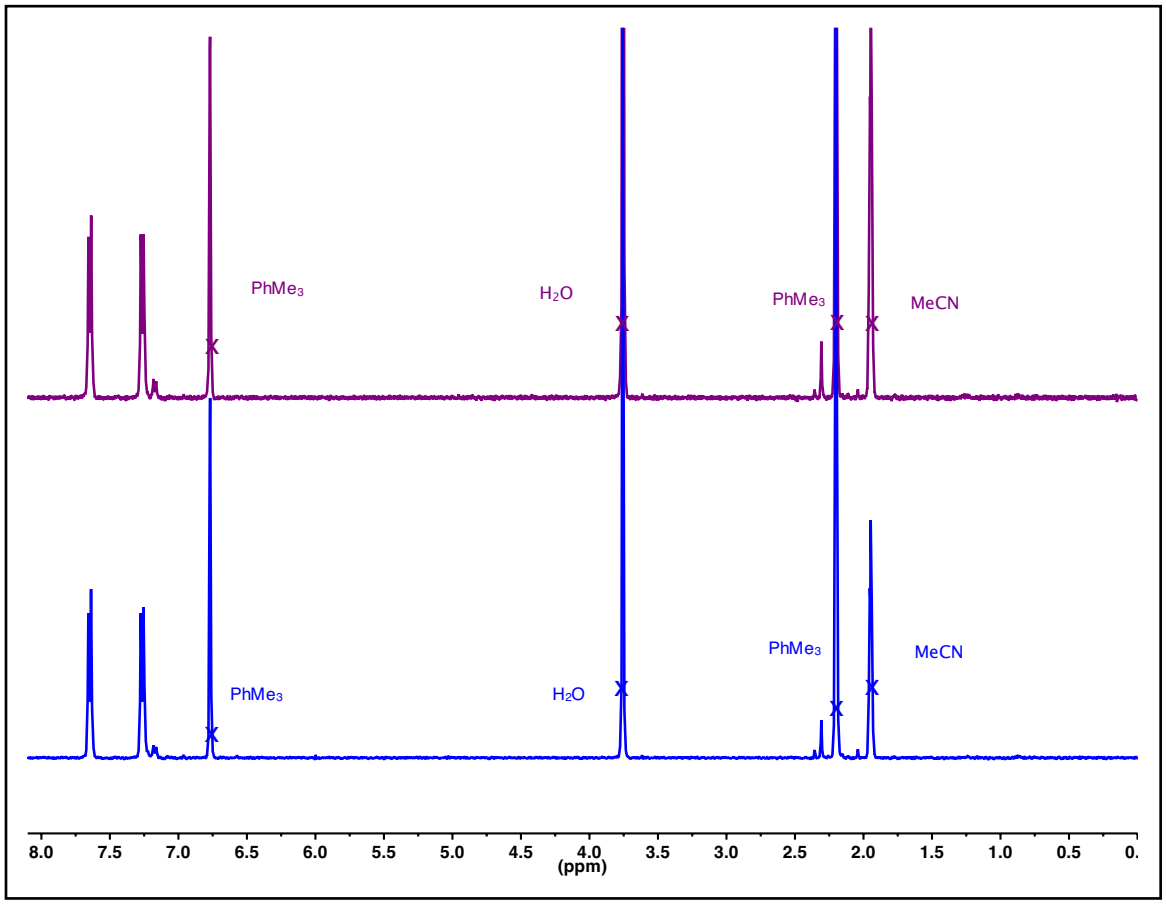

Figure A4.14 ^{1}H NMR spectra (400 MHz, 298 K, CD_3CN/D_2O (3:1 *v*/*v*)) of COF-102-tolyl (T_{Tolyl} =28%) before (purple) and after (blue) $CHCl_3$ activation.

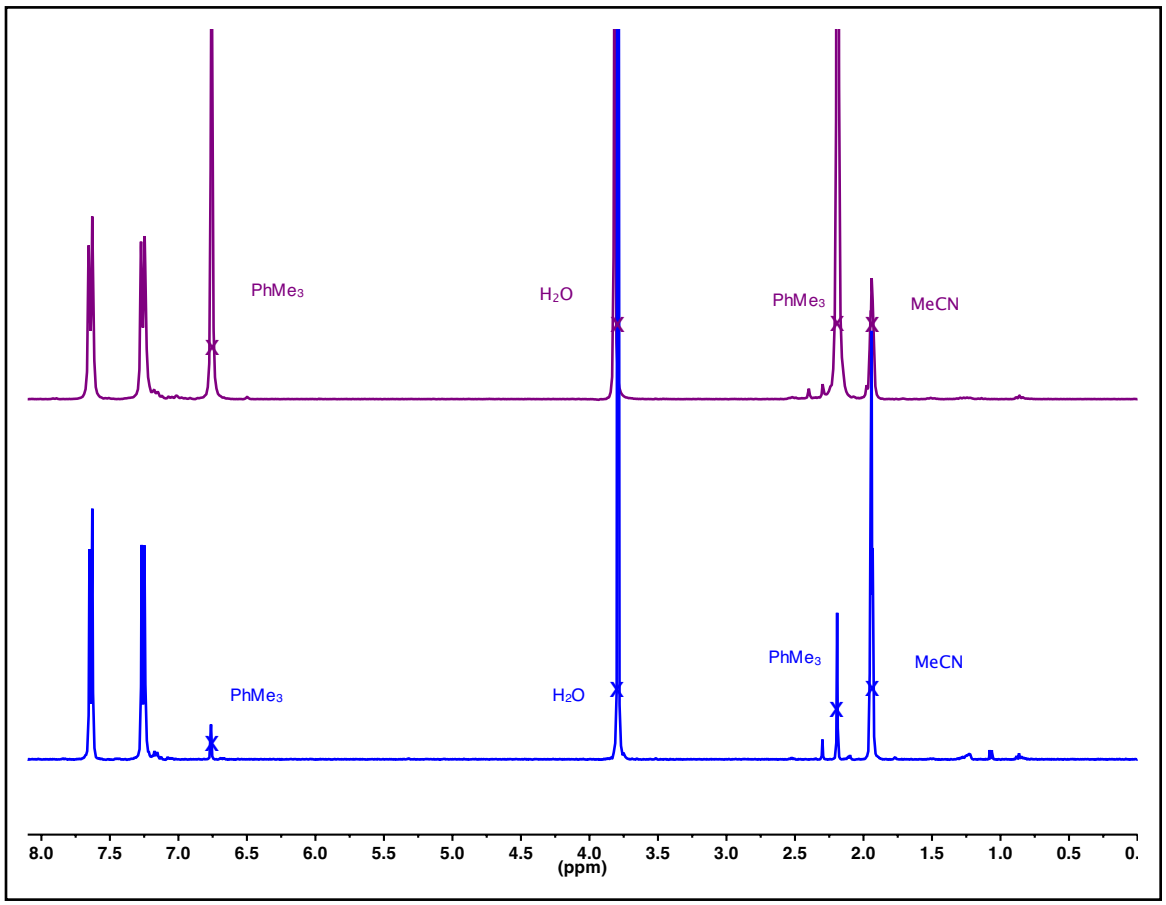

Figure A4.15 ^{1}H NMR spectra (400 MHz, 298 K, CD_3CN/D_2O (3:1 *v*/*v*)) of COF-102-tolyl (T_{Tolyl} = 31%) before (purple) and after (blue) $CHCl_3$ activation.

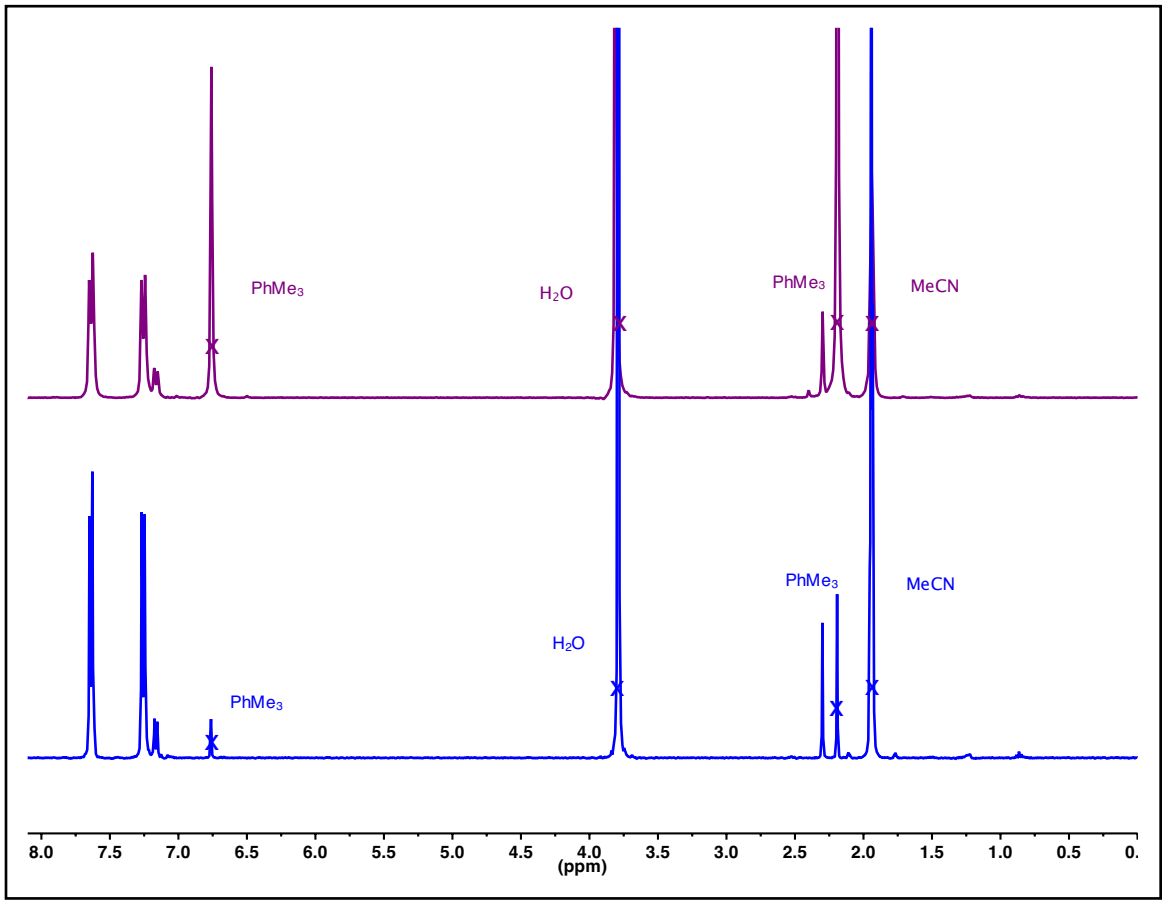

Figure A4.16 ^{1}H NMR spectra (400 MHz, 298 K, CD_3CN/D_2O (3:1 *v*/*v*)) of COF-102-tolyl (T_{Tolyl} = 32%) before (purple) and after (blue) $CHCl_3$ activation.

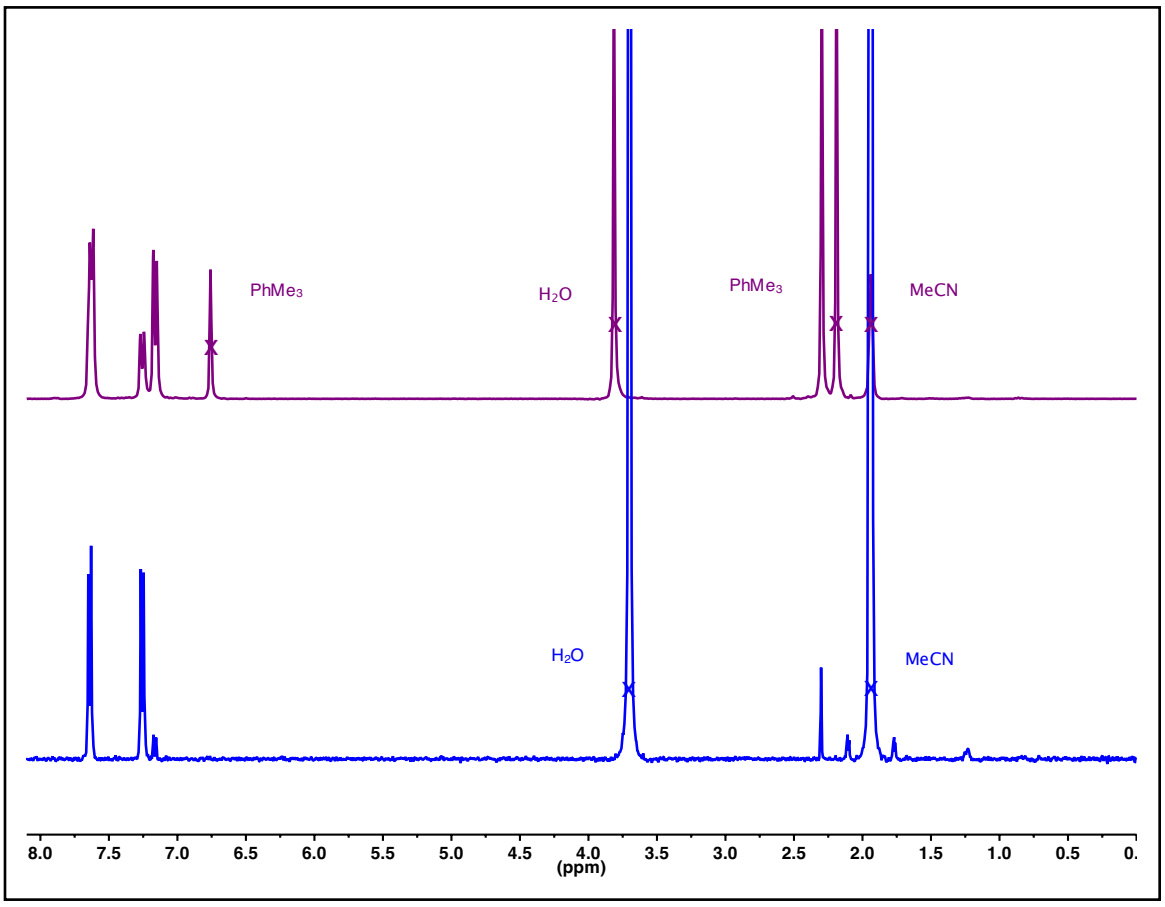

Table A4.1 Loadings of **4** obtained for COF-102-nonyl samples before and after $CHCl_3$ activation.

Feed Ratio of **4** (equiv)	Apparent T_{Nonyl} before activation (%)	T_{Nonyl} after activation (%)
0.5	6 ± 5	3
1	18 ± 4	12
2	26 ± 10	14
4	37 ± 2	29
6	56 ± 6	31
8	52 ± 9	36
10	51 ± 6	32
12	67 ± 1	37

Figure A4.17 ^{1}H NMR spectra (400 MHz, 298 K, CD_3CN/D_2O (3:1 *v*/*v*)) of COF-102-nonyl (T_{Nonyl} = 3%) before (gold) and after (blue) $CHCl_3$ activation.

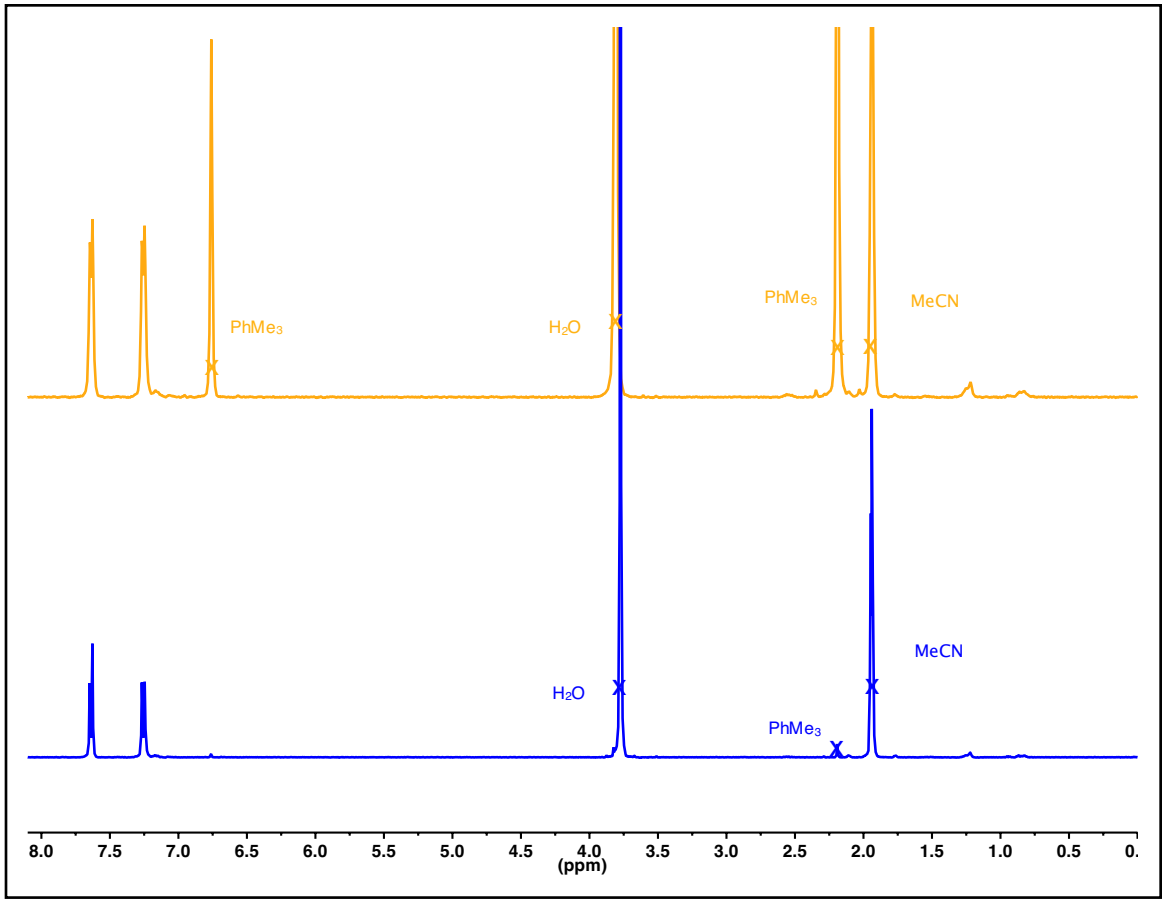

Figure A4.18 ^{1}H NMR spectra (400 MHz, 298 K, CD_3CN/D_2O (3:1 *v*/*v*)) of COF-102-nonyl (T_{Nonyl} = 29%) before (gold) and after (blue) $CHCl_3$ activation.

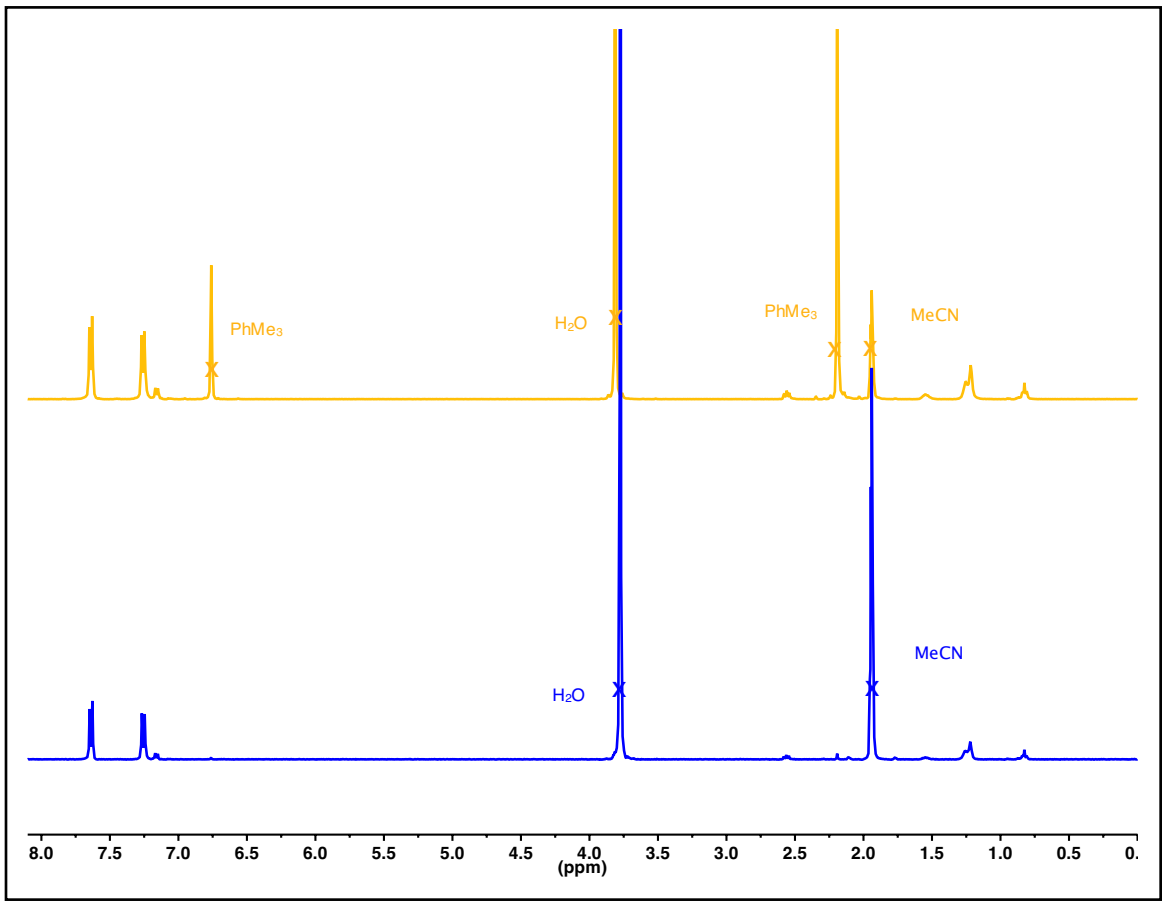

Figure A4.19 ^{1}H NMR spectra (400 MHz, 298 K, CD_3CN/D_2O (3:1 *v*/*v*)) of COF-102-nonyl (T_{Nonyl} = 37%) before (gold) and after (blue) $CHCl_3$ activation.

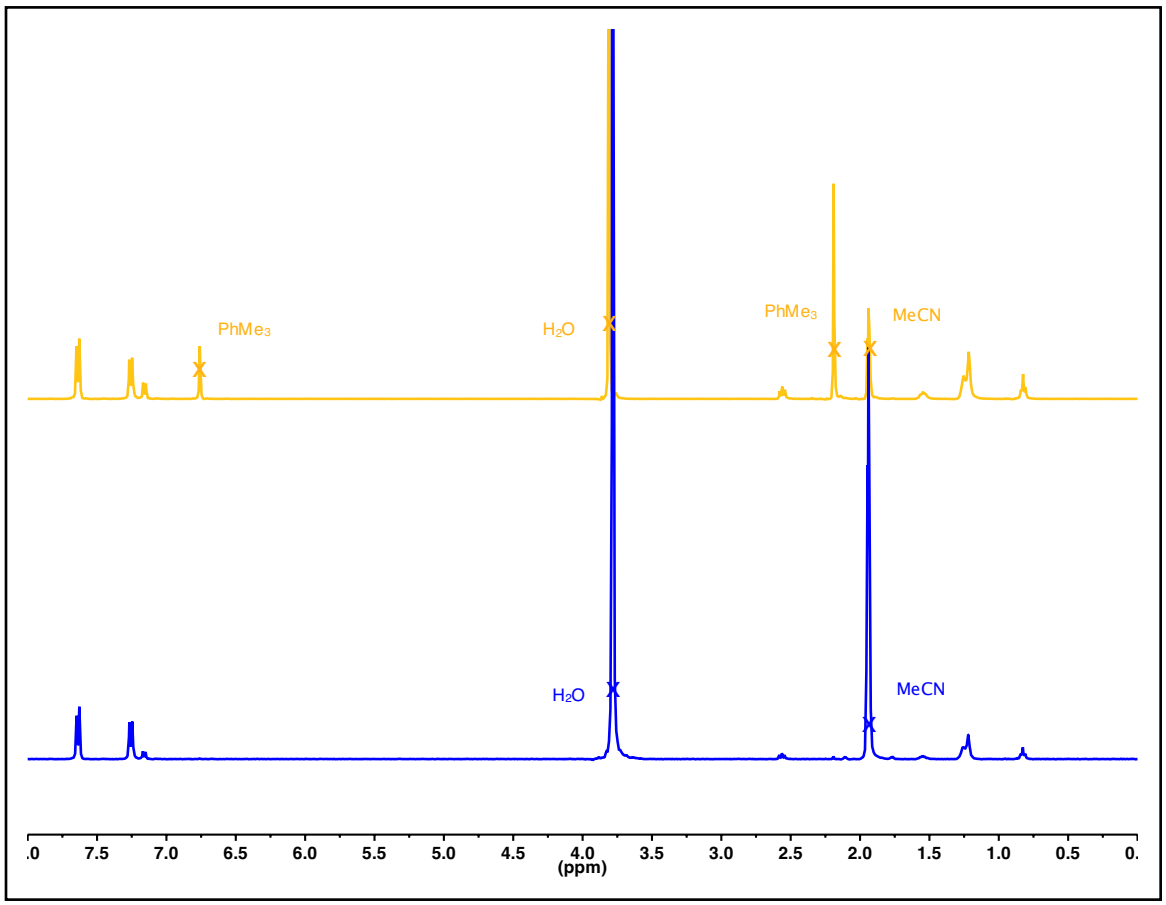

Figure A4.20 Scanning electron micrograph of COF-102. Scale bar is 200 nm.

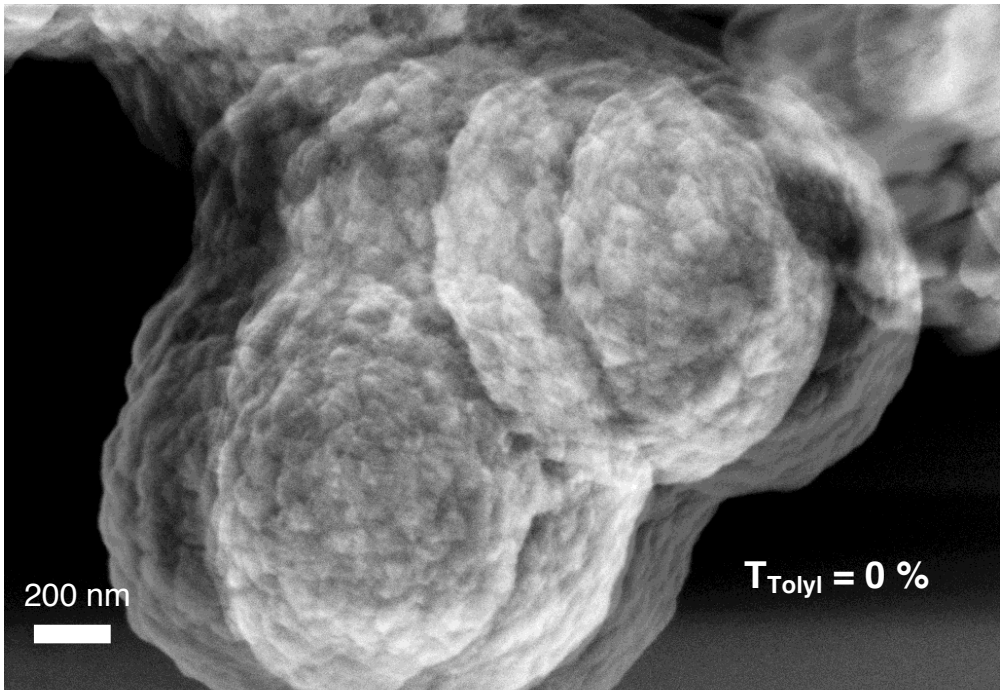

Figure S21. Scanning electron micrograph of COF-102-tolyl (2 eq **2**, unactivated). Scale bar is 300 nm.

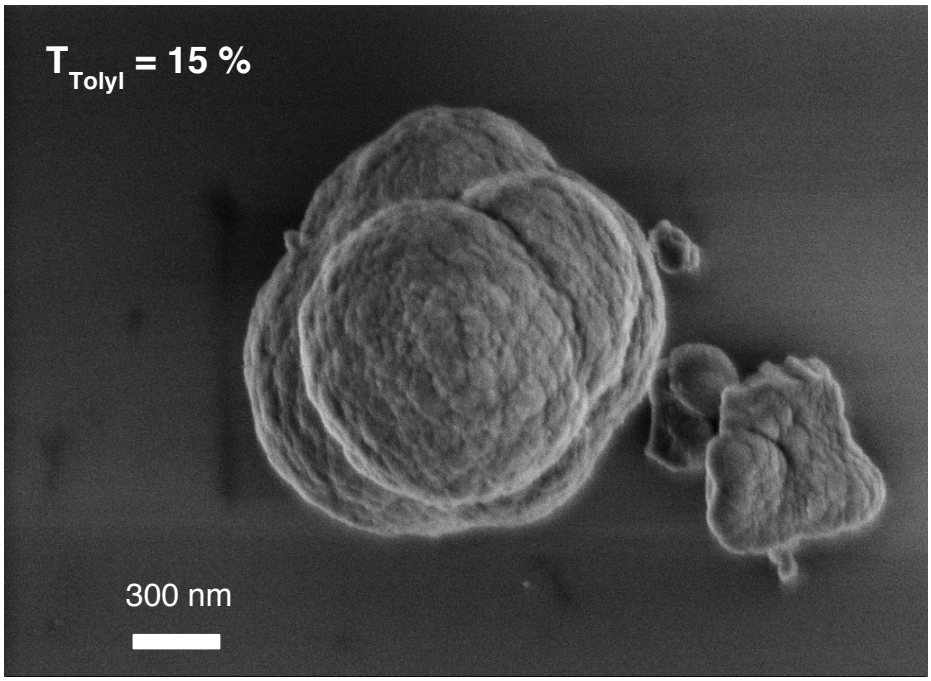

Figure A4.22 Scanning electron micrograph of COF-102-tolyl (6 eq **2**, activated). Scale bar is 200 nm.

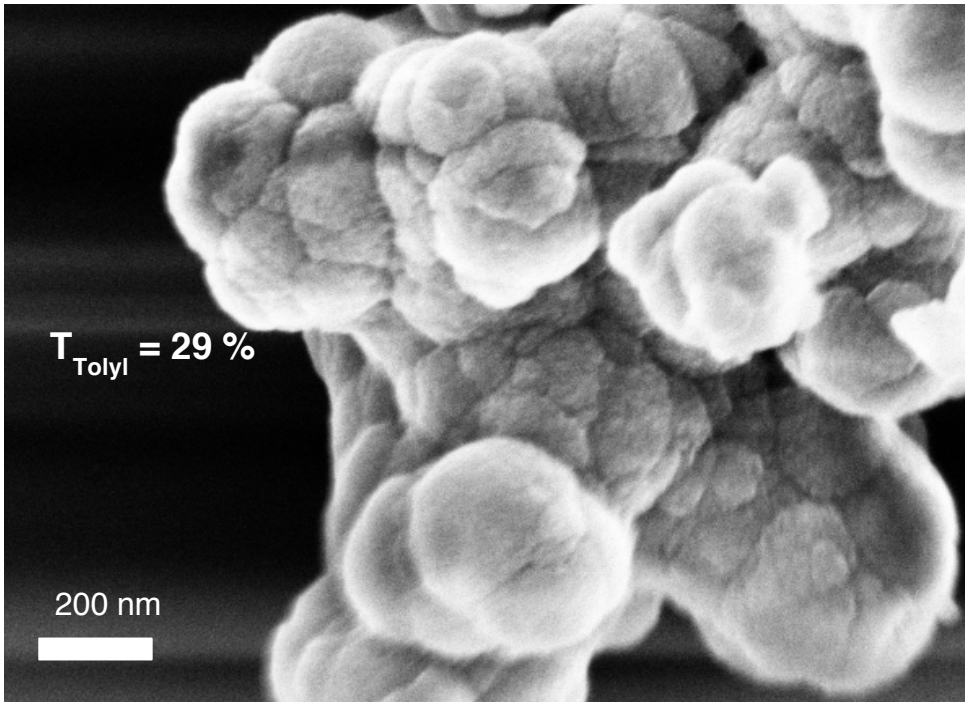

Figure A4.23 Scanning electron micrograph of COF-102-tolyl (36 eq **2**, unactivated). Scale bar is 200 nm.

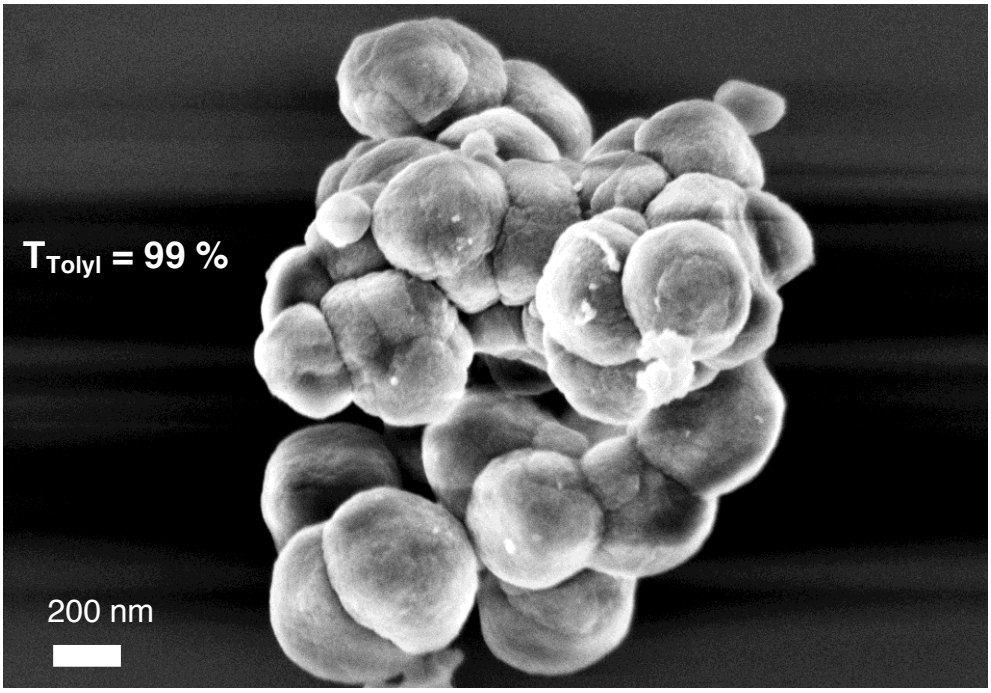

Figure A4.24 Scanning electron micrograph of COF-102-tolyl (36 eq **2**, activated). Scale bar is 500 nm.

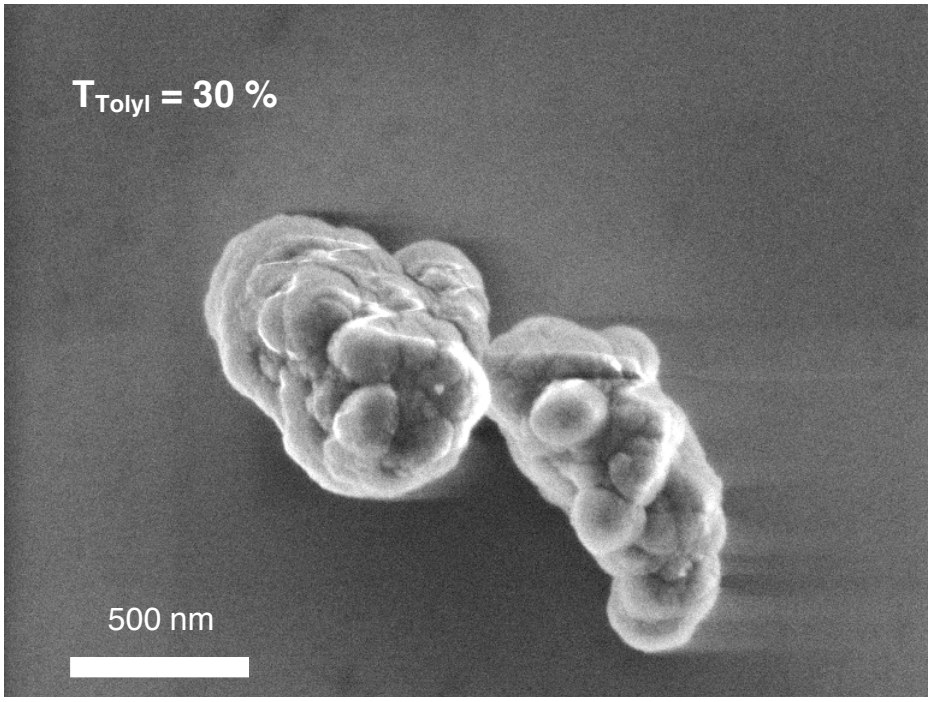

Figure A4.25 Scanning electron micrograph of COF-102 filtrate. Scale bar is 2 μm.

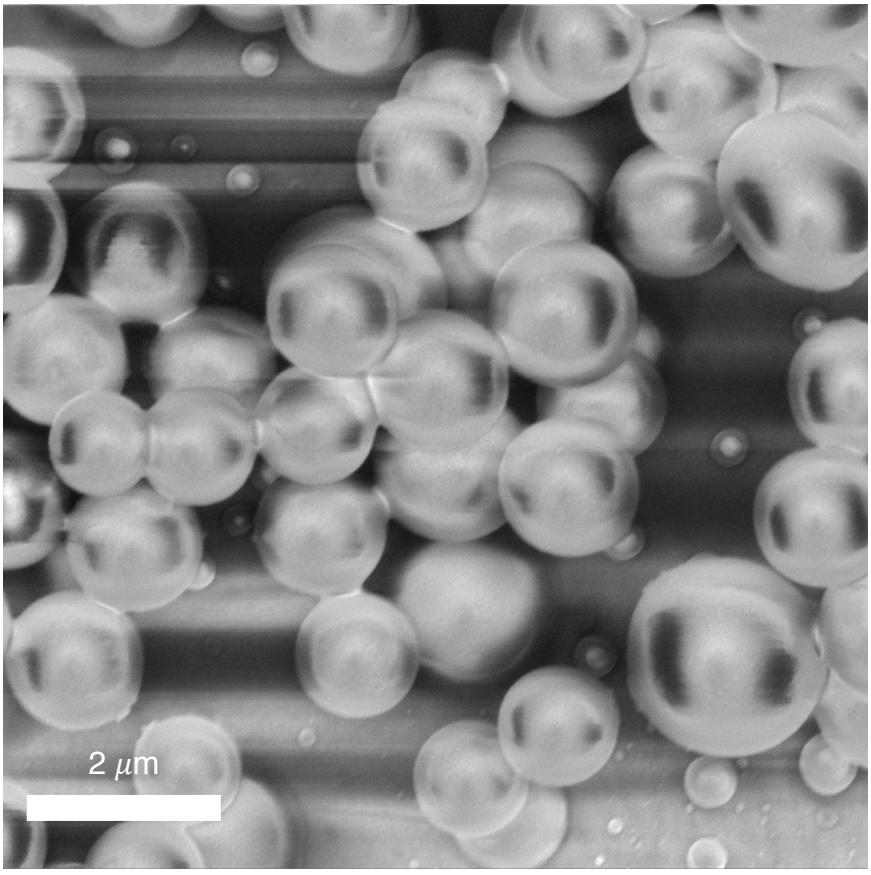

Figure A4.26 Scanning electron micrograph of COF-102-tolyl (36 eq **2**) filtrate. Scale bar is 500 nm.

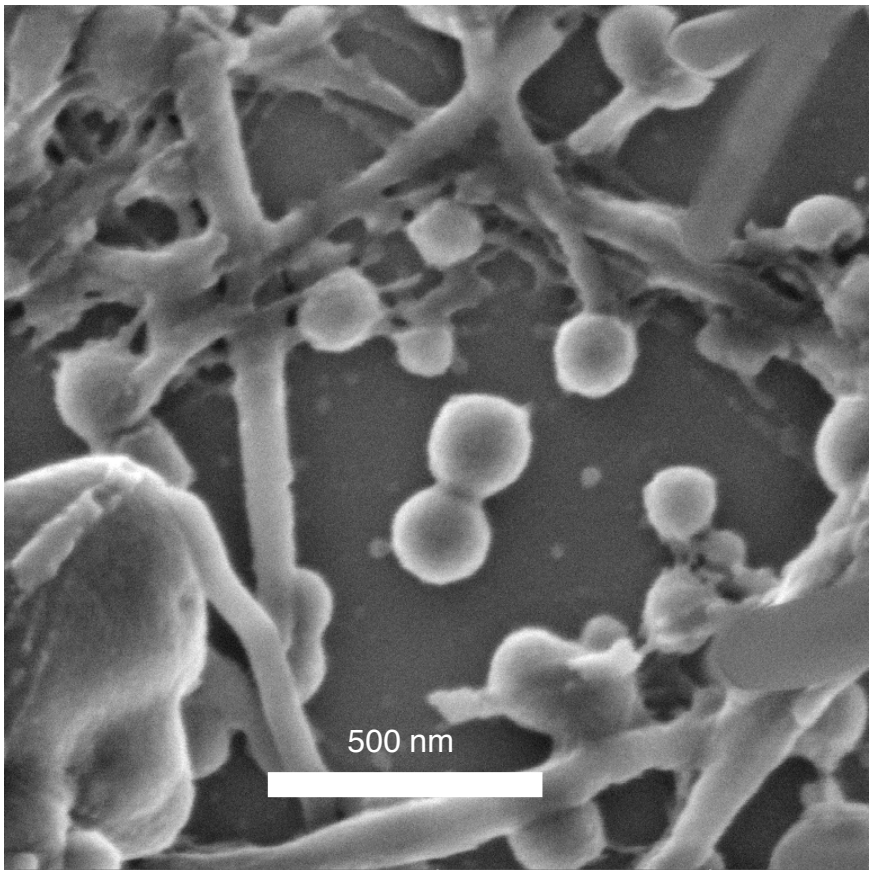

Chapter Five: Bulk Synthesis of 2D Polymers through Exfoliation of Hydrazone-Linked Covalent Organic Frameworks

Two-dimensional (2D) polymers exhibit periodic covalent bonding in two orthogonal directions such that they precisely organize chemical functionality over large areas. High-aspect-ratio 2D polymers might someday serve as lithographic templates, nanoporous membranes, photocurrent generators, or drug release platforms, but these applications remain speculative because reliable polymerization methods are only now emerging.[1] These polymerizations employ polyfunctional monomers that fuse into covalently bonded sheets whose formation is usually templated by a surface or a molecular interface. Covalent organic framework (COF) synthesis, in which monomers condense into crystalline networks under reversible bond forming conditions, is the most general 2D polymerization approach and typically provides multilayer polycrystalline powders.[2] Scalable methods to access single- or few-layer structures remain limited. 2D polymerizations on surfaces yield single-layer polymers amenable to atomically precise characterization, albeit in minute quantities.[2f,3] Sakamoto and coworkers elegantly demonstrated the first scalable synthesis of single- and few-layer structures, which employed a 2D topochemical polymerization within a layered crystal, followed by solvent-mediated exfoliation.[4] However, the generality of this method is unproven, as designing new monomers that form layered crystals capable of such topochemical reactions is not trivial.[5]

Exfoliating 2D COFs might provide access to various few-layer 2D polymers,[6] but this phenomenon is underexplored because 2D COFs feature high-surface-area interlayer van der Waals interactions[7] that template their formation. Only a single example of sonichemical exfoliation of a boronate ester-linked COF into few-layer structures has been reported.[8] Furthermore, boronate ester-linked COFs exhibit poor hydrolytic and oxidative stability[9] and

have appreciable interlayer stacking energies,[10] that are likely to complicate downstream applications of their few-layer forms. In contrast, acyl hydrazones, recently introduced as linkages in 2D COFs,[11] offer improved hydrolytic and oxidative stability and lack the interlayer B–O Lewis acid-base interactions present in boronate ester-linked COFs, both of which facilitate their exfoliation. Here we exfoliate the 2D hydrazone-linked COF-43 under mild conditions and confirm that long-range order is maintained in the resulting few-layer materials (Figure 5.1). We anticipate that these findings will prove general for 2D COFs with moderate interlayer stacking energies, providing a straight-forward means to rationally design few-layer or even single-layer 2D polymers.

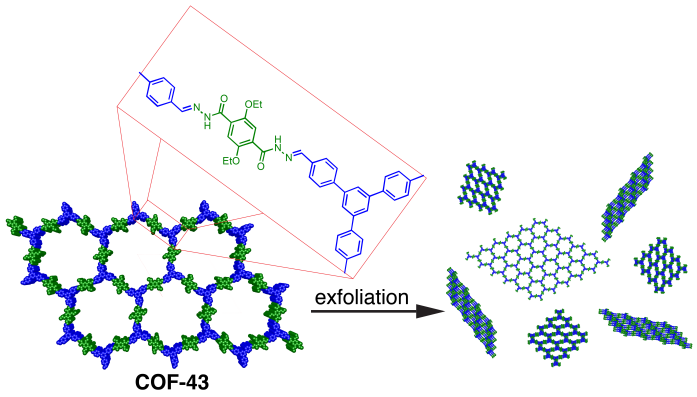

Figure 5.1 Exfoliation of COF-43 yields a suspension of few-layer 2D polymers.

COF-43 was crystallized under solvothermal conditions modified from those reported by Yaghi and coworkers,[11] and the resulting microcrystalline powder was washed with THF to remove residual byproducts and solvents. Powder X-ray diffraction (PXRD) of this material exhibited peaks characteristic of the COF-43 hexagonal network (Figure 5.2, black). The (100), (200), (010), and (300) reflections are observed at 2.46, 4.14, 4.86, and 6.42°, respectively. Given the expected stability of hydrazone linkages, we were surprised to observe a complete loss in crystallinity when COF-43 was immersed in dioxane under ambient laboratory conditions

(Figure 5.2, blue). We evaluated the generality of this phenomenon by re-exposing as-synthesized COF-43 to THF, as well as several common laboratory solvents. Samples exposed to THF, $CHCl_3$, PhMe, and MeOH retained their original diffraction patterns, while those exposed to dioxane, H_2O, and DMF appeared amorphous (Figure A5.3). Although crystallinity loss might arise from framework hydrolysis, hydrazones are typically stable under each of the above conditions.[12] We speculated that the apparent crystallinity loss might instead arise from exfoliation of the COF-43 multilayers without disrupting its covalent linkages.

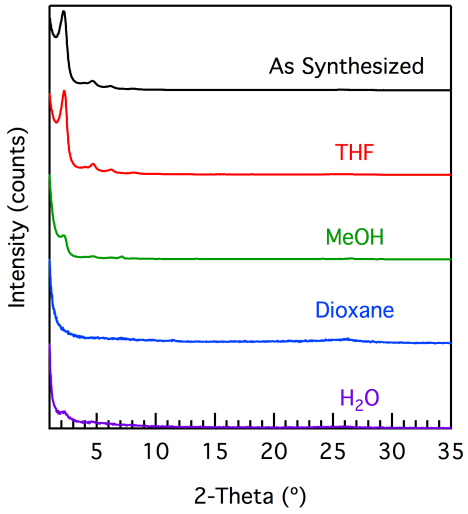

Figure 5.2 PXRD patterns of COF-43 immersed in various solvents for 2 h show a loss in bulk crystallinity for dioxane and H_2O. Results for soaking COF-43 in several additional solvents are shown in Figure A5.3.

We first ruled out the possibility of hydrolysis of the acyl hydrazone linkages within COF-43 using Fourier transform infrared spectroscopy (FTIR). These moieties exhibit characteristic absorbances that correspond to C=O and C=N stretches at 1656 and 1597 cm^{-1}, respectively. These signals remained unchanged in the reactivated powders that were exposed to each of the solvents listed above (Figures 5.3, A5.4). Furthermore, no additional peaks appear and the spectra are devoid of absorbances corresponding to free aldehyde and hydrazide

hydrolysis products (Figure A5.5). We also monitored solutions containing solid COF-43 for the appearance of soluble aldehydes and hydrazides using in situ IR spectroscopy. No new chemical species were detected while soaking COF-43 in THF, in which crystallinity is retained (Figure A5.7), or dioxane, in which crystallinity is lost (Figure A5.6). These solid and solution-state IR experiments demonstrate that hydrazone COFs are chemically stable in each solvent, such that their loss of crystallinity in dioxane, water, and DMF cannot be attributed to hydrolysis processes.

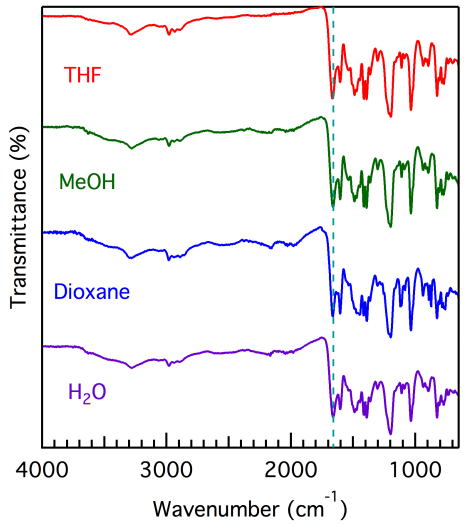

Figure 5.3 FTIR spectra of COF-43 after solvent exposure indicate no attenuation of the hydrazone C=O stretch (dashed line). New signals corresponding to aldehyde or hydrazide hydrolysis products are not observed. Similar spectra were obtained when COF-43 was soaked in other solvents (Figure A5.4).

Soaking COF-43 in solvent provided suspended or dispersed polymers whose size depended on whether the solvent induced apparent crystallinity loss. Atomic force microscopy (AFM) of suspensions sonicated in dioxane indicated intact, high aspect ratio platelets with lateral widths of 200 nm and average heights of 1.32 ± 0.37 nm (Figure 5.4b, A4.16), corresponding to 3-5 layers. Structures as thin as 3.3 Å were obtained after deposition from H_2O (Figures A5.21), suggesting the formation of bi- or even single-layer structures. Polymers deposited from

nonexfoliating solvents, such as THF, also yielded relatively high aspect ratio structures, but they were much thicker (Figure 5.4a) and were reminiscent of the discotic morphology seen in the scanning electron micrographs (SEMs) of the bulk powder (Figure A5.12). Micrographs of COF-43 dispersions in MeOH indicated few dispersed structures (Figure A5.17), and instead revealed thicker aggregates consistent with limited exfoliation. In all cases, the structures isolated showed lateral

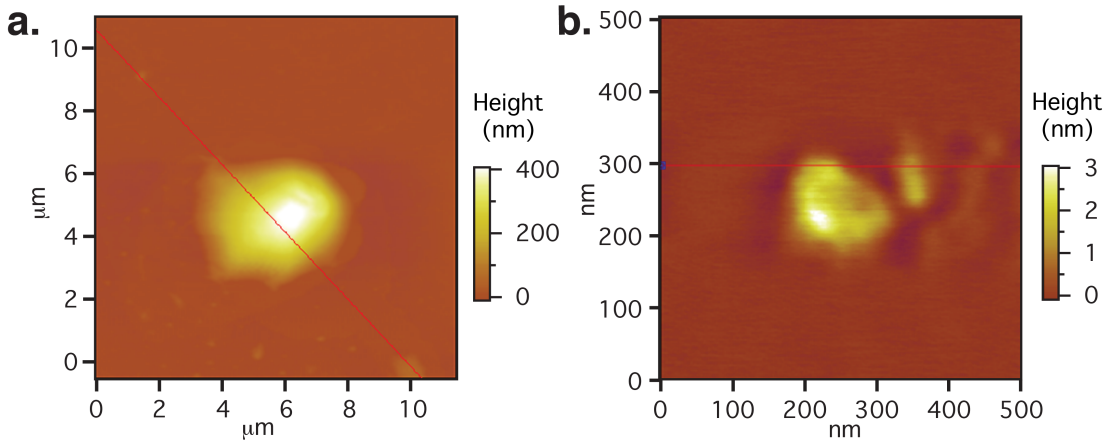

Figure 5.4 Atomic force micrographs of COF-43 deposited onto freshly cleaved mica from (a) THF indicate particle sizes corresponding to hundreds of layers, whereas micrographs from (b) dioxane show platelets corresponding to few-layer structures.

dimensions larger than the crystallite sizes measured by PXRD (17 ± 4 nm), indicating that these sheets of COF-43 are polycrystalline. Grain boundaries might serve as weak points in COF-43 assemblies, where sheet fracture is likely to occur during exfoliation. AFM analysis of suspensions stored on the bench for 50 d provided structures of similar size, indicating their long-term stability. Exfoliated COF-43 could also be interfaced with highly ordered pyrolytic graphite (HOPG), a conductive substrate, using the same exfoliation and drop-casting procedure (Figure A5.22). This procedure offers a route for future study of the electronic properties of these 2D polymers without requiring UHV deposition methods. The size of the dispersed 2D polymers

in solution was also characterized using dynamic light scattering (DLS). Significant size differences of these dispersed species were observed, depending on whether an exfoliating (H_2O, 447 ± 46 nm) or nonexfoliating (THF, 72.2 ± 3.6 nm) solvent was employed (Figures 5.5, A5.8). Taken together, these observations indicate that exfoliating solvents disperse high aspect ratio COF-43 platelets, whereas non-exfoliating solvents provide poorly defined COF-43 multilayers.

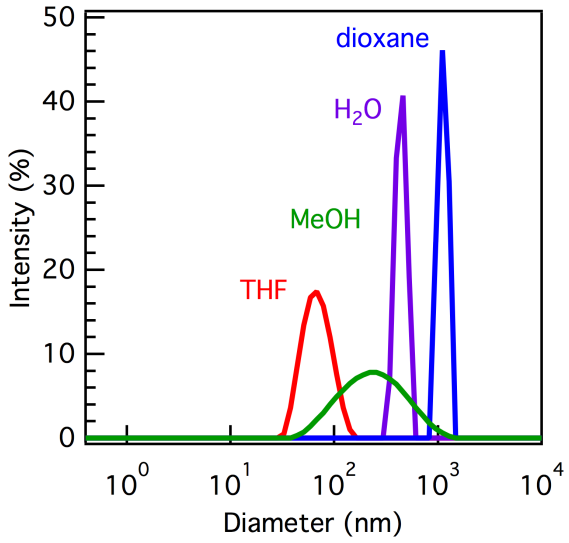

Figure 5.5 Average size of COF-43 dispersions derived from dynamic light scattering of solutions that were briefly sonicated in the presence of COF-43 powder and then passed through a 5 μm filter. Larger dispersed macromolecules are observed in exfoliating solvents (H_2O, dioxane) as compared to non-exfoliating solvents (THF, MeOH).

We next employed transmission electron microscopy (TEM) to confirm the presence of layered structures and probe the local ordering of the 2D polymers. Carbon-coated TEM grids were dip coated in unsonicated dispersions of COF-43 and imaged with a low accelerating voltage (80 kV) to minimize sample degradation in the electron beam. Micrographs of samples prepared from the nonexfoliating solvent THF revealed large structures reminiscent of COF-43 crystallites (Figure 5.6a). The presence of moiré fringes suggests that the layered crystallites adopt slight interlayer offsets typical of stacked aromatic systems that have been identified

computationally for 2D COFs.[10] Similar interference patterns have been observed with other layered 2D polymers, including bi- and trilayer graphene.[13] Selected area electron diffraction (SAED) of these multi layers was consistent with their polycrystalline, hexagonally ordered

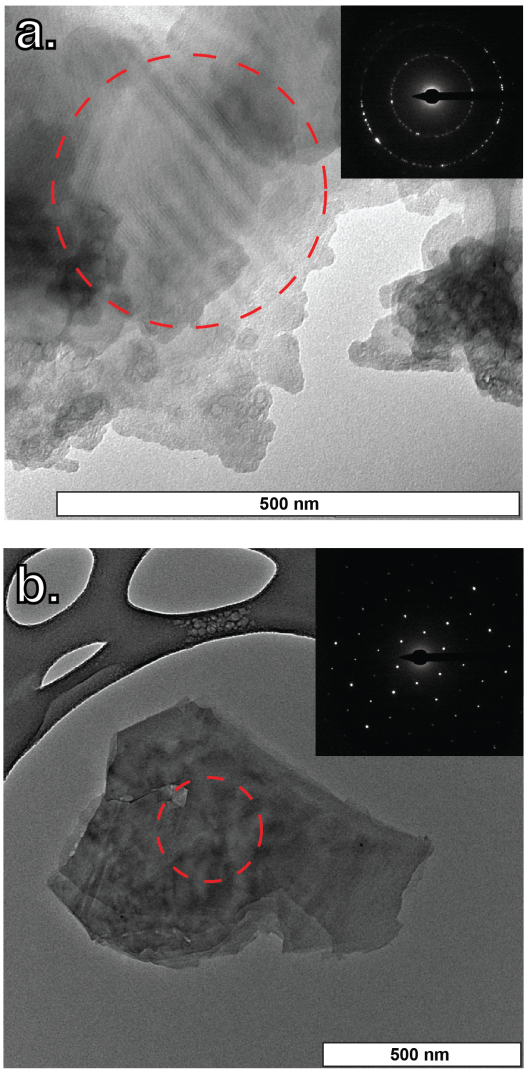

Figure 5.6 Transmission electron micrographs of COF-43 suspensions in (a) THF and (b) dioxane. Selected area electron diffraction (red circle) shows hexagonal order within the sheet (inset).

structure (Figure 5.6a, inset). In contrast, dioxane solutions, which exfoliate COF-43, revealed smaller structures (Figure 5.6b) with moiré fringes (Figure A5.23), suggesting the retention of some vertical stacking. While a thickness is not available from these measurements, assemblies

of similar lateral dimensions and 40 - 50 nm high were observed by AFM from unsonicated dispersions of COF-43 in dioxane (Figure A5.18). Notably, SAED of these materials exhibited a hexagonal diffraction pattern (Figure 5.6b, inset), indicative of ordering on the hundred-nanometer scale. This observation indicates that exfoliated COF-43 retains its long-range order within the covalently linked sheets. As is common for organic materials characterized by TEM, these materials visibly degraded during imaging, especially during electron diffraction, and the intensity of the diffraction pattern faded over time. Still, these observations implicate SAED as a means of characterizing the local crystallinity of multilayer COF samples. For COF-43 soaked in dioxane, these measurements confirm their long-range hexagonal ordering and indicate that periodicity is retained within the sheets after exfoliation.

We have demonstrated that 2D hydrazone-linked COFs have relatively weak interlayer interactions, such that they are exfoliated into few-layer 2D polymers under mild conditions. Immersion in several common laboratory solvents revealed an apparent loss of COF-43 crystallinity by PXRD, despite no apparent changes in its covalent linkages by solid-state and in situ FTIR. The exfoliated COF-43 polymers displayed high aspect ratios characterized by AFM, and SAED confirmed the hexagonal periodicity of few-layer samples. As such, exfoliating 2D COF multi-layers provides a means to obtain bulk quantities of dispersed 2D polymers. These findings are also important in the context of synthesizing new 2D COFs, because they demonstrate that exposure to an exfoliating solvent can obfuscate a sample's crystallinity, as measured by PXRD. COF synthesis is more modular than other 2D polymerization techniques, such that we anticipate that these findings will expand the scope of bulk-scale 2D polymers amenable to further study and facilitate the development of these emerging macromolecular architectures.

References

(1) For recent reviews and discussions of the definition of 2D polymers, see: (a) J. Sakamoto, J. van Heijst, O. Lukin, A. D. Schlüter, *Angew. Chem. Int. Ed.* **2009**, *48*, 1030. (b) J. W. Colson, W. R. Dichtel, *Nature Chem.* **2013**, *5*, 453. For a contemporary example, see: (c) K. Baek, G. Yun, Y. Kim, D. Kim, R. Hota, I. Hwang, D. Xu, Y, H. Ko, G. H. Gu, J. H. Suh, C. G. Park, B. J. Sung, K. Kim, *J. Am. Chem. Soc.* **2013**, *135*, 6523.

(2) (a) S. –Y. Ding, W. Wang, *Chem. Soc. Rev.* **2013**, *42*, 548. (b) X. Feng, X. Ding, D. Jiang, *Chem. Soc. Rev.* **2012**, *41*, 6010. (c) A. P. Côté, A. I. Benin, N. W. Ockwig, M. O'Keeffe, A. J. Matzger, O. M. Yaghi, *Science* **2005**, *310*, 1166. (d) S. Wan, J. Guo, J. Kim, H. Ihee, D. Jiang, *Angew. Chem. Int. Ed.* **2008**, *47*, 8826. (e) J. W. Colson, A. R. Woll, A. Mukherjee, M. P. Levendorf, E. L. Spitler, V. B. Shields, M. G. Spencer, J. Park, W. R. Dichtel, *Science* **2011**, *332*, 228. (f) J. F. Dienstmaier, A. M. Gigler, A. J. Goetz, P. Knochel, T. Bein, A. Lyapin, S. Reichlmaier, W. M. Heckl, M. Lackinger, *ACS Nano* **2011**, *5*, 9737.

(3) (a) L. Grill, M. Dyer, L. Lafferentz, M. Persson, M. V. Peters, S. Hecht, *Nat. Nanotechnol.* **2007**, *2*, 687. (b) L. Lafferentz, V. Eberhardt, C. Dri, C. Africh, G. Comelli, F. Esch, S. Hecht, L. Grill, *Nat. Chem.* **2012**, *4*, 215. (c) M. Abel, S. Clair, O. Ourdjini, M. Mossoyan, L. Porte, *J. Am. Chem. Soc.* **2011**, *133*, 1203. (d) M. Blunt, J. Russell, N. Champness, P. Beton, *Chem. Commun.* **2010**, *46*, 7157.

(4) P. Kissel, R. Erni, W. B. Schweizer, M. D. Rossell, B. T. King, T. Bauer, S. Götzinger, A. D. Schlüter, J. Sakamoto, *Nat. Chem.* **2012**, *4*, 287.

(5) T. Takami, H. Ozaki, M. Kasuga, T. Tsuchiya, A. Ogawa, Y. Mazaki, D. Fukushi, M. Uda, M. Aono, *Angew. Chem. Int. Ed. Engl.* **1997**, *36*, 2755.

(6) (a) E. L. Spitler, J. W. Colson, F. J. Uribe-Romo, A. R. Woll, M. R. Giovino, M. R.; Saldivar, A.; Dichtel, W. R. *Angew. Chem. Int. Ed.* **2012**, *51*, 2623. (b) Exfoliation of layered, inorganic clays was reviewed recently: V. Nicolosi, M. Chhowalla, M. G. Kanatzidis, M. S. Strano, J. N. Coleman, *Science* **2013**, *340*, 1226419.

(7) C. Hunter, K. Lawson, J. Perkins, C. Urch, *J. Chem. Soc. Perkin Trans. 2* **2001**, 651.

(8) (a) I. Berlanga, M. L. Ruiz-González, J. M. González-Calbet, J. L. G. Fierro, R. Mas-Ballesté, F. Zamora, *Small* **2011**, *7*, 1207. (b) For an example using an amorphous porous polymer, see I. Berlanga, R. Mas-Ballesté, F. Zamora, *Chem. Commun.* **2012**, *48*, 7976.

(9) L. Lanni, R. Tilford, M. Bharathy, J.Lavigne, J. *J. Am. Chem. Soc.* **2011**, *133*, 13975–13983.

(10) (a) B. Lukose, A. Kuc, J. Frenzel, T. Heine, *Beilstein J. Nanotechnol.* **2010**, *1*, 60. (b) B. Lukose, A. Kuc, T. Heine, *Chem. - Eur. J.* **2011**, *17*, 2388. (c) W. Zhou, H. Wu, T. Yildirim, *Chem. Phys. Lett.* **2010**, *499*, 103. (d) E. L. Spitler, B. T. Koo, J. L. Novotney, J. W. Colson, F. J. Uribe-Romo, G. D. Gutierrez, P. Clancy, W. R. Dichtel, *J. Am. Chem. Soc.* **2011**, *133*, 19416. (e) B. T. Koo, W. R. Dichtel, P. Clancy, *J. Mater. Chem.* **2012**, *22*, 17460. (f) X. Chen, M. Addicoat, S. Irle, A. Nagai, D. Jiang, *J. Am. Chem. Soc.* **2013**, *135*, 546. (g) M. J. Bojdys, N. Severin, J. P. Rabe, A. I. Cooper, A. Thomas, M. Antonietti, *Macromol. Rapid Commun.* **2013**, *34*, 850.

(11) F. J. Uribe-Romo, C. J. Doonan, H. Furukawa, K. Oisaki, O. M. Yaghi, *J. Am. Chem. Soc.* **2012**, *133*, 11478.

(12) J. Kalia, R. Raines, *Angew. Chem. Int. Ed.* **2008**, *47*, 7523.

(13) L. Brown, R. Hovden, P. Huang, M. Wojcik, D. A. Muller, J. Park, *Nano Lett.* **2012**, *12*, 1609.

Appendix 5-1: Supplementary Information

I. Materials and Instrumentation

Materials. All reagents were obtained from Sigma-Aldrich (Milwaukee, WI) and used as received. Anhydrous DMF was dried using a column (Al_2O_3) under Ar atmosphere on a custom built solvent purification system.

Instrumentation. Infrared spectra of solid samples were recorded using a Thermo Nicolet iS10 FT-IR spectrometer with a diamond ATR attachment and are uncorrected. In situ IR measurements were conducted on a Mettler Toledo ReactIR ic10 with spectra acquired at 10 s intervals. Peaks corresponding to monomer hydrazide and aldehyde stretches were determined in advance by acquiring a spectrum of the pristine compounds in the corresponding solvent.

NMR spectra were recorded on a Varian INOVA 500 MHz spectrometer using a standard $^{1}H\{^{13}C, ^{15}N\}$ Z-PFG probe with a 20 Hz sample spin rate.

Powder X-ray diffraction (PXRD) patterns were obtained on a Rigaku Smartlab X-Ray diffractometer in reflectance parallel beam/parallel slit alignment geometry. The measurement employed Cu Kα line focused radiation at 1760 W (40 kV, 44 mA) power and a Ge crystal detector fitted with a 1.0 mm incident slit. Samples were mounted on zero-background quartz sample holders and flattened with a glass microscope slide. No sample grinding or sieving was done prior to analysis. Samples were observed using a 0.0200° 2θ step scan from 2.0 – 34.0° with a scan speed of 5° min^{-1}. No peaks could be resolved from the baseline for $2\theta > 35°$ and this region was not considered for further analysis. Crystallite size was determined by applying the Scherrer equation to the powder patterns and an alumina standard was used to correct for instrumental broadening.

Transmission electron micrographs were obtained a FEI Technai T12 Spirit operating at 80 kV. Holey carbon grids (Ted Pella) were dipped into the corresponding solvent and the remaining solvent on the grid was wicked through with a piece of torn filter paper. Degradation of the sample in the electron beam was observed within 5 seconds.

Atomic force micrographs were taken on an Asylum MFP-3D-BIO operating in tapping mode and equipped with a Tap300DLC diamond-like carbon or Tap150Al-G Si tip with aluminum reflex coating (tip composition was not seen to affect image quality). Samples were subjected to the modified exfoliation procedure (unless otherwise noted), diluted between 3 and 7 fold with fresh solvent, and drop-cast onto freshly cleaved mica. We note that while dilution modulated the concentration of COF-43 sheets on the surface (suggesting these are not solvent impurities), it had no effect on their lateral size or thickness. Less volatile solvents (dioxane and water) were removed by mild heating and samples were used immediately for analysis. Images were analyzed using the Asylum MFP3D Software Version 12 (operating in Igor Pro). The total number of structures analyzed ranged from >30 (in nonexfoliating solvents, where a lower concentration of large particles was observed) to >3200 (in exfoliating solvents, where a larger number of small structures were observed). Structure selection was performed automatically in the software to reduce selection bias (in rare cases, particles missed by the software were included manually). These structures were then analyzed by height, area, volume, perimeter, and aspect ratio. Structures giving an erroneous result (e.g. a value of 0) for any of these values were excluded from all statistical analysis (e.g. a particle with a value of 0 for perimeter was not used for height, perimeter, and aspect ratio analysis).

Dynamic light scattering measurements were conducted with samples subjected to the modified exfoliation procedure on a Malvern Zetasizer Nano-ZS equipped with a 4 mW He-Ne

laser emitting at 633 nm. Measurements were optimized before each run and were taken in triplicate. The data were analyzed using Malvern Zetasizer Series Software v7.02.

Scanning electron micrographs were obtained on a LEO 1550 FESEM (Keck SEM) operating at 1.00 kV and a working distance of 3 mm. Samples were prepared by adsorption onto a silicon wafer, which was then attached to a flat aluminum platform sample holder. The sample was then placed directly into the instrument. No metal coating was applied.

Samples for the modified exfoliation procedure were sonicated in a Branson 3510 ultrasonic cleaner with a power output of 100W and a frequency of 42 kHz. Higher power sonication (Figure S8) was conducted on a Branson S-250A Analog Ultrasonic Cell Disruptor/Homogenizer (200 W) operated at 75% power at 1 pulse per second with a pulse length of 0.6 s for a total of 2 minutes. Mild heating of the sample was observed during this time.

II. Experimental Protocols

Figure A5.1 Synthesis of linear dihydrazide **1**.

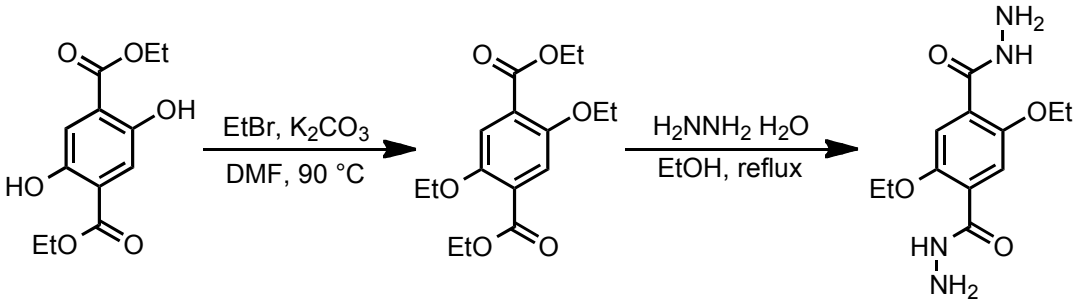

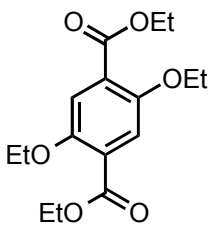

Diethyl 2,5-dihydroxyterephthalate (4.0 g, 15.7 mmol) and potassium carbonate (10.0 g, 72.3 mmol) were placed in a dry 150 mL round bottom flask equipped with a stir bar, which was then sealed with a septum, and purged with N_2. DMF (78.7 mL) and bromoethane (2.8 mL, 37.8 mmol) were subsequently added by syringe. The reaction mixture was heated to 90 °C for 8.5 h. Upon full

conversion by thin layer chromatography (9:1 hexanes/EtOAc *v/v*), the reaction was quenched with aqueous HCl (1 M, 10 mL) and the resulting precipitate was isolated by filtration and dried under vacuum. The resulting diethyl 2,5-diethoxyterephthalate (4.41 g, 98%) was isolated as a white solid that required no further purification. ^{1}H NMR (300 MHz, $CDCl_3$) δ 7.35 (s, 2H), 4.36 (q, 4H), 4.07 (q, 4H), 1.43 (t, 6H), 1.39 (t, 6H). This spectrum matched that previously reported.[1]

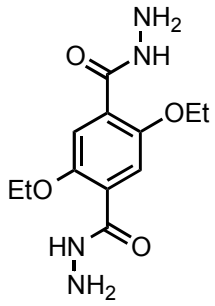

Diethyl 2,5-diethoxyterephthalate (4.5 g, 14.5 mmol) was dissolved in EtOH (58 mL) in a 150 mL round bottom flask equipped with a stir bar. Hydrazine hydrate (8.5 mL, 174 mmol) was added and the flask was then equipped with a condenser and heated to reflux for 15 h. The reaction was then allowed to cool to rt, and a while precipitate formed. The flask was then placed in the freezer for 3.5 h. The white needles were isolated by filtration, washed three times with EtOH, and dried under vacuum. Compound **1** was isolated as white needles (3.85 g, 94%). ^{1}H NMR (300 MHz, DMSO-d_6) δ 9.24 (t, 2H), 7.38 (s, 2H), 4.57 (d, 4H), 4.11 (q, 4H), 1.35 (t, 6H). IR (solid, ATR) 3394, 3206, 2985, 1641, 1568, 1514, 1490, 1470, 1442, 1404, 1389, 1364, 1335, 1298, 1245, 1205, 1156, 1108, 1035, 973, 927, 895, 838, 782, 774 cm^{-1}. These spectra matched that previously reported.[1]

Figure A5.2 Synthesis of trialdehyde **2**.

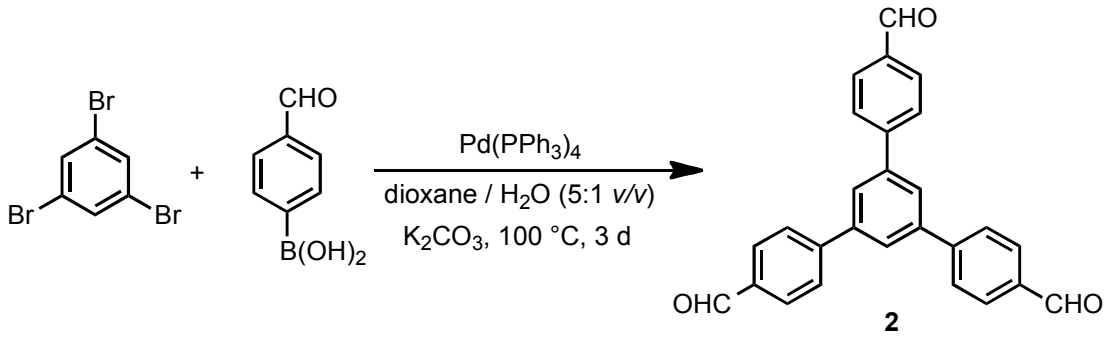

Tribromobenzene (5.0 g, 15.9 mmol), 4-formylphenyl boronic acid (14.3 g, 95.3 mmol), potassium carbonate (13.2 g, 95.3 mmol), and palladium tetrakis(triphenyl phosphine) (0.92 g, 0.794 mmol) were added to a 300 mL round bottom flask equipped with a stir bar and condenser. The flask was evacuated and backfilled with N_2 three times. Dioxane (133 mL) and H_2O (27 mL) were mixed and then added to the flask. The resulting suspension was subjected to three freeze-pump-thaw cycles. The reaction mixture was then heated to reflux for 48 h. The reaction mixture was cooled to rt, after which a precipitate formed that was washed with ethyl acetate and collected. This solid was saved and later identified as pure **2**. The supernatant was washed with H_2O, then brine, finally dried with $MgSO_4$, filtered, and the solvent was removed. The crude product isolated from the supernatant was then dissolved in DCM and run through a plug of SiO_2. The solvent was next evaporated and the resulting solid was recrystallized from MeCN. These isolated white solids were combined to yield **2** (3.83 g, 62%). ^{1}H NMR (400 MHz, $CDCl_3$) δ 10.11, (s, 3H), 8.02 (AA'BB', 6H), 7.91 (3H, s), 7.87 (AA'BB', 6H). FTIR (solid, ATR) cm^{-1}. This spectrum matched that previously reported.[2]

Synthesis of COF-43. Dihydrazide **1** (37.0 mg, 0.131 mmol) and trialdehyde **2** (34.0 mg, 0.087 mmol) were sonicated in 1 mL mesitylene / dioxane (9:1 *v/v*) in a 4 mL vial until a fine

suspension was obtained. The suspension was then transferred by pipet to a pre-scored 5 mL ampoule, 6 M acetic acid (0.1 mL) was added, and the whole mixture was flash frozen in $N_{2\,(l)}$ and flame sealed. The ampoule was put in an oven at 120 °C for 72 h, after which the ampoule was cooled to rt, opened, and the solvent was removed with a pipette. THF (2 mL) was added, and after 1 h, the solvent was removed with a pipette. This THF activation process was then repeated to provide COF-43 as an insoluble microcrystalline powder.

Exfoliation procedure. COF-43 (10 mg) was added to a 4 mL vial. 1 mL of solvent (see text for examples) was then added and the sample was allowed to soak (without sonication) for 2 h. For AFM analysis, this suspension was filtered through a 5 μm filter directly onto the substrate. For analysis of isolated powders, the solvent was removed with a pipette and 1 mL THF (non-exfoliating solvent) was added and the sample was soaked for an additional 2 h. At this time, the solvent was removed and the samples were dried under vacuum.

Modified exfoliation procedure. Samples of COF-43 (10 mg) were immersed in 1 mL of solvent and sonicated for 0.5 to 2 minutes. This supernatant was either used directly or filtered through a 5 μm filter filter for dynamic light scattering or drop cast onto mica or HOPG for atomic force microscopy.

III. Additional Characterization

Figure A5.3 (left) PXRD patterns of COF-43 immersed in various solvents for 2 h show a loss in bulk crystallinity for dioxane, H_2O, and DMF. Crystallite sizes were calculated to be 17 ± 4 nm from the (100) peak at 2.46°.

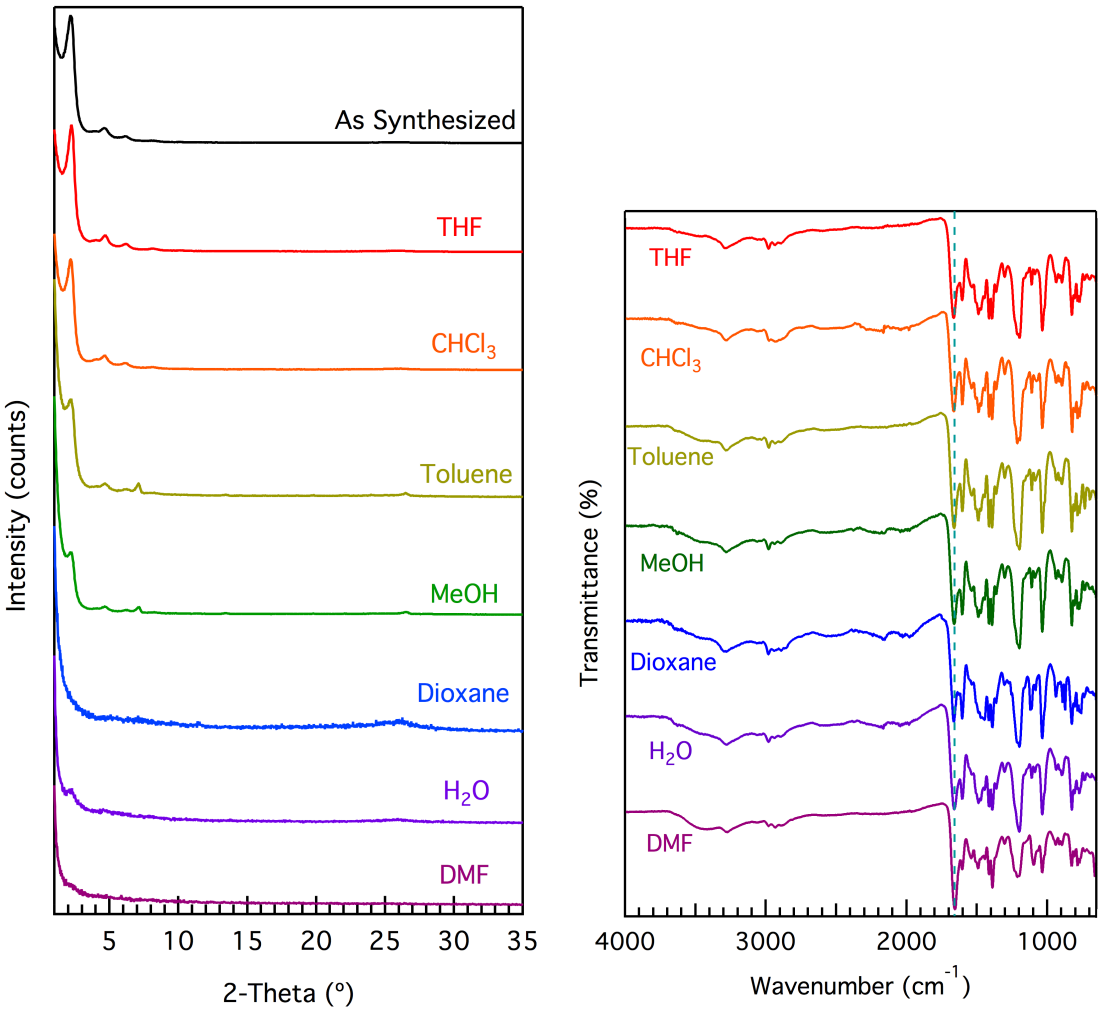

Figure A5.4 (right) FTIR spectra of COF-43 after solvent exposure indicate no attenuation of the hydrazone C=O stretch (1656 cm^{-1}, dashed line). New signals corresponding to aldehyde or hydrazide groups are not observed.

Figure A5.5 FTIR spectra of dihydrazide **1** (green), trialdehyde **2** (blue), and COF-43 (red) shows the complete reaction of free hydrazide and aldehyde within the framework.

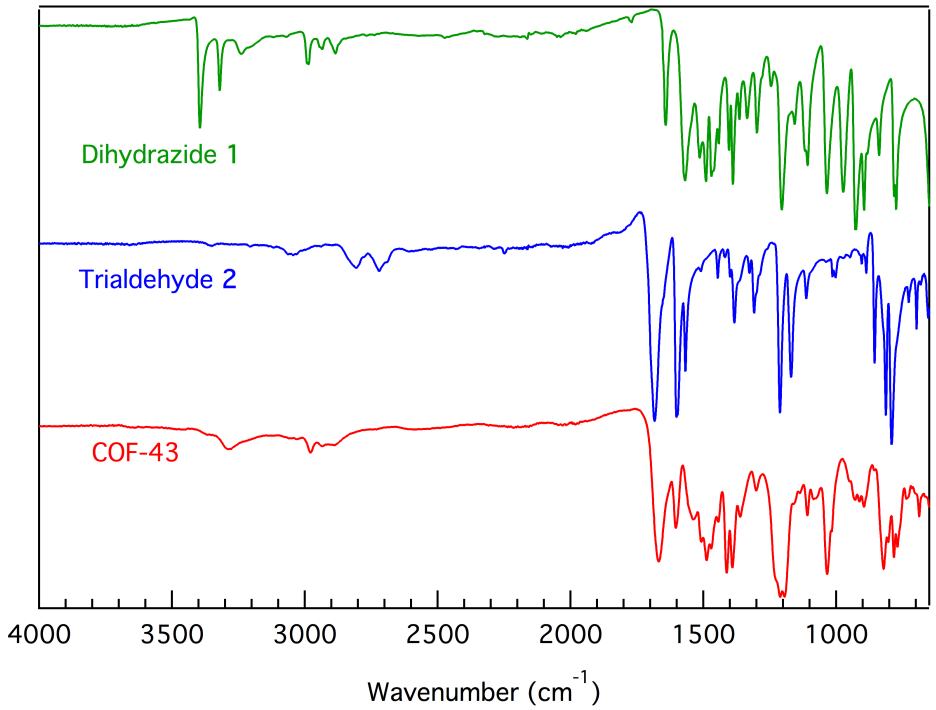

Figure A5.6 In situ IR trace of COF-43 soaked in dioxane (exfoliating solvent). The slight increase with time is attributed to baseline drift. Dashed lines indicate the expected absorbance of each species if the COF-43 sample was fully hydrolyzed.

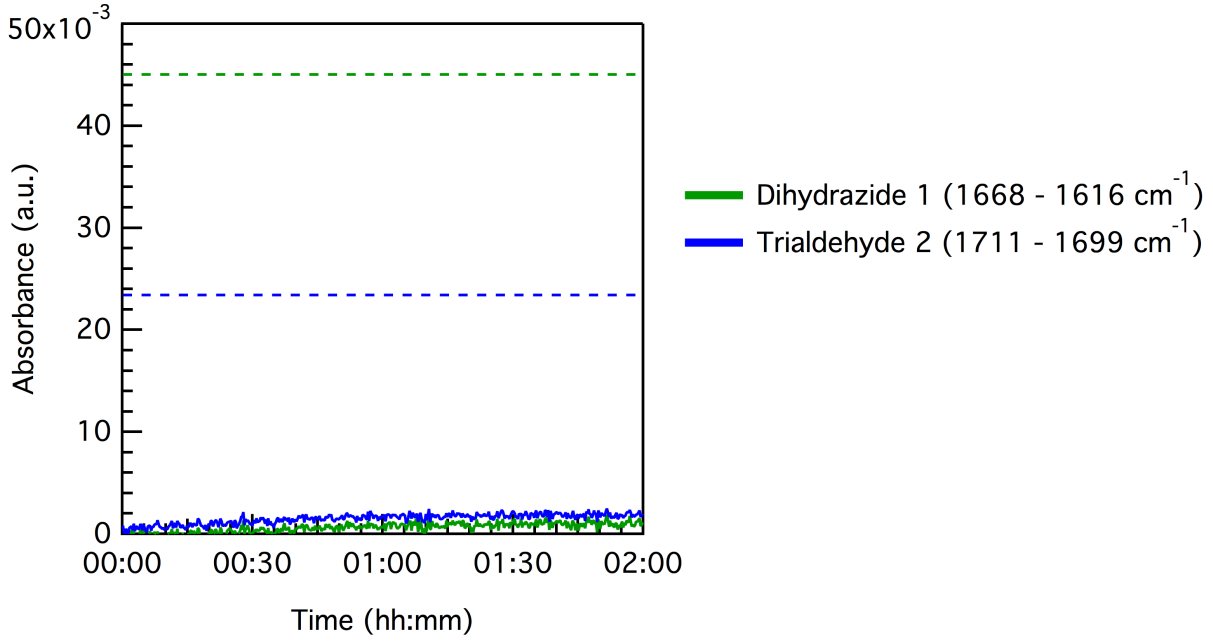

Figure A5.7 In situ IR trace of COF-43 soaked in THF (non-exfoliating solvent). The slight change with time is attributed to baseline drift. Dashed lines indicate the expected absorbance of each species if the COF-43 sample was fully hydrolyzed.

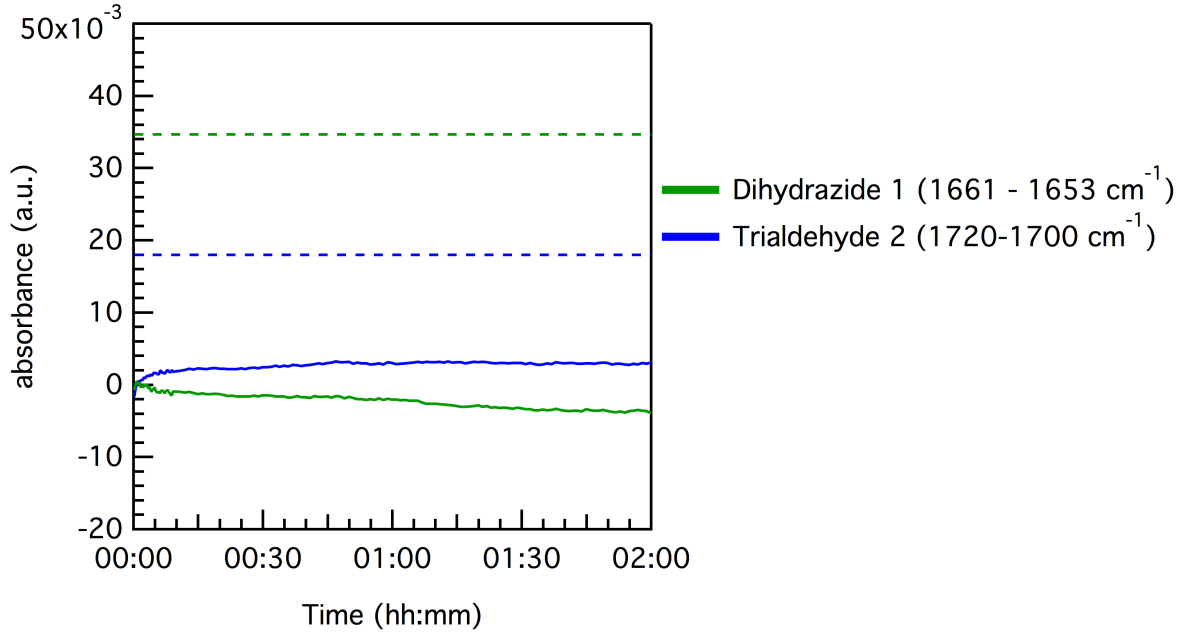

Discussion of Dynamic Light Scattering Measurements

The exfoliation of COF-43 disperses few-layer 2D polymers in solution, which were characterized using dynamic light scattering (DLS). Significant size differences of these dispersed species were observed, depending on whether an exfoliating or nonexfoliating solvent was employed. Activated COF-43 powder was suspended in H_2O, an exfoliating solvent, and immediately sonicated for 2 min. DLS performed on the decanted solution indicated dispersed polymers with a relatively narrow size distribution centered at 447 ± 46 nm (Figure S6 purple). When this procedure was employed using the nonexfoliating solvent THF, a narrower size distribution centered at 72.2 ± 3.6 nm was obtained (Figure S6, red). These observations proved general for the exfoliating solvent dioxane and nonexfoliating solvent MeOH (Figure S6, green) and are consistent with our hypothesis that bulk crystallinity loss originates from this phenomenon. Sonication in nonexfoliating solvents appears to only disrupt and disperse weakly bound polymer fragments, while most of the COF-43 assemblies remain intact. In contrast, the increased sizes observed in exfoliating solvents might result from their intercalation into the layered framework, forming larger aggregates of sheets that diffuse more slowly. The size of dispersed polymers in exfoliating solvents decreased slightly upon sonicating for longer times and with increased power (Figure S7), but always remained larger than the dispersions in nonexfoliating solvents. We also note that the size distributions determined from these measurements are inconsistent with those measured by AFM. DLS measurements yield a diffusion coefficient, which is converted to a hydrodynamic diameter (D_h) using the Stokes-Einstein equation, which is valid for spherical particles. The diffusion of high aspect ratio sheets, especially as it relates to DLS measurements,[3,4] is not well characterized and the presence of periodic porosity might further complicate their behavior. However, the results from these DLS

studies provide information on the relative sizes of dispersed COF-43 in the solvents investigated, suggesting that exfoliating solvents disperse larger aggregates of 2D polymers.

Figure A5.8 DLS intensity trace of COF-43 dispersions across several solvents reveal those that exfoliate stabilize larger dispersions. PDIs: THF = 0.269 ± 0.063; MeOH = 0.272 ± 0.046; H_2O = 0.729 ± 0.112; dioxane = 0.503 ± 0.071.

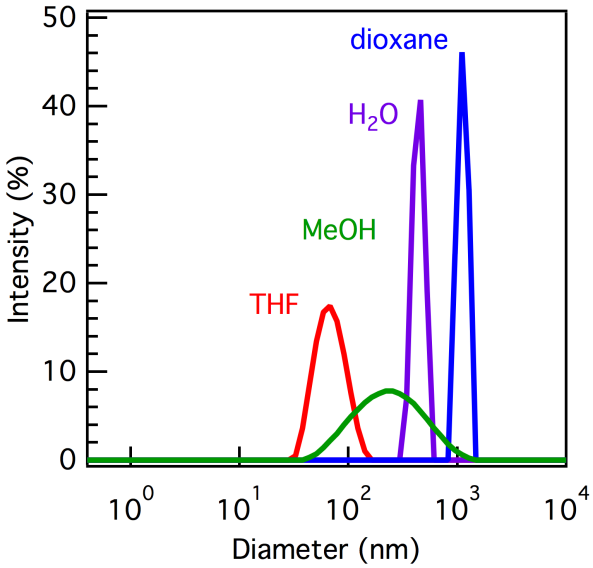

Figure A5.9 DLS intensity trace of COF-43 dispersions in H_2O (exfoliating solvent) after 2 min sonication in a bath sonicator or 2 min with a cone sonicator.

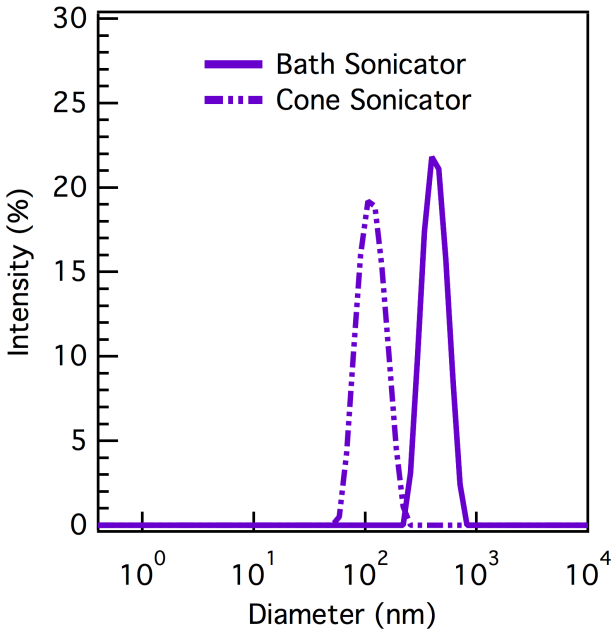

Figure A5.10 Scanning electron micrograph of COF-43 soaked in THF shows a discotic morphology.

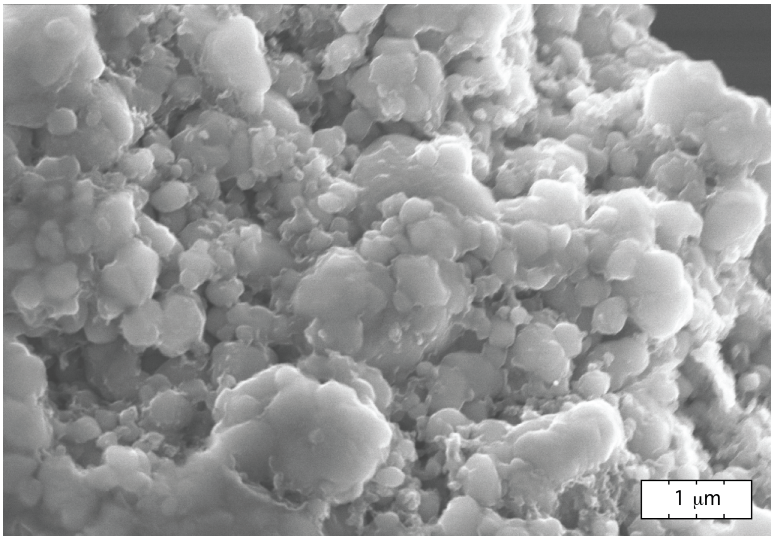

Figure A5.11 Average heights of COF-43 determined by AFM. Identical data are plotted with different y-axis scales to show differences among both exfoliating and non-exfoliating solvents.

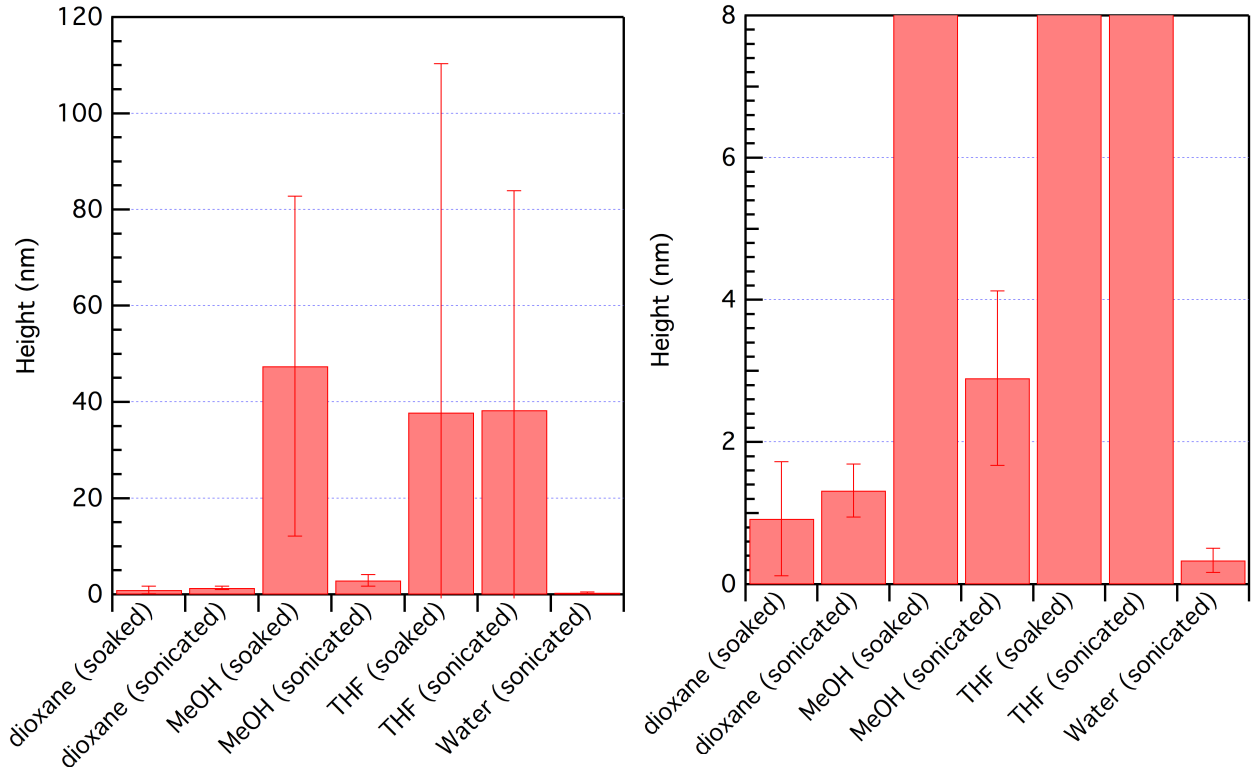

Figure A5.12 Maximum heights of COF-43 determined by AFM. Identical data are plotted with different y-axis scales to show differences among both exfoliating and non-exfoliating solvents.

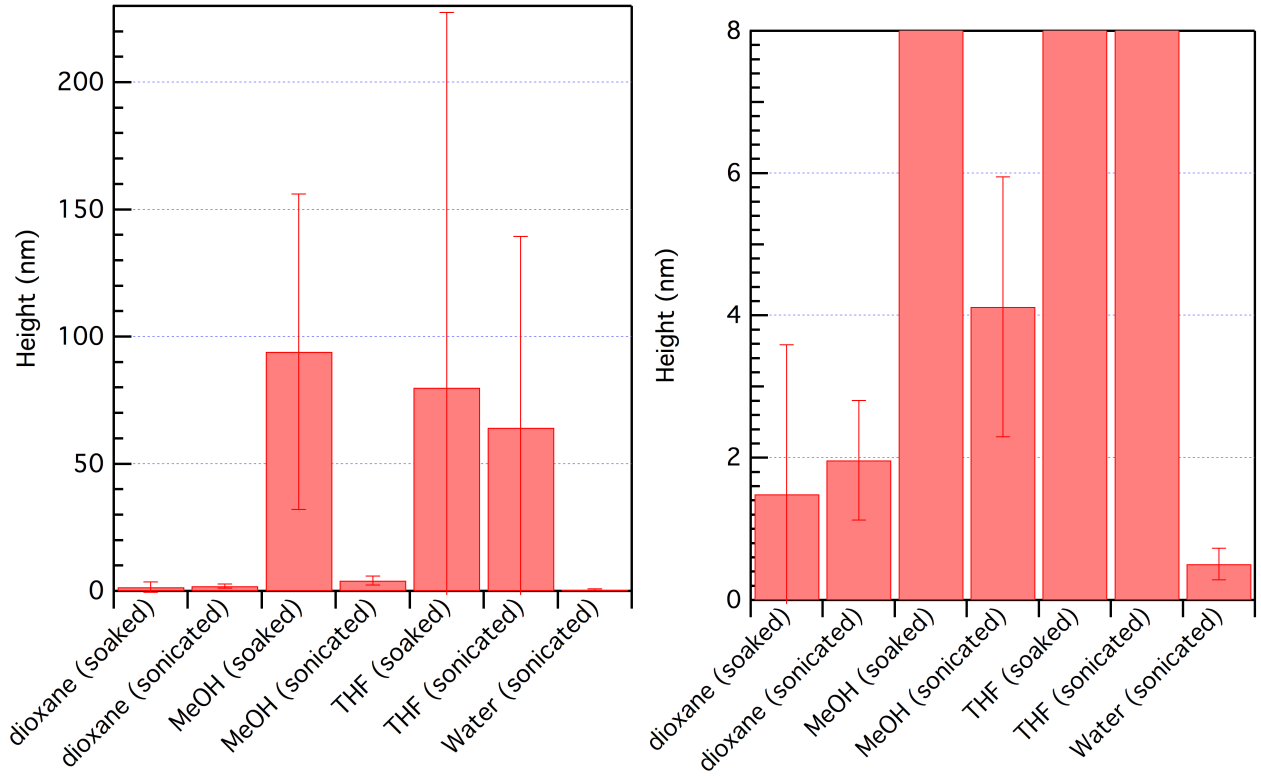

Figure A5.13 Perimeter Lengths of COF-43 samples determined by AFM. Identical data are plotted with different y-axis scales to show differences among both exfoliating and non-exfoliating solvents.

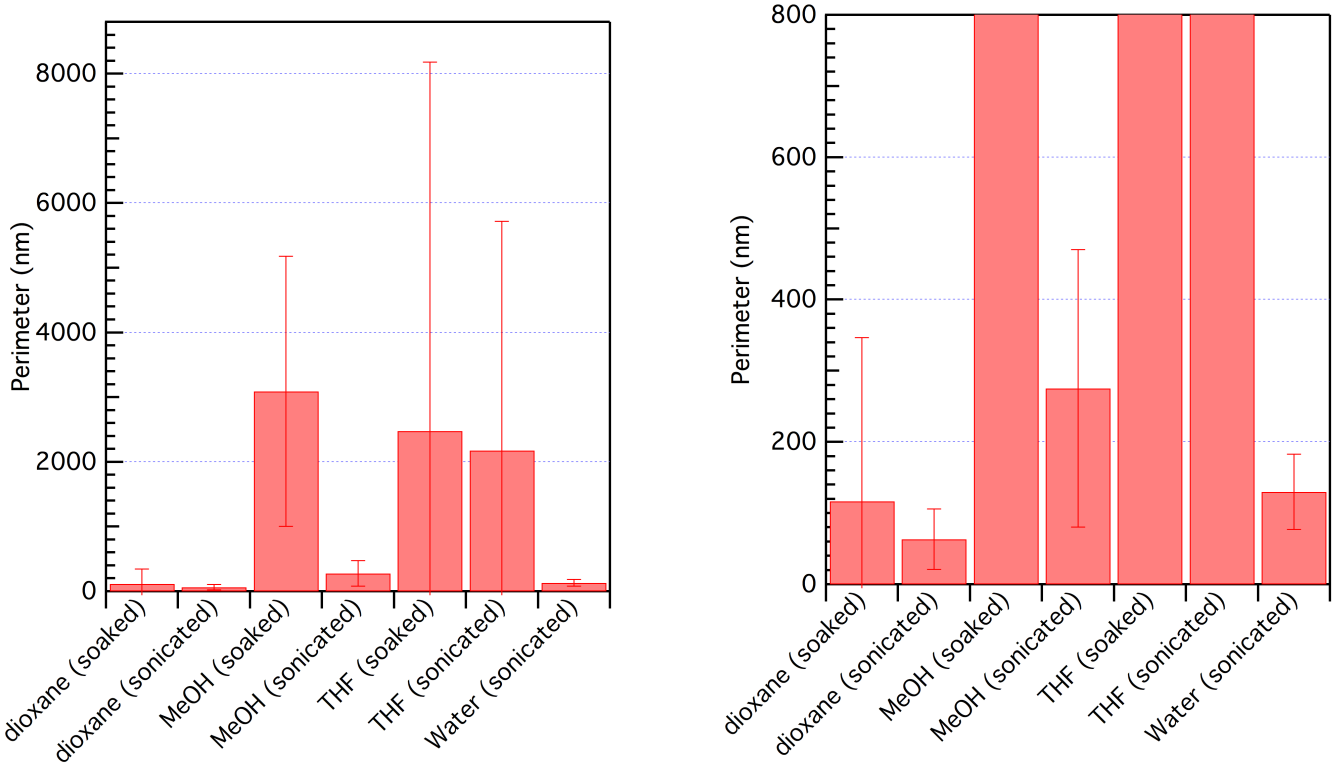

Figure A5.14 Areas of COF-43 sheets determined by AFM.

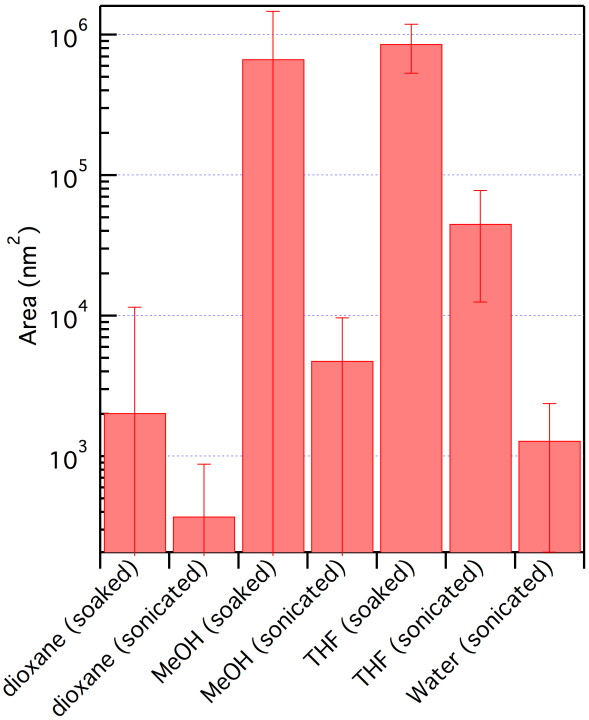

Figure A5.15 Aspect ratios of COF-43 determined by AFM.

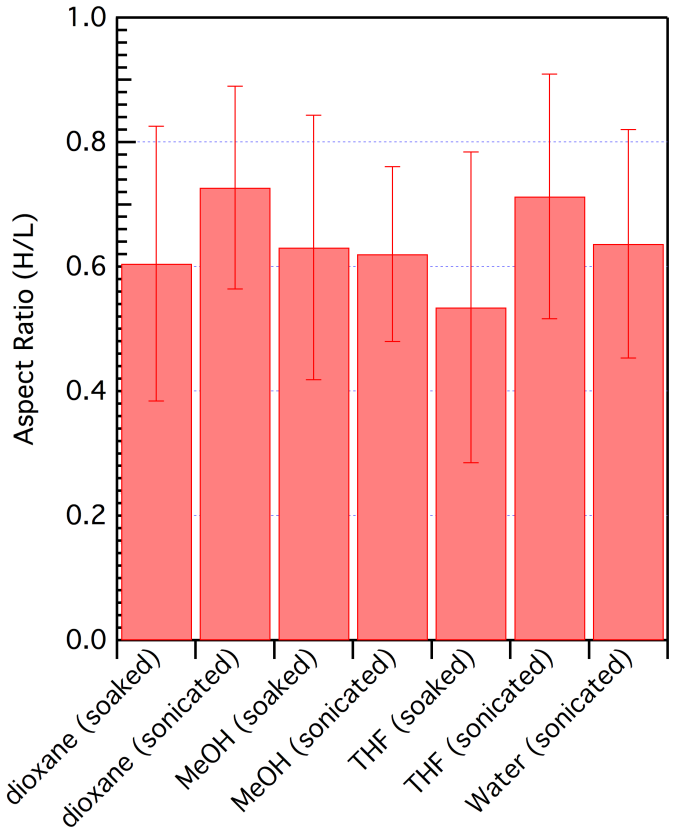

Table A5.1 Statistical analysis of structures obtained by AFM. Values reported are ± one standard deviation. Aspect ratios are reported as the width divided by the length.

	Average Height (nm)	Maximum Height (nm)	Perimeter (nm)	Area (nm^2)	Aspect Ratio (W/L)
Dioxane (soaked)	0.922 ± 0.804	1.49 ± 2.10	117 ± 230	2030 ± 9450	0.605 ± 0.221
Dioxane (sonicated)	1.32 ± 0.37	1.96 ± 0.84	63.4 ± 42.5	372 ± 504	0.727 ± 0.163
MeOH (soaked)	47.4 ± 35.3	94.0 ± 62.0	3090 ± 2090	670000 ± 792000	0.631 ± 0.212
MeOH (sonicated)	2.90 ± 1.23	4.12 ± 1.83	275 ± 195	4761 ± 4848	0.620 ± 0.141
THF (soaked)	37.8 ± 72.5	79.9 ± 148	2480 ± 5700	856000 ± 328000	0.535 ± 0.250
THF (sonicated)	38.3 ± 45.6	64.2 ± 75.1	2180 ± 3540	45000 ± 32500	0.713 ± 0.196
Water (sonicated)	0.334 ± 0.172	0.507 ± 0.222	130 ± 52	1286 ± 1079	0.637 ± 0.184

Figure A5.16 Atomic force micrograph of bare mica.

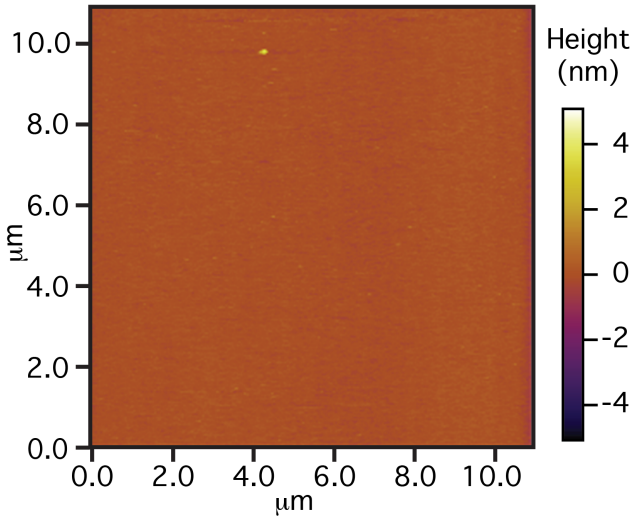

Figure A5.17 Atomic force micrograph of COF-43 dispersed in MeOH (sonicated) and drop cast onto mica.

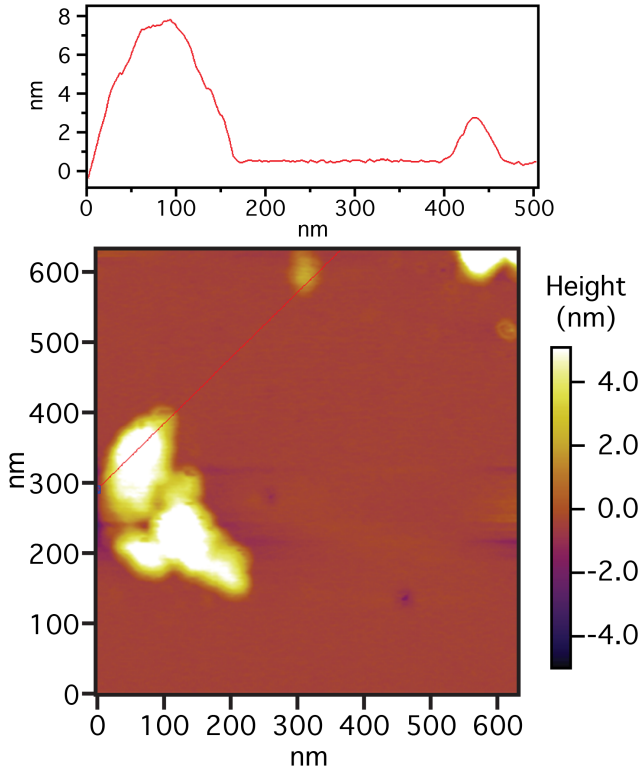

Figure A5.18 Atomic force micrograph of COF-43 exfoliation from dioxane (without sonication) reveals a small amount (<1% total structures) of larger COF-43 assemblies.

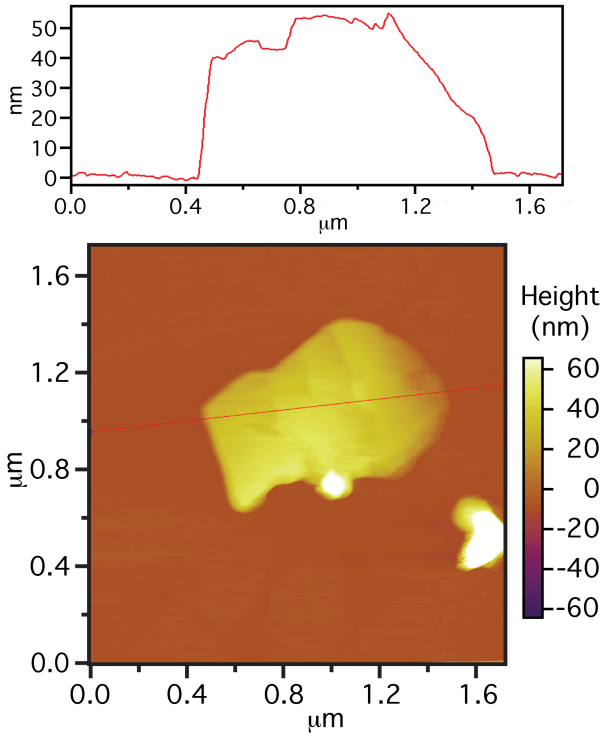

Figure A5.19 Atomic force micrographs of COF-43 exfoliated from dioxane (sonicated) showing high aspect ratio structures.

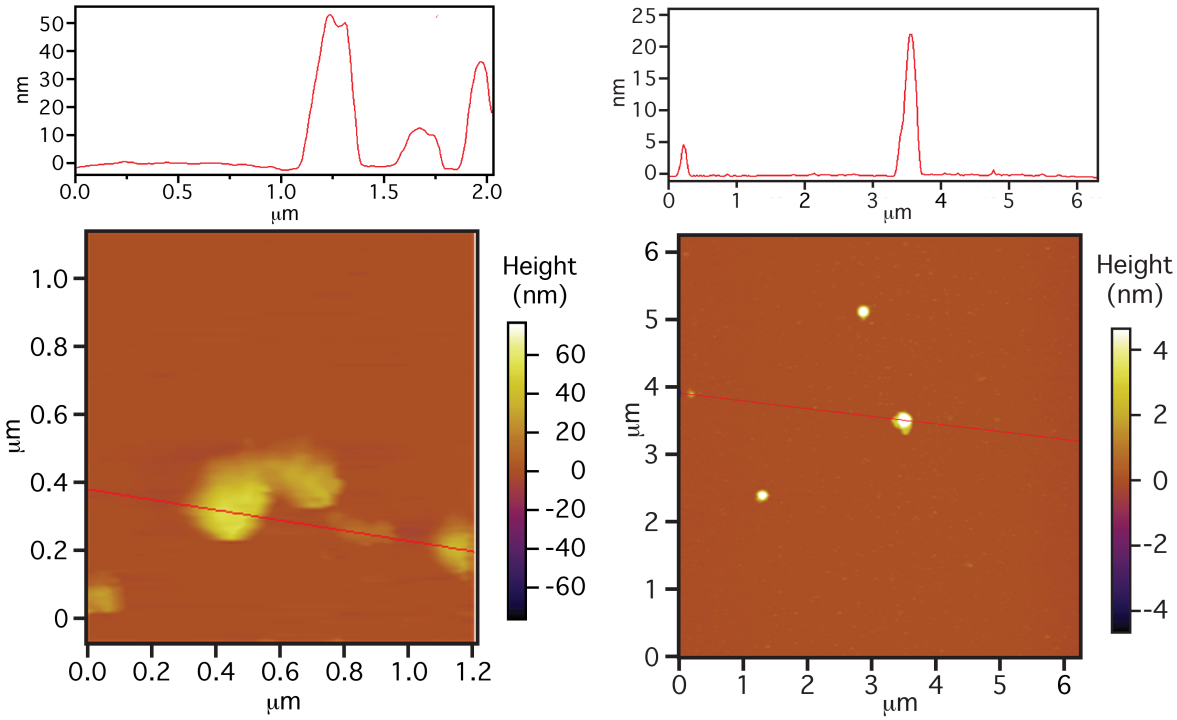

Figure A5.20 Atomic force micrographs of COF-43 exfoliated from H_2O (sonicated) showing high aspect ratio structures.

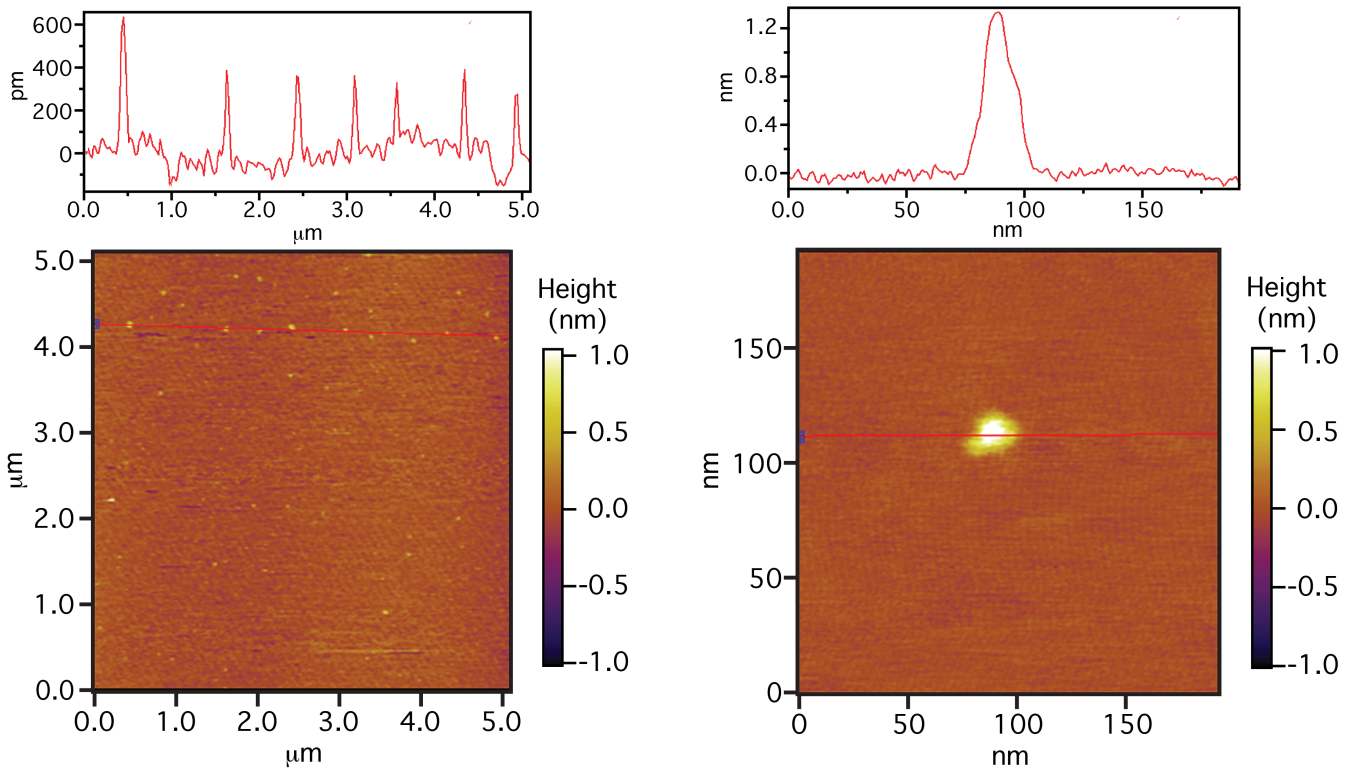

Figure A5.21 Atomic force micrograph of COF-43 drop cast from H_2O (sonicated) onto mica.

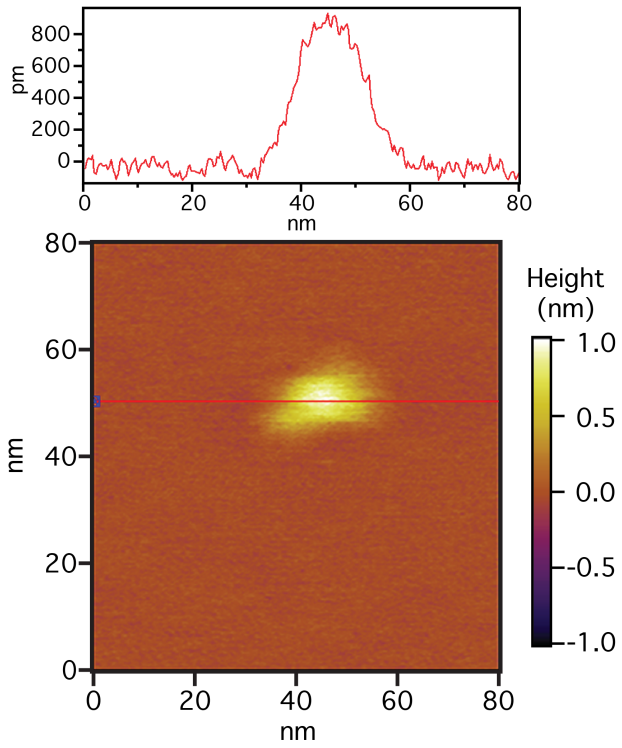

Figure A5.22 AFM micrograph of COF-43 drop cast from dioxane (sonicated) onto highly ordered pyrolytic graphite.

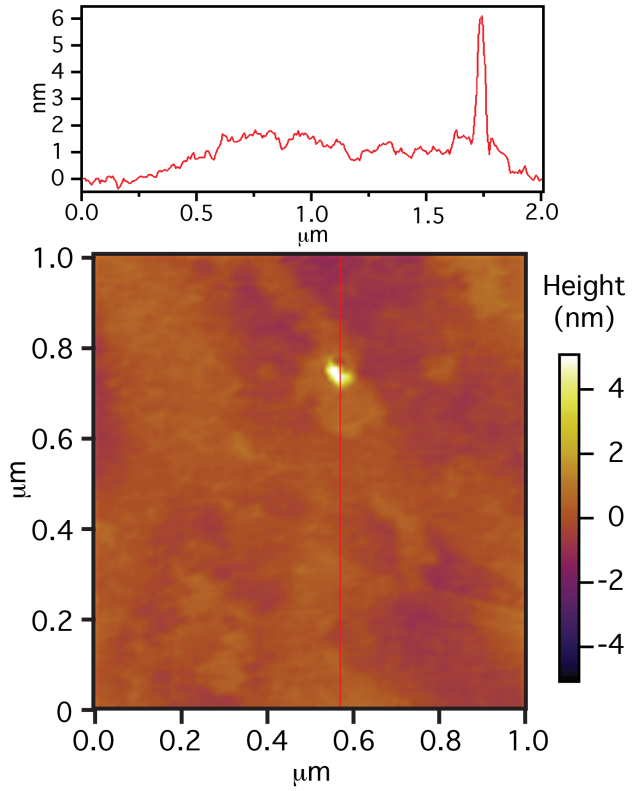

Figure A5.23 Transmission electron micrograph of COF-43 exfoliated in dioxane (without sonication) shows moiré fringes (lower right) indicative of an offset between the few-layer 2D polymers.

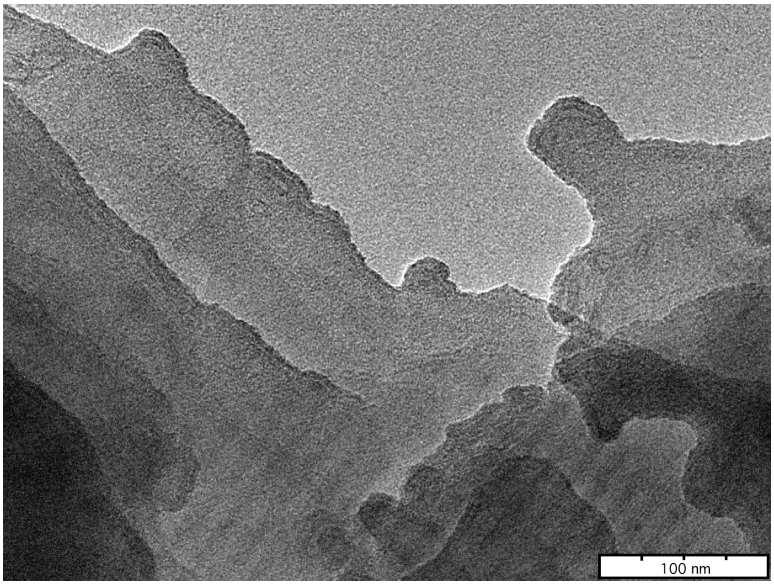

Figure A5.24 ^{1}H NMR spectrum (300 MHz, $CDCl_3$) of diethyl 2,5-diethoxyterephthalate.

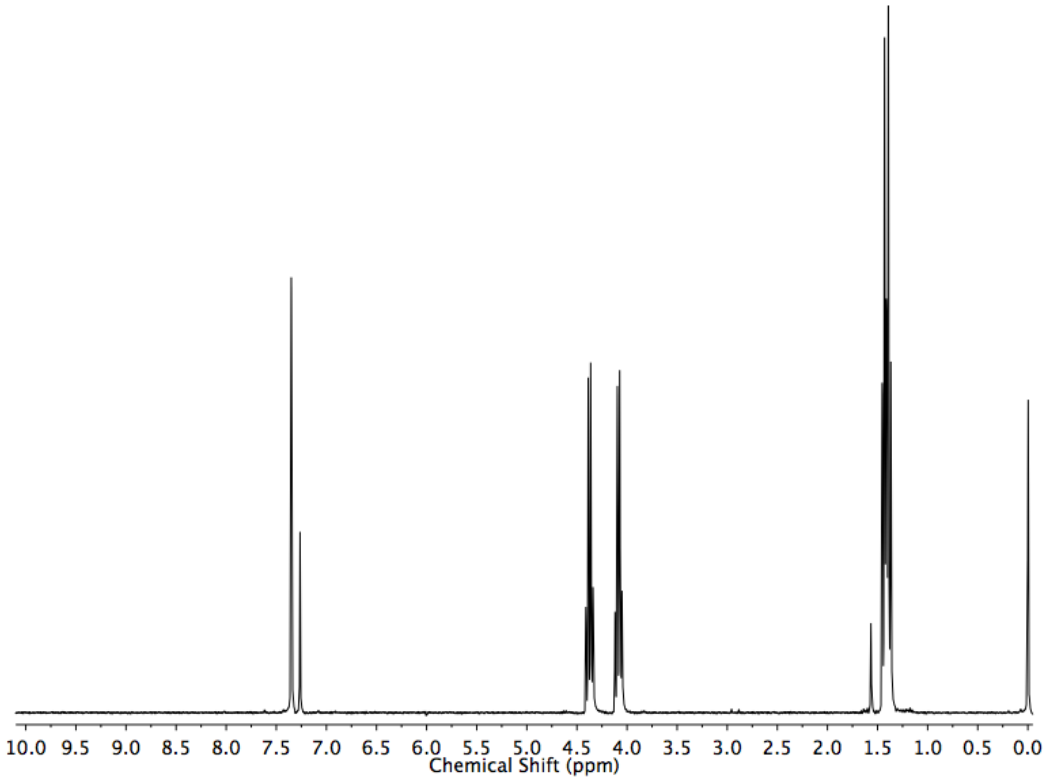

Figure A5.25 ^{1}H NMR spectrum (400 MHz, DMSO-d_6) of **1**.

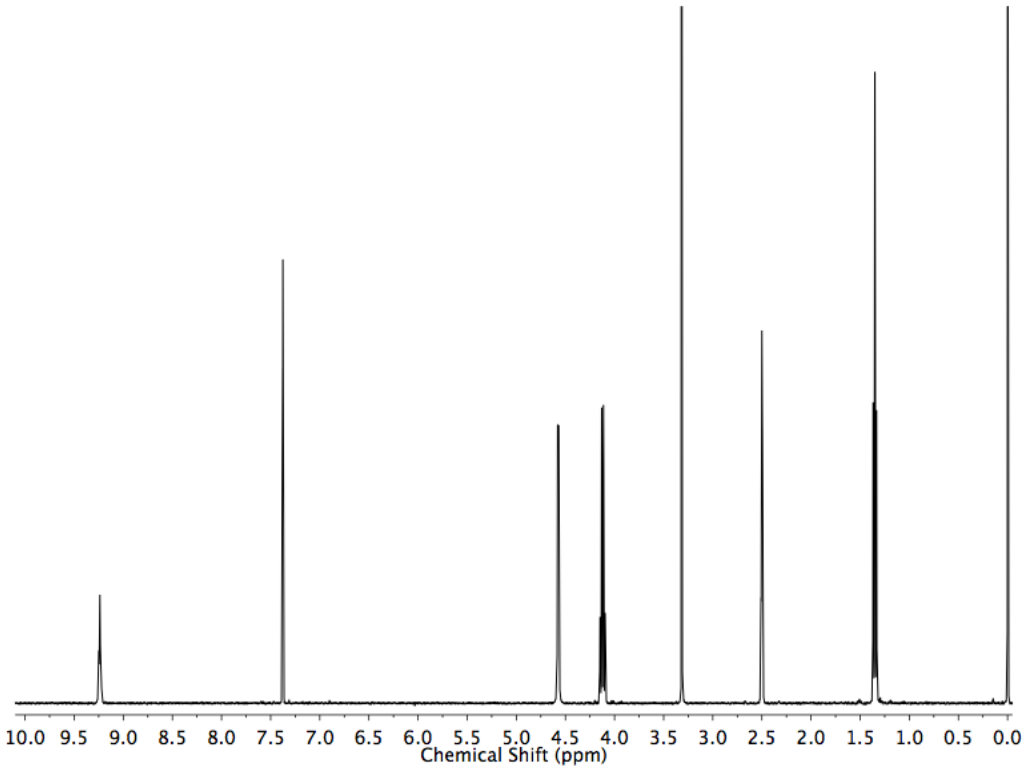

Figure A5.26 ^{1}H NMR spectrum (500 MHz, $CDCl_3$) of trigonal trialdehyde **2**.

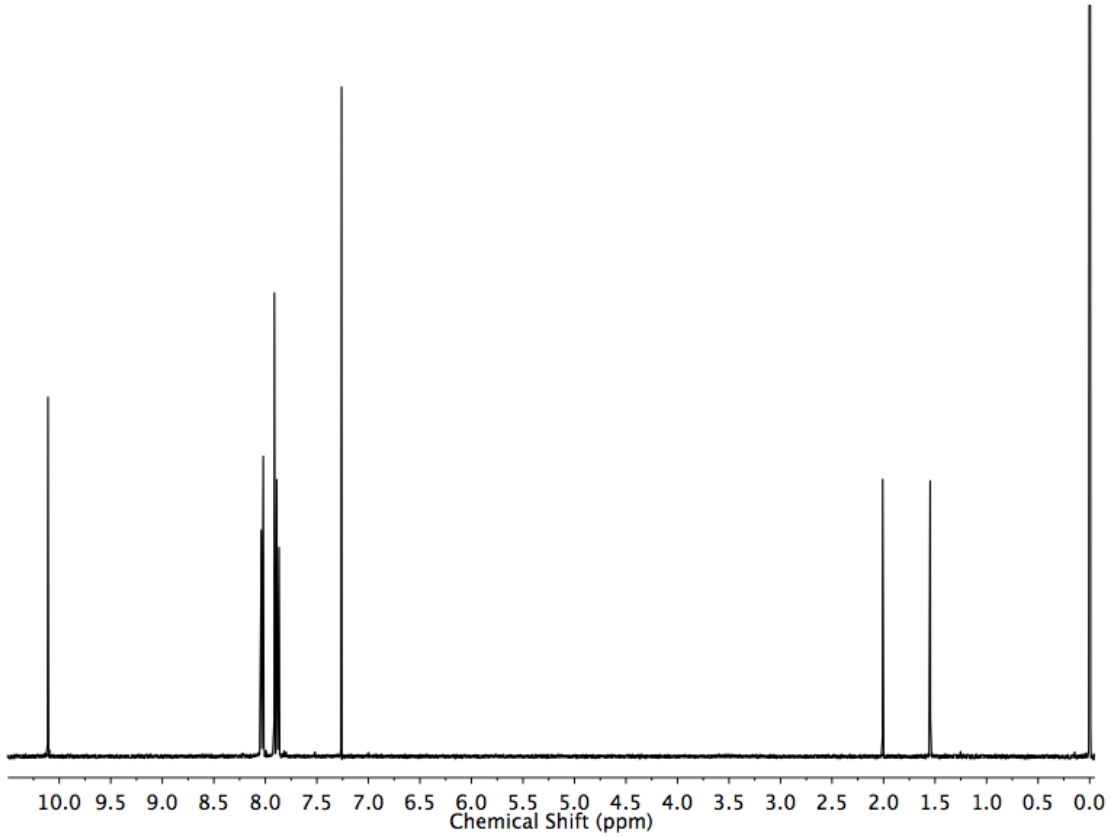

References
(1) Kim, H. S.; Kang, S. M.; Do, J. Y. *Macromol. Res.* **2008**, *16*, 360–366.
(2) Jiang, S.; Bacsa, J.; Wu, X.; Jones, J. T. A.; Dawson, R.; Trewin, A.; Adams, D. J.; Cooper, A. I. *Chem. Commun.* **2011**, *47*, 8919.
(3) Lotya, M.; Rakovich, A.; Donegan, J. F.; Coleman, J. N. *Nanotechnology* **2013**, *24*, 265703.
(4) Schmitz, K. S. *An introduction to dynamic light scattering by macromolecules*; Academic Press: Boston, 1990.

Chapter Six: Towards the Synthesis of Molecular Cages with Truncated Monomers

Molecular cages are discrete structures that possess a distinct interior microenvironment capable of protecting fragile pharmaceutical payloads[1] or stabilizing highly reactive molecules and transition states.[2–5] They are constructed from reversible linkages, such as boroxines,[6] boronate esters,[7–9] imines,[10,11] or metal-ligand bonds,[12–14] which enable error correction during synthesis to achieve highly symmetric products. Reactions with minimal or no reversibility have also been reported, but proceed with distinctly lower yields.[15] Deriving from a demonstrated reversibility in dynamic combinatorial chemistry[16–18] and utility for drug delivery,[19–21] acyl hydrazones are a particularly promising linkage for the synthesis of discrete molecular structures. However, there are currently no reported examples of hydrazone-linked cages. In addition to broadening our mechanistic understanding of cage formation, these are promising for use *in vivo*, as many other established linkers lack the integrity for long-term circulation.

The first examples of discrete macromolecules synthesized through reversible bond-forming reactions were reported by Fujita and coworkers,[22] who employed the 90° coordination geometry around Pd to synthesize molecular squares. Over the subsequent two decades, the concept of combining predictable bond angles with geometric intuition furnished a wide range of two-dimensional (2D) macrocycles and three-dimensional (3D) cages. Stang and coworkers have named this the directional bonding approach[13] because the geometry of constituent monomers can be used to rationally design and predict the structure of the resulting cage (Figure 6.1). By taking advantage of the wide range of geometries and degree of flexibility available to metal-coordination complexes,[14] a broad range of discrete 3D structures can be generated. In contrast, the geometries reliably accessible by organic molecules are more limited. While some systems circumvent this challenge by employing bowl-shaped monomers, such as resorcinarenes[9] or

cyclotricatechylenes,[7,10] the inherent difficulties synthesizing functional variants of such compounds limits the scope of accessible functionality on the cage exterior. Recent work by Cooper and coworkers[23–26] on a family of imine-linked structures highlights the importance of

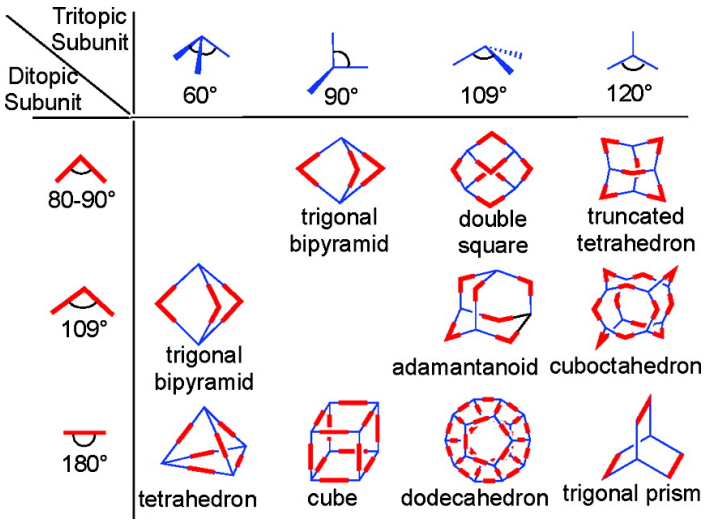

Figure 6.1 The directional bonding approach enables rational design of molecular cages. The original figure can be found in Reference 13.

general approaches to their synthesis. When new monomers with a bonding geometry identical to an established building block are included in the condensation, they reliably form new functional cages.[26] We hypothesize that this powerful strategy will generalize the predictable synthesis of

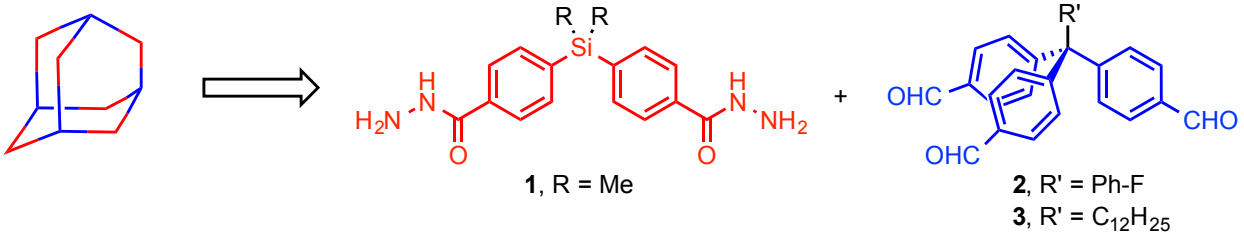

Figure 6.2 Retrosynthetic scheme of hydrazone-linked cage.

cages linked by other reversible-covalent bonds. We initially targeted a hydrazone-linked adamantoid cage, which is derived from the cocondensation of six bishydrazide (red) and four trialdehyde (blue) monomers (Figure 6.2). In addition to its large internal volume, this cage is compatible with many external functionalization strategies to tune its solubility and add targeting ligands.

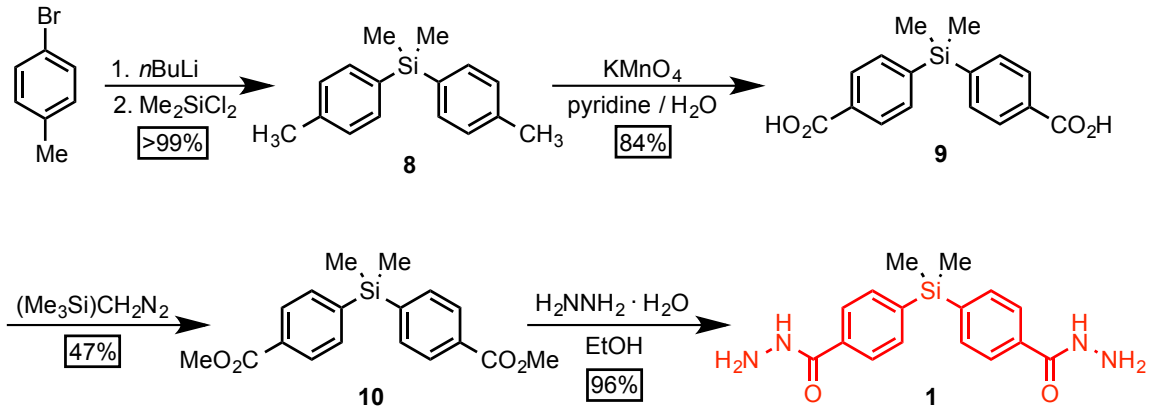

Figure 6.3 Synthetic route to bishydrazide **1**.

To synthesize bishydrazide **1** (Figure 6.3), bromotoluene was lithiated with *n*-BuLi and quenched with dichlorodimetylsilane (**8**). In addition to providing a rapid route to generate a precursor with the correct symmetry, the presence of a Si in the structure provides a convenient ^{29}Si NMR handle to study cage formation. This compound was oxidized with $KMnO_4$ under basic conditions to afford bis(carboxylic acid) **9** that was subsequently esterified with (trimethylsilyl)diazomethane (**10**). Methyl esters are conveniently transformed to hydrazides under reflux in the presence of hydrazine. Employing this methodology for the final step

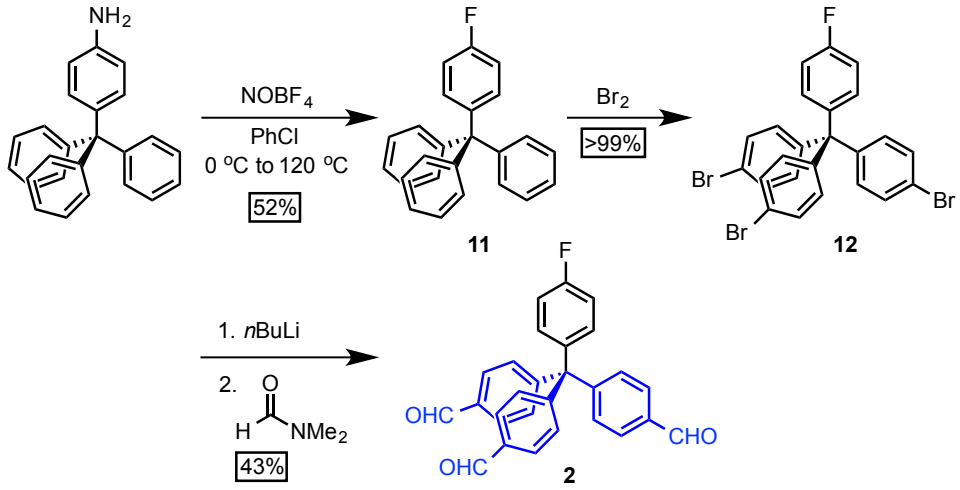

Figure 6.4 Synthetic route to trialdehyde **2**.

afforded **1** in acceptable yield. A complimentary trifuntional building block **2** (Figure 6.4) was fluorinated under Balz-Schiemann conditions. The resulting product was brominated neat Br_2,

which reacts with the remaining rings exclusively in the para positions. Tribromide **12** was lithiated with *n*-BuLi and quenched with dimethylformamide to yield **2**. This compound also bears a convenient NMR-active nucleus (^{19}F), which provides an orthogonal handle to study cage formation.

Hydrazone exchange occurs most rapidly under acidic conditions,[16,27] and we screened a range of acids and reaction conditions for **1** and **2**. A permanently insoluble precipitate formed in many cases, which are most likely polymeric hydrazone-linked species that become insoluble more rapidly than they can equilibrate into discrete species. In contrast, reactions performed in DMSO / dioxane (1:2 *v/v*) solutions in the presence of CH_3CO_2H provided transparent solutions that warranted further study. Variations of these conditions sometimes formed precipitates, but even these products redissolved after extended reaction times (11 d). Analysis of these reaction mixtures with matrix-assisted laser desorption/ionization time of flight (MALDI-TOF) mass spectrometry indicated an ion at *m/z* = 1745.09, which corresponds to the Na^+ adduct of a cage

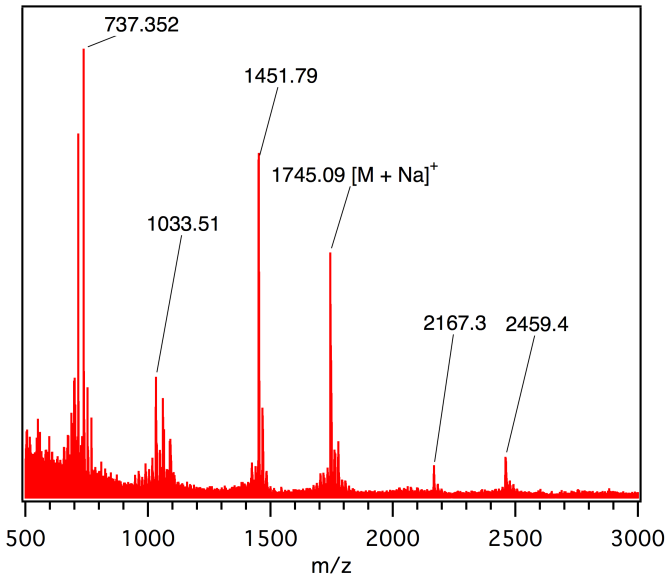

Figure 6.5 MALDI-TOF-MS indicates the formation of a 2:3 hydrazone-linked cage $[M+Na]^+$ among other condensation products from the reaction of **1** with **2**.

containing two trialdehydes and three bishydrazides (Figure 6.5). The 1 amu spacing of this peak's isotope pattern indicates that this species is monocationic, rather than a larger molecule bearing multiple charges, and is in good agreement with simulation (Figure 6.6). Additionally,

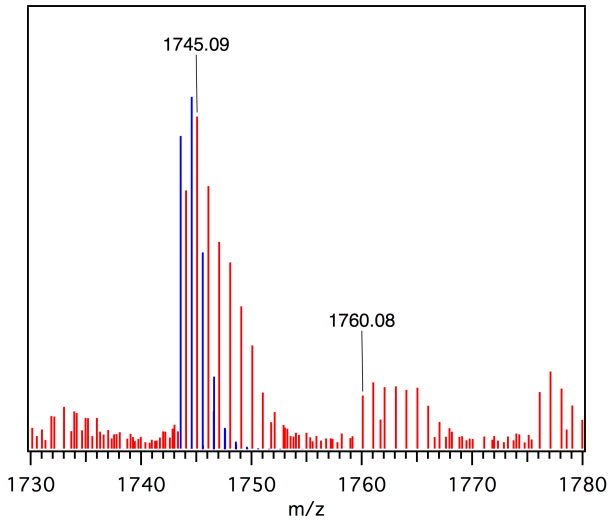

Figure 6.6 The peak corresponding to $[M+Na]^+$ of the trigonal bipyramidal cage formed from **1** and **2** shows a spacing of $m/z = 1$ (red), indicative of a monocationic species, and has reasonable agreement with the calculated distribution (blue).

no peaks corresponding to the larger adamantoid cage, which is comprised of four trialdehydes and six bishydrazides, were observed. These findings suggest that the condensation produces a trigonal bipyramidal (2:3) structure (Figure 6.7), which is entropically favored but not predicted by the directional bonding approach. This discrepancy might arise from the inherent flexibility of the monomers and/or rotation of the acyl hydrazone linkages, which are not conjugated to their adjacent arenes.

During sample preparation, it was observed that solvent removal or switching resulted in irreversible precipitation of the condensation products, which hindered characterization by other solution-based methods. This inconvenience necessitated studies in DMSO-d_6 / dioxane-d_8, in which the condensation products remained soluble. Under these conditions, the condensation

reaches a steady-state equilibrium after 4 d, as determined by ^{1}H NMR (Figure 6.8). New resonances at 11.72 and 8.45 ppm are consistent with hydrazone formation, while the aldehyde

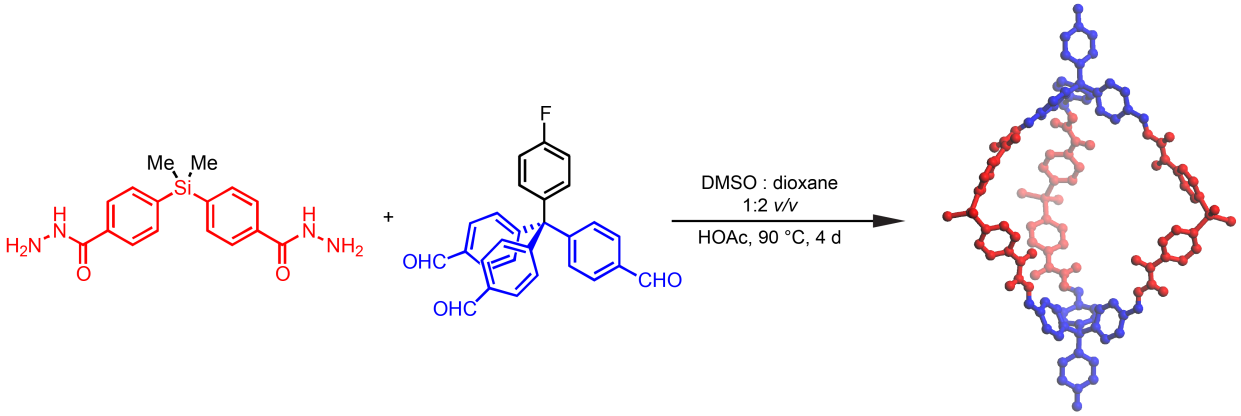

Figure 6.7 Condensation of bishydrazide **1** and trialdehyde **2** yielded trigonal bipyramidal (2:3) hydrazone-linked cages, rather than the expected adamantoid (4:6) structure.

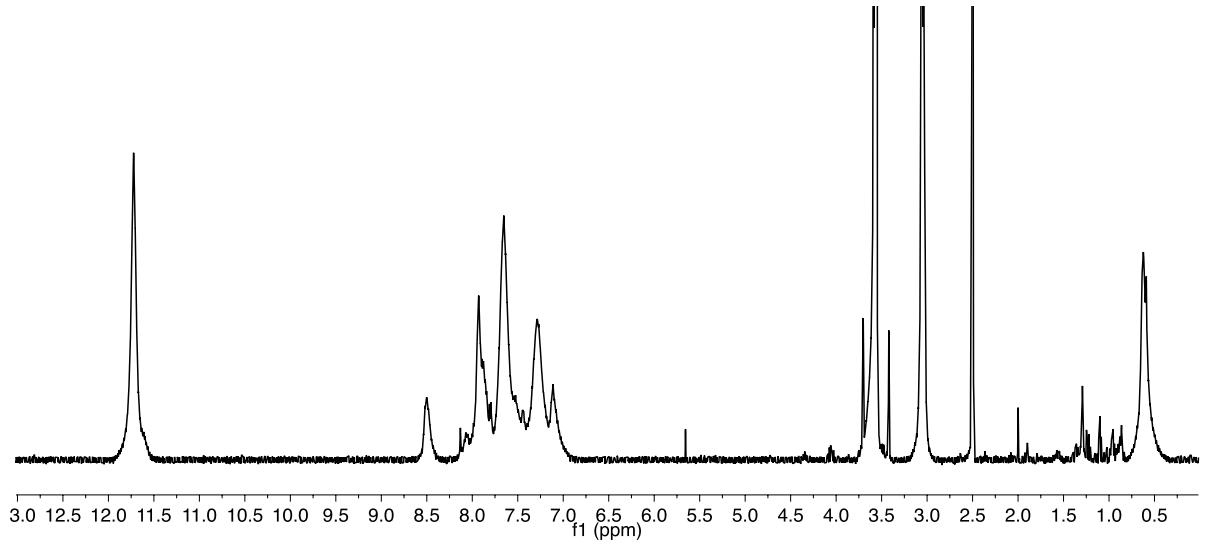

Figure 6.8 ^{1}H NMR spectrum of the condensation between **1** and **2** (400 MHz, DMSO-d_6 / dioxane-d_8, 1:2 *v/v*).

resonance at 9.99 ppm disappears over the course of the condensation. These observations indicate full conversion to a soluble, hydrazone-linked product. Simultaneous broadening of these peaks also suggests that additional condensation products are formed, and that these species are poorly soluble in this solvent system. To gain further insight into the relative sizes of

these dissolved species, we employed diffusion NMR on a sample of fully equilibrated, hydrazone-linked material. This technique provides each species' hydrodynamic diameter (d_H), derived from its diffusion coefficient (D) using the Stokes-Einstein equation:

$$D = \frac{k_B T}{3\pi\eta d_H}$$

where η is the solvent viscosity and T is temperature. In a diffusion NMR experiment, a pulse gradient (G_z) is applied along the length of the tube, which coils the magnetization vectors into a helix along the z-axis. After a specified time, the inverse gradient is applied, uncoiling the vectors, and a standard 1D ^{1}H NMR spectrum is subsequently acquired. Smaller species diffuse

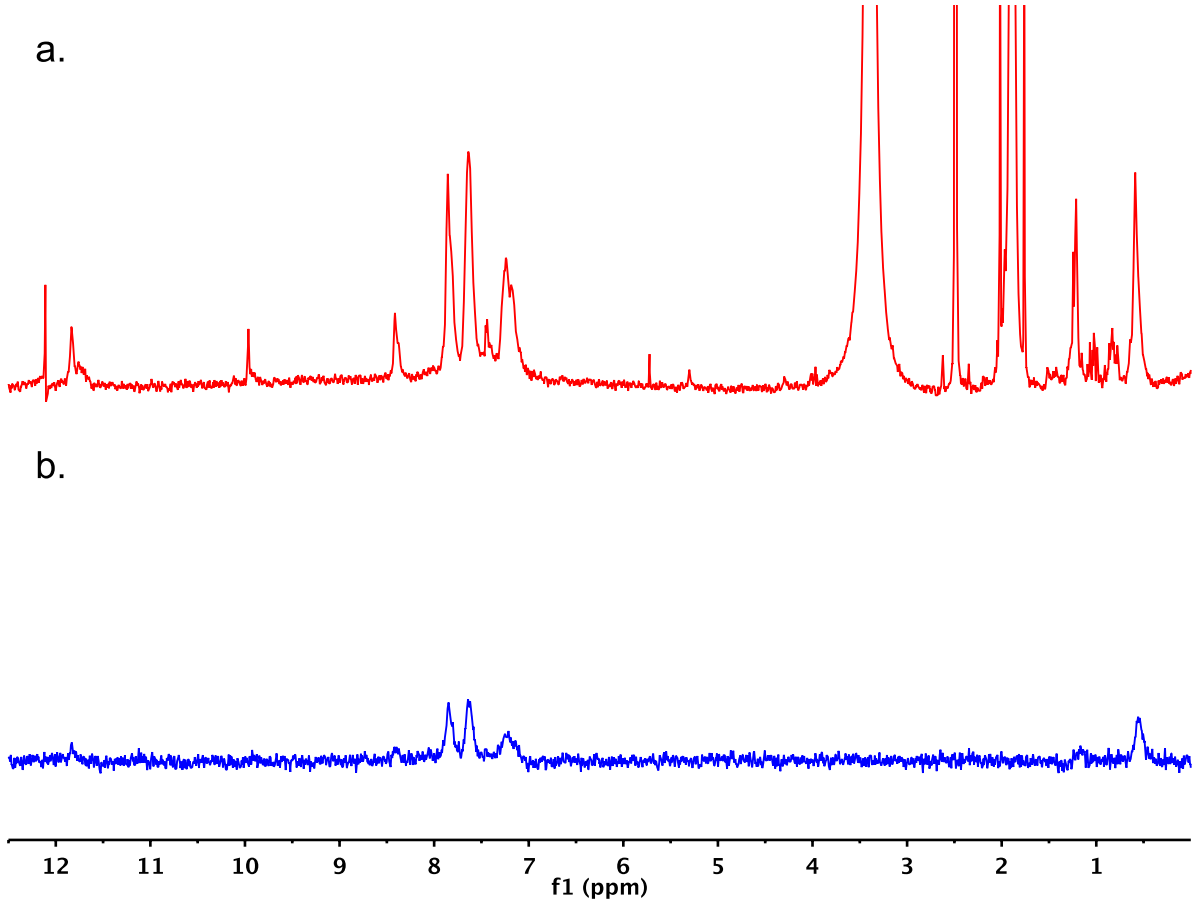

Figure 6.9 First (a, red) and last (b, blue) spectra in a diffusion NMR experiment (500 MHz, DMSO-d_6 / dioxane-d_8, 1:2 *v/v*). With increasing gradient strength, the resonances of small molecular species become weaker until they are undetectable.

further and loose their relative orientation faster than larger ones, causing their signals to disappear more rapidly with increased gradient strength. In other words, with increasing G_z, the resonances of smaller species disappear. This experiment is related to DOSY NMR, except that a second axis correlating diffusion constants to chemical shift isn't generated. Figure 6.9 shows the first (weakest gradient) and last (strongest gradient) ^{1}H NMR spectra acquired in a diffusion NMR experiment containing the hydrazone-linked cage. By the end of the experiment, only resonances corresponding to the largest hydrazone-linked species remain. We note that this sample still shows uncondensed aldehyde at 9.99 ppm, which may indicate some batch to batch variability in the condensations, but the resonance decreases rapidly with increasing G_z and is likely from some remaining uncondensed monomers or small oligomers. Diffusion constants were approximated by comparing the attenuation of each resonance to that of the DMSO signal as a function of gradient strength. This comparison (Figure 6.10) reveals a very rapid decrease of

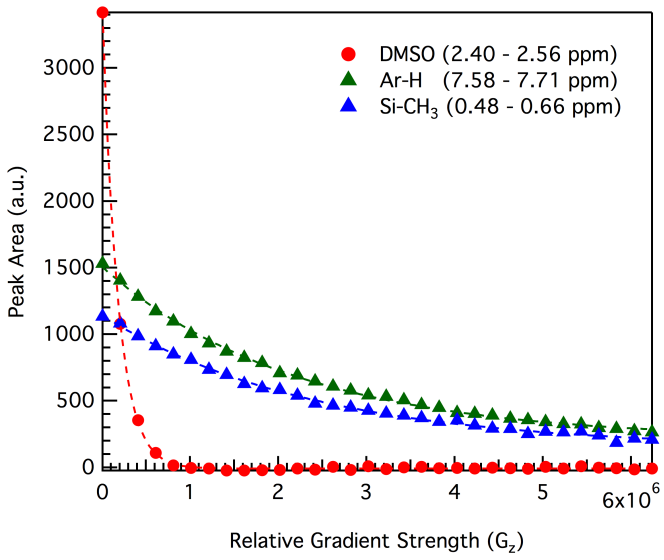

Figure 6.10 Comparisons of the residual peak area resonances corresponding to DMSO (red), Ar-H of the cage (green), and Si-CH_3 of the cage (blue) as a function of gradient strength (G_z). The resonances associated with the cage decrease much less rapidly than those of DMSO, indicating an increased hydrodynamic radius.

the DMSO resonance (2.49 ppm) relative to those associated with the Ar-H cage fragment coming from **2** (7.71 – 7.58 ppm) and the Si-CH_3 fragment from **1** (0.66 – 0.48 ppm). The relationship between peak integration relative to magnetic field strength in this experiment obeys the following expression:

$$I_G = I_{G=0}\exp\left(-(\gamma\delta G)^2 D\left(\Delta - \frac{\delta}{3}\right)\right)$$

where δ and Δ are delay times in the pulse sequence and γ is the gyromagnetic ratio. By linearizing these curves (Figure 6.11), the slopes from the cage and DMSO resonances along

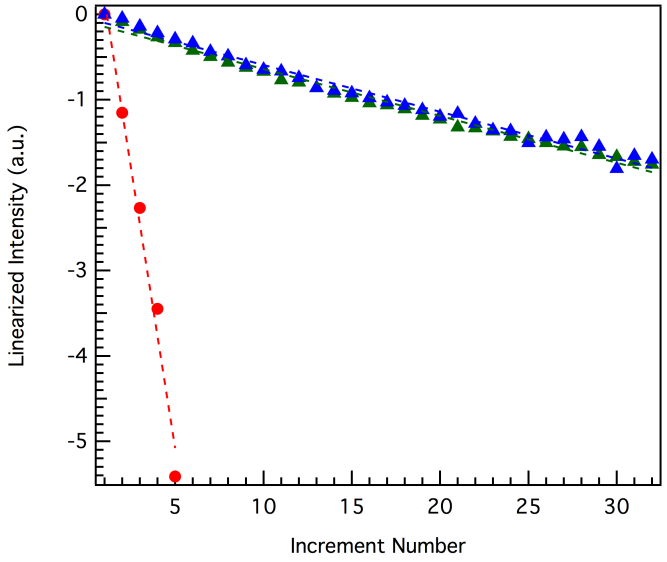

Figure 6.11 Plotting the natural log of the residual peak area against increment number provides linearized data for calculating D_{cage}.

with knowledge of the self-diffusion of DMSO (in DMSO)[28] were used to approximate D_{cage} and in turn, d_H. Linear fits of the integrations from **1** and **2** have identical slopes, which provide the same result. Moreover, these lines fit well (**1**: $r^2 = 0.991$, **2**: $r^2 = 0.993$) to the experimental data, which suggests a relatively narrow size distribution of products. If there were independent species of different sizes, one would expect to see significant breaks in the linearity of Figure 6.11. The diameter of the cage was approximated to 2.6 nm. Molecular modeling shows the Si-Si

bond distance across the cage to be 2.1 nm and F-F distance in the orthogonal direction to be 3.0 nm. Since a d_H would be a weighted average of the two dimensions plus a solvation shell, the value measured by diffusion NMR is reasonable. Along with analysis by MALDI-TOF, this evidence preliminarily supports the formation of a trigonal bipyramidal cage.

Because of the problems isolating and redissolving the condensation products bearing aryl fluorides, we next investigated second-generation trialdehyde **3** bearing a dodecyl chain. For its synthesis (Figure 6.12), triphenylmethane was alkylated with bromododecane at 10 °C and subsequently brominated with Br_2/Fe to generate tribrominated product **13**. The aryl bromides

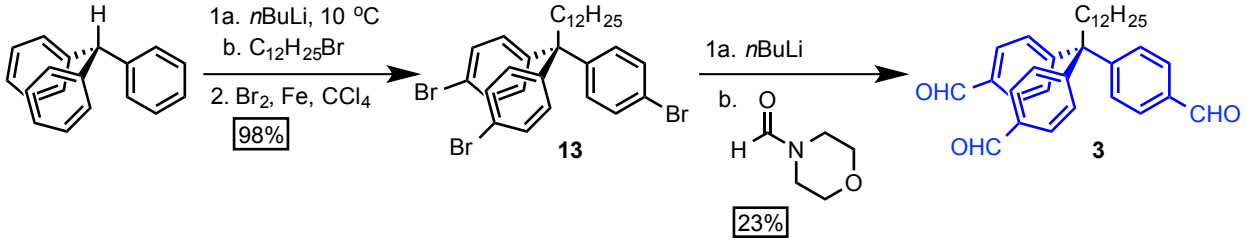

Figure 6.12 Synthesis of second generation tris(aldehyde) **3**.

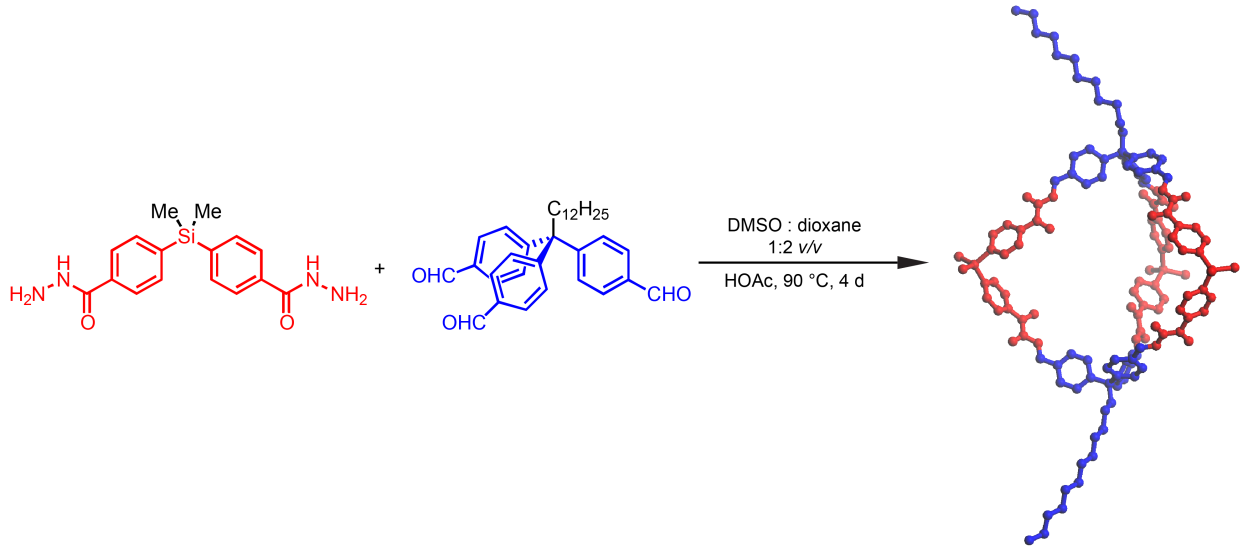

Figure 6.13 The dodecyl-functionalized cage was formed under conditions identical to those employed with **2**.

were then lithiated with *n*-BuLi and quenched with 4-formylmorpholine, forming trialdehyde **3** in moderate yields. Cocondensing **3** with **1** under identical conditions to those described above

(DMSO / dioxane 1:2 *v/v*) also yielded hydrazone-linked, soluble polymers (Figure 6.13). Analysis of the reaction mixture by MALDI-TOF indicated an ion at *m/z* = 1894.13, which

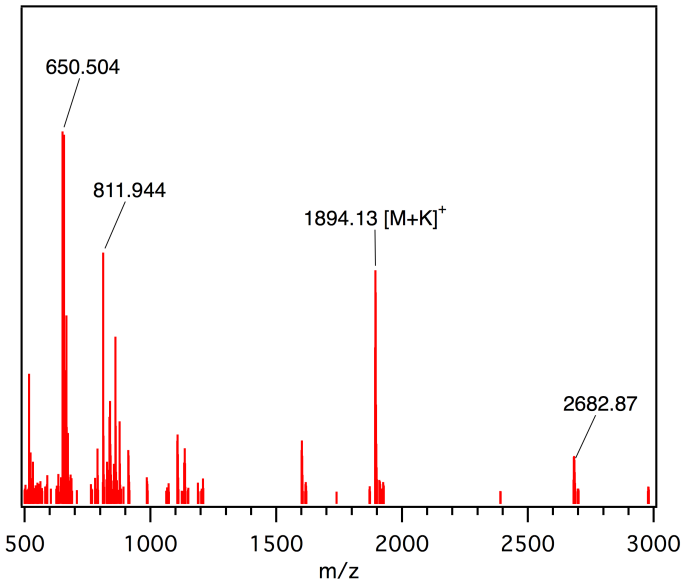

Figure 6.14 MALDI-TOF-MS of the condensation products from **1** and **3** also indicates the formation of a 2:3 hydrazone-linked cage $[M+K]^+$ among other molecular species.

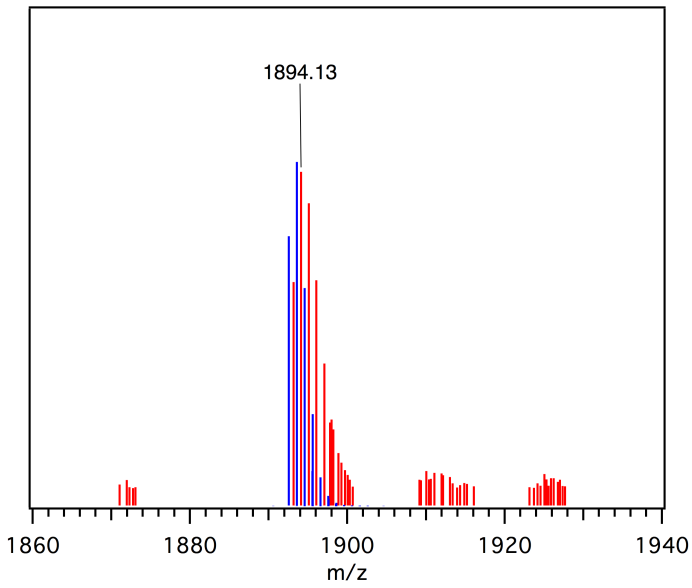

Figure 6.15 The peak corresponding to $[M+K]^+$ of the trigonal bipyramidal cage formed from **1** and **3** shows a spacing of *m/z* = 1 (red), indicative of a monocationic species, and has reasonable agreement with the calculated distribution (blue).

corresponds to the K^+ adduct of a cage containing two trialdehydes and three bishydrazides (Figure 6.14). This peak's isotope pattern also shows a 1 amu spacing, indicating a monocationic species and is in reasonable agreement with simulation (Figure 6.15). These results suggest that cages formed from **3** are also trigonal bipyramidal, similar to our observations with **2**.

To better understand the size distribution of these soluble condensation products, equilibrated mixtures of the dodecyl-functionalized cages were analyzed using dynamic light scattering (DLS). The average size from the number distribution was 5.17 ± 0.46 nm with PDI = 0.243 ± 0.003 (Figure 6.16). The end-to-end distance of the dodecyl chains was modeled to be

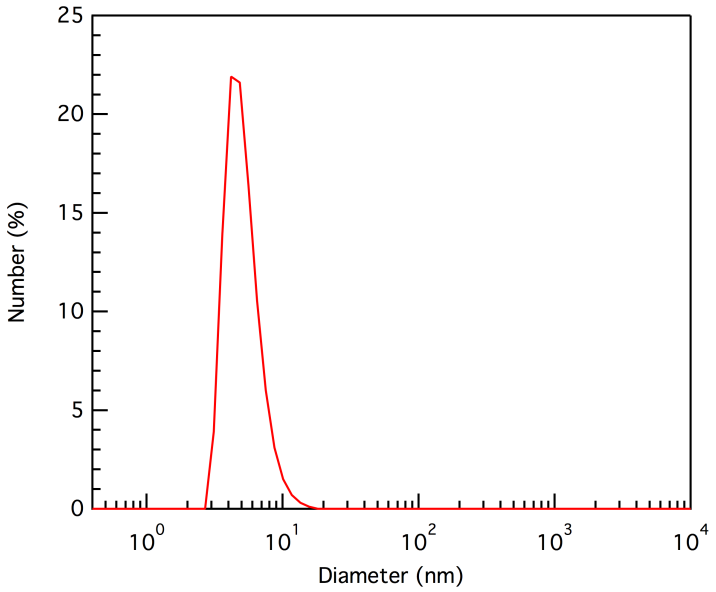

Figure 6.16 Dynamic light scattering (DLS) of dodecyl-functionalized cages reveals a monomodal size distribution around 5.17 ± 0.46 nm (PDI = 0.243 ± 0.003).

4.3 nm, thus d_H determined by DLS on this system is expected to be larger than the d_H of the first generation system (2.6 nm). Even though PDIs close to 0 are expected for a sample containing a single macromolecular product, in this system size differences among the species are below the detection limit of the instrument and provide a monomodal size distribution.

To evaluate the size change of the soluble products, the condensation was also monitored *in situ* by DLS (Figure 6.17). As the reaction proceeds, the average size increases until leveling

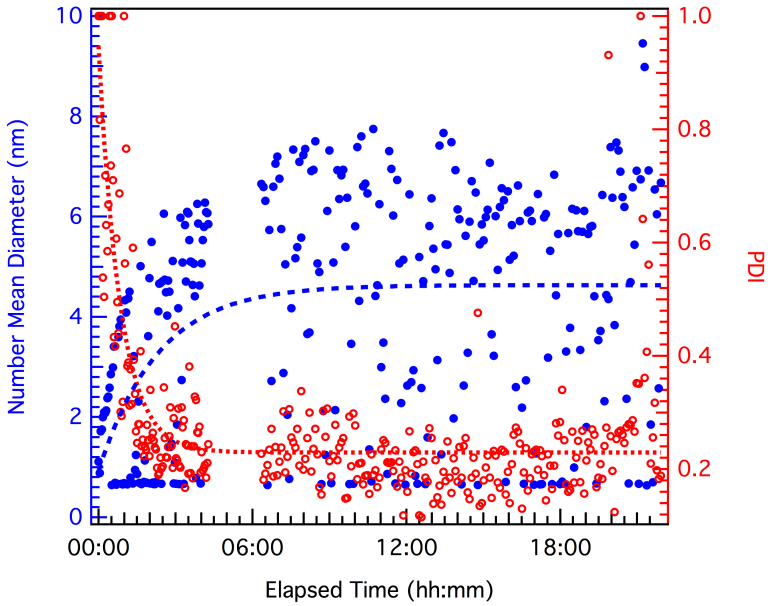

Figure 6.17 Cage formation was observed by DLS. Both the average diameter and PDI asymptote, which suggests the reaction is reaching a thermodynamic minimum.

off at around 5.5 nm. Conversely, the PDI of the solution starts at 1 and reaches a value close to 0.2 by the end of the experiment. This behavior is expected from a polymeric mixture that is self-correcting to form a discrete structure, as a rapid increase in size (and PDI) followed by precipitation would occur without a thermodynamic sync.[29] The significant scatter in the kinetic data is likely due to thermal fluctuations in the cuvette during the measurement. A possible solution to this issue would be to run the scans at timed intervals with stirring in between (but not during) the measurements. While DLS measurements on the dodecyl-functionalized species reveal relatively small condensation products that approach a constant size, we were still unable to isolate or crystallize pure products. Notably, dried cages were even insoluble in the parent reaction solvent. We propose two potential explanations: first, the side chains might not be sufficiently large to solubilize the cages, leading to irreversible aggregation. Alternatively, the evacuated cage structure might prove mechanically unstable to solvent evacuation.

We are currently investigating a third generation aldehyde, which stands to further improve cage solubility and is capable of accommodating a broad range of side chains through thiol-yne coupling reactions (Figure 6.18). In contrast to the synthesis of **2** and **3**, which have

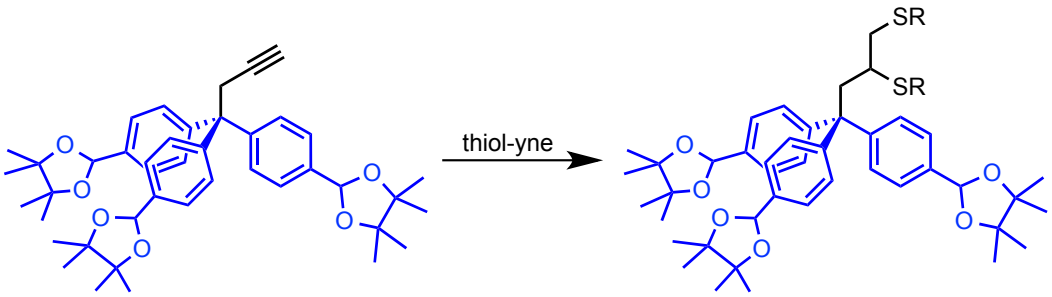

Figure 6.18 Targeted third generation monomer bearing a terminal alkyne for subsequent derivitization with thiol-yne coupling reactions.

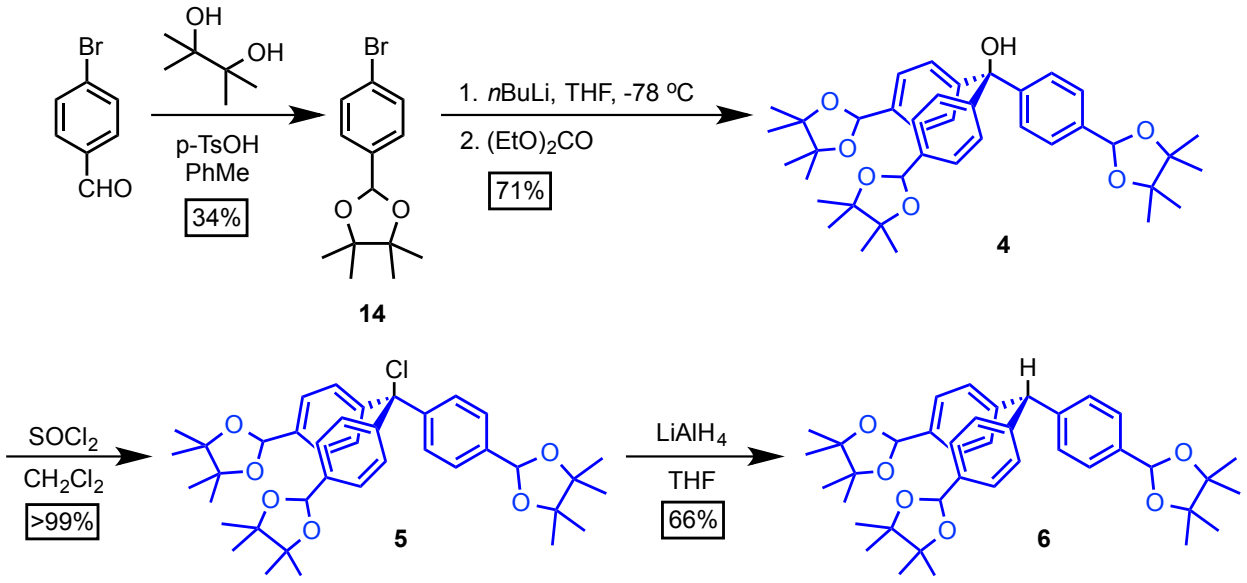

Figure 6.19 Third generation monomer synthesis.

limited functional group tolerance, this approach installs the protected aldehydes from the first step (Figure 6.19). First, 4-bromobenzaldehyde was condensed with pinacol to afford its acetal protected derivative (**14**). This species was then lithiated with *n*-BuLi and quenched with diethylcarbonate to generate trityl alcohol **4**, which could be transformed into trityl chloride **6** upon exposure to thionyl chloride under anhydrous conditions. Additionally, **5** could also be

reduced in the presence of $LiAlH_4$ to form triarylmethane **6**. Attempts to form a functionalized derivatives of the triacetal using **4**, **5**, or **6** are in progress. The possibility of cage collapse might be addressed by the addition of a molecular template. Small molecules chosen to fit within the cage interior would direct its condensation and upon evacuation or crystallization, stabilize its structure. Encapsulated guests also show significant changes in their ^1H NMR chemical shifts, helping establish a caged structure. Additionally, a judicious choice of a template might facilitate formation of the adamantoid (4:6) cage.

Through this work, we found preliminary evidence that the cocondensation of a trialdehyde and bishydrazide results in the formation of a trigonal bipyramidal (2:3) hydrazone-linked cage. The presence of exclusively monocationic 2:3 species by MALDI-TOF supports this assignment. Additionally, diffusion NMR and DLS studies indicated hydrazone-linked macromolecular species with a low size dispersity. Attempts to isolate these structures resulted in irreversible precipitation, hindering further characterization. Future work to isolate these species should focus on synthesizing monomers with improved solubility and identifying templates to promote cage stability. As of this writing, no hydrazone-linked cages have been reported in the literature, underscoring the importance of these studies to the field.

References

(1) M. Mastalerz, *Angew. Chem. Int. Ed.* **2010**, *49*, 5042.

(2) M. Yoshizawa, *Science* **2006**, *312*, 251.

(3) M. D. Pluth, R. G. Bergman, K. N. Raymond, *Science* **2007**, *316*, 85.

(4) P. Mal, B. Breiner, K. Rissanen, J. R. Nitschke, *Science* **2009**, *324*, 1697.

(5) T. -C. Lee, E. Kalenius, A. I. Lazar, K. I. Assaf, N. Kuhnert, C. H. Grün, J. Jänis, O. A. Scherman, W. M. Nau, *Nat. Chem.* **2013**, *5*, 376.

(6) K. Severin, *Dalton Trans.* **2009**, 5254.

(7) K. Kataoka, T. D. James, Y. Kubo, *J. Am. Chem. Soc.* **2007**, *129*, 15126.

(8) N. Christinat, R. Scopelliti, K. Severin, K. *Angew. Chem. Int. Ed.* **2008**, *47*, 1848.

(9) N. Nishimura, K. Kobayashi, *Angew. Chem. Int. Ed.* **2008**, *47*, 6255.

(10) D. Xu, R. Warmuth, *J. Am. Chem. Soc.* **2008**, *130*, 7520.

(11) K. Acharyya, S. Mukherjee, P. S. Mukherjee, *J. Am. Chem. Soc.* **2013**, *135*, 554.

(12) H. Piotrowski, K. Polborn, G. Hilt, K. Severin, *J. Am. Chem. Soc.* **2001**, *123*, 2699.

(13) R. Chakrabarty, P. S. Mukherjee, P. J. Stang, *Chem. Rev.* **2011**, *111*, 6810.

(14) D. J. Tranchemontagne, Z. Ni, M. O'Keeffe, O. M. Yaghi, *Angew. Chem. Int. Ed.* **2008**, *47*, 5136.

(15) D. J. Cram, D. M. Cram, *Container molecules and their guests*; Royal Society of Chemistry: Cambridge, 1997.

(16) P. T. Corbett, J. Leclaire, L. Vial, K. R. West, J. -L. Wietor, J. K. M. Sanders, S. Otto, *Chem. Rev.* **2006**, *106*, 3652.

(17) S. R. Beeren, J. K. M. Sanders, *J. Am. Chem. Soc.* **2011**, *133*, 3804.

(18) J. F. Folmer-Andersen, J. -M. Lehn, *J. Am. Chem. Soc.* **2011**, *133*, 10966.

(19) Y. Bae, K. Kataoka, *Adv. Drug Deliv. Rev.* **2009**, *61*, 768.

(20) J. Nicolas, S. Mura, D. Brambilla, N. Mackiewicz, P. Couvreur, P. *Chem. Soc. Rev.* **2013**, *42*, 1147.

(21) X. Chen, S. S. Parelkar, E. Henchey, S. Schneider, T. Emrick, *Bioconjug. Chem.* **2012**, *23*, 1753.

(22) M. Fujita, J. Yazaki, K. Ogura, *J. Am. Chem. Soc.* **1990**, *112*, 5645.

(23) T. Tozawa, J. T. A. Jones, S. I. Swamy, S. Jiang, D. J. Adams, S. Shakespeare, R. Clowes, D. Bradshaw, T. Hasell, S. Y. Chong, C. Tang, S. Thompson, J. Parker, A. Trewin, J. Bacsa, A. M. Z. Slawin, A. Steiner A. I. Cooper, *Nat. Mater.* **2009**, *8*, 973.

(24) K. E. Jelfs, X. Wu, M. Schmidtmann, T. J. A. Jones, J. E. Warren, D. J. Adams, A. I. Cooper, *Angew. Chem. Int. Ed.* **2011**, *50*, 10653.

(25) M. J. Bojdys, M. E. Briggs, J. T. A. Jones, D. J. Adams, S. Y. Chong, M. Schmidtmann, A. I. Cooper, *J. Am. Chem. Soc.* **2011**, *133*, 16566.

(26) T. Mitra, K. E. Jelfs, M. Schmidtmann, A. Ahmed, S. Y. Chong, D. J. Adams, A. I. Cooper, *Nat. Chem.* **2013**, *5*, 276.

(27) J. Kalia, R. T. Raines, *Angew. Chem. Int. Ed.* **2008**, *47*, 7523.

(28) M. Holz, H. Weingartner, *J. Magn. Reson. 1969* **1991**, *92*, 115.

(29) P. C. Hiemenz, T. P. Lodge, *Polymer chemistry*; 2nd ed.; CRC Press: Boca Raton, 2007.

Appendix 6-1: Supplementary Information

I. Materials and Instrumentation

Materials. All reagents were obtained from Sigma-Aldrich (Milwaukee, WI) and used as received. Anhydrous DMF was dried using a column (Al_2O_3) under Ar atmosphere on a custom built solvent purification system. Chlorobenzene for the Balz-Schiemann reaction was dried over activated sieves.

Instrumentation. Infrared spectra of solid samples were recorded using a Thermo Nicolet iS10 FT-IR spectrometer with a diamond ATR attachment and are uncorrected. In situ IR measurements were conducted on a Mettler Toledo ReactIR ic10 with spectra acquired at 10 s intervals. Peaks corresponding to monomer hydrazide and aldehyde stretches were determined in advance by acquiring a spectrum of the pristine compounds in the corresponding solvent.

NMR spectra were recorded on a Varian INOVA 500 MHz spectrometer using a standard $^{1}H\{^{13}C, ^{15}N\}$ Z-PFG probe with a 20 Hz sample spin rate.

Dynamic light scattering measurements were conducted on a Malvern Zetasizer Nano-ZS equipped with a 4 mW He-Ne laser emitting at 633 nm. Measurements were optimized before each run and were taken in triplicate. The data were analyzed using Malvern Zetasizer Series Software v7.02.

MALDI mass spectroscopy was performed on a Waters MALDI Micro MX equipped with a reflectron detector and operating in positive mode. Samples were prepared by first spotting the matrix followed by the reaction mixture and allowed to dry before placing the sample plate in the instrument. Note that the instrument was miscalibrated during the acquisition

of the data plotted in Figures 6.14 and 6.15 such that the peaks are off by ~1 amu. This does not affect the conclusions drawn from the data.

II. Experimental Protocols

Figure A6.1 Synthetic route to dihyrazide **1.**

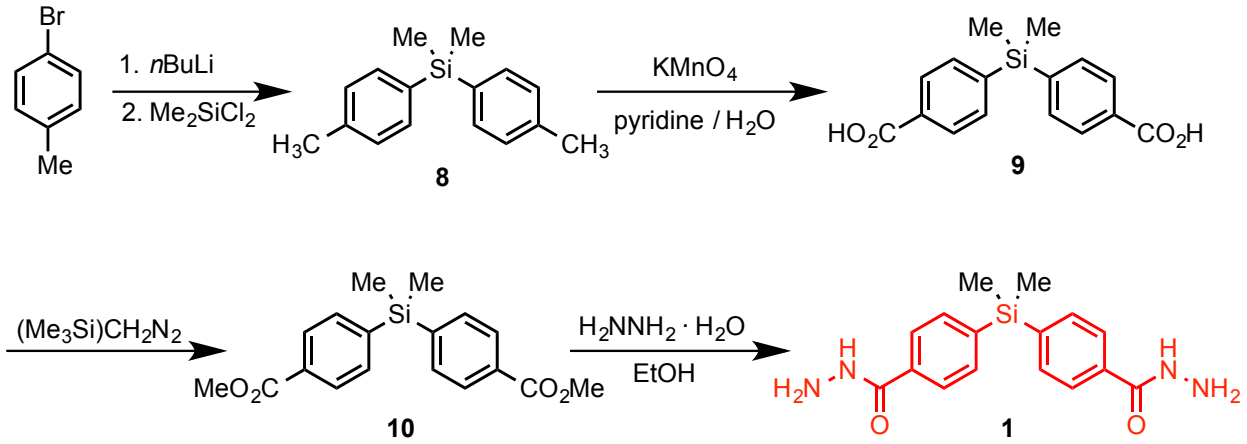

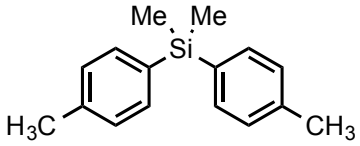

Ditolyldimethylsilane (8). Bromotoluene (5.0 g, 29.2 mmol) was added to a dry 250 mL round bottom flask equipped with a stir bar and a three-way vacuum adapter under N_2. Next, THF (117 mL, 0.250 M) was added and the solution was cooled to -78 C with a dry ice-acetone bath. After stirring for 10 min, *n*-BuLi (15.4 mL, 2.0 M in hexanes, 30.7 mmol) was added to the solution and it was allowed to stir for 30 min. Dichlorodimethylsilane (1.76 mL, 14.6 mmol) was then added to the reaction mixture, which was then stirred for 1 h. After that, the reaction was quenched with saturated $NH_4Cl_{(aq)}$, extracted with dichloromethane, and isolated. The crude product was run through a plug of SiO_2 and isolated as a white solid (3.60 g, >99%) Note: a 7% impurity by ^{1}H NMR was observed on this scale, but did not interfere with subsequent reactions.

8: ^{1}H NMR (400 MHz, $CDCl_3$, 298 K) δ 7.42 (AA'BB', Ar-**H**, 4H), 7.17 (m, Ar-**H**, 4H), 2.36 (s, Ar-C**H**$_3$, 6H), 0.53 (s, Si-C**H**$_3$, 6H).

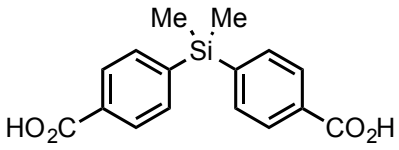

Benzoicacid-4,4'-bis(dimethylsilane) (**9**). **8** (2.54 g, 10.6 mmol) was suspended in a mixture of H_2O (6.45 mL) and pyridine (13.6 mL) in a 50 mL round bottom flask equipped with a stir bar and reflux condenser. $KMnO_4$ (13.4 g, 84.6 mmol) was added slowly through the condenser and the reaction was heated to reflux for 1.67 h. Upon completion of the reaction, the brown reaction mixture was allowed to cool to room temperature and MeOH was added. Next, the crude suspension was filtered through celite and volatile solvents were removed by rotary evaporation. Finally, the reaction mixture was acidified to pH = 1 and the resulting white precipitate was isolated by filtration (2.67 g, 83.9%). Any impurities present were carried to the next step. **9**: ^{1}H NMR (400 MHz, DMSO-d_6, 298 K) δ 7.94 (AA'BB', Ar-**H**, 4H), 7.63 (AA'BB', Ar-**H**, 4H), 0.59 (s, Si-C**H**$_3$, 6H).

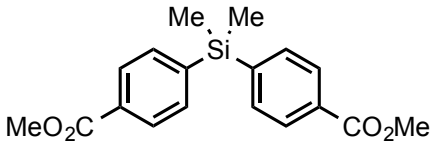

Methylbenzoate-4,4'-bis(dimethylsilane) (**10**). **9** (2.473 g, 8.2 mmol) was dissolved in a mixture of PhMe / MeOH (3:2 *v/v*, 54.9 mL, 0.15 M) in a 100 mL round bottom flask equipped with a stirbar. Next, (trimethylsilyl)diazomethane (9.9 mL of 2.0 M in Et_2O, 19.8 mmol) was added dropwise (**DANGER**: this reagent is a potent vasodilator and should be handled with extreme care, a deep breath of this will kill you). The reaction was allowed to stir at room temperature for 30 min, at which time the remaining (trimethylsilyl)diazomethane was quenched with acetic acid. The solvents and newly formed methyl acetate were removed in

vacuo and the crude product was chromatographed on SiO_2 to yield a white solid (1.28 g, 47.2%). **10**: ^{1}H NMR (400 MHz, $CDCl_3$, 298 K) δ 7.98 (AA'BB', Ar-**H**, 4H), 7.56 (AA'BB', Ar-H, 4H), 3.92 (s, -$CO_2C\mathbf{H}_3$, 6H), 0.60 (s, Si-C$\mathbf{H}_3$, 6H).

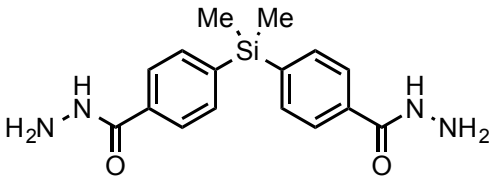

Benzhydrazide-4,4'-bis(dimethylsilane) 1. **10** (0.850 g, 2.59 mmol) was dissolved in EtOH (25.9 mL, 0.1 M) in a 50 mL round bottom flask equipped with a stirbar. Hydrazine hydrate (1.51 mL, 31.1 mmol) was added and the solution was heated to reflux for 18 h, during which time a precipitate formed. Upon cooling, even more precipitate crashed out as needles. The precipitate was isolated by filtration and dried in vacuo to yield **1** (0.812 g, 95.6%). **1**: ^{1}H NMR (500 MHz, DMSO-d_6, 298 K) δ 9.77 (s, CON**H**NH_2, 2H), 7.78 (AA'BB', Ar-**H**, 4H), 7.57 (AA'BB', Ar-**H**, 4H), 4.51 (s, CONHN$\mathbf{H}_2$, 4H), 0.57 (s, Si-C$\mathbf{H}_3$, 6H). ^{13}C NMR (125 MHz, DMSO-d_6, 298 K) δ 165.8, 141.1, 134.0, 133.8, 126.1, 0.12.

Figure A6.2 Synthetic route to trialdehyde **2**.

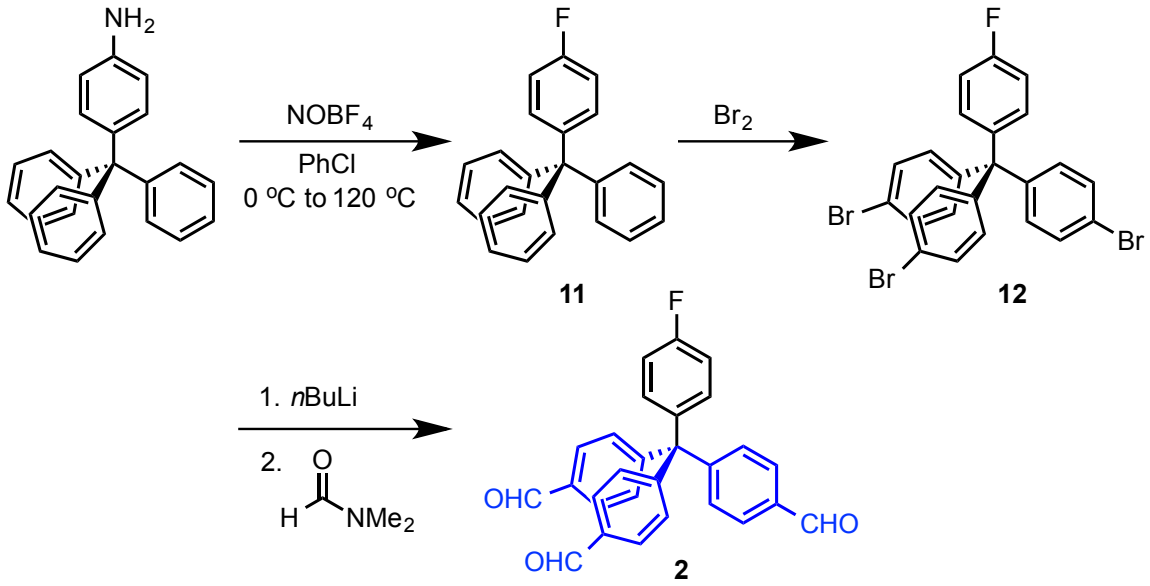

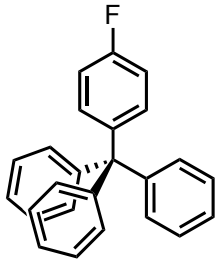

4-fluorotetraphenylmethane (**11**). Tritylaniline (2.0 g, 5.96 mmol) and nitrosyl tetrafluoroborate were added to a 250 mL round bottom equipped with a condenser and three-way vacuum adapter under N_2. The flask was placed in an ice bath, PhCl (60 mL, 0.1 M) was added, and the reaction mixture was allowed to stir for 1 h. After that, the reaction mixture was heated to 120 °C, during which time there was gas (BF_3) evolution. After gas evolution ceased (3 h), the reaction was cooled ot room temperature, quenched with saturated $NH_4Cl_{(aq)}$, and the aqueous phase was extracted three times with dichloromethane. The crude product was purified by sublimation to yield **11** as a white or off yellow solid (1.05 g, 51.8%). **11**: ^{1}H NMR (400 MHz, $CDCl_3$, 298 K) δ 7.25 (m, 7H), 7.19 (m, 12 H), 6.93 (t, 2H). ^{19}F NMR (375 MHz, $CDCl_3$, 298 K) δ -117.29.

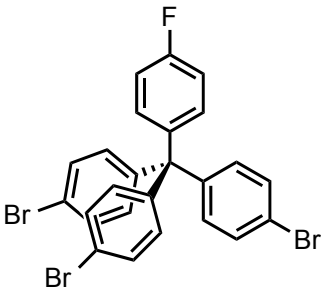

4-fluoro-4',4",4'"-tribromotetraphenylmethane (**12**). **11** (1.25 g, 3.69 mmol) was dissolved in neat Br_2 (1 mL, 19.5 mmol) and allowed to stir for 30 minutes. After that, the remaining bromine and HBr were removed in vacuo. The remaining solid was dissolved in $CHCl_3$ and run through a plug of SiO_2 to yield a white solid (2.23 g, >99%). **12**: ^{1}H NMR (400 MHz, $CDCl_3$, 298 K) δ 7.38 (AA'BB', Ar-**H**, 6H), 7.09 (AA'BB'C, Ar'-**H**, 2H), 7.00 (AA'BB', Ar-**H**, 6H), 6.96 (AA'BB'C, Ar'-**H**, 2H). ^{19}F NMR (375 MHz, $CDCl_3$, 298 K) δ -115.87.

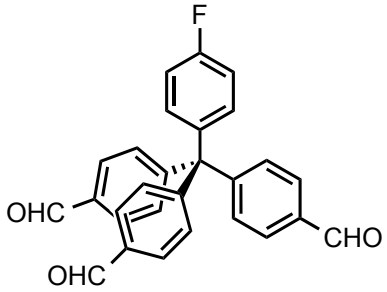

4-fluoro-4',4",4"'-tricarboaldelhydetetraphenylmethane (**2**). **12** (1.0 g, 1.74 mmol) was dissolved in anhydrous THF (116 mL, 0.015 M) under N_2 in a 250 mL round bottom flask

equipped with a stir bar and three-way vacuum adapter. The solution was then cooled to -78 °C and *t*-BuLi (11.0 mmol) was added dropwise. The reaction was allowed to stir for 45 min after which time dimethylformamide (1.6 mL, 20.9 mmol) was added all at once. The reaction mixture was then allowed to warm to room temperature and quenched with $HCl_{(aq)}$ (1 M, 15 mL). The aqueous layer was extracted three times with dichloromethane and solvents were removed *in vacuo*. The crude product was then purified by column chromatography (SiO_2) from to yield **2** (0.319 g, 43.3%). **2**: ^{1}H NMR (400 MHz, $CDCl_3$, 298 K) δ 10.01 (s, Ar-CHO, 3H), 7.81 (AA'BB', Ar-**H**, 6H), 7.40 (AA'BB', Ar-**H**, 6H), 7.17 (AA'BB'C, Ar'-**H**, 2H), 7.01 (AA'BB'C, Ar'-**H**, 2H). ^{19}F NMR (375 MHz, $CDCl_3$, 298 K) δ -114.86.

Figure A6.3 Synthetic route to trialdehyde **3**.

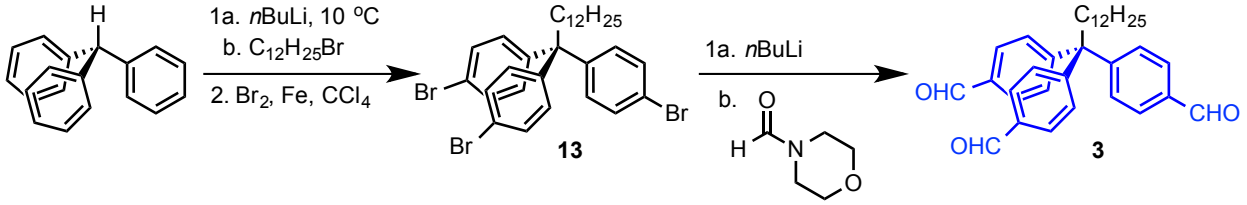

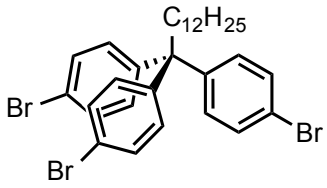

1,1',1"-tris(4-bromophenyl)tridecane (**13**) was synthesized according to Appendix 2-1, pp. 38-39.

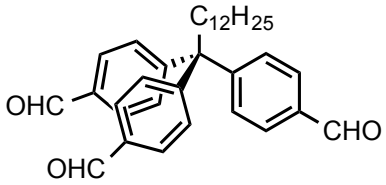

Tridecane-1,1',1"-tri(phenylcarboxaldehyde) (**3**). In a dry, degassed 250 mL round bottom flask, **13** (1.0 g, 1.54 mmol) was dissolved in anhydrous THF (103 mL, 0.015 M). The solution was cooled to -78 °C and *n*-BuLi (4.9 mL, 2.0 M in hexanes, 9.7 mmol) was added dropwise. After 45 min, 4-formylmorpholine (1.47 mL, 18.5 mmol) was added all at once and allowed to stir for 30 min. Next, the reaction mixture was quenched with $HCl_{(aq)}$ (15 mL, 1 M). The aqueous phase was extracted three times with dichloromethane and the solvent was then removed from

the combined organic fractions. The crude product was purified with column chromatography (SiO_2) to yield a yellow oil (0.176 g, 23%) that slowly solidified over months. **3**: ^{1}H NMR (400 MHz, $CDCl_3$, 298 K) δ 10.00 (s, C**H**O, 3H), 7.81 (AA'BB', Ar-**H**, 6H), 7.41 (AA'BB', Ar-H, 6H), 2.62 (m, Ar_3C-C**H**$_2$-CH_2-, 2H), 1.22 (br m, -(C**H**$_2$)$_8$- 18H), 1.02 (m, Ar_3C-$(CH_2)_{10}$-C**H**$_2$-CH_3, 2H) 0.87 (t, Ar_3C-$(CH_2)_{11}$-C**H**$_3$, 3H).

Figure A6.4 Synthetic route to next generation monomer.

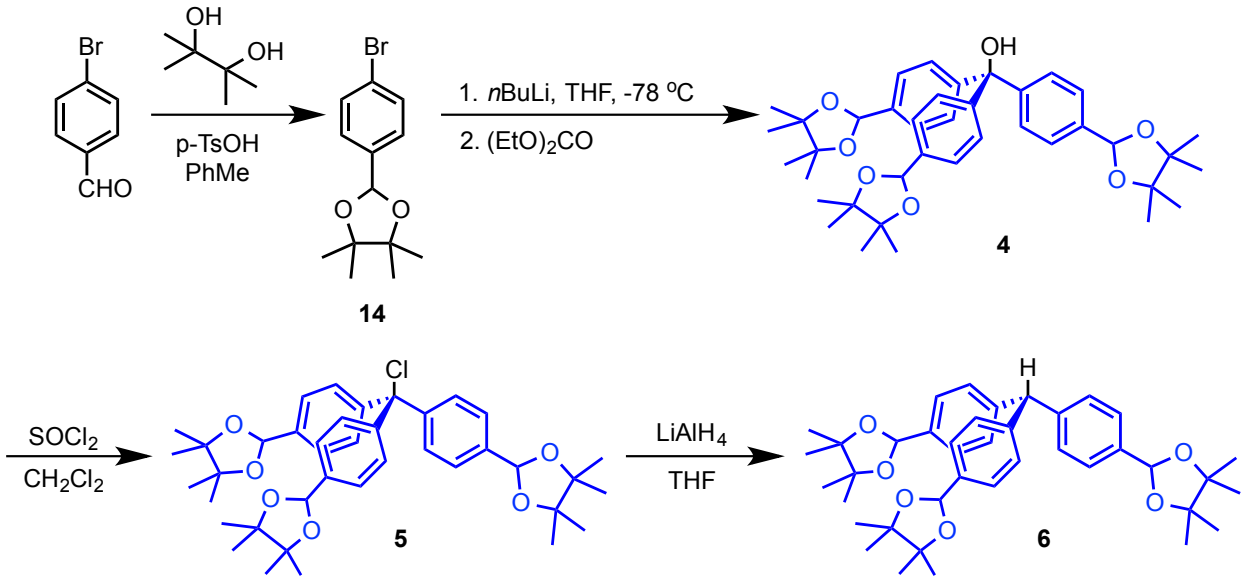

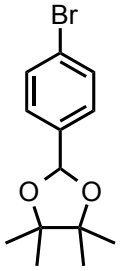

14. Bromobenzaldehyde (6.5 g, 35.1 mmol), pinacol (8.3 g, 70.26 mmol), and *p*-toluenesulfonic acid (0.668 g, 3.51 mmol) were added to a dry 500 mL round bottom flask and equipped with activated sieves, a stir bar, a condenser, and a three-way vacuum inlet adapter. Next, PhMe (175 mL, 0.2 M) was added and the reaction mixture was heated to reflux for 18 h. After that, the reaction was allowed to cool to room temperature, the sieves were removed by filtration, and the volatiles were removed in vacuo. The crude product was then purified with flash column chromatography (SiO_2, 5% EtOAc in hexanes) to afford white soild (3.44 g, 34.3%) as white crystals. **14**: ^{1}H NMR (400 MHz, $CDCl_3$,

298K) δ 7.47 (AA'BB', Ar-**H**, 2H), 7.35 (AA'BB', Ar-**H**, 2H), 5.93 (s, -C**H**-(O-C(CH_3)$_2$)$_2$, 1H), 1.31 (s, -CH-(O-C(C**H**$_3$)$_2$)$_2$, 6H), 1.24 (s, -CH-(O-C(C**H**$_3$)$_2$)$_2$, 6H).

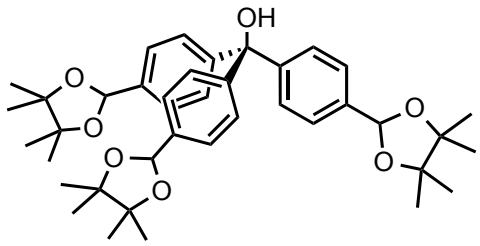

4. **14** (0.752 g, 2.64 mmol) was added to a dry, degassed 25 mL round bottom flask equipped with a stir bar and three-way vacuum adapter. Anhydrous THF (12.0 mL, 0.063 M) was added and the solution was subsequently cooled to -78 C. Next, *n*-BuLi (0.96 mL, 2.5 M in hexanes, 2.4 mmol) was added dropwise and the reaction mixture was allowed to stir for 45 min. After the lithation was complete, the reaction was quenched with diethylcarbonate (0.091 mL, 0.753 mmol) and allowed to warm to room temperature. The reaction was then quenched with saturated $NH_4Cl_{(aq)}$. The aqueous layer was extracted three times with dichloromethane and the resulting crude product was recrystallized from PhMe to yield white needles (0.536 g, 71%). **4**: δ ^{1}H NMR (400 MHz, $CDCl_3$, 278 K): 7.40 (AA'BB', Ar-**H**, 6H), 7.24 (AA'BB', Ar-**H**, 6H), 5.96 (s, Ar-C**H**-, 3H), 2.70 (s, Ar_3C-O**H**, 1H), 1.32 (s, -CH-(O-C(C**H**$_3$)$_2$)$_2$, 6H), 1.27 (s, -CH-(O-C(C**H**$_3$)$_2$)$_2$, 6H).

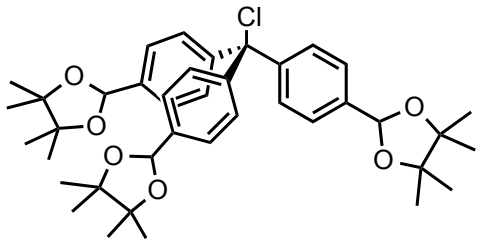

5. **4** (0.050 g, 0.078 mmol) was added to a dry, degassed 25 mL Schlenk tube equipped with a stir bar. Anhydrous dichloromethane (0.78 mL, 0.1 M), followed by thionyl chloride (0.031 mL, 0.426 mmol) were added and the reaction was allowed to stir for 8 h. After full conversion, the solvent and thionyl chloride were removed *in vacuo*. Note: the trityl chloride hydrolyzes on SiO_2, impeding monitoring by TLC. This yielded an off-white powder (0.052 g, >99%), which was stored in a desiccator or taken

directly to the next step. **5**: δ ^{1}H NMR (400 MHz, $CDCl_3$, 278 K): 7.39 (AA'BB', Ar-**H**, 6H), 7.20 (AA'BB', Ar-H, 6H), 5.96 (s, Ar-C**H**-, 3H), 1.32 (s, -CH-(O-C(C**H**$_3$)$_2$)$_2$, 6H), 1.28 ((s, -CH-(O-C(C**H**$_3$)$_2$)$_2$, 6H).

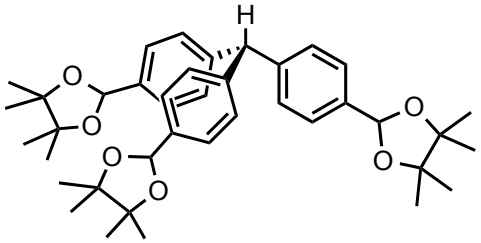

6. **5** (0.050 g, 0.078 mmol) and $LiAlH_4$ (0.015 g, 0.388 mmol) were added to a dry, degassed 25 mL Schlenk tube equipped with a stir bar and three-way vacuum adapter and subsequently placed in an ice bath (0 °C). Anhydrous THF (1.6 mL, 0.05 M) was added slowly and the reaction was allowed to stir for x h. After that, the reaction was quenched with saturated $NH_4Cl_{(aq)}$ (1 mL) and the aqueous layer was extracted three times with dichloromethane. The combined organic fractions were dried (MgSO4) and condensed *in vacuo*. The crude product was then purified by running it through a plug of SiO_2 to yield a white solid (0.033 g, 66.3%). **6**: δ ^{1}H NMR (400 MHz, $CDCl_3$, 278 K): 7.37 (AA'BB', Ar-**H**, 6H), 7.06 (AA'BB', Ar-**H**, 6H), 5.94 (s, Ar-C**H**-, 3H), 5.53 (s, Ar_3C-**H**, 1H) 1.31 (s, -CH-(O-C(C**H**$_3$)$_2$)$_2$, 6H), 1.27 ((s, -CH-(O-C(C**H**$_3$)$_2$)$_2$, 6H).

Synthetic route to hydrazone-linked cages.

Aryl fluoride functionalized cage. **1** (6 mg, 0.018 mmol) and **2** (5 mg, 0.012 mmol) were dissolved in a mixture of DMSO and dioxane (1:2 *v/v*, 1.18 mL) and transferred either to an NMR tube or 5 mL ampoule. Next, glacial acetic acid (4.5 μL) was added. The mixture was flash frozen and the vessel was sealed under ambient pressure and then heated for 4 – 11 d at 90 °C.

Dodecyl functionalized cage. The procedure above was followed, except using a mixture of **1** and **3** were dissolved in 1.01 mL of solvent mixture and 3.5 μL glacial acetic acid were used. For

^{1}H NMR studies, 5 mg (0.015 mmol) of **1** and 5 mg (0.010 mmol) of **3** were used. For DLS kinetics, 74 mg (0.227 mmol) **1** and 75 mg (0.151 mmol) **3** were dissolved in 15.1 mL solvent mixture and 52.5 μL glacial acetic acid.

III. ^{1}H NMR Spectra

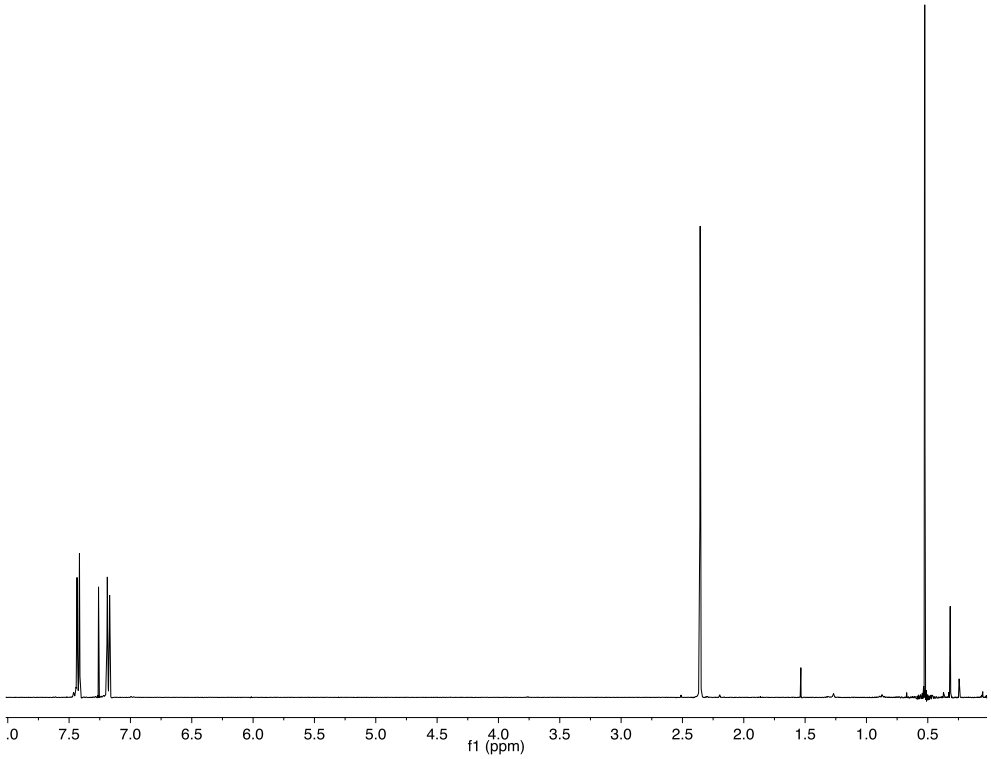

Figure A6.5 ^{1}H NMR spectrum of compound **8** (400 MHz, $CDCl_3$).

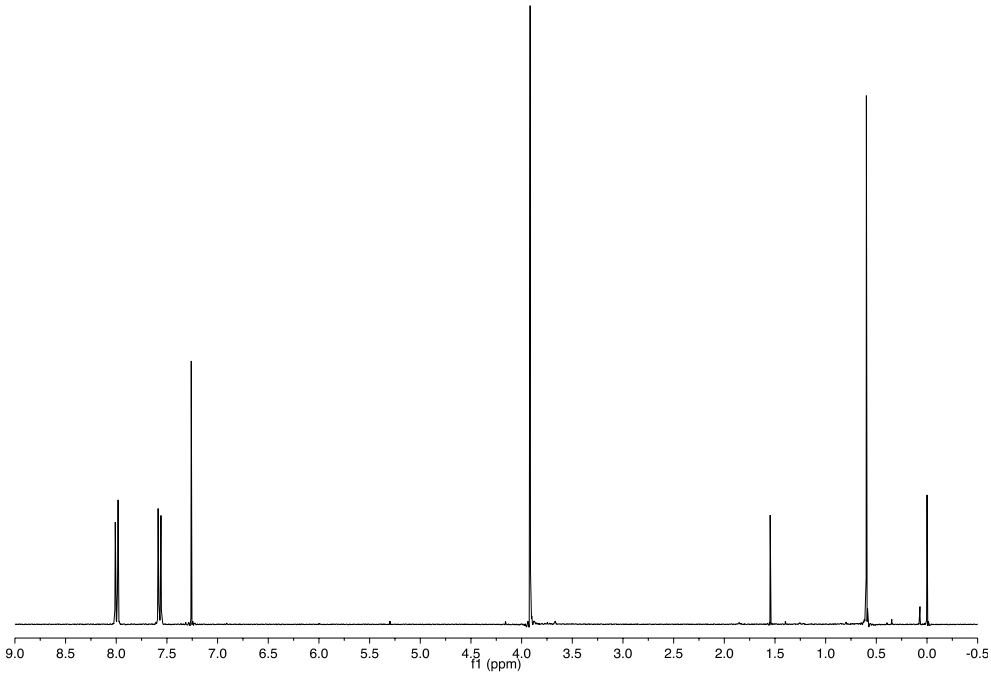

Figure A6.6 ^{1}H NMR spectrum of compound **10** (400 MHz, $CDCl_3$).

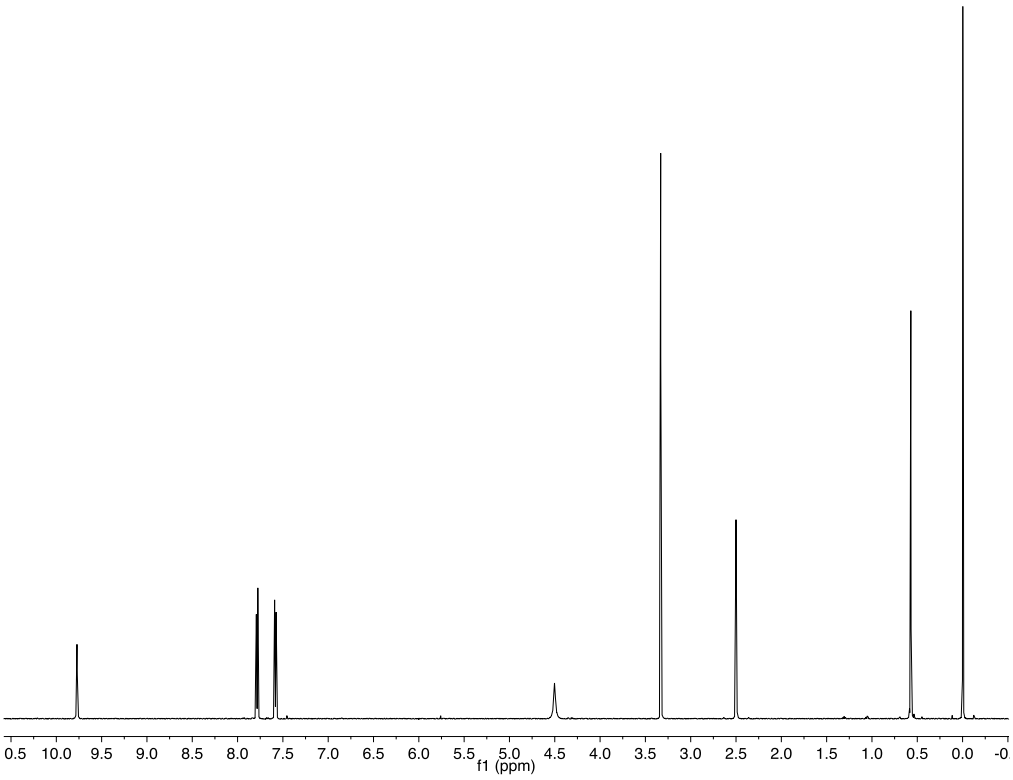

Figure A6.7 ^{1}H NMR spectrum of compound **1** (500 MHz, DMSO-d_6).

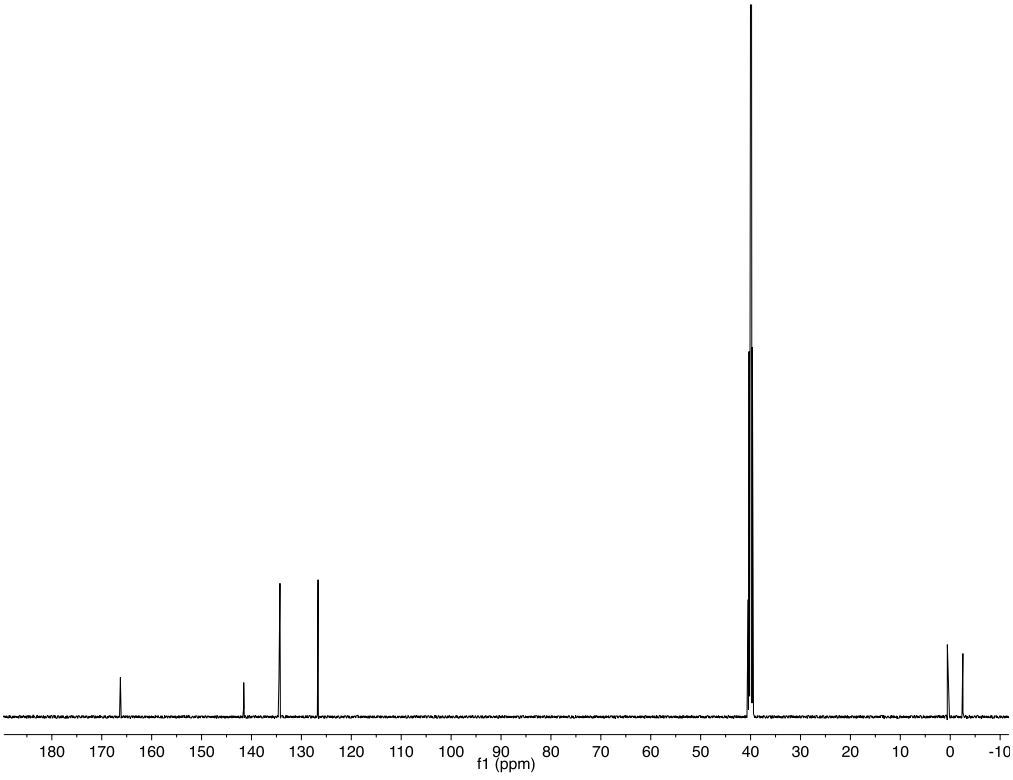

Figure A6.8 ^{13}C NMR spectrum of compound **1** (125 MHz, DMSO-d_6).

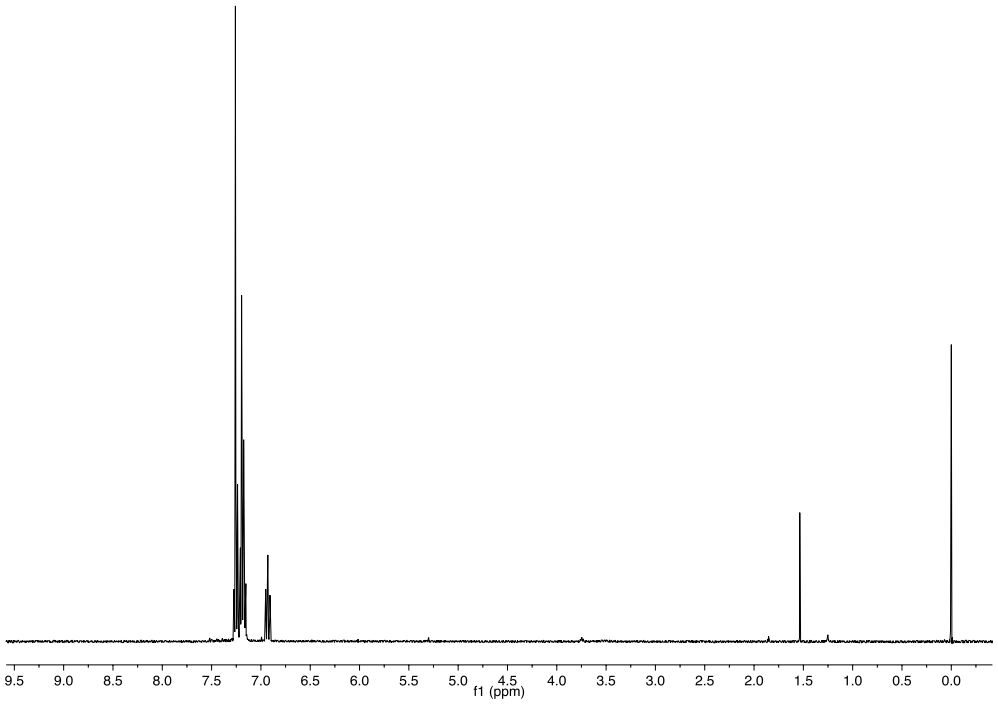

Figure A6.9 ^{1}H NMR spectrum of compound **11** (400 MHz, $CDCl_3$).

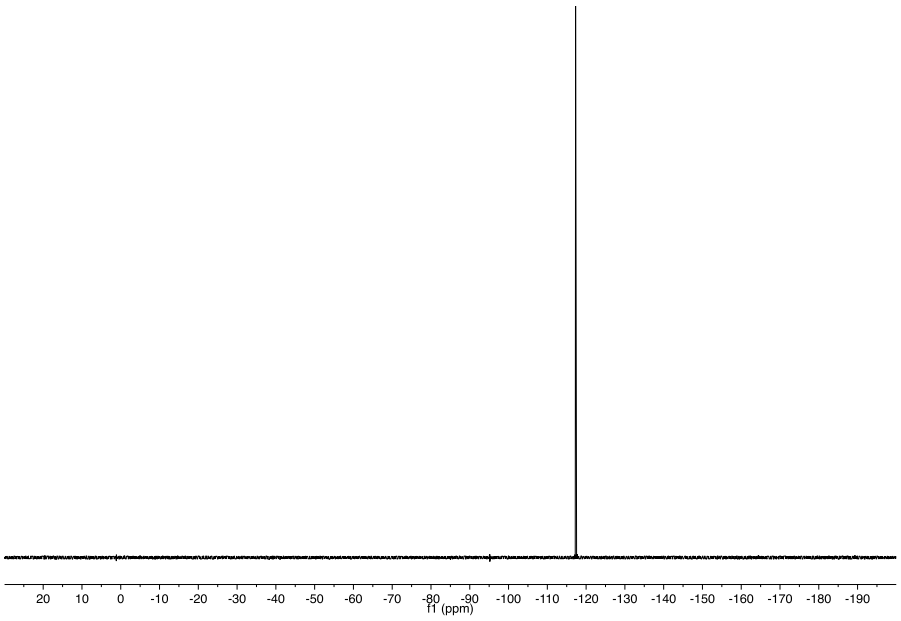

Figure A6.10 ^{19}F NMR spectrum of compound **11** (376 MHz, $CDCl_3$). The signal at -95.17 is likely a quadriture artifact.

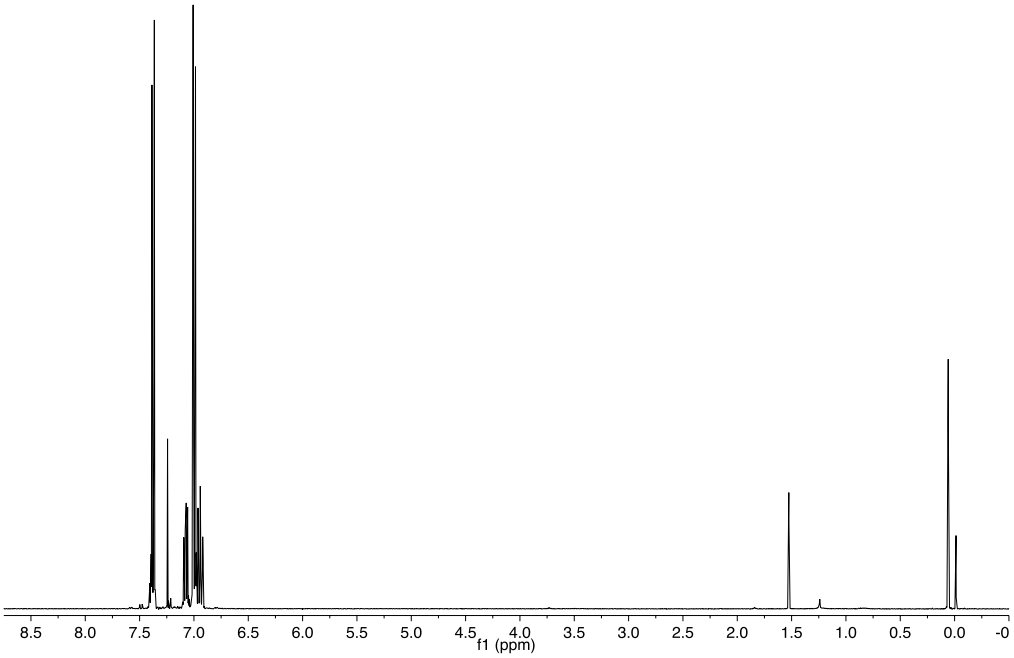

Figure A6.11 ^{1}H NMR spectrum of compound **12** (400 MHz, $CDCl_3$).

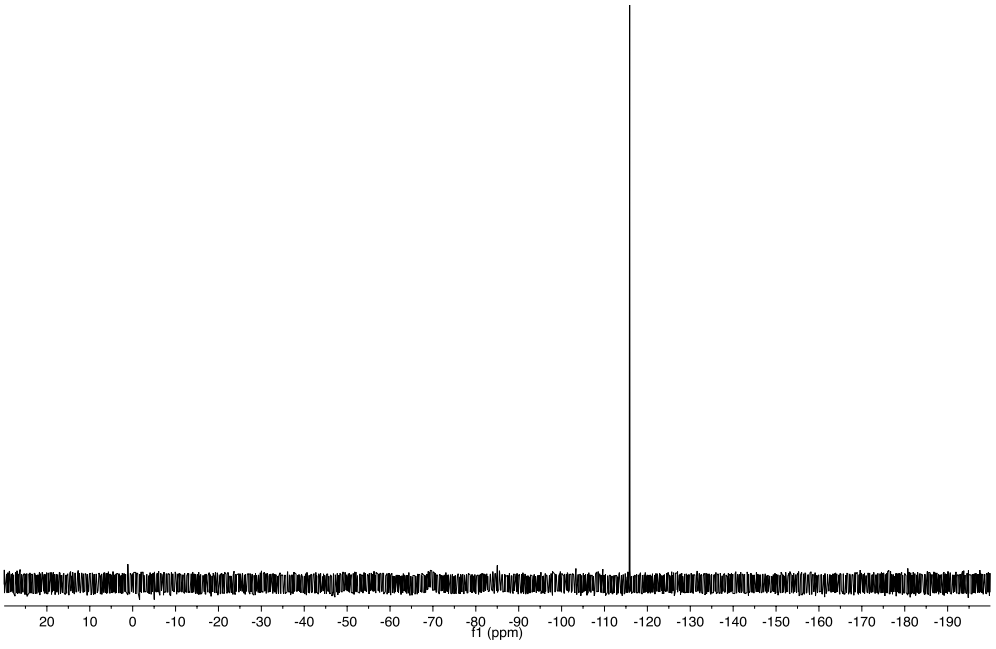

Figure A6.12 ^{19}F NMR spectrum of compound **12** (376 MHz, $CDCl_3$).

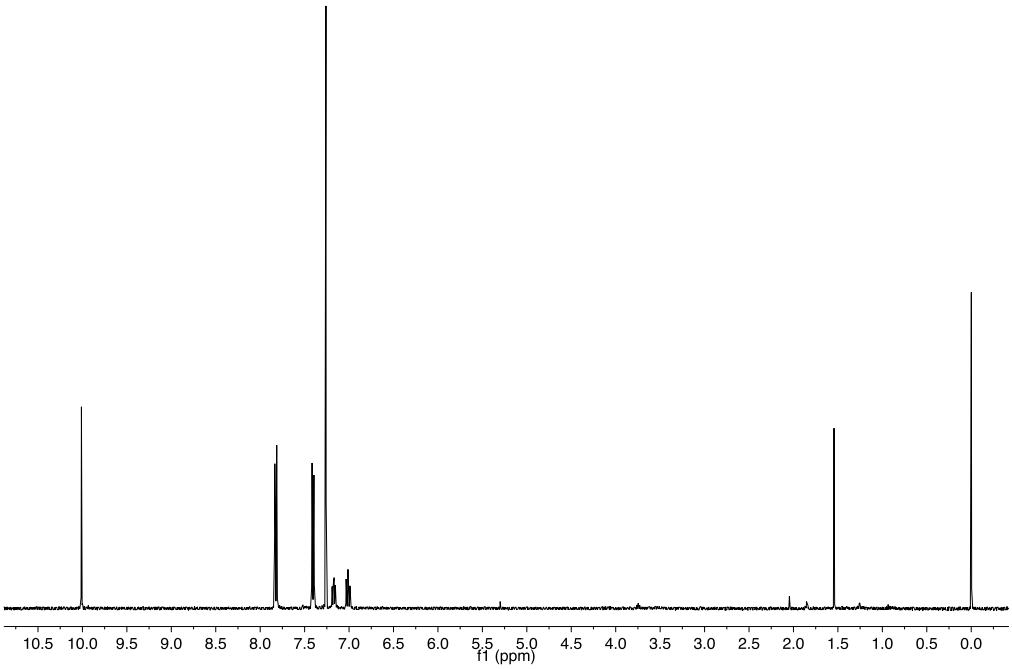

Figure A6.13 ^{1}H NMR spectrum of compound **2** (400 MHz, $CDCl_3$).

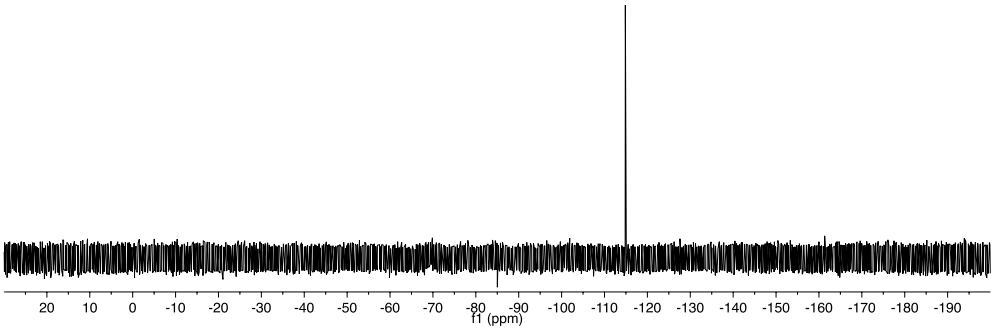

Figure A6.14 ^{19}F NMR spectrum of compound **2** (376 MHz, $CDCl_3$).

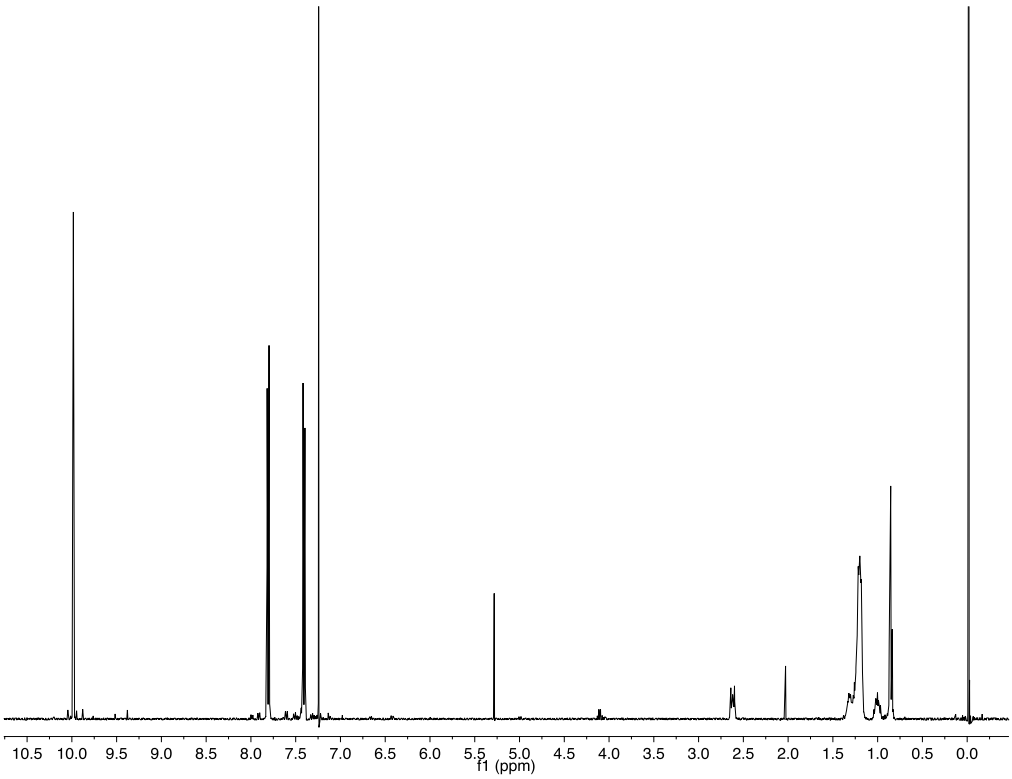

Figure A6.15 ^{1}H NMR spectrum of compound **3** (400 MHz, $CDCl_3$). The resonance at 5.30 ppm is to residual CH_2Cl_2.

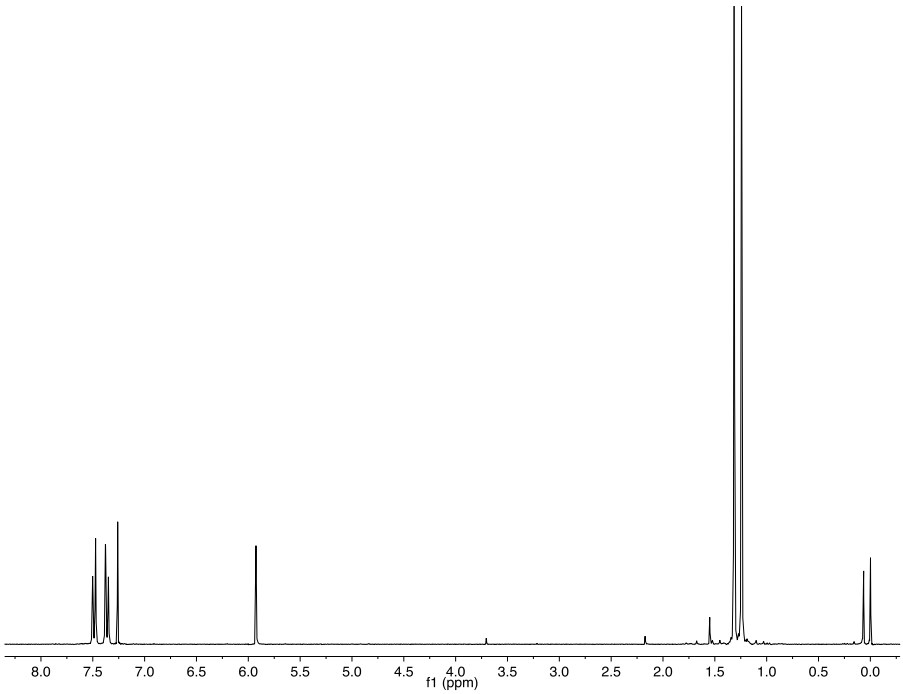

Figure A6.16 ^{1}H NMR spectrum of compound **14** (400 MHz, $CDCl_3$).

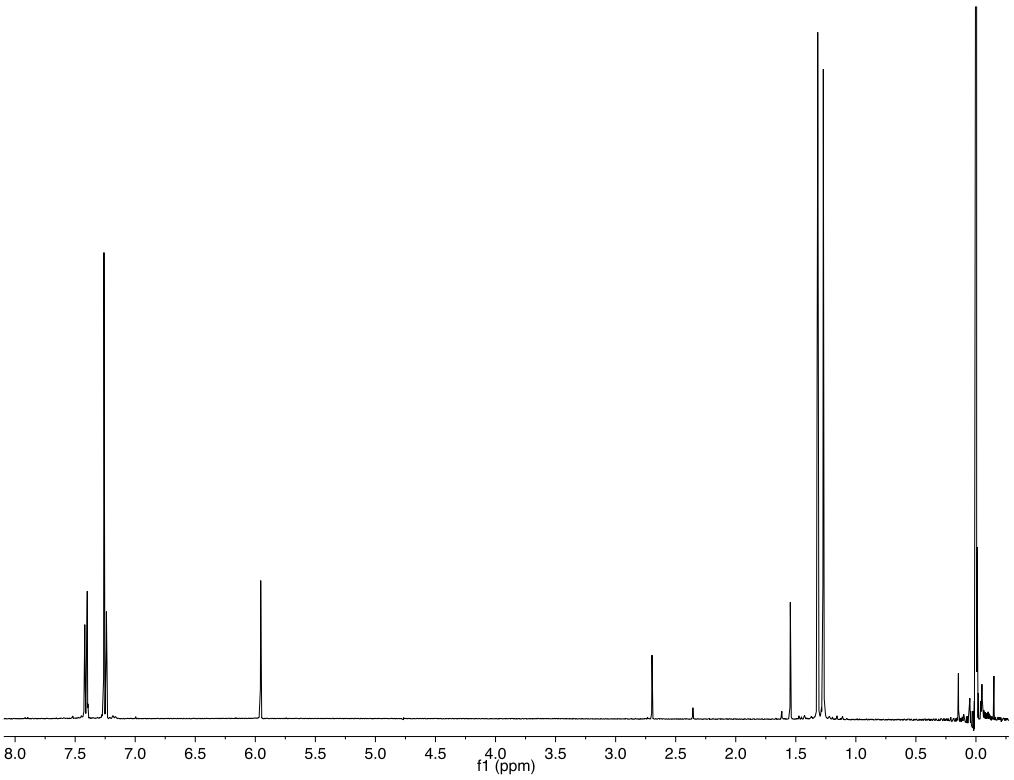

Figure A6.17 ^{1}H NMR spectrum of compound **4** (400 MHz, $CDCl_3$).

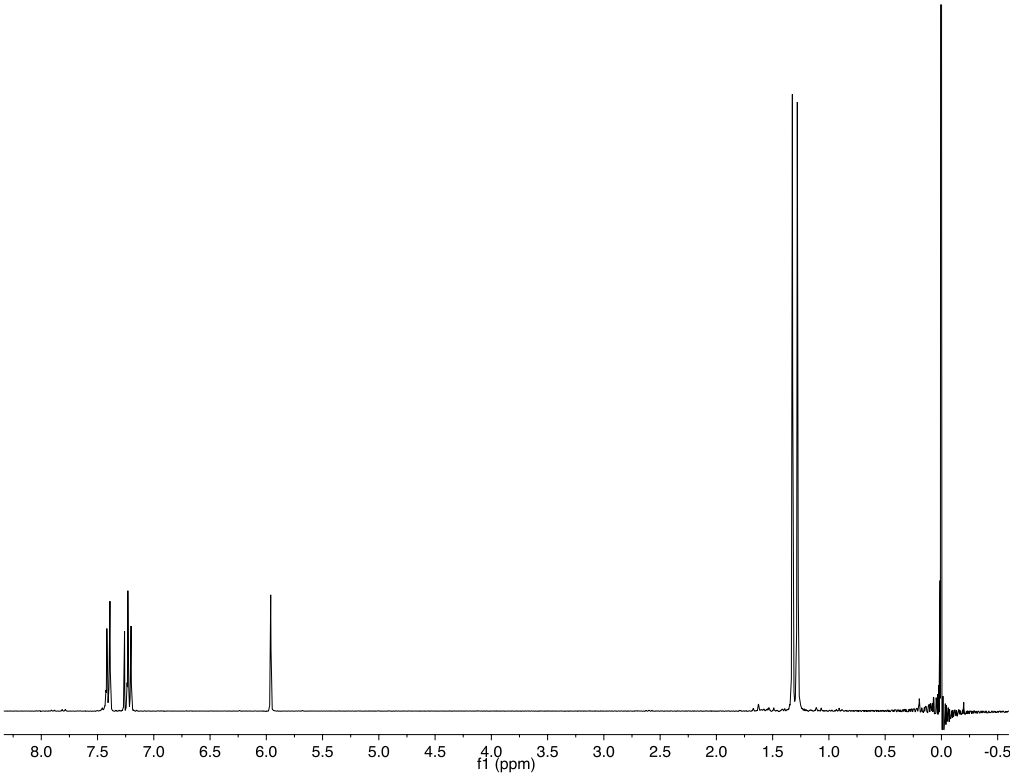

Figure A6.18 ^{1}H NMR spectrum of compound **5** (400 MHz, $CDCl_3$).

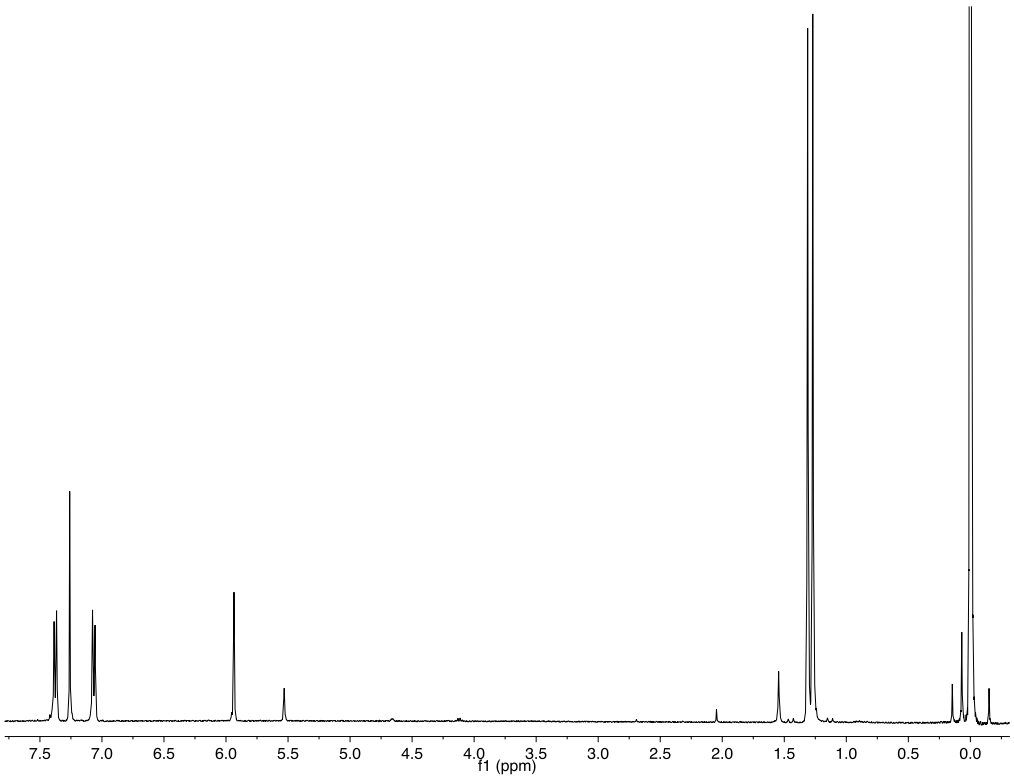

Figure A6.19 ^{1}H NMR spectrum of compound **6** (400 MHz, $CDCl_3$).